Effets du taux de déformation sur la rupture ductile des aciers à haute performance : Expériences et modélisation

Matthieu Dunand

Thèse présentée pour obtenir le grade de

DOCTEUR DE L'ECOLE POLYTECHNIQUE

Spécialité : Mécanique

Par

MATTHIEU DUNAND

Effect of strain rate on the ductile fracture of Advanced High Strength Steel Sheets: Experiments and modeling

Soutenue le 25 juin 2013, devant le jury composé de :

Alexis RUSINEK	LaBPS, ENIM	Président
Tore BØRVIK	SIMLab, NTNU	Rapporteur
Vincent GROLLEAU	LIMB, Univ. Bretagne Sud	Rapporteur
Patricia VERLEYSEN	Universiteit Gent	Examinatrice
Han ZHAO	LMT, ENS Cachan	Examinateur
Gérard GARY	LMS, Ecole Polytechnique	Encadrant
Dirk MOHR	LMS, Ecole Polytechnique	Directeur de thèse

Résumé

L'industrie automobile emploie massivement les Aciers à Haute Performance (AHP) pour la fabrication des caisses en blanc, en raison de leur rapport résistance/masse élevé. Ils sont utilisés afin d'augmenter la sécurité des occupants en cas de crash, ou de réduire la masse du véhicule grâce à une diminution des sections utiles. En parallèle, le prototypage virtuel est omniprésent dans le processus de conception des nouveaux véhicules. En prenant l'exemple d'une caisse en blanc automobile, la conception de la structure globale et des procédés de mise en forme de ses composants nécessite des modèles prédictifs et fiables décrivant le comportement et la rupture des matériaux utilisés. Des efforts soutenus ont été entrepris ces cinq dernières années pour développer des modèles prédisant la rupture des AHP sous chargement statique. Pourtant les taux de déformations rencontrés lors d'opération de mise en forme sont de l'ordre de 10 s^{-1}, et peuvent atteindre 10^3 s^{-1} lors de crashs.

Le but de cette thèse est de développer une méthode fiable permettant d'évaluer l'influence du taux de déformation et de l'état de contrainte sur la rupture ductile d'AHP initialement non-fissurés. Une procédure expérimentale est conçue pour caractériser le comportement et l'initiation de la rupture dans des tôles chargées en traction à grande vitesse de déformation. La précision du dispositif est évaluée grâce à des validations numériques et expérimentales. Par la suite, une série d'expériences est réalisée à petite, moyenne et grande vitesse de déformation sur différents types d'éprouvettes de traction, afin de couvrir un spectre étendu d'états de contraintes. Une analyse détaillée de chaque expérience par la méthode des Éléments Finis permet de déterminer le trajet de chargement et l'état de déformation et de contrainte à la rupture dans chaque éprouvette, tout en prenant en compte les phénomènes de striction. La déformation à la rupture est significativement plus élevée à grande vitesse de déformation qu'à basse vitesse. De plus, les résultats montrent que l'influence du taux de déformation sur la ductilité ne peut pas être découplée de l'état de contrainte.

Le modèle de comportement constitue un élément essentiel de cette approche hybride expérimentale-numérique. Un modèle de plasticité dépendant du taux de

déformation est proposé pour prédire la réponse mécanique des AHP sur toute la plage de déformation, taux de déformation et état de contrainte couverte par le programme expérimental. La précision du modèle est validée par comparaison de mesures expérimentales globales et locales aux prédictions numériques correspondantes. De plus, l'influence de la discrétisation spatiale utilisée dans les simulations par Eléments Finis sur la précision de l'approche hybride expérimentale-numérique est quantifiée. Il est montré qu'un maillage fin d'éléments hexaédriques est nécessaire pour obtenir des prédictions précises jusqu'à la rupture. Ce type de maillage n'est pas compatible avec des applications industrielles à grande échelle pour des raisons évidentes d'efficacité numérique. C'est pourquoi une méthode de remaillage dynamique d'éléments coque vers des éléments solides est présentée et évaluée. Cette méthode permet d'obtenir des prédictions fiables de l'initiation de la rupture dans des tôles sans compromettre dramatiquement l'efficacité numérique obtenue grâce aux éléments coque.

La seconde partie de ce travail s'intéresse aux micro-mécanismes responsables de la rupture ductile du matériau étudié. Une analyse micrographique du matériau soumis à différents niveaux de déformation permet d'identifier l'enchainement des mécanismes d'endommagement. Ces observations suggèrent que le mécanisme critique conduisant à la rupture est la localisation de la déformation plastique dans une bande de cisaillement à l'échelle du grain. Un model numérique reposant sur la déformation d'une cellule élémentaire 3D contenant une cavité est développé pour modéliser ce phénomène. Il est montré que le mécanisme de localisation à l'échelle micro de l'écoulement plastique dans une bande de cisaillement permet d'expliquer la dépendance de la ductilité à l'état de contrainte et au taux de déformation observée à l'échelle macro.

Acknowledgement

Contents

List of figures

List of Tables

Chapter 1
General introduction

Contents

1.1 Industrial context

The automotive industry has widely incorporated Advanced High Strength Steels sheets (AHSS) in vehicle structures due to their high strength to weight ratio: they are used to improve the vehicle safety or to reduce the vehicle weight through the use of thinner gages. At the same time, new vehicle design relies heavily on virtual prototyping practices. In the specific example of automotive structures, both the engineering of the production process and of the final product require reliable models of plasticity and fracture. Consequently, great efforts have been undertaken during the last five years to develop models that can predict the fracture of AHSS under static conditions (e.g. Wierzbicki et al., 2010, [190]). However, rates of deformation encountered in sheet metal forming operations are typically of the order of $10s^{-1}$, while they can be as high as 10^3 s^{-1} under accidental crash loading. Therefore, there is a need to investigate the effect of strain rate on deformation behavior and fracture of AHSS, and to assess whether models developed for static loading conditions can satisfactorily be used in industrial applications.

1.2 Objective and structure of the thesis

This project was carried out in collaboration between the Solid Mechanics Laboratory (CNRS-UMR 7649, Ecole Polytechnique) and the Impact and Crashworthiness Laboratory (Massachusetts Institute of Technology).

The present research work consists of two main parts. The first part aims at developing a reliable methodology for evaluating the influence of strain rate as well as stress state on the ductile fracture properties of initially uncracked Advanced High Strength Steel sheets. An experimental procedure is designed to characterize the deformation behavior and the onset of fracture of sheet materials under tensile loading at high strain rate. Numerical and experimental validations of the proposed setup are performed to evaluate its accuracy. Then an experimental program is carried out at low, intermediate and high strain rates on different type of tensile specimens, thereby covering a range of stress states. Detailed Finite Element analyses of each experiment are used to determine the loading history and the material state at fracture in each experiment. A key component of this hybrid experimental-numerical approach is the constitutive model: a rate-dependent plasticity model is proposed to predict the mechanical response of AHSS over all the range of strains, strain rates and stress states reached in the experiments. The model accuracy is validated by comparing global and local test measurements to the corresponding simulation predictions. In addition, the influence of the geometric discretization used in Finite Element analysis on the accuracy of the hybrid experimental-numerical approach is evaluated. It is shown that fine meshes of brick elements are required for accurate fracture predictions, but cannot be used in industrial applications because of inadequate computational efficiency. A technique of shell-to-solid re-meshing is presented and evaluated, that allows for accurate predictions of the onset of ductile fracture in sheet materials without compromising the numerical efficiency of shell elements.

The second part of this work is concerned with the micro-mechanisms responsible for ductile failure. Micrographs of specimens corresponding to different stages of loading prior to failure are analyzed to identify the sequence of damage processes leading to fracture. Observations suggest that the governing failure mechanism is the localization of plastic deformation into shear bands at the grain level.

A numerical model based on three dimensional unit cell calculations is developed to assess whether the mechanism of shear localization of the plastic flow at the micro-scale can explain the dependence of the material ductility to both stress state and strain rate that was observed at the macro-scale.

The thesis is organized as follow:

In Chapter 2, background information is given on the characterization and modeling of plasticity and ductile fracture of AHSS under static loading conditions. In addition, variables that will be used throughout the manuscript to describe the stress state are precisely defined. Finally, Split Hopkinson Pressure Bar systems, used for characterizing mechanical behavior of materials under compression at high rates of deformation, are presented.

In Chapter 3, a high strain rate tensile testing technique for sheet materials is presented which makes use of a modified split Hopkinson pressure bar system in conjunction with a load inversion device. With compressive loads applied to its boundaries, the load inversion device introduces tension into a sheet specimen. Detailed finite element analysis of the experimental set-up is performed to validate the design of the load inversion device. It is shown that under the assumption of perfect alignment and slip-free attachment of the specimen, the measured stress-strain curve is free from spurious oscillations at a strain rate of $1000s^{-1}$. Validation experiments are carried out using tensile specimens, confirming the oscillation-free numerical results in an approximate manner.

In Chapter 4, the effect of strain rate on ductile fracture properties of the TRIP material is characterized using a hybrid experimental-numerical method. Tensile experiments are carried out at low ($\dot{\varepsilon}\sim10^{-3}s^{-1}$), intermediate ($\dot{\varepsilon}\sim1s^{-1}$) and high strain rates ($\dot{\varepsilon}\sim10^{3}s^{-1}$). The experimental program includes notched as well as uniaxial tension specimens. Local displacements and surface strain fields are measured optically in all experiments using Digital Image Correlation. Constitutive equations derived from the Mechanical Threshold Stress theory are proposed to describe the rate-dependent behavior as well as plastic anisotropy of the sheet material. Detailed Finite Element simulations of all experiments reveal that the model accurately predicts experimental

results, including force displacement curves and local surface strain evolution. In particular, the behavior at large strain (beyond the onset of necking) is well predicted. Stress and strain histories where fracture initiates are also obtained from the simulations in order to characterize the dependence of the material ductility to both strain rate and stress state. If the fracture strain is higher at high strain rate in all experiments, results show that the effect of strain rate on ductility cannot be considered independently from the state of stress.

In Chapter 5, the influence of the finite element modeling on predictions of mechanical response and ductile fracture in sheet structures is analysed. The inability of shell elements to accurately predict the post-necking behavior of sheet materials is highligted. On the contrary predictions independent from the mesh characteristics are obtained with solid elements if sufficiently fine meshes are used. However, intensive computation efforts associated with the use of fine meshes of solid elements to model sheet structures such as automotive parts make it unsuitable to an industrial environment. A dynamic shell-to-solid re-meshing technique is considered to benefit from both the numerical efficiency of shells and the accuracy of fine solid meshes. Comparisons between numercial predictions using re-meshing and experimental results show a significant increase of the accuracy of fracture predictions compared to shell simulations, and substantial time savings compared to solid simulations.

In Chapter 6, the evolution of damage and the mechanisms responsible for ductile failure are identified in the TRIP steel sheet submitted to different stress states, using optical and scanning electron microscopy. Experiments are performed on tensile specimens and on disk specimens submitted to out-of-plane hemispherical punching, thereby covering stress states from uniaxial to equi-biaxial tension. For each specimen geometry, experiments have been interrupted prior to fracture at different stages of deformation: onset of through the thickness necking and 95%, 99% of the displacement at which fracture initiates. Micrographs of samples extracted from the deformed specimens permit to evaluate the material damage for increasing amounts of accumulated plastic strain, and identify rupture mechanisms. It is shown that the critical mechanism responsible for material failure is the localization of the plastic deformation in a shear band initiating at a grown and isolated void. The orientation of the fracture surface is controlled by the shear band direction.

In Chapter 7, a numerical model is developped to investigate the influence of the stress state and strain rate on the onset of localization of the plastic flow in a void-containing material. A three-dimensional unit cell containing an initially spherical void is submitted to proportional loadings in the macroscopic stress space. Fully periodic boundary conditions are applied. The range of stress states considered are limited to biaxial tension, i.e. from uniaxial to equi-biaxial tension under plane stress conditions. The model is able to predict qualitatively the dependence of ductility to the stress state observed experimentaly, as well as the increase of ductility at high strain rate.

1.3 Material

All the experimental work presented in this manuscript is performed on specimens extracted from 1.4mm thick TRIP780 steel sheets provided by POSCO (Korea). This particular representative of the AHSS family has been chosen as its plastic behavior and ductile fracture properties under static loading conditions have been extensively studied (Mohr et al., 2010, [122]; Dunand and Mohr, 2010, 2011, [48-50]). The chemical composition of the present TRIP780 material as measured by energy-dispersive X-ray analysis is given in Table 1-1. Micrographs (Fig. 1-1) reveal a fine grain structure with a maximum grain size of about $10\mu m$ and show that martensite and austenite grains (in blue/brown in Fig. 1-1) tend to segregate in bands parallel to the sheet rolling direction.

Table 1-1: Chemical composition of the TRIP780 material in wt-%

C	Al	Mn	Si	Mo
1.70	0.47	2.50	0.59	0.08

TRansformation Induced Plasticity (TRIP) steels present complex multi-phase microstructures consisting of a ferritic matrix and a dispersion of multiphase grains of bainite, martensite and metastable retained austenite (Jacques et al., 2001, [86]). The austenitic phase transforms to martensite when subject to mechanical or thermal loading (e.g. Angel, 1954, [4]; Lecroisey and Pineau, 1972, [103]; Olsen and Cohen, 1975, [142]; Stringfellow et al.,1992, [167]). The austenite-to-martensite formation is displacive which gives rise to internal stresses that may cause the yielding of the surrounding austenite matrix (e.g. Greenwood and Johnson, 1965, [69]). The active formation of martensite substantially increases the macroscopic work-hardening rate while the associated transformation strain contributes to the ductility of TRIP steels.

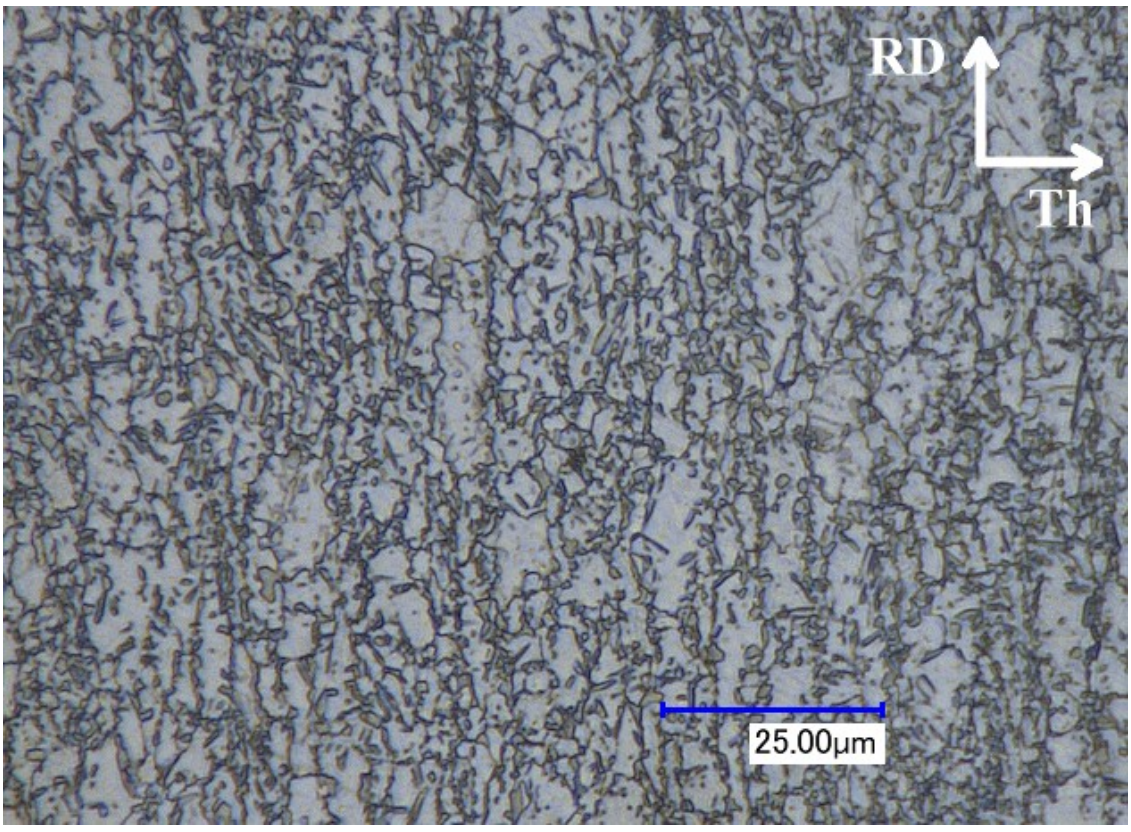

Figure 1-1: Optical micrograph of the undeformed TRIP material. The *RD* and *Th* orientations correspond to the sheet rolling and through-the-thickness directions, respectively.

Chapter 2

Preliminaries

Contents

Abstract

Variables that will be used throughout the manuscript to describe the stress state are precisely defined. In addition, background information is given on the characterization and modeling of plasticity and ductile fracture of AHSS under static loading conditions. Finally, Split Hopkinson Pressure Bar systems, used for characterizing mechanical behavior of materials under compression at high rates of deformation, are presented.

2.1 Characterization of the stress state

2.1.1 Stress invariants

Throughout our discussion, a clear description of the stress state is important. The frame invariant part of the stress is described through the first invariant of the Cauchy stress tensor $\boldsymbol{\sigma}$, and the second and third invariants of the corresponding deviatoric stress tensor, $\boldsymbol{s} = \boldsymbol{\sigma} - (\mathrm{tr}\boldsymbol{\sigma}/3)\mathbf{1}$,

$$I_1 = \mathrm{tr}(\boldsymbol{\sigma}) \tag{2-1}$$

$$J_2 = \frac{1}{2}\boldsymbol{s}:\boldsymbol{s} \tag{2-2}$$

and

$$J_3 = \det(\boldsymbol{s}) \tag{2-3}$$

Note that the hydrostatic stress σ_m and the von Mises equivalent stress σ_{VM} are respectively proportional to the first and second invariants,

$$\sigma_m = \frac{1}{3}I_1 \tag{2-4}$$

$$\sigma_{VM} = \sqrt{3J_2} \tag{2-5}$$

The stress state may be characterized through two dimensionless functions of the above invariants. We define the stress triaxiality η as the ratio of the mean stress and equivalent von Mises stress,

$$\eta = \frac{\sigma_m}{\sigma_{VM}} = \frac{\mathrm{I}_1}{3\sqrt{3J_2}} \tag{2-6}$$

with $-\infty \leq \eta \leq \infty$. The normalized third invariant ξ_3 is written as (Ilyushin, 1963, [84])

$$\xi_3 = \frac{27}{2}\frac{J_3}{{\sigma_{VM}}^3} = \frac{3\sqrt{3}}{2}\frac{J_3}{{J_2}^{\frac{3}{2}}} \tag{2-7}$$

and lies in the range $-1 \leq \xi_3 \leq 1$; it characterizes the position of the second principal stress σ_{II} with respect to the maximum and minimum principal stresses σ_I and σ_{III}.

Alternatively the third invariant can be described in terms of the so-called Lode angle parameter

$$\bar{\theta} = 1 - \frac{2}{\pi}\arccos(\xi_3) \tag{2-8}$$

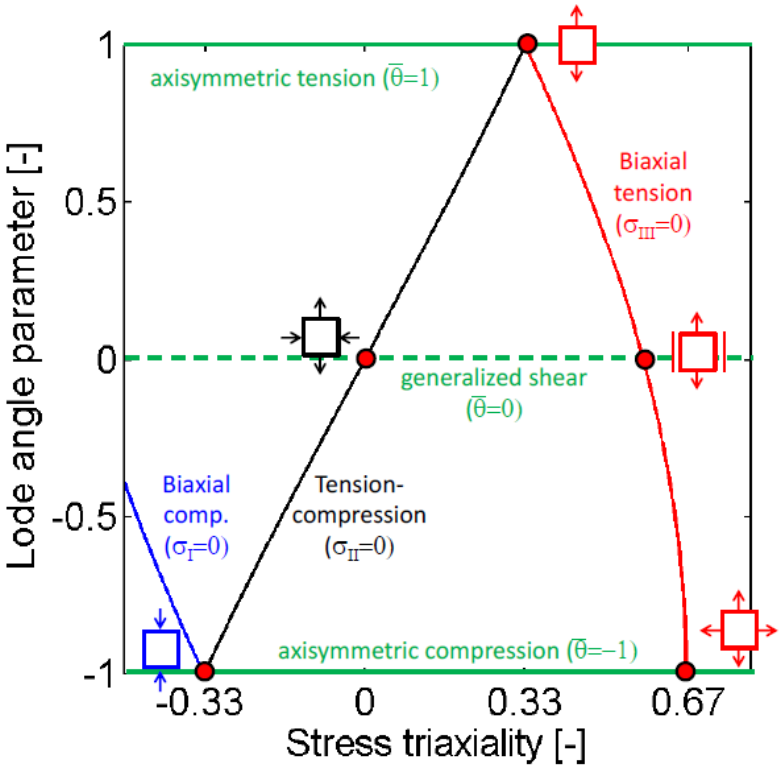

Figure 2-1: Characterization of the stress states in terms of stress triaxiality and Lode angle parameter. The blue, black and red lines highlight the plane stress states as described by Eq. (2-16).

According to the definition above, the Lode angle parameter approximates the negative Lode number μ (Lode, 1925, [113]),

$$\mu = 2\frac{\sigma_{II} - \sigma_{III}}{\sigma_I - \sigma_{III}} - 1 \cong -\bar{\theta} \tag{2-9}$$

Note that the principal stresses σ_I, σ_{II} and σ_{III} are got back using

$$\sigma_I = \bar{\sigma}[\eta + f_I(\bar{\theta})] \tag{2-10}$$

$$\sigma_{II} = \bar{\sigma}[\eta + f_{II}(\bar{\theta})] \tag{2-11}$$

$$\sigma_{III} = \bar{\sigma}[\eta + f_{III}(\bar{\theta})] \tag{2-12}$$

with the deviator dependent functions

$$f_I(\bar{\theta}) = \frac{2}{3}\cos\left(\frac{\pi}{6}(1-\bar{\theta})\right) \tag{2-13}$$

$$f_{II}(\bar{\theta}) = \frac{2}{3}\cos\left(\frac{\pi}{6}(3+\bar{\theta})\right) \tag{2-14}$$

$$f_{III}(\bar{\theta}) = -\frac{2}{3}\cos\left(\frac{\pi}{6}(1+\bar{\theta})\right) \tag{2-15}$$

Throughout this manuscript, the term stress state is employed to make reference to the pair of parameters $(\eta, \bar{\theta})$. Well-known stress states that we will refer to frequently are:

- Uniaxial tension $(\eta = 0.33, \bar{\theta} = 1)$
- Pure shear $(\eta = 0., \bar{\theta} = 0)$
- Generalized shear $(\bar{\theta} = 0)$
- Axisymmetric tension $(\bar{\theta} = 1)$
- Axisymmetric compression $(\bar{\theta} = -1)$

A representation of the $(\eta, \bar{\theta})$ stress state space is depicted in Fig. 2-1.

2.1.2 Plane stress condition

In sheet materials, the plane stress condition often prevails: one of the principal stress directions is parallel to the sheet thickness direction and the corresponding principal stress is equal to zero.

In case of plane stress, the stress triaxiality η and the normalized third invariant ξ are uniquely related according to the relationship

$$\xi_3 = -\frac{27}{2}\eta\left(\eta^2 - \frac{1}{3}\right) \quad \text{for} \quad -\frac{2}{3} \leq \eta \leq \frac{2}{3} \tag{2-16}$$

In this investigation we focus more specifically on stress states in the vicinity of biaxial tension, i.e. plane stress states between uniaxial tension and equi-biaxial tension. In this case the stress triaxiality varies between 1/3 (uniaxial tension) and 2/3 (equi-biaxial

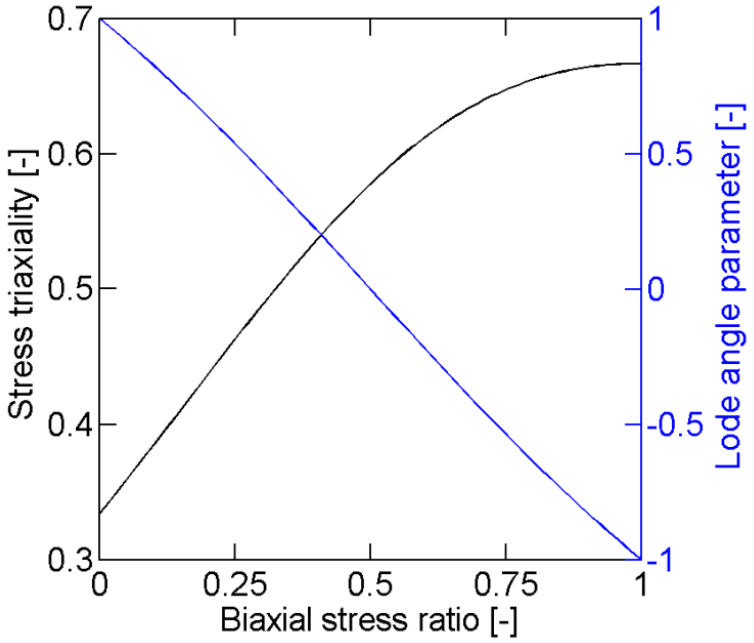

Figure 2-2: Relation between the stress triaxiality η, the Lode angle parameter $\bar{\theta}$ and the stress ratio ψ in case of biaxial stress states.

tension). At the same time, the third invariant decreases from 1 (uniaxial tension) to -1 (equi-biaxial tension).

Denoting $\sigma_I \geq \sigma_{II} \geq \sigma_{III}$, $\sigma_{III} = 0$ the principal values of the Cauchy stress tensor, the stress state in biaxial tension is then fully characterized by the biaxial stress ratio

$$\psi = \frac{\sigma_{II}}{\sigma_I} \tag{2-17}$$

with $0 \leq \psi \leq 1$. The stress triaxiality then reads

$$\eta = \frac{1+\psi}{3\sqrt{\psi^2 - \psi + 1}} \tag{2-18}$$

Figure 2-2 depicts the relationship between the stress triaxiality η (black line in Fig. 2-2) and the Lode angle parameter $\bar{\theta}$ (blue line in Fig. 2-2) to the biaxial stress ratio in case of a biaxial stress state.

2.2 Ductile fracture modeling

Ductile fracture is the result of a progressive material deterioration occurring during plastic deformation, generally identified as the nucleation and growth of micro-voids that ultimately link to form cracks. The early investigations of McClintock (1968, [119]) and Rice and Tracey (1969, [152]) on the evolution of cylindrical and spherical holes in ductile matrices have set the foundation for numerous studies on the micromechanics associated with void growth. The most prominent is that of Gurson (1977, [70]), who proposed a porous plasticity model based on the micromechanical analysis of a thick spherical shell subject to hydrostatic pressure. The model describes the growth of voids and its influence on the material's stress carrying capacity at large mean stresses (but becomes less accurate for shear loads). The original Gurson model has been repeatedly modified to account for additional processes responsible for the material deterioration and subsequent ductile fracture: void nucleation (e.g. Chu and Needleman, 1980, [35]), loss of load-carrying capacity associated with void coalescence (e.g. Tvergaard and Needleman, 1984, [181]), enhanced strain hardening models (e.g. Leblond et al., 1995, [102]), void shape effects (e.g. Gologanu et al., 1993, [67]; Gologanu et al., 1994, [68]; Garajeu et al., 2000, [62]; Pardoen and Hutchinson, 2000, [146]) and plastic anisotropy (e.g. Benzerga et al., 2004, [18]). The reader is referred to Lassance et al. (2007, [100]) and Benzerga and Leblond (2010, [19]) for a comprehensive review of successive improvements of the Gurson model. Gurson type of models are not only used to describe macroscopic plastic behavior of materials with small void volume fractions, but also to predict ductile fracture assuming that fracture occurs as the void volume fraction reaches a critical value. As a result, "traditional" Gurson models are unable to predict fracture under shear-dominated loading conditions, where the void growth mechanism is inactive. Numerical investigations of an initially spherical void contained in a cubic unit cell submitted to various tri-axial loadings (e.g. Zhang et al., 2001, [196]; Gao and Kim, 2006, [59]) showed that the third stress invariant (or Lode parameter) has a strong influence on void shape evolution and on coalescence. The influence of the third stress invariant on the ductility of metals is

[1] This Section is reproduced from: Dunand, M. and D. Mohr (2011). "On the predictive capabilities of the shear modified Gurson and the modified Mohr–Coulomb fracture models over a wide range of stress triaxialities and Lode angles". *Journal of the Mechanics and Physics of Solids* **59**(7): p. 1374-1394.

also shown experimentally (e.g. Barsoum and Faleskog, 2007, [15]). This particular shortcoming of Gurson models has been addressed by the recent models of Xue (2008, [193]) and Nahshon and Hutchinson (2008, [130]). The latter consider the void volume fraction as damage parameter, and introduce a dependency of the damage evolution on the third stress invariant. This empirical modification has been introduced in an ad-hoc manner to deal with the material deterioration due to void distortion and inter-void linking under shearing. As a result, the Nahshon-Hutchinson model can predict failure under shear-dominated loading, such as during the cutting of sheet metal (Nahshon and Xue, 2009, [131]). However, Nielsen and Tvergaard (2009, [137]) found that this modification is inadequate in the case of high stress triaxialities, compromising the predictive capabilities of the original Gurson model for loading conditions where void growth is the main damage mechanism. Consequently, Nielsen and Tvergaard (2010, [138]) proposed a slight modification of the Nahshon-Hutchinson model, making the damage accumulation under shear-dominated stress states active only for low stress triaxialities. It is noted that these two recent shear-modified Gurson models do not account for the effect of void distortion at large shear strains. Micromechanical models that are able to deal with general ellipsoidal void shape evolution are still at an early stage of development and require further validation (e.g. Leblond-Gologanu, 2008, [101]).

As an alternative to Gurson type of models, uncoupled fracture models have been developed for metals where standard incompressible plasticity models are used in conjunction with a separate fracture model (e.g. Fischer et al., 1995, [57]). Unlike in Gurson models, it is assumed that the evolution of damage has no effect on the effective stress-strain response of the material before fracture occurs. Within this framework, damage is measured through the scalar variable D, and its increase $dD \geq 0$ is defined though the increment of the equivalent plastic strain $\bar{\varepsilon}^p$ with respect to a stress-state dependent reference failure strain $\hat{\epsilon}$,

$$\mathrm{dD} = \frac{d\bar{\varepsilon}^p}{\hat{\varepsilon}(\boldsymbol{\sigma})} \tag{2-19}$$

Assuming an initial value of $D = 0$ for the material in its undeformed configuration, it is postulated that fracture initiates as $D = 1$. The reference failure strain may be

interpreted as a weighting function and corresponds to the strain to fracture for monotonic proportional loading. It is either chosen empirically or inspired by micromechanical results. A comparative study of various weighting functions (including models based on the work of McClintock (1968, [119]), Rice and Tracey (1969, [152]), LeRoy et al. (1981, [108]), Cockcroft and Latham (1968, [37]), Oh et al. (1979, [140]), Brozzo et al. (1972, [24]), and Clift et al. (1990, [36])) showed that none of them can accurately describe the fracture behavior of a aluminum 2024 over a large range of stress triaxialities (Bao and Wierzbicki, 2004, [11]). Wilkins et al. (1980, [192]) proposed a weighting function depending on the asymmetry of the deviatoric principal stresses in addition to hydrostatic pressure. It was assumed that the effect of hydrostatic pressure and stress asymmetry on ductility were separable. Attempts to define a more general fracture criterion have lead to the introduction of the third invariant of the stress tensor in the weighting function (e.g. Wierzbicki and Xue, 2005, [191]). Recently, Bai and Wierzbicki (2010, [6]) transposed the classical Mohr Coulomb fracture criterion into the space of stress triaxiality, Lode angle and equivalent plastic strain, defining the so-called Modified Mohr-Coulomb (MMC) fracture criterion.

There exist two more widely-used alternatives to the above two modeling approaches: Continuum Damage Mechanics (CDM) and Forming Limit Curves (FLC). In the framework of Continuum Damage Mechanics, material degradation is modeled through an internal damage variable while the constitutive equations are derived from the first and second principles of thermodynamics for continuous media (e.g. Lemaitre, 1985, [107]; Chaboche, 1988, [31, 32]). Most sheet metal forming processes are still designed against failure based on the concept of FLCs. The FLC is typically constructed in the space of the principal in-plane strains based on the experimental results for uniaxial tension and a series of Nakazima tests (e.g. Banabic et al., 2000, [9]). It is then assumed that failure (either necking or fracture) occurs as the strain path in a sheet metal forming operation crosses the FLC. In this approach, it is assumed that the FLC is independent of the loading path.

2.3 Rate-independent plasticity of AHSS

From a mechanical point of view, TRIP-assisted steels may be considered as composite materials at the micro-scale. Papatriantafillou et al. (2006, [145]) made use of homogenization techniques for nonlinear composites (e.g. Ponte Castaneda, 1992, [148]) to estimate the effective properties of TRIP-assisted steels. Based on the work by Stringfellow et al. (1992, [167]) for fully austenitic TRIP steels, Papatriantafillou et al. (2006, [145]) formulated the computational procedure for a four phase metallic composite with evolving phase volume fractions and isotropic viscoplastic phase behavior. Turteltaub and Suiker (2005, [176]) presented a more detailed multi-scale model for TRIP-assisted steels which includes anisotropic features associated with the phase crystal orientations and the martensite twinning. A mean-field model which describes DP steels as a composite of isotropic elasto-plastic phases with spherical inclusions has been proposed by Delannay et al. (2007, [44]). This model has been enhanced further to TRIP-assisted steels (Delannay et al., 2008, [45]) using the assumption that spherical austenite inclusions transform instantaneously into spherical martensite inclusions. Based on the intermediate strain rate tensile testing of TRIP600 and DP600 steels, Huh et al. (2008, [82]) conclude that both the flow and ultimate tensile strength increase as the level of pre-strain increases.

Most AHSS exhibit a pronounced Bauschinger effect. Banu et al. (2006, [10]) adopted an isotropic Swift law combined with saturated kinematic hardening of the Amstrong-Frederick type to model a series of Bauschinger simple shear tests on a DP600 steel. The accurate modeling of the cyclic behavior of AHSS is important in drawing operations where the sheet material is both bent and unbent. Using a stack of laminated dogbone specimens along with an anti-buckling device, Yoshida et al. (2002, [194]) measured the response of a DP590 steel under cyclic uniaxial tension-compression loading at large strains. Their study shows that the combination of isotropic, non-linear kinematic and linear kinematic hardening provides a satisfactory model for the observed transient and permanent softening in the dual phase steel. As Yoshida et al. (2002, [194]), Lee et al. (2005, [105]) emphasize the importance of an

[2] This Section is reproduced from: Mohr, D., M. Dunand, and K.H. Kim (2010). "Evaluation of associated and non-associated quadratic plasticity models for advanced high strength steel sheets under multi-axial loading". *International Journal of Plasticity* **26**(7): p. 939-956.

accurate description of the Bauschinger and transient behavior in view of springback computations. Based on the comparison of uniaxial experiments on a DP steel and simulations, Lee et al. (2005, [105]) concluded that a modified Chaboche type combined isotropic-kinematic hardening law provides a good representation of the Bauschinger and transient behavior. However, a recent study by Tarigopula et al. (2008, [172]) on a DP800 steel demonstrated that the modeling of transient anisotropy in plastic flow induced by strain-path changes cannot be represented correctly when using a non-linear combined isotropic-kinematic hardening model. Broggiato et al. (2008, [22]) performed 3-point-bending tests on two DP600 and a TRIP700 steel. Their results show that the cyclic hardening behavior of both steel grades is very similar and can be modeled using a non-linear combined isotropic-kinematic hardening model. Using a double-wedge device, Cao et al. (2008, [29]) performed uni-axial tension-compression tests on 1.6mm thick DP600 steel. They modeled their experiments using using a modified Chaboche type combined isotropic-kinematic hardening law (with permanent softening and non-symmetric reloading) as well as the two-surface model by Lee et al. (2007, [104]). Note that the present thesis focuses only on monotonic loadings of the sheet material. Considerations on possible kinematic hardening will therefore be disregarded in the present work.

Different yield surfaces have been used in the past to model advanced high strength steels: von Mises yield surface (e.g. Yoshida et al., 2002, [194]; Durrenberger et al., 2007, [51]), quadratic anisotropic Hill (1948, [78]) yield function (e.g. Banu et al., 2006, [10]; Padmanabhan et al., 2007, [143]; Broggiato et al., 2008, [22]; Chen and Koc, 2007, [34]), high exponent isotropic Hershey (1954, [77]) yield function (Tarigopula et al., 2008, [172]), non-quadratic anisotropic Barlat (2003, [13]) yield function (Lee et al., 2005, 2008, [105, 106]). The reader is referred to Chaboche (2008, [33]) for a recent review of macroscopic plasticity theories.

The plastic behavior of the present TRIP780 material has been extensively characterized by Mohr et al. (2010, [122]). Using both uniaxial tension as well as biaxial shear-tension experiments (Mohr & Oswald, 2008, [126]), they measured the material response at low strain rate for more than twenty different stress states in the range of pure shear to transverse plane strain tension. A characteristic feature of this material is that almost same stress-strain curves are measured for uniaxial tension along

different material orientations (as shown in Fig. 2-3), indicating a planar isotropic yield behavior. At the same time the plastic flow exhibits a strong anisotropy: the Lankford ratios[3] are r_0=0.67, r_{45}=0.96 and r_{90}=0.85 for tension along the rolling direction, the 45° direction and the transverse direction, respectively. Mohr et al. (2010, [122]) proposed a rate-independent plasticity model made of (a) a planar isotropic quadratic yield surface, (b) a orthotropic quadratic non-associated flow rule and (c) isotropic strain hardening to capture this behavior.

Note that the discussion of non-associated formulations in metal plasticity has been partially initiated by the experimental observations of Spitzig and Richmond (1984, [162]). Non-associated plasticity models for metals have been considered by Casey and Sullivan (1985, [30]), Brünig and Obrecht (1998, [27]), Brünig (1999, [25]), Lademo et al. (1999, [99]), Stoughton (2002, [164]), Stoughton and Yoon (2004, 2008, [165, 166]) and Cvitanic et al. (2008, [41]).

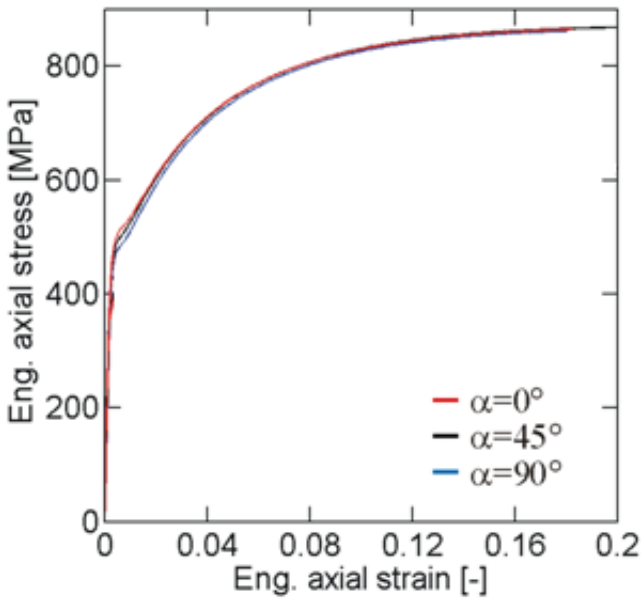

Figure 2-3: Uniaxial tensile testing – engineering stress strain curve along the sheet rolling direction (red), transverse direction (blue) and 45° direction (black).

[3] Lankford ratios, or r-values, characterize the preferred direction of plastic flow under uniaxial tension and correspond to the ratio of width to thickness plastic strain rate: $r = d\varepsilon_w^p / d\varepsilon_{th}^p$. They are a widely used indicator of plastic anisotropy.

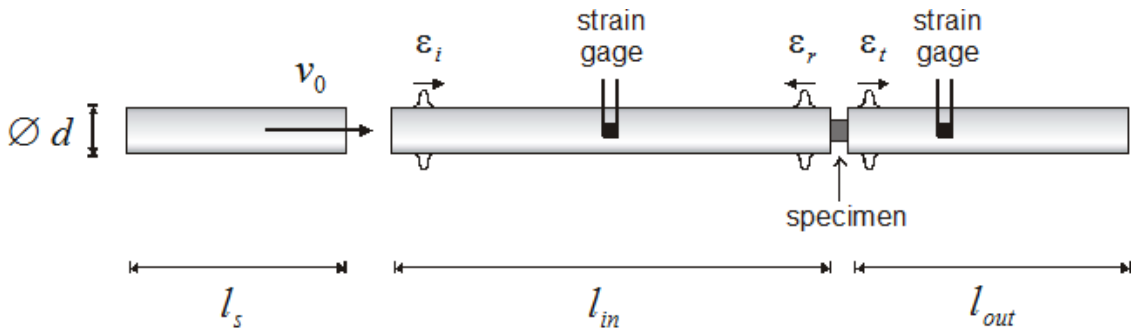

Figure 2-4: Schematic of a Split Hopkinson Pressure Bar system

2.4 Split Hopkinson Pressure bar systems

The experimental characterization of the mechanical behavior of a material at high rates of deformation requires specific experimental techniques. Issues particular to high strain rate testing include generating an appropriate loading pulse (a high velocity loading, of the order of 10m/s, with a rise time of a few tens of microseconds is required) and measuring forces applied to the tested specimens (in view of the extremely high accelerations occurring in high strain rate experiments, measured forces can easily be perturbed by spurious inertia effects). For an comprehensive review of high strain rate experimental techniques, the reader is referred to Field et al. (2004,[56])

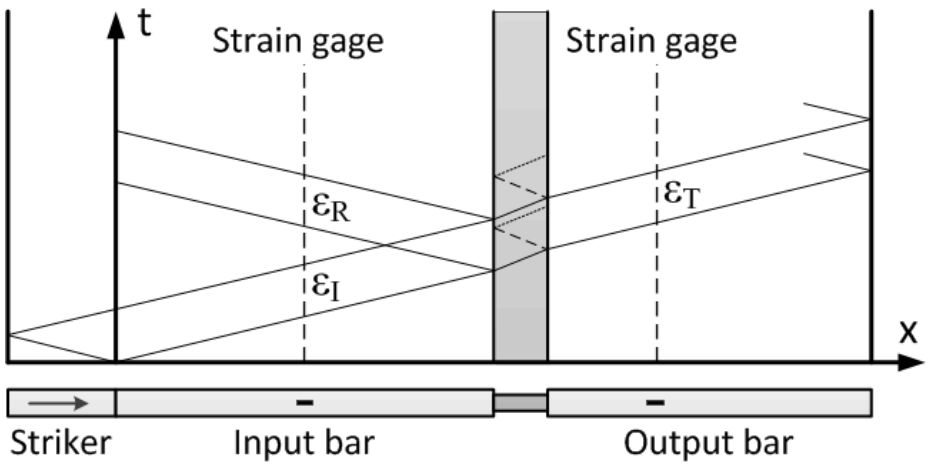

Figure 2-5: Wave-propagation diagram depicting the propagation of elastic waves in the SHPB system through space (horizontal axis) and time (vertical axis).

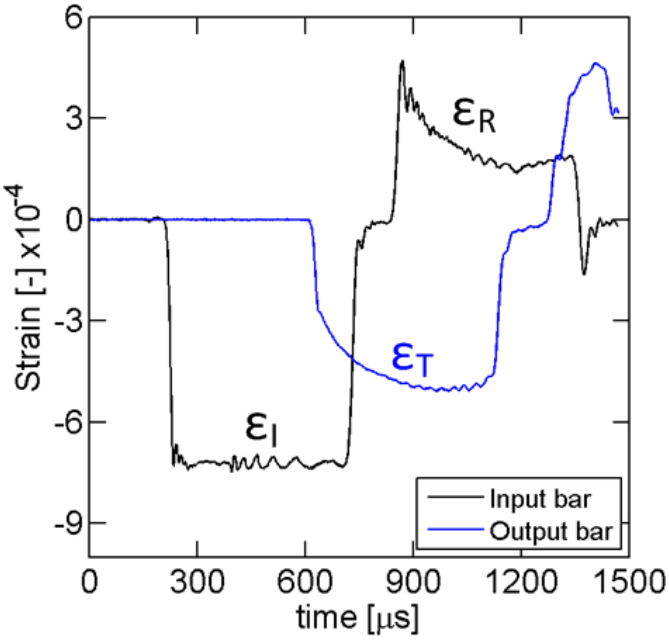

Figure 2-6: Example of signals measured in a SHPB experiment by the input (black line) and output (blue line) strain gages.

In this work, we will make use of a Split Hopkinson Pressure Bar (SHPB) system (Hopkinson, 1914, [80]; Davis, 1948, [43]; Kolsky, 1949, [96]) to perform high strain rate experiments. This type of apparatus has been widely used over the last 40 years to characterize the high strain rate behavior of materials under compression (e.g. Kolsky, 1949, [96]), and modified versions have been proposed for tension (e.g. Harding et al., 1960, [73]) or torsion (e.g. Duffy et al., 1971, [46]) loadings. SHPB systems permit to perform experiments with strain rates ranging from a few hundreds to a few thousands s^{-1}.

A typical SHPB system is shown in Fig. 2-4. It consists of two coaxial slender bars that sandwich the specimen to be tested. The bars can be made of steel, aluminum, polymers (e.g. Zhao et al., 1997, [200])… depending on the strength of the specimen. During an experiment, the free end of the input bar (left side in Fig. 2-4) is impacted by a slender striker at a velocity v_0. As a result, a compressive pulse is generated and propagates in the input bar towards the specimen. The propagation of the elastic waves in the system during an experiment is depicted in Fig. 2-5. When reaching the input bar/specimen interface, the loading pulse, or incident wave ε_I, is partially reflected in

the input bar (reflected wave ε_R) and partially transmitted to the specimen. Similarly, when the wave inside the specimen reaches the specimen/output bar interface, it is partially reflected back in the specimen and partially transmitted to the output bar (transmitted wave ε_T). The time-history of the elastic waves are recorded at specific locations in the input and output bars by strain gages. Examples of measured signals are shown in Fig. 2-6. Strain waves at any locations within the bars, and especially at the bar/ specimen interfaces, are reconstructed using analytical methods that describe the propagation of longitudinal waves in elastic cylindrical bars (e.g. Zhao and Gary, 1995, [197]) and then used to obtain the forces and velocities applied by the bars to the specimen boundaries (see Section 3.3.2 for more details).

Chapter 3

High strain rate tensile experiments

Contents

Abstract

A high strain rate tensile testing technique for sheet materials is presented which makes use of a split Hopkinson pressure bar system in conjunction with a load inversion device. With compressive loads applied to its boundaries, the load inversion device introduces tension into a sheet specimen. Detailed finite element analysis of the experimental set-up is performed to validate the design of the load inversion device. It is shown that under the assumption of perfect alignment and slip-free attachment of the specimen, the measured stress-strain curve is free from spurious oscillations at a strain

[4] This Chapter is reproduced from: Dunand, M., G. Gary, and D. Mohr (2013). "Load-Inversion Device for the High Strain Rate Tensile Testing of Sheet Materials with Hopkinson Pressure Bars". *Experimental Mechanics* (In Press). DOI: 10.1007/s11340-013-9712-y.

rate of $1000s^{-1}$. Validation experiments are carried out using tensile specimens, confirming the oscillation-free numerical results in an approximate manner.

3.1 Introduction

The stress-strain response of engineering materials at high strain rates is typically determined based on uniaxial compression experiments on Split Hopkinson Pressure Bar (SHPB) systems (Kolsky, 1949, [96]). In the case of sheet materials, it is difficult to perform a reliable dynamic compression experiment due to limitations associated with buckling. Different techniques have been developed in the past for the high strain rate tensile testing of materials. The key challenges lie in the generation of the tensile loading pulse and the attachment of the specimen to the Hopkinson bars. The specimen gage section is always subject to a tensile pulse, but it is worth differentiating between techniques where the specimen boundaries are subject to tensile loading and those where a compressive loading is applied to the specimen. In the case where the specimen is subject to compressive loading, the loading pulse is inverted within the specimen. When a tensile loading is applied to the specimen boundaries, one may differentiate further between techniques where a tensile loading pulse is generated in the input bar and those where a compressive loading pulse is generated. Throughout our discussion of SHB systems, we will always assume a left-to-right positioning of the specimen, the input bar and the output bar.

Harding et al. (1960, [73]) proposed a technique where the specimen boundaries are subject to tensile loading while a compressive loading pulse is generated in the input bar. They placed a round inertia bar (output bar) inside a hollow tube (input bar). The right specimen shoulder is then connected to the right end of the tube, while the left shoulder is connected to the right end of the inertia bar; both connections are established through mechanical joints (Fig. 3-1a). A rightward travelling compressive loading pulse is generated in the tube which loads the specimen under tension. Only the elastic waves propagating in the output bar are measured in this experiment, therefore requiring two tests with the same loading pulse (one with a specimen, one with the output bar directly connected to the mechanical joint) to measure the force and velocities applied to the specimen boundaries. Nicholas (1981, [135]) and Ellwood et

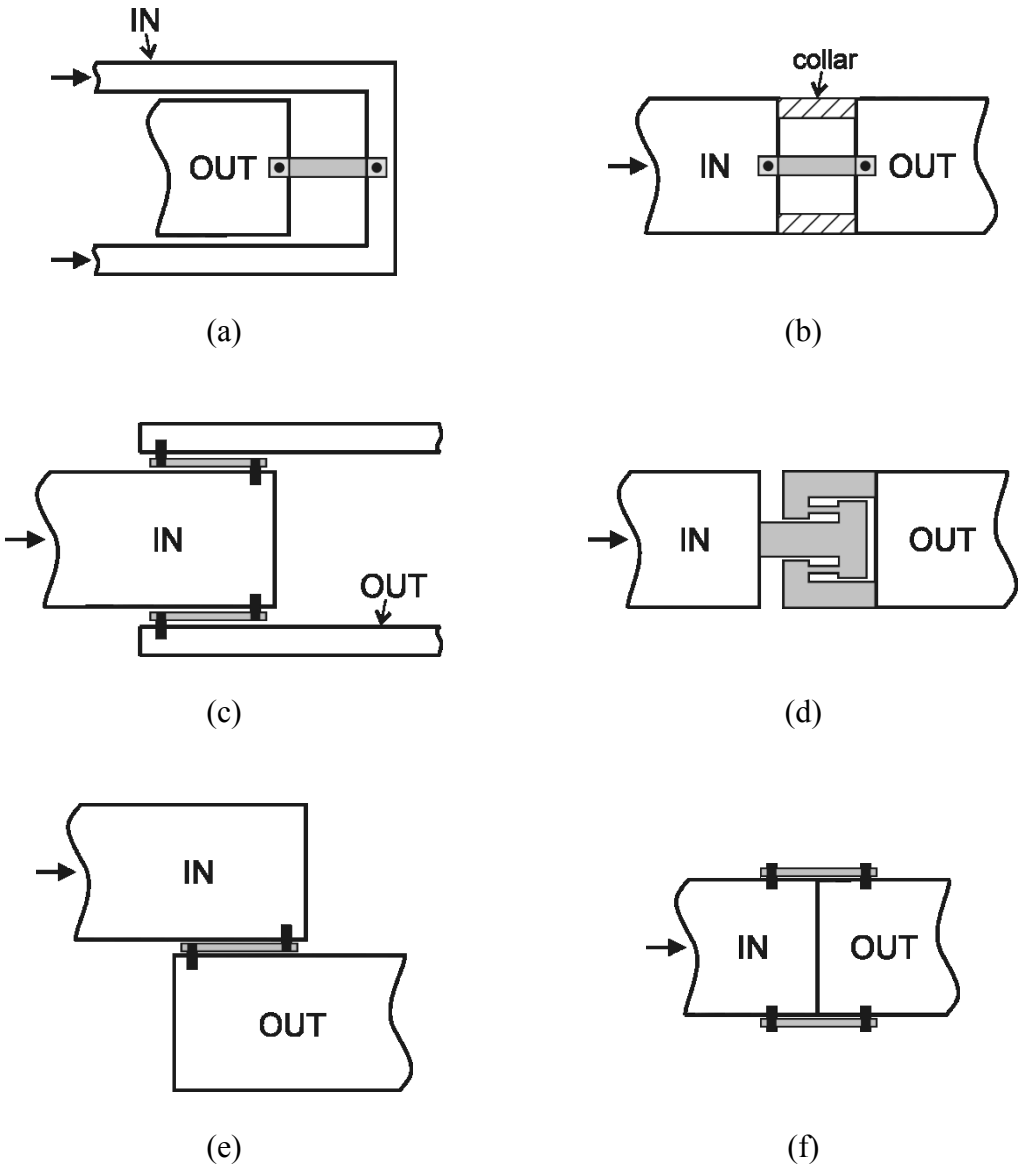

Figure 3-1: Configurations for tensile testing with SHPB systems. The arrows highlight the direction of the incident wave (which is always compression). These schematics just illustrate the basic principle. The black pin-like symbol just indicates the approximate location of specimen attachment and may also correspond to an adhesive or other mechanical joint in reality.

al. (1982, [54]) developed a tensile experiment based on a SHPB system, in which an axisymmetric tension specimen is attached to the bar ends and surrounded by a collar initially in contact with the right end of the input bar and the left end of the output bar (Fig. 3-1b**).** The generated compressive loading pulse is transmitted to the output bar through the collar, without inducing any plastic deformation in the specimen. The loading pulse is then reflected into a tensile pulse at the free right output bar end which then loads the specimen under tension.

As an alternative to inverting the compressive loading pulse within the bars prior to loading the specimen, different techniques have been proposed where the loading pulse is inverted at the specimen level. Lindholm and Yeakley (1968, [112]) developed a hat-shaped specimen (Fig. 3-1c) which is put over the right end of the input bar (input bar diameter equals the hat's inner diameter), while the hat's rim is connected to a tubular output bar that partially overlaps with the input bar (inner output bar diameter equals the hat's outer diameter). Four gage sections are machined in the hat's cylindrical side wall to guarantee a uniaxial stress state at the specimen level. Mohr and Gary (2007, [123]) proposed an M-shaped specimen to transform a compressive loading at the specimen boundaries into tensile loading of the two gage sections (Fig. 3-1d). The M-shaped specimen is used for transverse plane strain tension, which allows shorter gage sections and therefore higher strain rates, and has been validated for strain rates higher than 4,000/s. The key advantage of their technique is that there is no need to attach the specimen to the bars.

For sheet materials, Tanimura and Kuriu (1994, [171]) proposed a non-coaxial SHPB system (Fig. 3-1e). The input and output bars are laterally shifted while a pin joint is used to attach the sheet specimen to the sides of the bars. Mouro et al. (2000, [129]) used a co-axial SHPB system to perform high strain rate tension experiments on sheet metal. They modified the shape of the bar ends such that a two-dimensional multi-gage section hat-shaped sheet specimen can be inserted between the input and output bars of a SHPB system. The specimen must be bent into the hat geometry prior to testing which introduces additional geometric inaccuracies. Haugou at al. (2006, [74]) adopted a configuration where four specimens are bonded to the external part of two threaded sleeves initially in contact and screwed to the input and output bars (Fig. 3-1f**),** thus permitting to use optical strain measurement methods. Similar to the

technique proposed by Nicholas (1981, [135]), the compressive incident wave is thus directly transmitted to the output bar, before the reflected tensile pulse loads the specimens. Instead of inverting a compressive loading pulse, a tensile loading pulse may be directly generated in the input bar using a Split Hopkinson Tensile Bar (SHTB) system. Albertini and Montagnani (1974, [3]) and Staab and Gilat (1991, [163]) generated the tensile loading pulse in the input bar by releasing the elastic energy initially stored in a clamped and pre-stressed section of the input bar. The authors report a rising time of about 40μs to 50μs which is significantly larger than that in SHPB experiments; this is due to the time needed to release the clamping of the pre-stressed input bar. The tensile loading pulse can also be generated through a tubular striker surrounding the input bar and impacting an anvil attached to the input bar end (Ogawa, 1984, [139]). This technique is widely used (e.g. Wang et al., 2000, [188]; Huh et al., 2002, [81]; Smerd et al., 2005, [160]; Van Slycken et al., 2007, [182]; Verleysen et al., 2011, [185]; Guzman et al., 2011, [71]; Song et al., 2011, [161]). It can achieve rising times of the loading pulse of 20μs (Li et al., 1993, [109]). The loading pulse duration is often less than 300 μs in case of steel strikers (e.g. Song et al., 2011, [161]; Gerlacht et al., 2011, [65]) because of technological difficulties in supporting the input bar and the distance required for accelerating the striker bar, but longer pulse durations can be reached with polymeric strikers.

Split Hopkinson bar systems are typically used to perform experiments at strain rates in the range of a few hundreds to a few thousands s^{-1}. In classical Hopkinson bar set-ups, the useful measuring time is limited by the length of the bars, imposing a compromise between the minimum achievable strain rate and the maximum achievable strain. Deconvolution techniques accounting for wave dispersion (e.g. Lundberg and Henchoz, 1977, [115]; Zhao and Gary, 1997, [199]; Bussac et al., 2002, [28]) have been developed to extend the available measuring time, allowing for large deformation experiments at intermediate strain rates. Alternative experimental techniques have also been proposed to perform tensile experiments in the intermediate and high range of strain rates, such as high velocity servo-hydraulic testing machines (e.g. Haugou et al., 2004, [75]; Rusinek et al., 2008, [154]) or direct impact methods (e.g. Tanimura et al., 2003, [171]).

Apart from the method used to generate the tensile loading, a specific issue with high strain rate tensile experiments lies in the attachment of the specimen to the testing apparatus. In the specific case of sheet materials, specimens can be either attached through pin connections (e.g. Tanimura and Kuriu, 1994, [171]), glued (e.g. Haugou et al., 2006, [74]), welded (e.g. Quik et al., 1997, [149]) or hold by friction through curvature (Mouro et al., 2000, [129]) or directly applying high lateral pressure (e.g. Huh et al., 2002, [81]). Pin joints lead to high stress concentrations around the pin/specimen interface, non-negligible deformations outside the specimen gage section and oscillations due to the vibration of the specimen shoulders. The use of epoxy adhesives for specimen attachment appears to reduce the oscillations in the measured force histories. However, it is speculated that this is due to the fact that adhesives act as mechanical filters and therefore suppress the oscillations from the measurements even though these are present within the specimen gage section. In particular, further research is needed to evaluate the influence of the visco-elastic behavior of epoxies on the accuracy of force measurements in SHTB experiments. High pressure clamps appear to be the suitable for attaching the specimen if the applied pressure is large enough to avoid slipping of the specimen and if the inertia of the clamp (including possible screws) is either negligible or matches the impedance of the bar.

In standard Hopkinson bars experiments, measurements of elastic waves propagating in the input and output bars with strain gages permit one to derive the history of force and velocity applied by the bars to each boundary of the specimen (Kolsky, 1949, [96]). In the case of tension experiments where specimen shoulders are wider than the gage section (dogbone shape), bar end displacement can only give an approximation of the strain in the gage section, as it does not take into account the deformation of the transition zones between the gage and clamping sections of the specimen. Optical methods are now widely used for a direct measurement of the strain history in the specimen gage section, such as laser beams (Li and Ramesh, 2007, [110]), Moiré techniques (e.g. Verleysen and Degrieck, 2004, [183]) and digital correlation of high speed video images from a single camera (e.g. Tarigopula et al., 2008, [173]) or stereo DIC with two cameras (e.g. Gilat et al., 2009, [66]).

In this chapter, we propose a new experimental technique for the tensile testing of a single sheet specimen in a modified split Hopkinson Pressure Bar apparatus made of

one input bar and two output bars. The proposed technique is particularly adapted to the experimental characterization at high strain rate of the onset of fracture of ductile sheet materials, where large strains need to be reached. A Load Inversion Device (LID) is designed to transform the compressive loading imposed by the bars into tensile loading of the specimen, while limiting the development of bending waves in the output bars. Assuming quasi-static equilibrium of the specimen during loading, the applied force is derived from the stress waves propagating in the output bars, while the deformation of the specimen is measured by Digital Image Correlation (DIC) of high speed video images. Detailed finite element simulations of the experimental apparatus are carried out to evaluate the ability of the device to accurately measure the material behavior. The proposed experimental technique is used to investigate the high strain rate deformation and fracture behavior of TRIP780 steel sheets. In addition to uniaxial experiments, tensile tests are performed on notched specimens at strain rates ranging from 200/s to 1,000/s.

3.2 Load inversion device

3.2.1 Design objective and strategy

The goal is to devise an experimental technique for the tensile testing of Advanced High Strength Steel (AHSS) sheets at strain rates of about 10^2-10^3 s^{-1}. It is worth noting that the ultimate tensile strength of these materials can exceed 1GPa with an engineering strain to fracture of 40% or more. In these experiments, two characteristics of the loading pulse are of critical importance: the rise time and the pulse duration. The rise time must be short enough[5] so that the material is deformed at an approximately constant strain rate before the onset of necking. Note that for example for a rise time of 50μs in an experiment at 1000/s, the material is deformed up to 2.5% strain before a constant strain rate is reached. In addition, the pulse duration must be long enough so that the specimen is deformed up to fracture: at a strain rate of 500/s, a pulse duration of 1ms is required to reach an elongation of 50%. As discussed in the

[5] It is noted that the rise time can also be too short. Very short rise times (e.g. less than 10μs) introduce non-negligible oscillations in the loading.

introduction, it is difficult to achieve a short rise time and a long pulse duration with SHTB systems. Here, we will chose a SHPB system to generate the loading pulse, since reasonably short rise times can be obtained, while the pulse duration can be increased with little technological effort by increasing the length of the striker and input bars.

The use of a SHPB system for tensile testing requires the inversion of the pressure loading pulse either at the specimen level or through a special inversion device. Mouro et al. (2000, [129]) employed a hat-shaped specimen to transform the incoming pulse from compression into tension. However, the hat concept for load inversion is only valid if the mechanical system remains symmetric throughout the entire experiment. In case symmetry is lost, the force acting on individual gage sections can no longer be determined from the measurement of the total force. Since the symmetry is typically lost with the onset of necking, hat-shaped specimens are not suitable for studying the post-necking and fracture behavior of materials. We therefore focus on the development of a load inversion device that allows for the use of a single gage section specimen.

For a SHPB system with the left to right order of striker bar, input bar, specimen, and output bar, the basic principle of load inversion is very simple: instead of attaching the input bar to the left specimen shoulder, it is attached to the right shoulder. Similarly, the output bar is attached to the left specimen shoulder (Fig. 3-1e). As a result, the pressure pulse in the input bar causes the tensile loading of the specimen followed by the compressive loading of the output bar. In reality, this configuration requires an eccentricity of input bar, specimen and output bar axes to avoid contact among these elements. Preliminary finite element analysis revealed that the total force acting on the specimen cannot be determined with satisfactory accuracy when bending waves are present in the output bar. A configuration where two output bars are placed symmetrically on each side of the specimen is therefore chosen. For this configuration, bending waves in the output bars are theoretically omitted. Furthermore, the specimen gage section is no longer obstructed by the bars, thereby enabling the high speed video imaging (HSVI) of the specimen gage section throughout testing. The strains and the instant of onset of fracture can thus be determined from digital image correlation.

3.2.2 Proposed design

The load inversion device is designed to be positioned between the input and output bars of a SHPB system to perform dynamic tension tests. The sheet specimen is attached to the load inversion device, while there is no need for attachments between the device and the bars (transmission of compression through flat contact surfaces only). The proposed device is shown in detail in Fig. 3-2. Its two main components are:

(1) A "pusher" (green) which is positioned between the specimen and the input bar. It comprises a cover plate (grey) and eight screws which apply the clamping pressure necessary to hold the specimen. The pusher inverts the incoming compressive pulse into a tensile loading of the specimen. With the clamping plate attached, it features the same cross-sectional area as the 20mm diameter input bar.

(2) A "stirrup" (red) which holds the specimen and transmits the applied force to the output bars. Each leg of the stirrup matches the cross-sectional area of the corresponding output bar. The shape of the transverse section of the stirrup is optimized to minimize its inertia while limiting its bending during loading, in order to reduce perturbations on the measured force. Note that a slot of the thickness of the sheet specimen has been cut into the stirrup instead of using a floating clamp.

A base plate along with a set of linear guides is used as a positioning system to ensure accurate alignment of the pusher and the stirrup. The linear guides are also used to reduce the bending of the pusher. Note that the eccentricity of the specimen with respect to the input bar is the sum of half the pusher thickness and half the stirrup thickness. All parts of the loading device are made of 4140 alloy steel. The linear guides are made of brass, and contacts with steel parts are lubricated with silicon-based grease to limit friction.

The exact dimensions of the tensile specimen are shown in Fig. 3-3a. It features a 15mm long and 5mm wide gage section. The corresponding elastic wave travel time is about 3μs which is sufficiently short to guarantee the quasi-static loading conditions at the specimen level. Note that a duration of 10μs is needed to apply a strain of 1% at a strain rate of 1000/s.

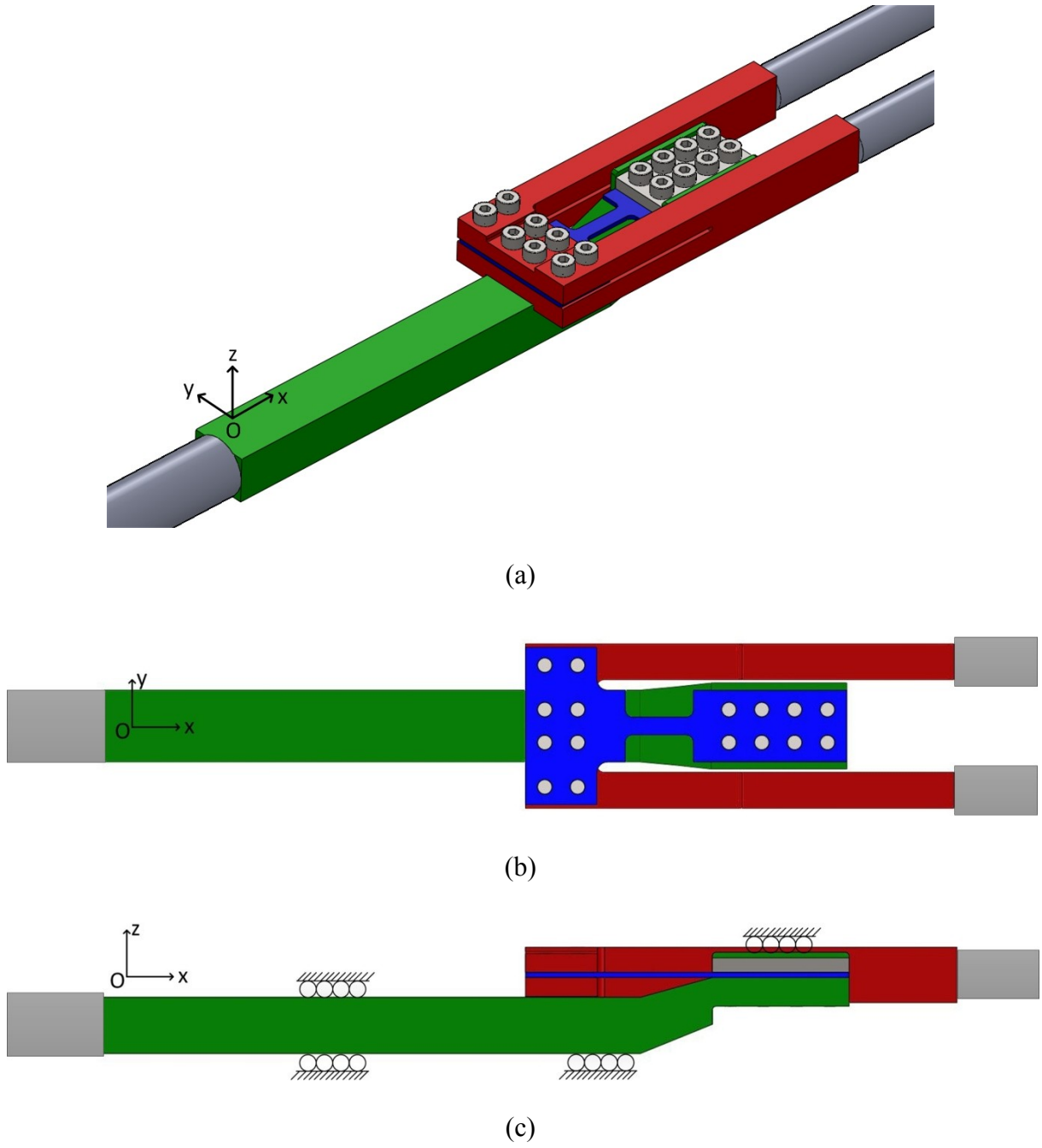

Figure 3-2: Schematic of the Load Inverting Device (LID) including the pusher (green), the stirrup (red) , the specimen (blue) and the input and output bars (grey): (a) isometric view, (b) top view, (c) side view.

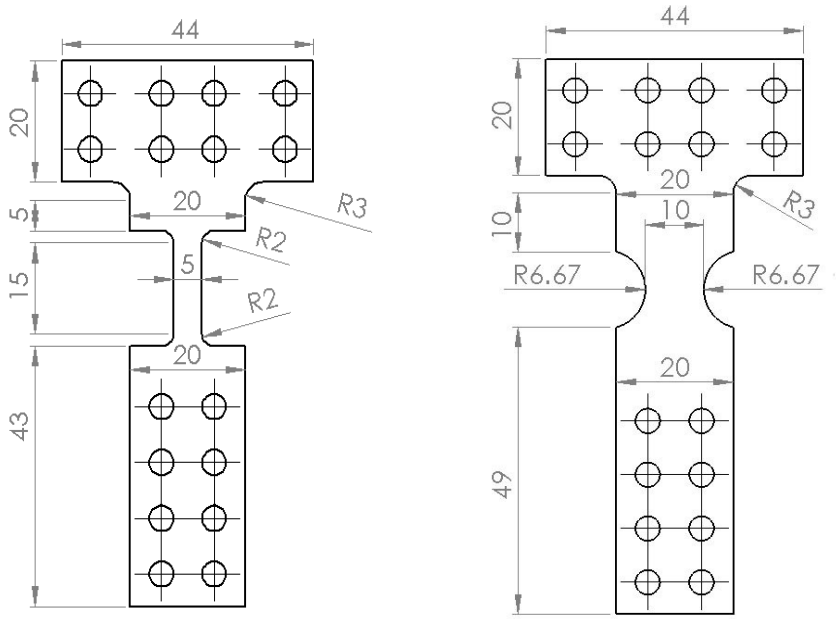

Figure 3-3: Drawings of the specimens for (a) uniaxial tension, and (b) notched tension with cutouts of radius R=6.67mm

3.3 Experimental procedure

3.3.1 Split Hopkinson Pressure Bar (SHPB) system

The SHPB system used in this work consists of the following steel bars:

(1) one 1204*mm* long striker bar of 20*mm* diameter

(2) one 3021*mm* long input bar of 20*mm* diameter; a strain gage is positioned at the center of the input bar;

(3) two 2041*mm* long output bars of 14*mm* diameter; each output bar is equipped with a strain gage positioned at a distance of 299*mm* from the bar-stirrup interface.

As defined by the tensile testing device, the two output bars are positioned at a center-to-center distance of 36*mm*. The rightmost ends of the output bars are attached to a fixed support. This has no effect on the output bar measurements and is only done for

initial alignment purposes. It is very important to guarantee an accurate alignment of the output bar ends which are in contact with the stirrup. Note that any misalignment of those surfaces generates spurious waves in the measured output bar signals.

The amplified signal of the strain gages is recorded at a frequency of 1MHz. The recorded strain signals are post-processed with the software package DAVID (Gary, 2005, [64]) to reconstruct the time histories of the axial strain at the end of the input and output bars, following the procedures described in Zhao and Gary (1996, [198]). Low pass filtering, with a cutoff frequency of 100kHz, is used during post processing to remove electrical noise. Accounting for wave dispersion, the measured incident and reflected waves are "transported" to the input bar/loading device interface. Analogously, the measured transmitted waves in the output bars are transported to the output bar/loading device interfaces.

3.3.2 Forces and velocities at the specimen boundaries

The velocities $v_{in}^{LD}(t)$ and $v_{out}^{LD}(t)$ as well as the forces $F_{in}^{LD}(t)$ and $F_{out}^{LD}(t)$ at the boundaries between the SHPB system and the load inversion device are readily given by the formulas (Kolsky, 1949, [96])

$$F_{in}^{LID}(t) = E_{in}A_{in}\left[\varepsilon_{inc}(t) + \varepsilon_{ref}(t)\right] \tag{3-1}$$

$$F_{out}^{LID}(t) = E_{out}A_{out}[\varepsilon_{tra,1}(t) + \varepsilon_{tra,2}(t)] \tag{3-2}$$

and

$$v_{in}^{LID}(t) = -c_{in}\left[\varepsilon_{inc}(t) - \varepsilon_{ref}(t)\right] \tag{3-3}$$

$$v_{out}^{LID}(t) = -c_{out}\varepsilon_{tra,1}(t) = -c_{out}\varepsilon_{tra,2}(t) \tag{3-4}$$

where E is the Young's modulus, A the cross section area, and c the elastic wave velocity. The subscripts "in" and "out" are used to indicate respective reference to the input and output bar properties. $\varepsilon_{inc}(t)$ and $\varepsilon_{ref}(t)$ are the histories of incident and reflected wave at the input bar/pusher interface. $\varepsilon_{tra,1}(t)$ and $\varepsilon_{tra,2}(t)$ are the histories of transmitted wave at the interfaces between the output bars and the stirrup.

The determination of the force and velocity histories at the specimen boundaries requires another "transport" of the signals. Dispersive effects and local structural impedance discontinuities within the LID are neglected because of the short wave travel distances. Assuming an input bar to specimen interface wave travel time of Δt_p, the force at the specimen interface with the pusher is written as

$$F_{in}^{Kolsky}(t) \cong -E_{in}A_{in}\left[\varepsilon_{inc}\left(t-\Delta t_p\right)+\varepsilon_{ref}\left(t+\Delta t_p\right)\right] \tag{3-5}$$

Analogously, denoting time for a wave to travel from the specimen/stirrup interface to the output bar interface as Δt_s, the force at the specimen/stirrup interface reads

$$F_{out}^{Kolsky}(t) \cong -E_{out}A_{out}\sum_{i=1,2}\varepsilon_{tra,i}(t+\Delta t_s) \tag{3-6}$$

It is emphasized that F_{in}^{Kolsky} and F_{out}^{Kolsky} are obtained assuming wave propagation in a slender cylindrical bar. They do not account for possible perturbations of the elastic waves due to geometry or bending of the LID.

Furthermore, we can calculate the corresponding velocities at the specimen boundaries,

$$v_{in}^{Kolsky}(t) \cong -c_{in}\left[\varepsilon_{inc}\left(t-\Delta t_p\right)-\varepsilon_{ref}\left(t+\Delta t_p\right)\right] \tag{3-7}$$

$$v_{out}^{Kolsky}(t) \cong -\frac{c_{out}}{2}\sum_{i=1,2}\varepsilon_{tra,i}(t+\Delta t_s) \tag{3-8}$$

and compute an approximation of the spatial average of the engineering axial strain in the specimen gage section

$$e_{bar}(t) \approx \frac{1}{l_0}\int_0^t [v_{in}(t)-v_{out}(t)]dt \tag{3-9}$$

l_0 is the initial length of the specimen gage section. Note Eq. 3-9 becomes an exact equality if the specimen is perfectly rigid outside the gage section. The wave travel times $\Delta t_p = 41\mu s$ and $\Delta t_s = 28\mu s$ have been determined from finite element analysis. Note that Δt_p is equal to the propagation time of a uniaxial wave in a slender bar of the same length as the pusher.

3.3.3 Local displacement measurements

A high speed video system (Phantom v7.3 with 90mm macro lenses) is employed to record pictures of the specimen surface at a frequency of 111kHz (1 frame every 9μs). A resolution of 448x32 pixels is chosen. The camera is positioned at a distance of about 400mm from the specimen surface, which results in a square pixel edge length of 44μm. A thin layer of white matt paint is applied to the specimen surface along with a black speckle pattern of a speckle size of about 70μm. An exposure time of 1μs is set up with a 150W halogen bulb providing the necessary lighting of the gage section. The video recording is triggered at $t = T_{tr}$ when the input bar strain gage detects the rising edge of the loading pulse.

The virtual extensometer function of the digital image correlation software VIC2D (Correlated Solutions, SC) is used to determine the relative displacement of two points located on the axis of symmetry of the specimen gage section. For this, a quadratic transformation of a 23x23 pixel neighborhood of each point is assumed. Spline-cubic interpolation of the grey values is used to achieve sub-pixel accuracy. The results are reported in terms of the engineering axial strain

$$e_{DIC}(t_{DIC}) = \frac{\Delta u_{DIC}(t_{DIC})}{\Delta x} \tag{3-10}$$

with Δu denoting the relative displacement of two points of an initial spacing $\Delta x = 6.6mm$, corresponding to 150 pixels. The time coordinate is denoted as t_{DIC} to highlight that the DIC measurements need to be synchronized with the time coordinate t of the SHPB system using the relationship $t_{DIC} = t - T_{tr}$.

3.3.4 Determination of the stress-strain curve

The output force history is used to estimate the stress within the specimen. Its measurement accuracy is significantly higher than that of the input force due to the presence of bending waves in the pusher and the uncertainty associated with the calculation of the difference between the incident and reflected waves. Among the strain measures, the local DIC extensometer measurement is selected to eliminate uncertainties associated with the definition of the effective gage length in Eq. 3-9, and

with perturbations affecting the reflected wave. The input bar strain gage measurement is thus only used for validation purposes. Denoting the initial cross-sectional area of the specimen as A_0, the engineering stress is formally defined as

$$S(t) = \frac{F_{out}^{Kolsky}(t)}{A_0} \tag{3-11}$$

while the engineering stress-strain curve is obtained from the combination

$$S(e) = [S \circ e_{DIC}^{-1}](e) \tag{3-12}$$

Cubic spline interpolation is used to approximate the strain history between two successive DIC measurements. Note that after the onset of necking (e.g. after reaching the maximum engineering stress), the measured engineering strain must be interpreted as normalized relative displacement. While inverse analysis is needed to determine the stress-strain curve in the post-necking range, the logarithmic axial strain $\varepsilon(t)$ and true axial stress $\sigma(t)$ prior to the onset of necking are given by the well-known relationships

$$\varepsilon(t) = \ln\big(1 + e(t)\big) \tag{3-13}$$

$$\sigma(t) = S(t)[1 + e(t)] \tag{3-14}$$

It is emphasized that the determined stress-strain curve is only valid if the assumption of quasi-static equilibrium is satisfied at the specimen level. This can be verified by comparing the input and output force histories at the specimen boundaries. Due to the poor measurement accuracy of the input force, it is recommended to make use of transient finite element analysis to verify the assumption of quasi-static equilibrium.

3.4 FEA-based validation

The ability of the experimental technique to measure accurately the mechanical specimen response relies on two main hypotheses:

(1) the specimen gage section is loaded under quasi-static equilibrium, and

(2) the loading device, and especially the stirrup, does not significantly perturb the propagation of elastic waves, so that histories of the forces measured in the output bars correspond to the history of force applied to the specimen boundary.

Here, a detailed finite element analysis of a dynamic experiment is performed to assess the validity of these assumptions. As compared to the experimental validation, the FEA approach has the advantage of validating the experimental design independent of possible practical problems associated with the alignment of parts or the clamping of the specimens. Our 3D model of the experimental setup includes the specimen, load inverting device as well as the input and output bars. The striker bar impact is not modeled. Instead, the measured incident wave pulse is directly applied to the free end of the input bar.

3.4.1 Finite element model

The explicit solver of the finite element analysis software Abaqus (2011, [1]) is used to perform the analysis. All parts are meshed with reduced integration 3D solid elements (type C3D8R from the Abaqus element library). The elements of the bar meshes have an edge length of 5mm in the axial direction, and 2mm in the radial direction, allowing for an accurate description of axial frequencies of up to 50 kHz and possible bending waves. The different parts of the loading device are meshed with the same type of elements with an edge length of 1mm. The mesh of the 12mm long and 5mm wide specimen features an edge length of 0.4mm and four elements along the sheet thickness direction. Due to the symmetry of the mechanical system (with respect to the x-y plane defined in Fig. 3-2), only one half of each component is modeled along with the corresponding symmetry boundary conditions. A penalty contact algorithm with a friction coefficient of 0.2 is chosen to model the interaction between the loading device and the bar ends. A tie constraint is defined between the specimen and the LID to represent a slip-free rigid attachment. The specimen material is modeled as isotropic elasto-plastic assuming rate-independent J_2-plasticity. Elements in the gage section are deleted when the equivalent plastic strain reaches a value of 1 at their integration point. All other parts are defined as linear elastic ($E = 210GPa, \nu = 0.3, \rho = 7.82g/cm^3$ for

the loading device and the output bars, $E = 185GPa, \nu = 0, \rho = 8.1g/cm^3$ for the input bar). The loading pulse shown in Fig. 4a is applied at the free end of the input bar as surface pressure history. It corresponds to a stress pulse measured experimentally (and transported analytically to the specimen interface) for a striker velocity of 14.8m/s, corresponding to an equivalent plastic strain rate of about 860/s before necking. Note that Poisson ratio of $\nu = 0$ is chosen for the input bar material to avoid geometric dispersion effects on the loading pulse. The numerical simulation is run for 2ms which includes about $630\mu s$ of incident wave travel up to the input bar/pusher interface. A stable time increment of 4.69 10^{-8}s is used by the Abaqus/Explicit solver.

3.4.2 Simulation results

The simulation results include (1) the strain histories at the integration points of elements located at the locations of the input and output bar strain gages (in Fig. 3-4), and (2) the relative displacement of two nodes located on the surface of the specimen gage section (in Fig. 3-5) at an initial distance of 3mm (correspond to the DIC based optical extensometer). The above data processing procedure is applied to these simulation results to determine the stress-strain response of the specimen material. Fig. 3-6a compares the determined true stress versus logarithmic strain curve (solid black line) with the input constitutive behavior (solid red line). The two curves lie almost perfectly on top of each other up to a strain of about 0.25, which confirms the validity of the proposed experimental technique for the determination of the stress-strain response of a typical AHSS sheet material at a strain rate of 900/s. In particular, the assumption that the history of force applied by the specimen to the stirrup is transmitted to the output bars without excessive perturbations is validated through this result. The curves diverge at a strain of 0.25 due to the onset of necking. Beyond this point, the assumption of an approximately uniform strain distribution within the gage section breaks down and the application of Eq. 3-14 is no longer valid. Note that local heterogeneities of the stress and strain fields, inherent to explicit calculations, are sufficient to trigger necking in this simulation as no initial defects were introduced to the mesh.

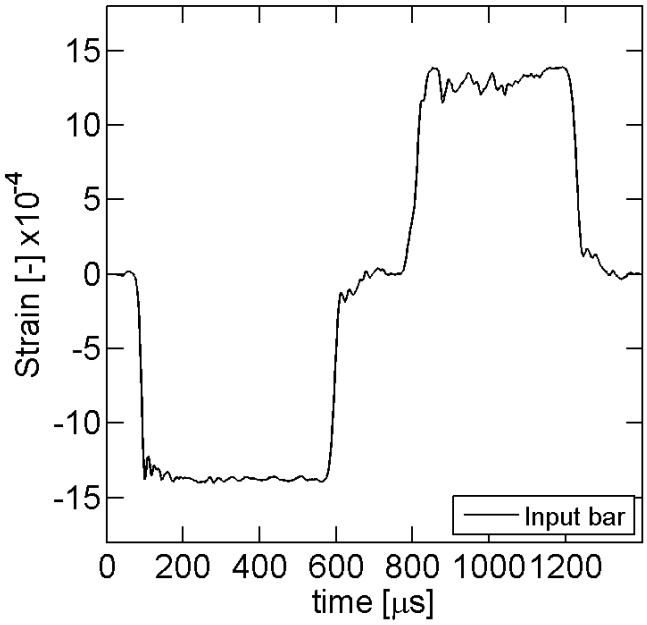

(a)

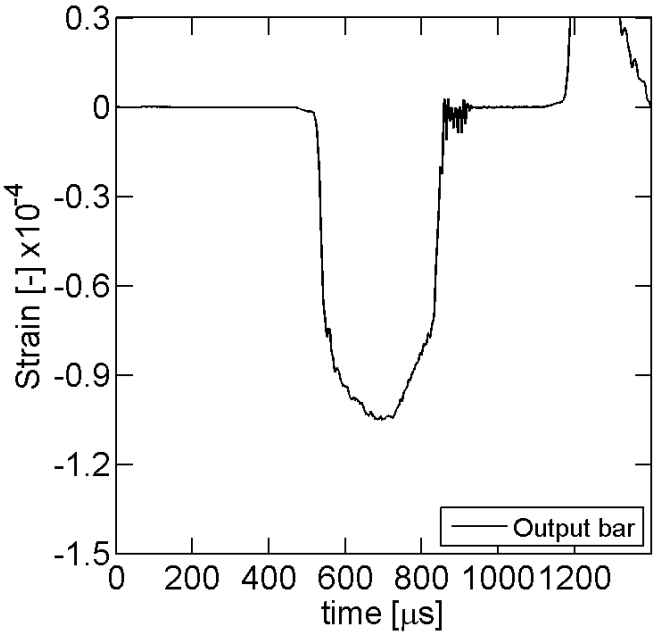

(b)

Figure 3-4: Results from a FE simulation of a uniaxial tension experiment at an average pre-necking equivalent plastic strain of 900/s: signals of (a) the input bar strain gage and (b) the output bar strain gage.

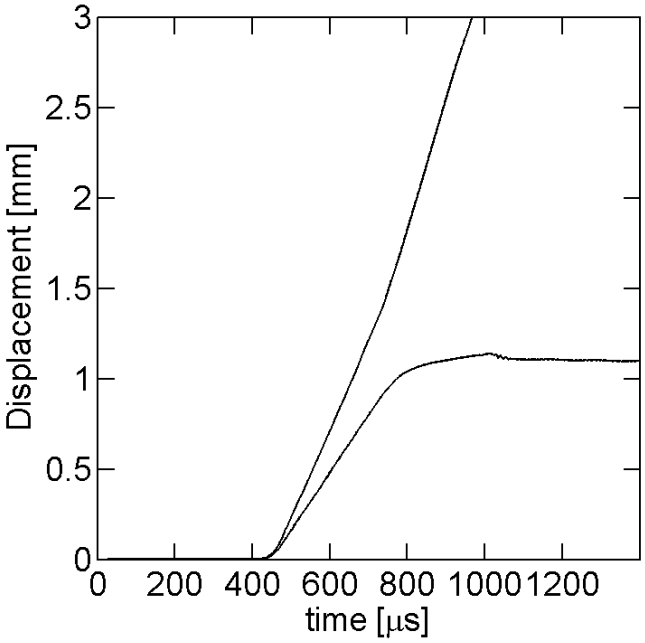

Figure 3-5: Displacement of two nodes located on the surface of the specimen gage section at an initial distance of 3mm, as obtained from a FE simulation of a uniaxial tension experiment at an average pre-necking equivalent plastic strain of 900/s.

To evaluate the assumption of quasi-static equilibrium, we determined the history of the axial forces applied at each boundary of the specimen gage section. The solid curves shown in Fig. 3-6b are obtained by integrating the stress contribution of all integration points located on a cross section of the wide unclamped parts of the specimen. The two curves lie almost perfectly on top of each other, which indicates that the hypothesis of quasi-static equilibrium of the specimen gage section during loading holds true. It is worth noting that despite the short rise time and the omission of pulse shaping, the specimen gage section is in stress equilibrium throughout the entire experiment (except for a very small initial period). The force applied at the stirrup/output bar interface and derived from the transmitted wave measured in the output bar, $F_{out}^{LID,Kolsky}$, is also shown in Fig. 3-6b (as a dashed red line). The force-time signal is delayed by $\tau_{tra} \cong 28\mu s$ which corresponds to the duration associated with the wave travel through the stirrup. However, the amplitude-frequency spectra of both force-time signals are approximately identical, thereby confirming the assumption of negligible axial wave perturbation by the stirrup. On the other hand, the approximation

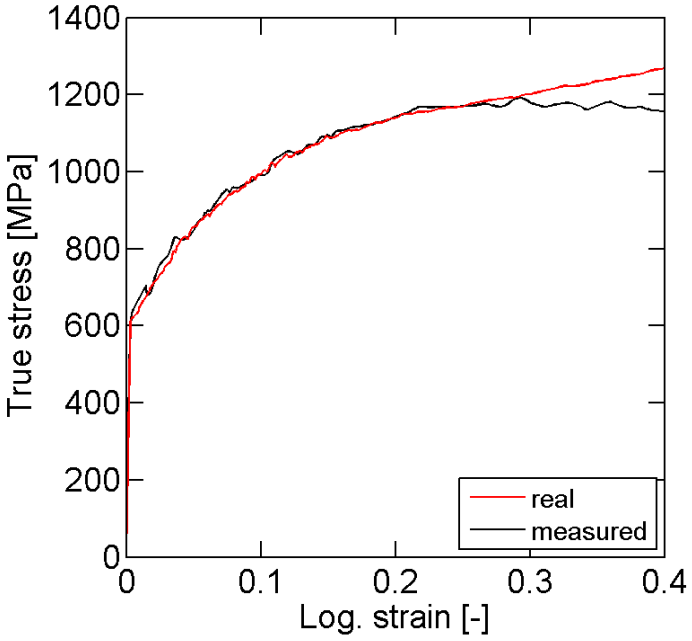

(a)

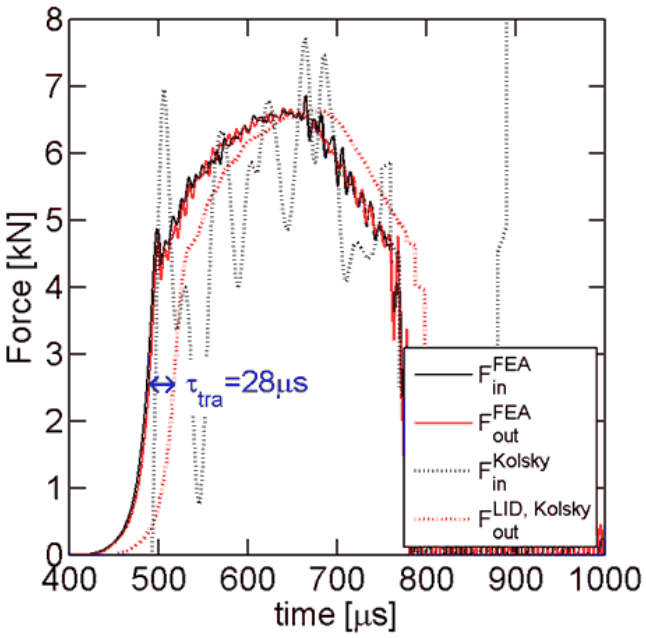

(b)

Figure 3-6: FE-based validation of the experimental technique for uniaxial tension with an equivalent plastic strain rate of about 900/s: (a) Comparison of the stress-strain curve as determined from the virtual measurements (black curve) with the simulation input data (red curve); (b) forces applied at the gage section boundaries by the pusher (solid black line), by the stirrup (solid red curve) and Kolsky approximations, based on elastic waves measured in the bars, of the forces applied at the gage section boundary by the pusher (dashed balck line) and at the output bars/stirrup interface (dashed red line).

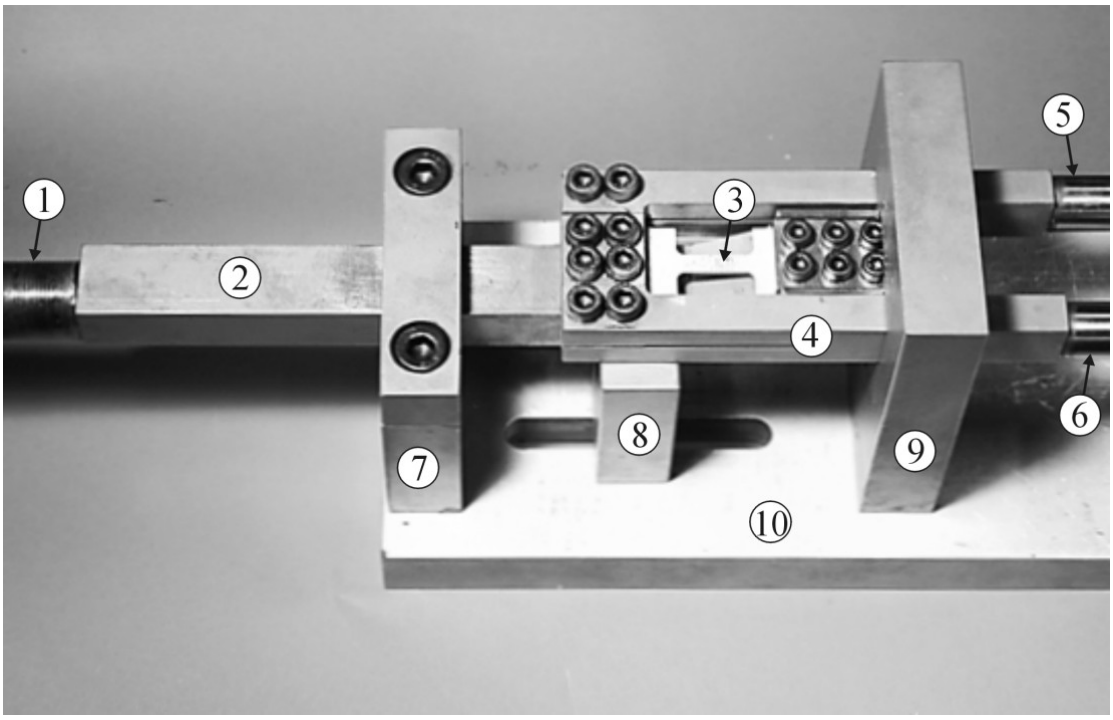

Figure 3-7: Photograph of the load inversion device : (1) input bar, (2) pusher, (3) specimen, (4) stirrup, (5) first output bar, (6) second output bar, (7), (8), (9) guide blocks, and (10) base plate.

of the force applied by the pusher F_{in}^{Kolsky} (dashed black line in Fig. 3-6b), derived from elastic waves measured in the input bar, exhibits strong oscillations compared to the actual applied force F_{in}^{FEA}.Perturbations of the reflected wave due to bending deformation of the pusher have been identified as the major cause of those oscillations, and make the approximation of the applied force measured from the input bar F_{in}^{Kolsky} highly inaccurate.

3.5 Validation experiments

3.5.1 High strain rate uniaxial tension experiments

The uniaxial tension specimens sketched in Fig. 3-3a are extracted from the sheet material through water jet cutting. Within the scope of the present study, the specimen

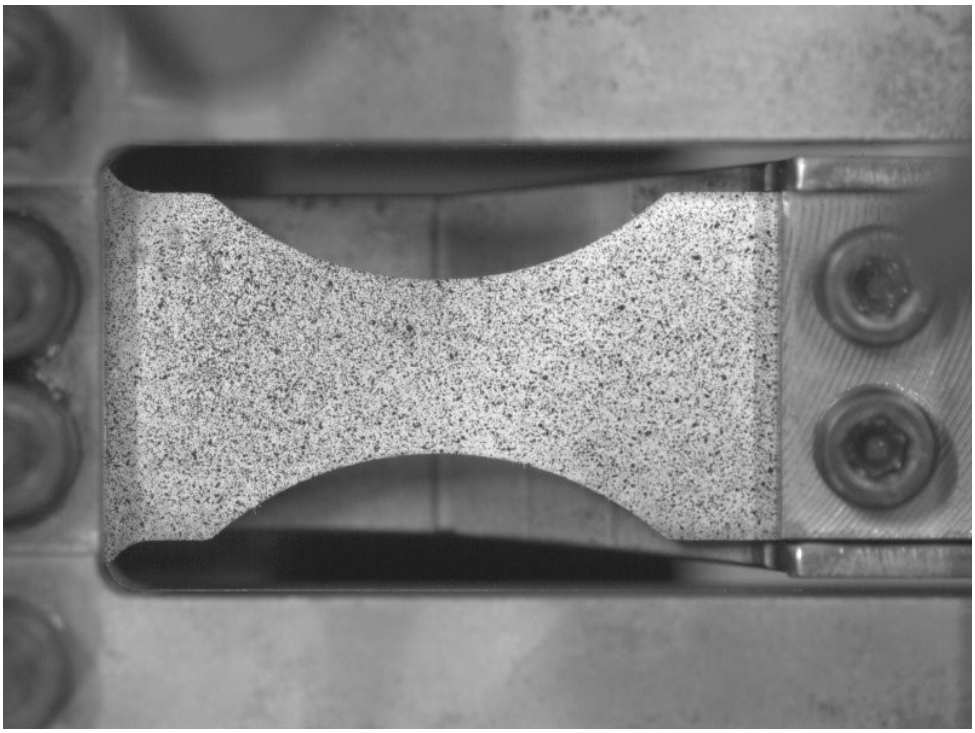

Figure 3-8: Close-up view of a notched specimen positioned in the load inversion device.

loading axis is always aligned with the sheet rolling direction. The dynamic experiments are carried out with striker velocities of 4.2, 11.8 and 14.6 m/s.

Experimental measurements from the test carried out with a striker velocity of 11.8m/s are summarized in Fig. 3-9 to 3-11. The strain history from the input strain gage is shown in Fig. 3-9a while strain histories from output strain gages on both output bars are shown in Fig. 3-9b. Note that the time duration of the recorded reflected wave (Fig. 3-9a) is about $80\mu s$ shorter than the incident wave. After the compressive incident wave pulse is completely transferred into the pusher, contact between the input bar and the pusher is lost. The tail of the tensile reflected wave is thus trapped in the pusher and not recorded by the input strain gage. Before carrying out the test, a static compressive load is applied to the SHPB system. An equal distribution of the load between the two output bars permits to validate the symmetric positioning of the specimen. The two transmitted waves (in Fig. 3-9b**)** are very close to each other, thereby confirming that the force applied at the specimen/stirrup interface, F_{in}, is split

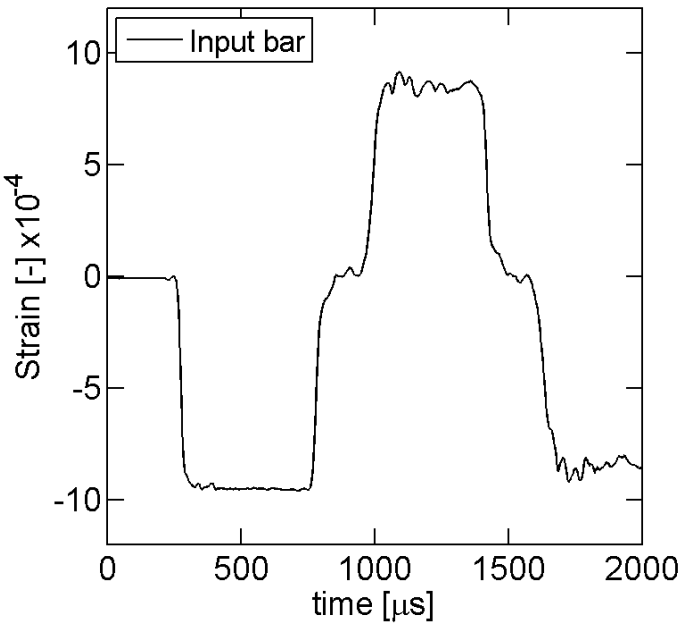

(a)

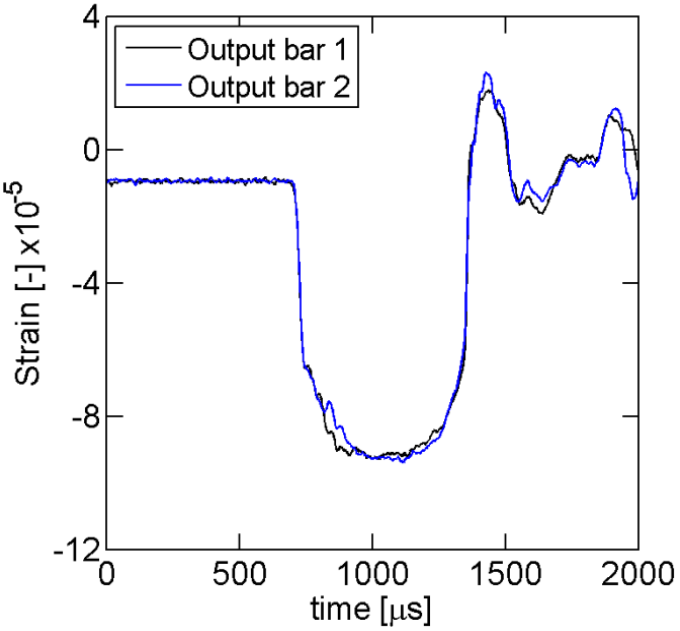

(b)

Figure 3-9: Strain histories of (a) the incident and reflected wave measured from the input bar and (b) the transmitted waves measured from both output bars, during the uniaxial tension experiment with a striker velocity of 11.8m/s.

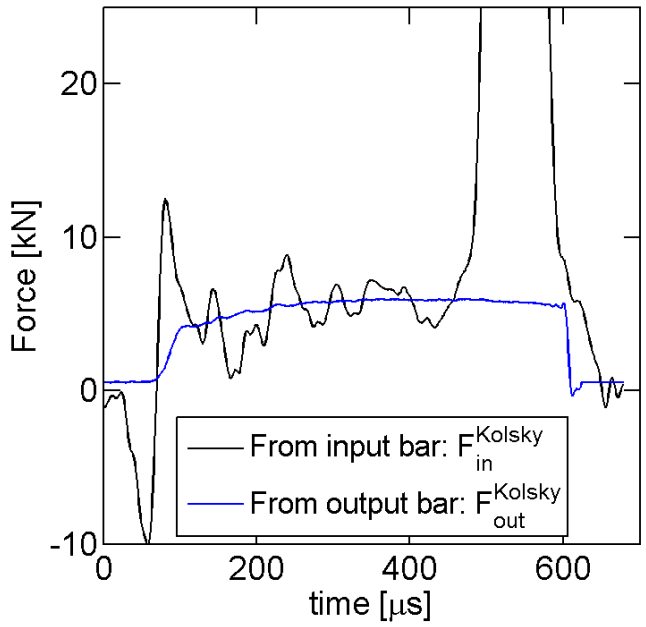

Figure 3-10: Approximation of the forces applied at the specimen/pusher interface , derived from strain waves in the input bar (in black) and at the specimen/stirrup interface, derived from strain waves measured in the output bars (in blue) during the uniaxial tension experiment with a striker velocity of 11.8m/s.

almost symmetrically between both output bars. Small asymmetric perturbations, of less than 3% of the signal in magnitude, can nonetheless be observed. The forces applied at the specimen/pusher interface, F_{in}^{Kolsky}, and the specimen/stirrup interface, F_{out}^{Kolsky}, as derived from strain wave measurements through Eqs. (3-5) and (3-6), are depicted in Fig. 3-10**.** Recall that F_{out}^{Kolsky} is obtained by summing the forces measured in each output bar. The output force F_{out}^{Kolsky} (in blue in Fig. 3-10) exhibits almost no oscillations. On the contrary, the input force F_{in}^{Kolsky} (in black in Fig. 3-10) shows very large oscillations, of the order of the force itself. Beyond those oscillations, both forces have the same magnitude. The oscillations are due to perturbations of the reflected wave created by bending deformations of the pusher during loading. In addition, the input force F_{in}^{Kolsky} largely overestimates the applied force in the last stages of loading because the tail of the reflected wave is trapped in the pusher and not recorded by the strain gage. Therefore, the force obtained from wave measurements in the input bar, F_{in}^{Kolsky}, does not represent accurately the force applied at the specimen/pusher inter-

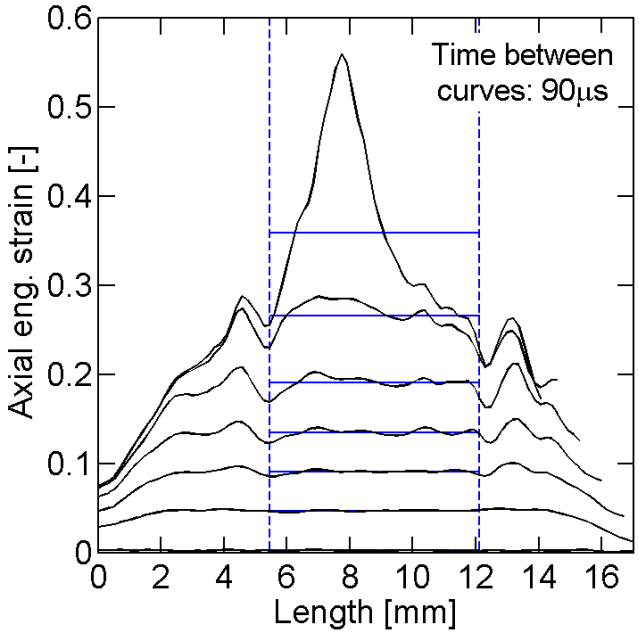

Figure 3-11: Axial engineering strain distribution along the specimen gage section (black solid lines) at different moments in time, as measured by DIC in the uniaxial tension experiment with a striker velocity of 11.8m/s. A time interval of $90\mu s$ is taken between two consecutive curves. The average engineering strain (defined by Eq. 10) is shown with blue solid lines, and the initial position of the optical extensometer is depicted with blue dashed lines.

face, as already shown by the FE simulation results presented in Section 3.4.2. Note that knowing accurately the output force only is sufficient to get the force applied to the specimen, since equilibrium of the specimen gage section has been verified numerically for strain rates of 900/s. The strain distribution along the specimen axis is shown by black lines in Fig. 3-11 at different moments in time. The initial position of the optical extensometer used to measure the engineering strain of the gage section in Eq. (3-11) is depicted with dashed blue lines, while the average engineering strain corresponding to the different strain distributions is shown by solid blue lines in Fig. 3-11. For strains lower than 0.2, the local strain is approximately uniform inside the optical extensometer, with relative variations to the average engineering strain of less than 5%. The DIC also shows that for strains higher than 0.2, the strains begin to localize at the gage section center, which corresponds to the onset of necking. It is also worth noting

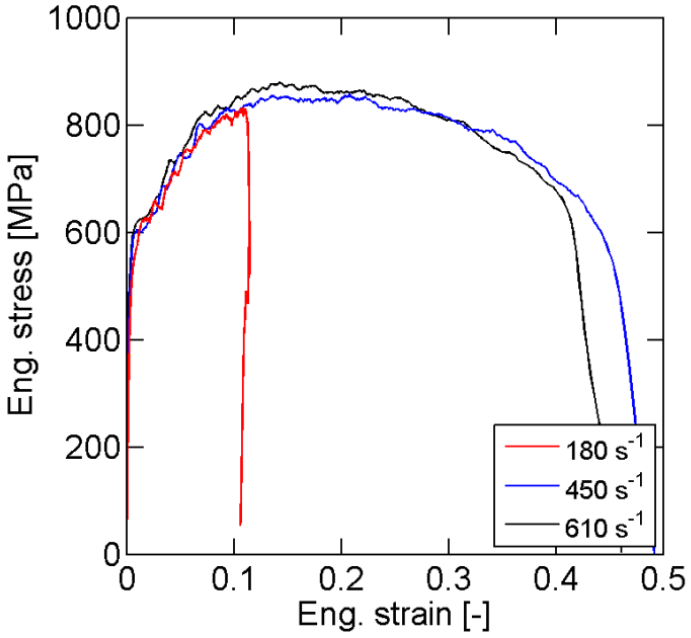

(a)

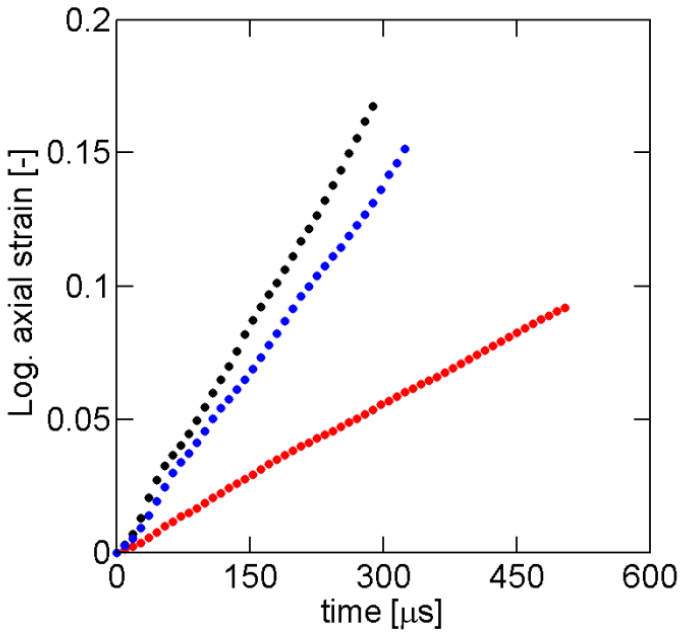

(b)

Figure 3-12: Summary of experimental results for different equivalent plastic strain rates. (a) engineering stress-strain curves. (b) Logarithmic axial strain histories up to the onset of necking (DIC measurements).The time origin corresponds to the first instant when a non-zero strain is measured.

that two local maxima of strain also appear on each side of the gage section. It is speculated that these are due to geometric imperfections of the specimen.

The experimental results for the different striker velocities, as determined through the above experimental procedure, are summarized in Fig. 3-12. The history of the DIC based logarithmic axial strain before the onset of necking is shown in Fig. 3-12b. After about 1% strain corresponding to the rise time of the loading pulse, all strain histories have an approximately constant slope which defines the average pre-necking strain rate. The respective average pre-necking strain rates for the present experiments are 180/s, 450/s and 610/s. The corresponding engineering stress-strain curves are shown in Fig. 3-12a. The same 1200mm long striker bar is used for all experiments resulting in a loading pulse duration of about 550μs. Except for the experiment at 185/s, this duration is long enough to deform the specimens all the way to failure. The onset of necking (characterized by the force maximum) is observed at an engineering strain of about 0.16 for all experiments. The three curves lie approximately on top of each other, indicating that the material exhibits no noticeable effect of strain rate on the flow stress and strain hardening for the range of high strain rates considered (from 180/s to 610/s). The true stress versus logarithmic strain curve at a strain rate of 610/s is shown up to the point of necking in Fig. 3-13 (solid line). Its comparison with the low strain rate result (dashed line) reveals that for a given strain level, the yield stress is about 100MPa higher in the high strain rate experiments.

The experimentally-measured stress-time signals exhibit small oscillations. Their magnitude appears to be independent of the loading velocity. Oscillations of a magnitude of less than $\pm 10MPa$ are observed for all experiments, corresponding to oscillations of $\pm 75N$ on the force signal measured in the output bars. It is worth noting that the simulated experiment for $900s^{-1}$ (Fig. 3-6b) shows a response with oscillations of about the same magnitude ($\pm 5MPa$). Note that perfect interface conditions (no slip) and perfect alignment of all components are assumed in the simulation. It is therefore concluded that the realization of the high strain rate experiment has been successful from a technical point-of-view, while the remaining small oscillations are attributed to the nature of the mechanical system.

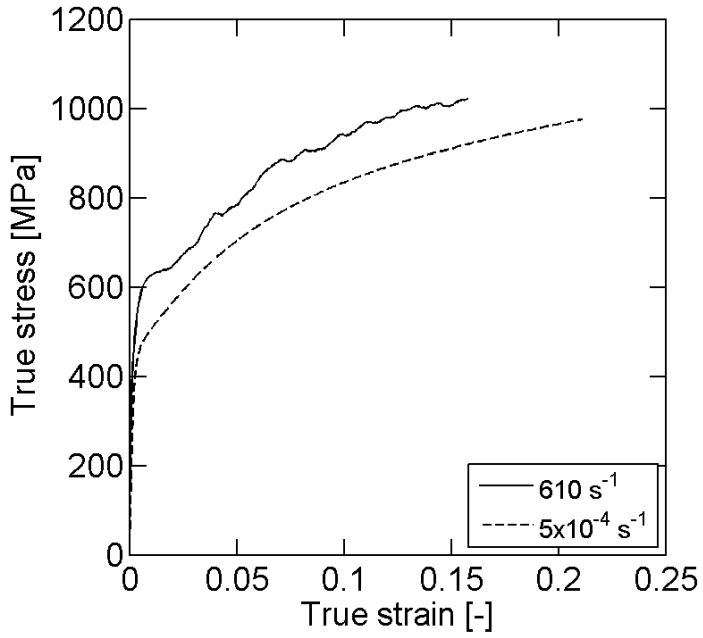

Figure 3-13: True stress-strain curves at pre-necking plastic strain rates of $5x10^{-4}$/s (dashed line) and 610/s (solid line).

3.5.2 Notched tension experiments

The application of the proposed load inversion device is not limited to uniaxial tensile experiments. For illustration, dynamic experiments are performed on notched tensile specimens. These experiments allow for the characterization of the effect of stress state on ductile fracture (see Chapter 4 for details). Here, we perform experiments on specimens with a b=10mm wide notched gage section and notch radii of R=6.67mm (Fig. 3-3b). All tested specimens are cut with their loading axis aligned with the sheet rolling direction. Experiments are performed with striker velocities of 7.1m/s and 10.5m/s. Throughout each experiment, the relative axial displacement between two points on the specimen shoulders is measured using DIC and synchronized with the corresponding axial force history measurements. The initial length of the optical extensometer is $l_0 = 30mm$. The force-displacement curves for high strain rate loading obtained for the $R = 6.67mm$ geometry are shown in Fig. 3-14a (solid lines) next to the curve for low strain rate loadings (dashed line, crosshead velocity of 0.5mm/min. As for the uniaxial tension experiments, the results are almost independent from the striker velocity for the two geometries. However, the force level

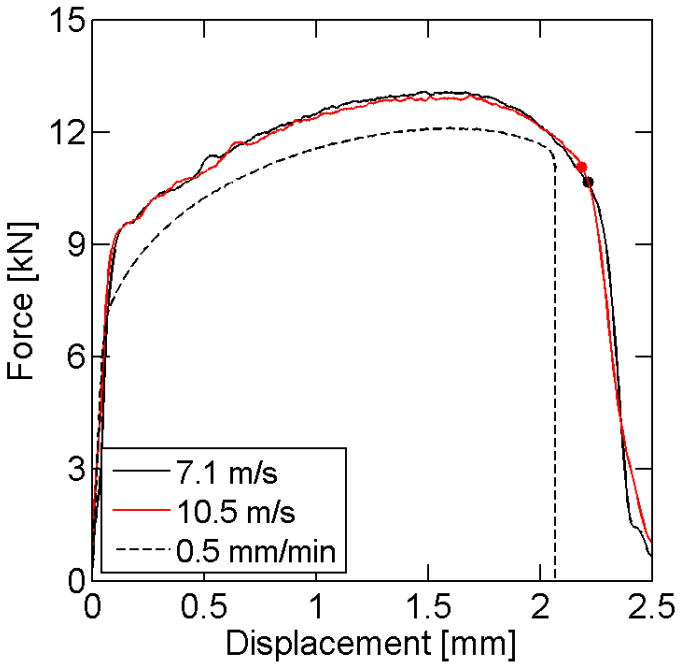

(a)

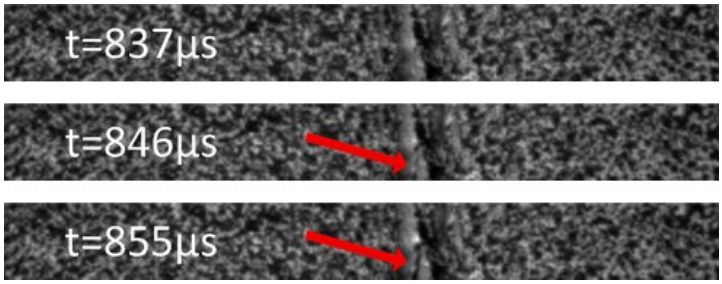

(b)

Figure 3-14: Experiments on a notched tensile specimen. (a) Force-displacement curves for high strain rate loading at different striker velocity (solid lines) and for a low strain rate experiment (dashed line) with a notch radius of *R=6.67mm*. Solid dots depict the instant of the onset of fracture in high strain rate experiments as determined from the occurrence of first surface cracks on (b) high speed photographs taken at a frequency of 110 kHz: the red arrows indicate the location of the first visible surface crack. Note that the time indicated on the pictures is on a shifted time scale.

is about 10% higher than that measured in the low strain rate experiment. The occurrence of a first visible crack on the specimen surface (Fig. 3-14b), corresponding to the onset of material fracture, is highlighted through a solid dot on the measured force-displacement curves. In the case of the slow experiment, a sharp drop in force level is observed at this instant. However, the curves for high strain rate loading exhibit a smooth decrease instead. It is therefore critically important to identify the instant of onset of fracture through high speed photography. The current HSVI system operates at a frequency of 111kHz. Thus, an uncertainty of $\pm 0.05mm$ is associated with the measured displacement to fracture of $2.20mm$.

3.6 Conclusions

A load inversion device is proposed to perform high strain rate tension experiments on sheet materials on conventional split Hopkinson pressure bar (SHPB) systems. The load inversion device includes a pusher which is in contact with the input bar, and a specially designed stirrup which transfers the tensile load in the specimen as compression to two parallel output bars. Two output bars are used to minimize the creation of spurious waves throughout the conversion of the output force from tension to compression. The strains on the specimen surface are measured through planar digital image correlation of high speed video images, while the stresses are computed based on the output bar recordings. As compared to split Hopkinson tensile bar (SHTB) systems, the proposed experimental setup has the technological advantage that the incident wave may be created through a conventional striker-input bar system. The generation of loading pulses with a short rise time and of long duration is therefore easily achieved. These two features are of particular importance when testing sheet materials all the way to fracture at strain rates of only a few hundred s^{-1}.

Detailed finite element simulations are performed to validate the proposed experimental technique. It is shown that for an experimental set-up without any inaccuracies (perfect alignment and gripping of the specimen), the measured stress-strain curve at strain rates of $1000s^{-1}$ would be almost free from oscillations. Validation experiments on specimens extracted from 1.4mm thick TRIP780 steel sheets

are also performed which confirm this result in an approximate manner. In addition, experiments are performed on notched tensile specimens to demonstrate the capability of the proposed experimental technique for studying the onset of fracture at high strain rates.

Chapter 4

Hybrid experimental-numerical characterization of the effect of strain rate on fracture

Contents

Abstract

Tensile experiments are carried out on a TRIP780 steel sheet at low ($\dot{\varepsilon}\sim10^{-3}s^{-1}$), intermediate ($\dot{\varepsilon}\sim1s^{-1}$) and high strain rates ($\dot{\varepsilon}\sim10^{3}s^{-1}$). The experimental program

[6] This Chapter is reproduced from: Dunand & Mohr, "Rate-dependent behavior of Advanced High Strength Steels under multi-axial loading: characterization and modeling at large strains", *submitted for publication*.

includes notched as well as uniaxial tension specimens. Local displacements and surface strain fields are measured optically in all experiments using Digital Image Correlation. Constitutive equations derived from the Mechanical Threshold Stress theory are proposed to describe the rate-dependent behavior as well as plastic anisotropy of the sheet material. Detailed Finite Element simulations of all experiments reveal that the model accurately predicts experimental results, including force displacement curves and local surface strain evolution. In particular, the behavior at large strain, beyond the onset of necking, is well predicted. Stress and strain histories where fracture initiates are also obtained from the simulations in order to characterize the dependence of the material ductility to both strain rate and stress state. If the fracture strain is higher at high strain rate in all experiments, results show that the effect of strain rate on ductility cannot be considered independently from the state of stress.

4.1 Introduction

The plastic deformation behavior of AHSS steels under uniaxial tension has been extensively studied during the last decade, indicating that this class of material experiences positive strain rate sensitivity (e.g. Khan et al., 2012, [91]). Experiments in the intermediate range of strain rates (1 - $10s^{-1}$) are typically carried out in servo-hydraulic testing machines (e.g. Huh et al., 2008, [82]) while high strain rate experiments (100 – $1{,}000s^{-1}$) are usually performed in Split Hokinson bar systems (e.g. Van Slycken et al., 2007, [182]; Dunand et al., 2013, [47]) or direct impact setups (e.g. He et al., 2012, [76]). A key advantage of uniaxial tension experiments is that they give a direct access to the material response at small strain levels, and especially to the dependence of flow stress to strain rate. Indeed, force and local displacement measurements are straightforwardly related to the stress and strain within the range of uniform elongation. Used in conjunction with optical strain measurement methods, it also permits to evaluate the effect of strain rate on plastic anisotropy of AHSS sheets (e.g. Huh et al., 2013, [83]). With the exception of a few experimental results reported for shear loading conditions (e.g. Rusinek & Klepaczko., 2001, [155]; Peirs et al., 2011, [147]), virtually no data can be found in the literature describing the multi-axial behavior of AHSS sheets at high rates of strain.

The effect of strain rate on the ductility of AHSS has comparatively been less evaluated. Most experimental investigations are limited to characterizing uniaxial tension parameters such as the ultimate elongation (e.g. Olivier et al., 2007, [141]; Huh et al, 2008, [82]), thereby putting aside the effect of stress state on ductile fracture. Results presented do not permit to draw a clear trend in the dependence of ultimate elongation to strain rate for AHSS steels. Kim et al. (2013, [94]) measured increasing ultimate elongations for increasing strain rates (ranging from $0.1s^{-1}$ to $200s^{-1}$) in case of a DP780 and a TRIP780 steel. Similarly an elongation twice higher at $1000s^{-1}$ than at $0.001s^{-1}$ is found for a TRIP steel by Verleysen et al. (2011, [185]). On the other hand, Wei et al. (2007, [189]) report decreasing ultimate elongations with increasing strain rates in case of two different TRIP-aided steels, while Curtze et al. (2009, [40]) find almost the same elongation at $10^{-3}s^{-1}$ and $750s^{-1}$ for both DP600 and TRIP700 steels. It is emphasized that the ultimate elongation in a uniaxial tension experiment is a structural characteristic and not an intrinsic material property. It depends strongly on the specimen geometry (Verleysen et al., 2008, [184]; Sun et al., 2012, [168]) and is thus a questionable indicator of material ductility. A somewhat more reliable evaluation of the fracture strain in uniaxial tension experiments may be obtained by measuring the reduction of the cross-section area on fractured specimens and assuming a uniform strain distribution through the sheet thickness. Based on this Reduction of Area method, Kim et al. (2013, [94]) report a decreasing fracture strain for increasing strain rates in case of a TRIP780 steel, and a non-monotonic dependence of ductility to strain rate for DP780 steel.

In most fracture experiments on sheet materials, however, the localization of plastic deformation through necking cannot be avoided and represents a major difficulty in the accurate characterization of the material state at fracture. After necking, the stress and strain fields within the specimen gage section become non-uniform and of three-dimensional nature (stresses in the thickness direction develop). Consequently, the stress history prior to fracture can no longer be estimated from the force history measurements using simple analytical formulas: stress and strain histories prior to fracture need to be determined in a hybrid experimental-numerical approach (Dunand & Mohr, 2010, [48]). In other words, a detailed finite element analysis of the experiment is required to identify the stress and strain fields up to the onset of fracture.

The plasticity model used in the numerical simulation is one of the key elements controlling the accuracy of the method.

An extremely wide variety of constitutive equations describing the rate- and temperature-dependent plastic behavior of metals have been proposed. The goal of constitutive equations is to relate the flow stress to strain, strain rate and temperature (and possibly other internal variables) in order to describe the basic mechanisms of strain hardening, strain rate sensitivity and thermal softening (and possibly damage, phase transformation, texture evolution…). Rate-dependent plasticity models can be categorized into two main branches. On the one hand phenomenological models are based on the separation of the effects of strain, strain rate and temperature (e.g. Johnson and Cook, 1983, [88]; Cowper and Symonds, 1952, [39]). Strain hardening, strain rate sensitivity and thermal softening mechanisms are described by means of basic functions, depending respectively on strain, strain rate and temperature only, which may be arbitrarily combined in additive or multiplicative manners to build an ad-hoc model. A partial review of phenomenological basic functions can be found in Sung et al. (2010, [169]). Integrated phenomenological models in which variables are not separated have also been proposed. They allow for description of more complex mechanisms: temperature-dependent strain hardening (e.g. Sung et al., 2010, [169]), rate-dependent strain hardening (e.g. Khan et al., 2004, [93])… On the other hand, attempts have been made to incorporate a description of the mechanisms of plasticity into physics-based constitutive models (e.g. Zerilli and Armstrong, 1987, [195]; Follansbee and Kocks, 1988, [58]; Voyiadjis and Abed, 2005, [187]; Rusinek et al., 2007, [157]). Most physics-based models make use of the theory of thermally activated plastic deformation to relate flow stress, strain rate and temperature (Conrad, 1964, [38]; Kocks et al., 1975, [95]). Additional internal variables can also be introduced in the constitutive equations to account for history effects (Bodner and Partom, 1975, [20]; Durrenberger et al., 2008, [52]). Comparisons between phenomenological and physics-based models against experimental data tend to show that the latter offer better predictive capabilities when a wide range of strain rates and/or temperatures is considered (Liang and Khan, 1999, [111]; Abed and Makarem, 2012, [2]; Kajberg and Sundin, 2013, [90]).

When dealing with sheet materials, plasticity model calibration is usually done based on uniaxial tension experiments in the range of uniform elongation, as experimental measurements give direct access to stress, strain and strain rate. The material behavior at large strains (beyond uniform elongation) is then assumed by extrapolating the strain hardening at low strains with analytical functions (e.g. Hollomon, 1945, [79]; Swift, 1952, [170]; Voce, 1948, [186]…). This extrapolation may lead to inaccurate predictions of the material behavior at large strains. Sung et al. (2010, [169]) calibrated six different hardening functions for a DP780 based on the uniaxial data in the range of uniform elongation. Even though all models fit the data correctly, significant differences are reported at large strains: most extrapolated models did not represent accurately the material behavior beyond uniform elongation.

In this chapter, tensile experiments are carried out at low, intermediate and high strain rates to characterize the rate-dependent behavior of a TRIP780 steel. In addition to uniaxial tension specimens, the experimental program includes tensile specimens with circular notches. Experiments at high strain rates are performed in the Split Hopkinson Pressure Bar system described in Chapter 3. Constitutive equations adapted from the Mechanical Threshold Stress model (Follansbee and Kocks, 1988, [58]) are proposed to model the dependence of the material behavior to strain rate, as well as plastic anisotropy. After calibration using an inverse method, the predictive capabilities of the model are assessed over multiple strain rates and stress states through detailed Finite Element Simulations of all the experiments. A very good agreement is found between numerical and experimental results. In particular, accurate predictions of the post-necking behavior of the sheet material are obtained. A hybrid experimental-numerical approach is taken to characterize the dependence of ductility to strain rate and stress state. It is found that the TRIP material exhibits a higher ductility at high strain rates. However the evolution of ductility between low and intermediate strain rates depends on the stress state.

4.2 Experimental program

4.2.1 Tensile experiments at low and intermediate strain rate

Tensile experiments are performed on straight specimens (Fig. 4-1a) and on flat specimens with circular cutouts (Fig. 4-1c and 4-1d). The specimen loading axis is always oriented along the rolling direction. All specimens are extracted from the sheet material using waterjet cutting. Notched specimens are 20mm wide and feature a b=10mm wide notched gage section. Specimens with two different notched radii are prepared: R=20mm and R=6.65mm. Experiments are carried out in a servo-hydraulic testing machine under displacement control, specimens being hold by friction in custom-made high pressure clamps. The force applied to the specimen is measured by a MTS 250kN static load cell, while displacements and strains in the gage section are measured by Digital Image correlation, as detailed in Section 4.2.4. Two ranges of strain rates are investigated. For low strain rates, a constant crosshead velocity of 0.84mm/min is imposed to the straight specimens, while a velocity of 0.5mm/min is chosen for notched specimens. To reach intermediate strain rates, velocities of 22mm/s and 8.3mm/s are selected for the straight and notched specimens, respectively. All experiments are carried out at room temperature. Note that the static load cell used is not correctly dimensioned for intermediate strain rate experiments, leading to noticeable oscillations in the force measurements (about 1.2% of the measured signal in amplitude) as visible in Figs. 4-2 to 4-4.

4.2.2 Tensile experiments at high strain rate

The modified Split Hopkinson Pressure Bar system (SHPB) presented in chapter 3 is used to performed high strain rate tensile experiments. In all experiments presented here, the compressive stress pulse has a total duration of 550μs and a rise time of about 30μs, its magnitude being controlled by the striker velocity. A specifically designed load-inversion device is used to transform the compressive loading pulse into tensile loading of the specimen gage section. During deformation of the specimen, the load is transmitted through the load-inversion device as a compressive stress wave into the

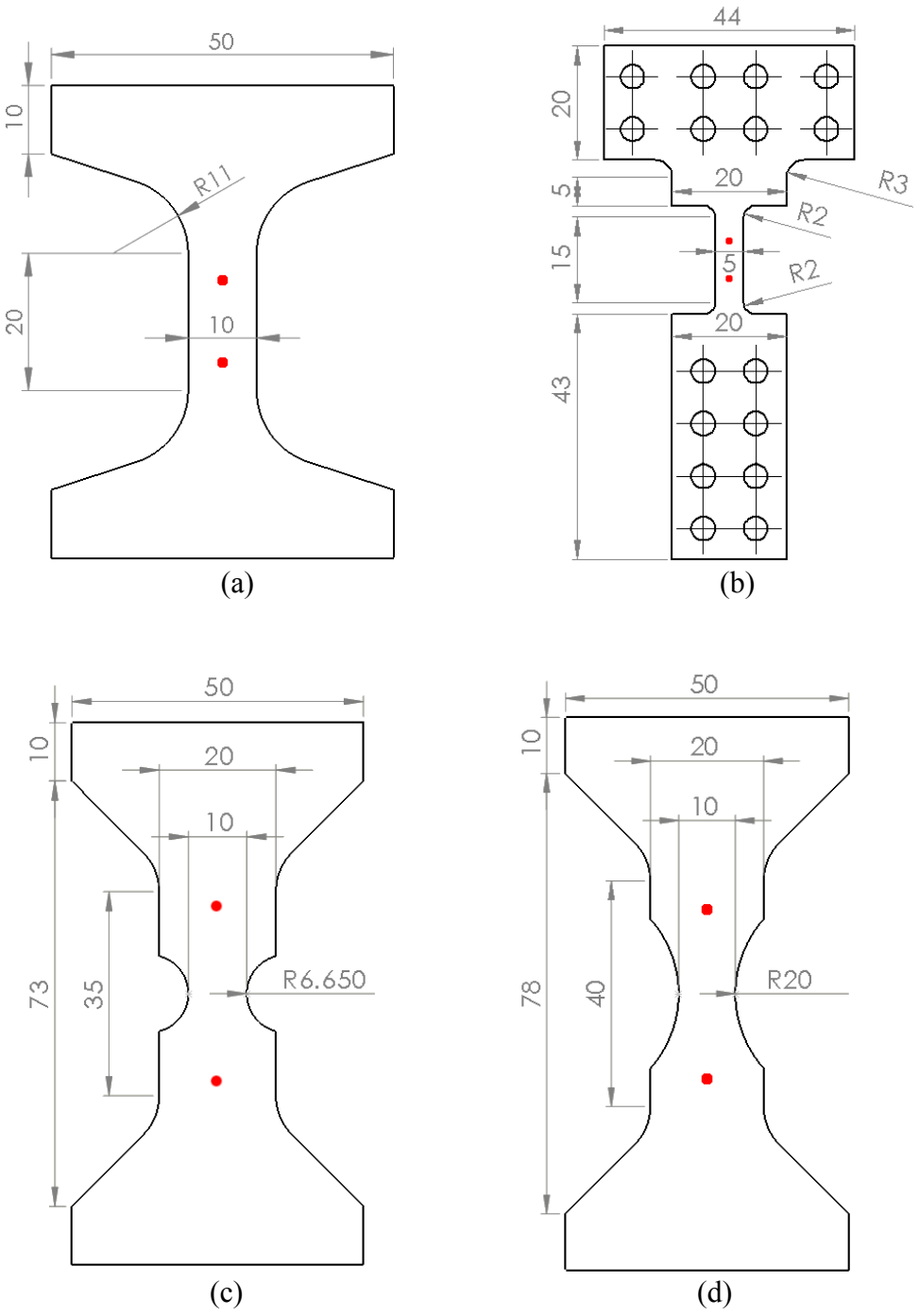

Figure 4-1: Uniaxial tension specimens for (a) low and intermediate strain rate and (b) high strain rate experiments, tensile specimens with a notched radius of (c) 6.65mm and (d) 20mm. Red dots depict the location of the reference points used to measure displacements.

output bars. The specimen is hold by friction in the load-inversion device, the gripping pressure being applied by 8 M5 screws. The force applied to the specimen gage section is derived from elastic waves propagating in the output bars (Eqn. 3-6), while displacements and strains in the specimen gage section are measured by means of high speed imaging and digital image correlation. The reader is referred to Chapter 3 for more details on the experimental set-up and testing procedure.

High strain rate experiments are performed on uniaxial tension specimens, as well as notched tensile specimens with notch radii of R=20mm and R=6.65mm. Note that the geometry of the uniaxial specimen, sketched in Fig. 4-1b, is different from the one used at low and intermediate strain rates. The gage section is shorter (l=15mm instead of 20mm) and narrower (w=5mm instead of 10mm). On the other hand, the gage section geometry of the notched tensile specimens is the same at low and high strain rate. A series of experiments are performed on the three geometries at room temperature with striker velocities of ranging from 4m/s to 14m/s.

4.2.3 Local displacements and strain measurements

In all tensile experiments, pictures of the specimen surface are recorded to perform optical-based displacement and strain measurements. For that purpose a thin layer of white matt paint is applied to the specimen surface along with a black speckle pattern of a speckle size of about 70µm.

In low strain rate experiments, an AVT Pike F505B with 90mm macro lenses takes about 300 pictures (resolution of 2048x1024 pixels) before the onset of fracture. The camera is placed at 1.5m from the specimen surface, resulting in a square pixel edge length of 23µm. In intermediate and high strain rate experiments, a high speed video system (Phantom v7.3 with 90mm macro lenses) is used. For intermediate strain rate experiments, it operates at a frequency of 1kHz with an exposure time of 50µs. A resolution of 800x600 pixels is chosen. The camera is positioned at a distance of about 400mm from the specimen surface (square pixel edge length of 55µm). In high strain rate experiments the acquisition frequency is set to 100kHz with a exposure time of 2µs, limiting the spacial resolution to 560x32 pixels. The camera is positioned at a

distance of about 550mm from the specimen surface (square pixel edge length of 70μm).

The virtual extensometer function of the digital image correlation software VIC2D (Correlated Solutions, SC) is used to determine the relative displacement of two reference points located on the axis of symmetry of the specimen gage sections. For this, a quadratic transformation of a 23x23 pixel neighborhood of each point is assumed. Spline-cubic interpolation of the grey values is used to achieve sub-pixel accuracy. The position of the DIC reference points on the specimen surface is shown in Fig. 4-1 with solid red dots. For notched tensile specimens, an initial spacing between the reference points of $\Delta x = 30mm$ is used to compute the relative displacement imposed to the specimen, while surface strains at the center of the gage sections are calculated with an initial spacing of $\Delta x = 1mm$. For uniaxial tension, a value of $\Delta x = 11.5mm$ (resp. $\Delta x = 6.6mm$) is chosen at low and intermediate strain rates (resp. high strain rate). Based on the relative displacement Δu of the two reference points, the engineering axial surface strain is computed as

$$\varepsilon = \frac{\Delta u}{\Delta x} \tag{4-1}$$

4.3 Experimental results

4.3.1 Uniaxial tension

Figure 4-2 depicts the engineering stress-strain curves measured under uniaxial tension in the three ranges of strain rates. The instant of fracture is indicated with a solid dot. For low and intermediate strain rates (in black and red in Fig. 4-2, respectively) the onset of fracture corresponds to a sudden drop of the specimen load carrying capacity. In the high strain rate experiment, however, the force level decreases smoothly to zero. The instant of the onset of fracture is therefore identified from the DIC pictures as the instant at which a first crack appears on the specimen surface. In all three experiments, a maximum of force corresponding to the onset of localization of the plastic flow (i.e. necking) is observed. Note that the necking strain decreases as strain

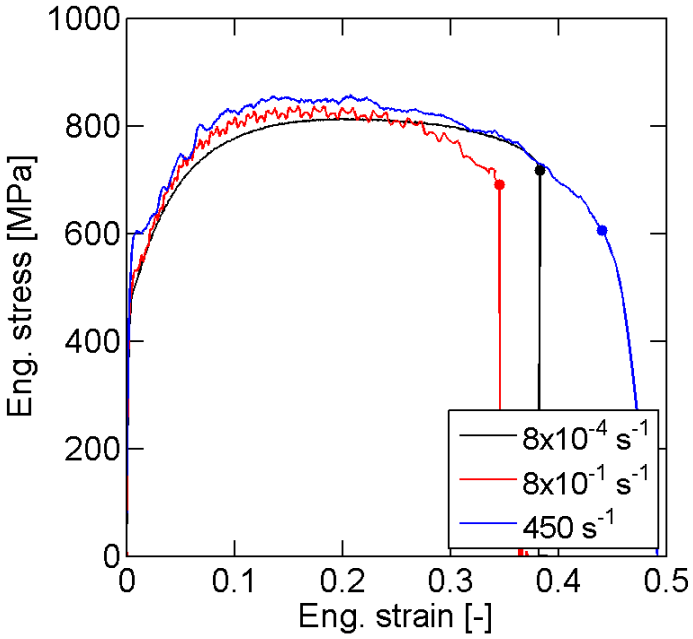

Figure 4-2: Experimental engineering stress-strain curves under uniaxial tension. Results for low strain rates are shown in black, intermediate strain rates in red and high strain rates in blue. Solid dots correspond to the onset of fracture.

rate increases. Necking occurs at an engineering strain of about 0.2 at low strain rate (black curve in Fig. 4-2) while it is only 0.14 at high strain rate (blue curve in Fig. 4-2). For each experiment, a pre-necking strain rate is defined as the time-average of the axial plastic strain rate (measured by DIC) between initial yielding and the onset of necking. A pre-necking strain rate of $\dot{\varepsilon} = 8.10^{-4}\ s^{-1}$ is measured for the experiment at low strain rate (black curve in Fig. 4-2), $\dot{\varepsilon} = 8.10^{-1}\ s^{-1}$ for intermediate strain rate (red curve in Fig. 4-2) and $\dot{\varepsilon} = 450\ s^{-1}$ for high strain rate (blue curve in Fig. 4-2). Note that after the onset of necking, stress and strain fields are no longer uniform in the specimen gage section. Therefore engineering stress and strains should be interpreted as normalized forces and displacements, which are structure-level measurements, rather that local stress and strain measures.

The plastic behavior of the sheet exhibits a weak dependency to strain rate. Both the initial yield stress and strain hardening are rate-sensitive. The material has the same initial yield stress but a higher hardening modulus at intermediate strain rate than at low strain rate. In addition it has a higher initial yield stress but approximately the same

initial hardening modulus at high strain rate than at low strain rate. Before necking, the stress level is about 100MPa higher in the high strain rate experiment than at low strain rate. Note that a comparison of the post-necking part of the curves is not meaningful as different specimen geometries have been used.

4.3.2 Notched tension

Experimental results for the tensile specimen with 20mm notch radii and 6.65mm notch radii are presented in Fig. 4-3 and Fig. 4-4, respectively. Force displacement curves for the three strain rates are depicted in Figs. 4-3a and 4-4a, while the evolution of the engineering axial surface strain at the center of the gage section are plotted in Figs. 4-3b and 4-4b. The onset of fracture is indicated by a solid dot on all curves. As for uniaxial tension experiments, it corresponds to a sharp drop of force in low and intermediate strain rate experiments (in black and red in Figs. 4-3a and 4-4a, respectively), and to the appearance of the first surface crack in the high strain rate experiment (in blue in Figs. 4-3a and 4-4a). Note that surface strain measurements are not available for the high strain rate experiment. Very high strains reached at the center of the gage section combined with high rates of deformation lead to cracking and unsticking of the painted pattern used for correlation.

For the 20mm notched specimen, the relative velocities measured between the two DIC reference points (red points in Fig. 4-1c) are 0.5mm/min for the low strain rate experiment, 8mm/s for the intermediate strain rate experiment and 7.0m/s for the high strain rate experiment, respectively. For the 6.65mm notched specimen, the relative velocities are 0.5mm/min for the low strain rate experiment, 8mm/s for the intermediate strain rate experiment and 4.5m/s for the high strain rate experiment, respectively. Note that the reference point locations are the same in all experiments.

Regardless of the geometry or strain rate, all force-displacement curves feature a maximum of force which corresponds approximately to the onset of localization of the plastic flow in-plane and through the thickness of the sheet (Dunand & Mohr, 2010, [48]). Because of the notched geometry, necking always occurs at the center of the gage section. After the onset of necking, the specimen experiences a loss of load carrying capacity until fracture occurs. With the 20mm notched specimen (Fig. 4-3a), the loss of

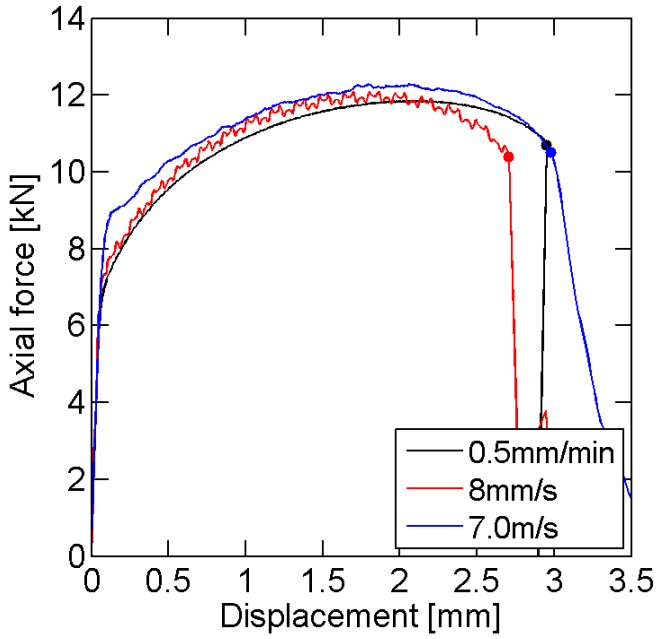

(a)

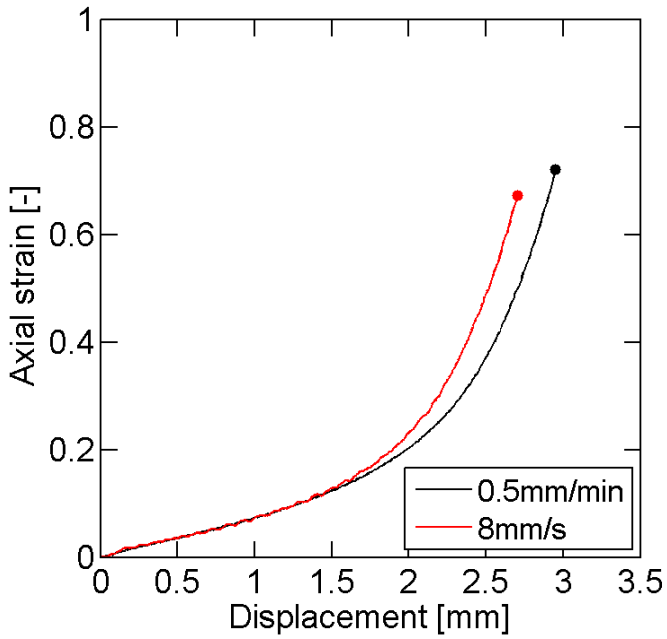

(b)

Figure 4-3: Experimental results of notched tensile specimens with a 20mm radius. (a) Force displacement curves and (b) Evolution of engineering axial surface strain at the center of the gage section. Results for low strain rates are shown in black, intermediate strain rates in red and high strain rates in blue. Solid dots correspond to the onset of fracture.

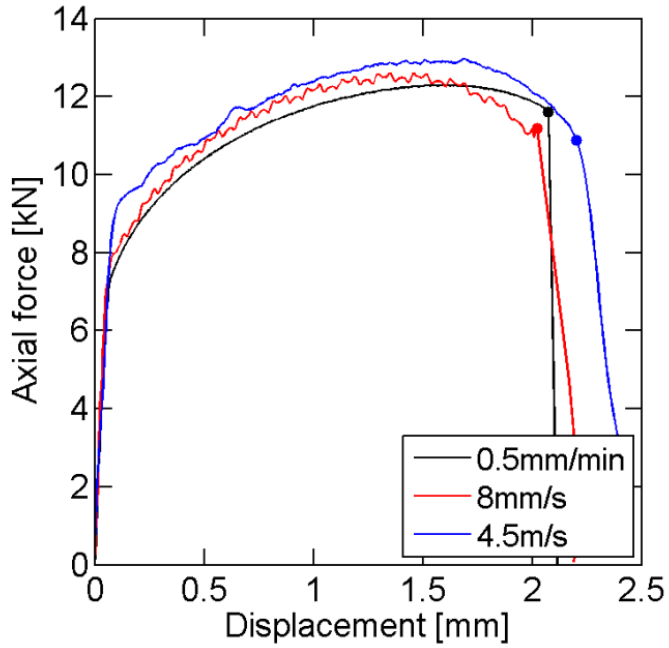

(a)

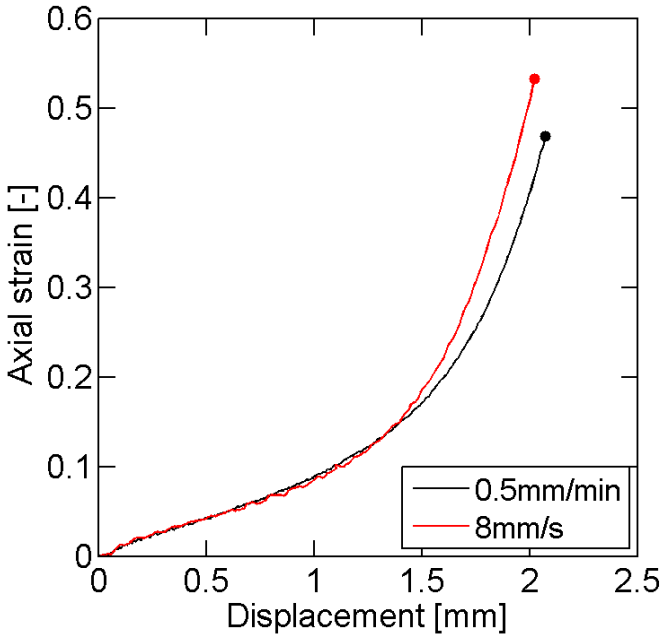

(b)

Figure 4-4: Experimental results of notched tensile specimens with a 6.65mm radius. (a) Force displacement curves and (b) Evolution of engineering axial surface strain at the center of the gage section. Results for low strain rates are shown in black, intermediate strain rates in red and high strain rates in blue. Solid dots correspond to the onset of fracture.

load carrying capacity is about 13% for all strain rates. In case of the 6.65mm geometry (Fig. 4-4a), however, the force drop before fracture increases with strain rate, from 6% at low strain rate to 15% at high strain rate. Note that the onset of necking has a non-monotonic dependence to strain rate. For both geometries, necking occurs at a lower displacement at intermediate strain rate than at low strain rate, and at a higher displacement at high strain rate than at intermediate strain rate.

The evolutions of axial surface strain, depicted in Figs. 4-3b and 4-4b for the 20mm and 6.65mm geometries, show a pronounced increase of axial surface strain rate, which corresponds to localization of the plastic flow. Note that the slope of the curves plotted in Figs. 4-3b and 4-4b does not correspond, but is proportional to engineering strain rate as low and intermediate strain rate experiments are run at almost constant imposed velocity. The change of slope occurring earlier in the intermediate experiments (in red in Figs. 4-3b and 4-4b) confirms that necking happens at a lower displacement at intermediate strain rate than at low strain rate. A noticeable difference between the two geometries concerns the surface strain reached at the onset of fracture at the center of the gage section. With a notch radius of 20mm (Fig. 4-3b), the surface axial strain at fracture is lower by 7% at intermediate strain rate ($\varepsilon = 0.67$) than at low strain rate ($\varepsilon = 0.72$), whereas it is higher by 13% at intermediate strain rate ($\varepsilon = 0.53$) than at low strain rate ($\varepsilon = 0.47$) with a 6.65mm notch radius (Fig. 4-4b).

4.4 Rate- and temperature-dependent plasticity modeling

4.4.1 Constitutive equations

A phenomenological approach is taken to model the material behavior. The material state is described through the Cauchy stress tensor $\boldsymbol{\sigma}$ and the absolute temperature θ, in conjunction with a set of internal variables: the plastic strain tensor $\boldsymbol{\varepsilon^p}$, the equivalent plastic strain rate $\dot{\bar{\varepsilon}}^p$ and a hardening variable s representing the material resistance to plastic deformation.

Incremental plasticity, based on an additive decomposition of the logarithmic strain tensor $\boldsymbol{\varepsilon}$ is employed

$$\boldsymbol{\varepsilon} = \boldsymbol{\varepsilon}^{\boldsymbol{e}} + \boldsymbol{\varepsilon}^{\boldsymbol{p}} \tag{4-2}$$

The constitutive equation for stress classically reads

$$\boldsymbol{\sigma} = \boldsymbol{\mathcal{C}_{el}} : \boldsymbol{\varepsilon}^{\boldsymbol{e}} \tag{4-3}$$

where $\boldsymbol{\mathcal{C}_{el}}$ is the fourth-order isotropic elasticity tensor, characterized by the Young's modulus E and the Poisson ratio ν. The effect of thermal expansion is neglected in this work.

The magnitude of the Cauchy stress is characterized by the equivalent stress

$$\bar{\sigma} = \mathcal{F}(\boldsymbol{\sigma}) \tag{4-4}$$

while the flow rule describing the evolution of the plastic strain tensor is defined as

$$\dot{\boldsymbol{\varepsilon}}^{\boldsymbol{p}} = \dot{\lambda} \frac{\partial \mathcal{G}}{\partial \boldsymbol{\sigma}} \tag{4-5}$$

where $\dot{\lambda}$ is a plastic multiplier, and $\mathcal{G}(\boldsymbol{\sigma})$ represents the plastic potential. Note that when $\mathcal{F} = \mathcal{G}$, Eq. 4-5 corresponds to an associated flow rule, while non-associated flow is modeled otherwise.

The equivalent plastic strain rate $\dot{\bar{\varepsilon}}^{p}$ is defined as the work-conjugate to the equivalent stress

$$\mathcal{D} = \bar{\sigma} \dot{\bar{\varepsilon}}^{p} = \boldsymbol{\sigma} : \dot{\boldsymbol{\varepsilon}}^{\boldsymbol{p}} \tag{4-6}$$

where $\mathcal{D}$ is the rate of plastic work. Upon evaluation of this relationship for the plastic flow defined in Eq. 4-5, we obtain the following relationship between the equivalent plastic strain rate and the plastic multiplier

$$\dot{\bar{\varepsilon}}^{p} = \dot{\lambda} \frac{\mathcal{G}}{\mathcal{F}} \tag{4-7}$$

The choice of an associated flow rule yields $\dot{\bar{\varepsilon}}^{p} = \dot{\lambda}$.

The rate and temperature sensitivity of the material behavior is introduced through the relationship

$$\dot{\bar{\varepsilon}}^p = f(\bar{\sigma}, s, \theta) \tag{4-8}$$

Finally the material hardening during straining is described by the evolution equation

$$\dot{s} = g(\bar{\sigma}, s, \theta) \tag{4-9}$$

Since this work focuses on monotonic loadings only, kinematic hardening is not considered.

In high strain rate deformation processes, the material is submitted to a temperature increase due to quasi-adiabatic heating. For the adiabatic case, the temperature rises according to

$$\rho c \dot{\theta} = \zeta \bar{\sigma} \dot{\bar{\varepsilon}}^p \tag{4-10}$$

Where ρ is the density, c the specific heat and ζ the ratio of plastic work converted to heat. Typically a value of $\zeta = 0.9$ is used (Rusinek and Klepaczko, 2009, [156]).

4.4.2 Model specialization

The constitutive model defined in Section 4.4.1 is fully characterized by the four functions $\mathcal{F}(\boldsymbol{\sigma})$, $\mathcal{G}(\boldsymbol{\sigma})$, $f(\bar{\sigma}, s, \theta)$ and $g(\bar{\sigma}, s, \theta)$. Specific forms permitting to model accurately the plastic behavior of the TRIP material are given thereafter.

4.4.2.1 Equivalent stress and flow potential

For the present sheet material, nearly the same stress-strain curve is measured in uniaxial tension for different specimen orientations even though the Lankford coefficients are direction dependent. As detailed in Mohr et al. (2010, [122]), we therefore make use of planar isotropic quadratic yield function, along with a non-associated flow rule based on a quadratic anisotropic flow potential.

$$\mathcal{F} = \sqrt{(\boldsymbol{F}\boldsymbol{\sigma}) \cdot \boldsymbol{\sigma}} \tag{4-11}$$

and

$$\mathcal{G} = \sqrt{(\boldsymbol{G}\boldsymbol{\sigma}) \cdot \boldsymbol{\sigma}} \tag{4-12}$$

F and **G** are symmetric positive-semidefinite matrices, with $\mathcal{F} = 0$ and $\mathcal{G} = 0$ if and only if $\boldsymbol{\sigma}$ is a hydrostatic stress state. $\boldsymbol{\sigma}$ denotes the Cauchy stress vector in material coordinates,

$$\boldsymbol{\sigma} = [\sigma_0 \quad \sigma_{90} \quad \sigma_n \quad \tau \quad \tau_{0n} \quad \tau_{90n}]^T \tag{4-13}$$

The components σ_0, σ_{90} and σ_n represent the true normal stress in the rolling, transverse and out-of-plane directions; τ denotes the corresponding in-plane shear stress, while τ_{0n} and τ_{90n} represent the corresponding out-of-plane shear stresses. Note that in the specific case of quadratic stress and flow potentials defined by Eq. 4-11 and 4-12, Stoughton (2002, [164]) demonstrated that the non-associated flow rule is consistent with laws of thermodynamics. As shown in Mohr et al. (2010, [122]), the matrices **F** and **G** have only 3 independent coefficients: F_{12}, F_{22} and F_{33}, G_{12}, G_{22} and G_{33}.

4.4.2.2 Strain hardening

A review of existing strain hardening functions g and rate sensitivity functions f, governing $\dot{s}$ and $\dot{\bar{\varepsilon}}^p$ respectively, can be found in Sung et al. (2010, [169]). Here, the hardening modulus $h = \partial s / \partial \varepsilon$ is considered as stress- and temperature- independent. Equation 4-9 can therefore be reduced to

$$\dot{s} = h(s)\dot{\bar{\varepsilon}}^p \tag{4-14}$$

Among the numerous hardening laws present in the literature, a saturation hardening law is selected as it can account for large hardening capabilities of TRIP steels at low strains as well as a vanishing hardening at very high strains,

$$h(s) = H_0 \left(1 - \frac{s}{s_\infty}\right)^r \tag{4-15}$$

4.4.2.3 Strain rate and temperature sensitivity

A constitutive relation derived from the Mechanical Threshold Stress theory (MTS; Follansbee and Kocks, 1988, [58]) is chosen to describe the dependence of the equivalent plastic strain rate $\dot{\bar{\varepsilon}}^p$ to the applied stress $\bar{\sigma}$, the deformation resistance s and temperature θ. This physics-inspired plasticity model considers dislocation motion as the only source of plastic deformation and describes it as a thermally activable process.

The deformation resistance to dislocation motion s is conceptually decomposed into two parts,

$$s = s_{th} + s_a \tag{4-16}$$

where s_a represents the part of resistance due to athermal obstacles (typically long range obstacles such as grain boundaries or large precipitates) and s_{th} represents the part of the resistance due to thermally activable obstacles which can be overcome by thermal fluctuations (typically short range obstacles such as the Peierls resistance, forest dislocations or solute atoms). Therefore, a lower stress is required to overcome the short range resistance s_{th} at higher temperatures. Introducing an effective "thermal" stress

$$\bar{\sigma}_{th} = \bar{\sigma} - s_a \tag{4-17}$$

then the rate of deformation is described by an Arrhenius expression of the form (Conrad, 1964, [38])

$$\dot{\bar{\varepsilon}}^p = f(\bar{\sigma}, s, \theta) = \begin{cases} 0 & \text{if } \bar{\sigma}_{th} \leq 0 \\ \dot{\varepsilon}_0 \exp\left\{-\dfrac{\Delta G(\bar{\sigma}_{th}, s_{th})}{k_B \theta}\right\} & \text{if } 0 < \bar{\sigma}_{th} \leq s_{th} \end{cases} \tag{4-18}$$

where $\dot{\varepsilon}_0$ is a material constant, k_B the Boltzmann's constant and ΔG is the Gibbs' free energy required to overcome the obstacles to dislocation motion with an applied stress, which is phenomenologically modeled as (Kocks et al., 1975, [95])

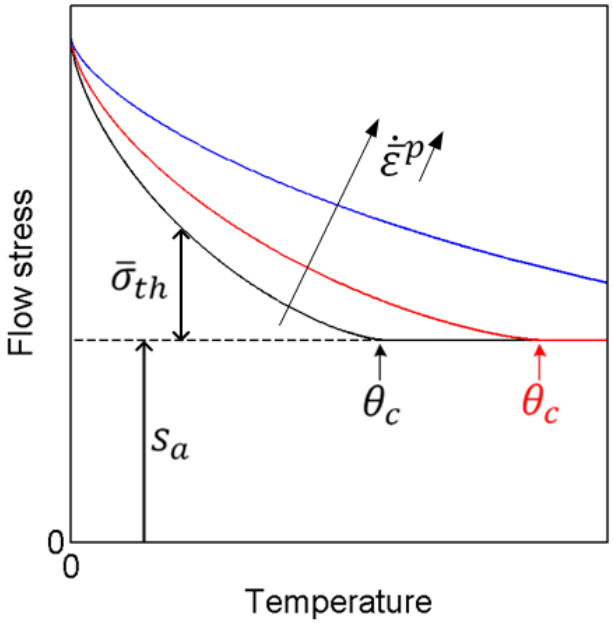

Figure 4-5: Dependence of flow stress to temperature for low strain rate (in black), intermediate strain rate (in red) and high strain rate (in blue), at fixed deformation resistance s. θ_c is the temperature, depending on strain rate, above which there is enough thermal energy to overcome short range barriers by thermal activation only.

$$\Delta G(\bar{\sigma}_{th}, s_{th}) = \Delta F \left[1 - \left(\frac{\bar{\sigma}_{th}}{s_{th}}\right)^p\right]^q \tag{4-19}$$

ΔF is the activation free energy required to overcome the obstacles to dislocation motion without the aid of an applied stress.

Strain hardening of the material can be described either by an increase of s_a (e.g. Kothari and Anand, 1998, [98]), of s_{th} (e.g. Follansbee and Kocks, 1988, [58]) or both (e.g. Balasubramanian and Anand, 2002, [8]) during plastic loading. Here we assume that both s_a and s_{th} increase at the same rate: the ratio $\chi = s_{th}/s_a$ is kept constant throughout loading. Therefore, Eq. 4-18 can be rewritten as

$$\bar{\sigma} = s_a + Z(\dot{\bar{\varepsilon}}^p, \theta) s_{th} = \frac{1 + \chi\, Z(\dot{\bar{\varepsilon}}^p, \theta)}{1 + \chi} s \tag{4-20}$$

where

$$Z = \left\{ 1 - \left[\frac{\theta}{\theta_c(\dot{\bar{\varepsilon}}^p)} \right]^{\frac{1}{q}} \right\}^{\frac{1}{p}} \leq 1 \quad \text{with} \quad \theta_c = \frac{\Delta F}{k_B \ln\left({\dot{\varepsilon}_0}/{\dot{\bar{\varepsilon}}^p} \right)} \tag{4-21}$$

Figure 4-5 depicts the dependence of the flow stress to temperature for different strain rates. As detailed in Balasubramanian and Anand (2002, [8]), θ_c is the critical temperature above which there is enough thermal energy for the barriers to be overcome by thermal fluctuation only, without applying stress. Therefore, at a given equivalent plastic strain rate $\dot{\bar{\varepsilon}}^p$, the temperature $\theta_c(\dot{\bar{\varepsilon}}^p)$ is the limit of applicability of this plasticity model.

4.4.3 Calibration procedure

The rate- and temperature- dependent constitutive model defined in Sections 4.4.1 and 4.4.2 features 17 independent material parameters overall: 2 elastic coefficients, 3 coefficients defining the equivalent stress function $\mathcal{F}$ (Eq. 4-11), 3 coefficients defining the plastic flow potential $\mathcal{G}$ (Eq. 4-12), 4 coefficients defining the strain hardening function g (Eq. 4-15) and 5 coefficients defining the rate sensitivity function f (Eq. 4-18). The calibration procedure is given thereafter. The set of parameters calibrated for the present TRIP material are given in Table 4-1.

The equivalent stress function $\mathcal{F}$ and plastic flow potential $\mathcal{G}$ are calibrated based on uniaxial tension experiments carried out at low strain rate. Corresponding matrices **F** and **G** are calibrated following the procedure described in Mohr et al. (2010, [122]). Since the spacial resolution of high speed imaging system is not sufficient to measure the Lankford coefficients in high strain rate tension experiments, it is assumed that the anisotropy of the plastic flow observed at low strain rate is independent from the strain rate. The flow potential $\mathcal{G}$ is therefore assumed rate-independent. Note that because of a lack of experimental data characterizing the out-of-plane behavior of the sheet material, coefficients of **F** and **G** corresponding to out-of-plane shear are set equal to 3 (isotropic value).

An optimization based inverse method is carried out to calibrate the coefficients of the strain hardening and rate sensitivity functions. The objective of the optimization

Table 4-1: Material parameters for the rate-dependent model

Elastic constants		Strain hardening parameters			
E [MPa]	ν [-]	s_0 [MPa]	s_∞ [MPa]	H_0 [MPa]	r [-]
185,000	0.3	503	1,383	41,505	2.513
Strain rate sensitivity parameters					
$\dot{\varepsilon_0}$ [s^{-1}]	ΔF [J]	p [-]	q [-]	χ [-]	
67,457	8.794E-20	1.911	1.861	0.1949	
Equivalent stress and flow potential parameters					
F_{11} [-]	F_{22} [-]	F_{33} [-]	F_{44} [-]	F_{12} [-]	F_{13} [-]	F_{23} [-]
1	1	1.076	2.925	-0.462	-0.538	-0.538
G_{11} [-]	G_{22} [-]	G_{33} [-]	G_{44} [-]	G_{12} [-]	G_{13} [-]	G_{23} [-]
1	0.873	1.071	3.13	-0.401	-0.599	-0.472

process is to find the set of parameters that leads to the best prediction of the force-displacements curves of the notched tensile specimen with a 6.65mm radius measured in low, intermediate and high strain rate experiments. For a given set of parameters $\boldsymbol{\alpha}$, numerical simulations of the 6.65mm notched tensile specimen are carried out for the three different strain rates, using the Finite Element model described in Section 4.5.1. Then the three predicted force-displacement curves are compared to experimental measurements up to the fracture displacement u_f to evaluate the cost function E for the set of parameters $\boldsymbol{\alpha}$

$$E^2(\boldsymbol{\alpha}) = \sum_N \left\{ \frac{1}{u_f} \int_0^{u_f} \eta(u) [F_{FEA}(u) - F_{EXP}(u)]^2 \, du \right\} \tag{4-22}$$

where $N = 3$ is the number of calibration tests and η is a weighting factor used to focus the fitting process on the part of the force-displacement curves located between maximum force and the onset of facture. Before maximum force is reached $\eta = 1$,

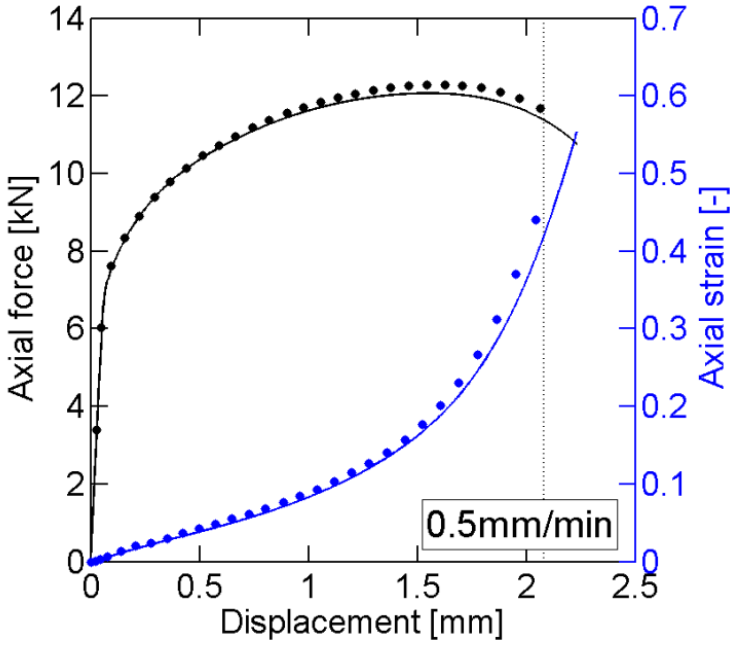
Axial force [kN]
Axial strain [-]
Displacement [mm]
0.5mm/min
0
2
4
6
8
10
12
14
0
0.1
0.2
0.3
0.4
0.5
0.6
0.7
0
0.5
1
1.5
2
2.5

(a)

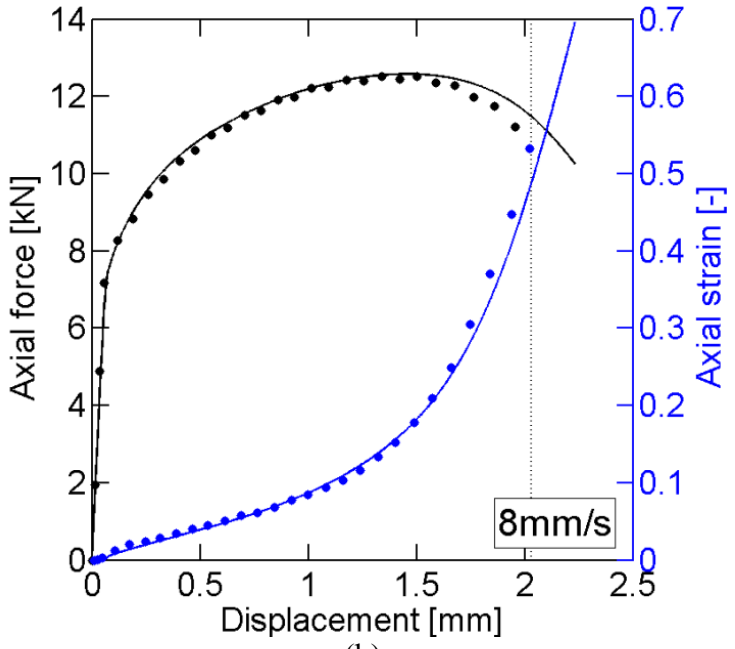
Axial force [kN]
Axial strain [-]
Displacement [mm]
8mm/s
0
2
4
6
8
10
12
14
0
0.1
0.2
0.3
0.4
0.5
0.6
0.7
0
0.5
1
1.5
2
2.5

(b)

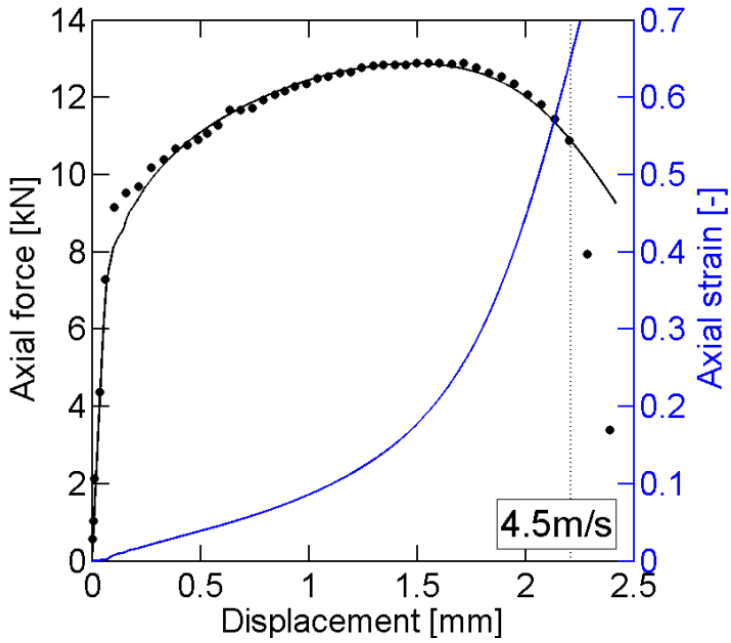

(c)

Figure 4-6: Experimental (points) and simulation (solid curves) results for the notched tensile specimen with a $R = 6.65mm$ radius, at (a) low, (b) intermediate and (c) high strain rate. Force displacement curves are in black and engineering axial strain versus displacement curves in blue. The dashed lines depict the instant of fracture.

while $\eta = 5$ beyond maximum force. A downhill simplex minimization algorithm (Nelder and Mead, 1965, [133]) is used to find the set of parameters $\boldsymbol{\alpha_{min}}$ that minimizes E, as it requires the evaluation of the error function only, but not its derivatives

$$\boldsymbol{\alpha_{min}} = \underset{\boldsymbol{\alpha}}{\operatorname{argmin}}\, E(\boldsymbol{\alpha}) \tag{4-23}$$

Overall 640 iterations were required to converge to a minimum. Corresponding force displacement curves are shown in Fig. 4-6. Numerical predictions (solid black lines in Fig. 4-6) are in very close agreement with experimental results (black dots in Fig. 4-6) for all three strain rates, including after the maximum of force is reached. Note that the resulting set of optimal parameters, given in Table 4-1, corresponds only to a local minimum of the error function E. This optimal set might not be the unique set of parameters minimizing E, and it is not necessarily the best possible set (absolute minimum of E).

4.5 Numerical analysis and plasticity model validation

4.5.1 Finite element model

Dynamic explicit simulations of each tensile experiment are carried out using the commercial Finite Element Analysis package Abaqus (2011, [1]). The constitutive model described in Section 4.4 is implemented as a user material through the VUMAT interface (see Appendix A for details on the implementation). Specimens are meshed with reduced integration brick elements with a temperature degree of freedom (type C3D8RT of the Abaqus library). Exploiting the symmetry of the notched specimen geometries, material properties and loading conditions, only one eighth of the notched specimens are modeled: the mesh represents the upper right quarter of the tensile specimens, with half the thickness. The distance between the center of the gage section and the upper mesh boundary corresponds exactly to half the length of the virtual extensometer used to measure displacements during the experiments. Note that experimental observations demonstrate that plastic localization also respects the specimen symmetries. Reduced meshes can therefore be used to model the post-necking behavior of notched tensile specimens. In uniaxial tension experiments, however, so-called diffuse necking leads to a slanted band of plastic localization that does not respect the initial symmetries. The meshes used for uniaxial tension model the full specimen geometries, including the specimen shoulders.

In all tensile experiments carried out, the plastic flow localizes before the onset of fracture, leading to steep gradients of stresses and strains both in-plane and through the sheet thickness. To capture accurately the post-necking behavior, a fine mesh featuring 8 elements through the half-thickness and an element in-plane dimension of 0.1mm at the center of the gage section is used (see Chapter 5 for details).

Simulations of each loading condition are performed. For that purpose half the experimental velocity measured by DIC is uniformly imposed to the upper boundary of the mesh. A zero normal displacement condition is imposed to boundaries corresponding to symmetry planes. Simulations are run slightly beyond the displacement at which fracture occurs in the experiment. To speed up calculations, uniform mass scaling is used in the low strain rate simulations. The material density is

artificially adjusted to reach the fracture displacement within 300,000 time increments. High strain rate experiments are simulated with the real material density ($7.8 g/cm^3$), resulting in an initial stable time increment of $1.1x10^{-8}$s and about 50,000 increments.

To account for both temperature increase due to plastic work and heat diffusion due to temperature gradients, the "temperature-displacement analysis" capability of the Abaqus/Explicit solver is used to simulate the intermediate and high strain rate experiments. In this type of Finite Element analysis, both the equilibrium and heat transfer equations are solved. Since most plastic deformation and thus most heat generation are localized at the center of the gage section, no heat flow is modeled on the upper boundary of the mesh. In addition, a no heat flow condition is also imposed to the boundaries corresponding to symmetry planes. Furthermore, no heat transfer is considered at the specimen surface. A material specific heat of 490 J/K/kg and a conductivity of 45 J/s/m/K are chosen. Low strain rate experiments are modeled as isothermal.

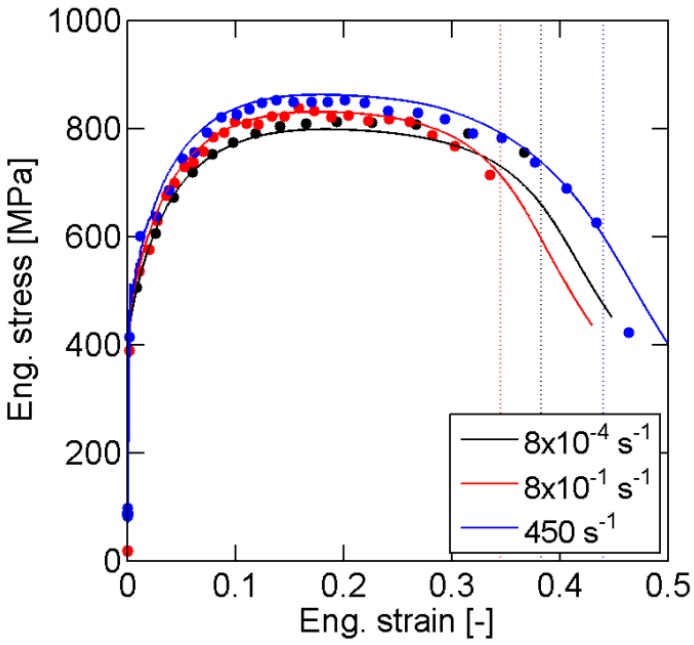

Figure 4-7: Experimental (points) and simulation (solid curves) results for uniaxial tension at low (black curve), intermediate (red curve) and high strain rate (blue curve). The dashed lines depict the instant of fracture.

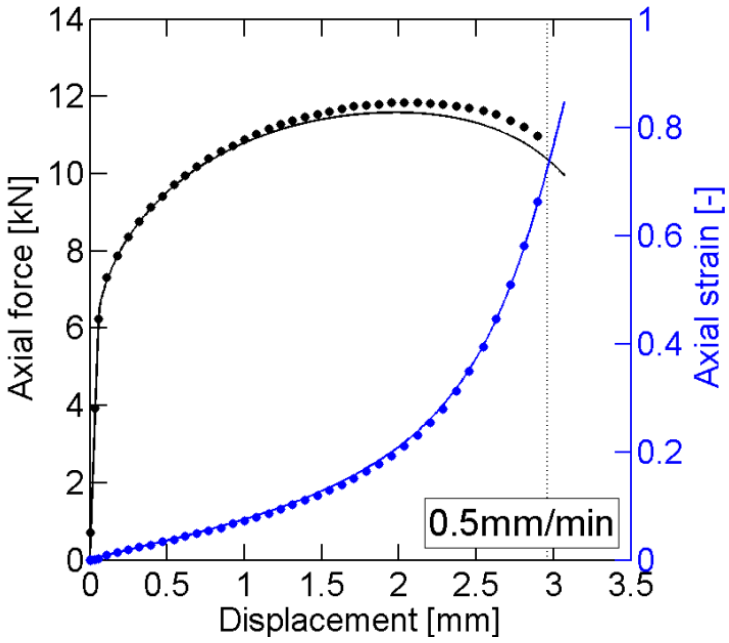
Axial force [kN]
Axial strain [-]
Displacement [mm]
0.5mm/min

(a)

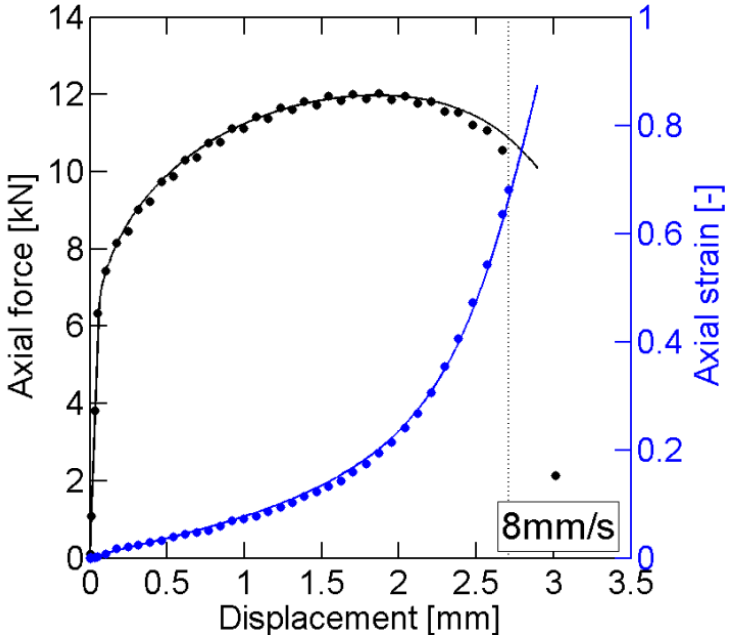
Axial force [kN]
Axial strain [-]
Displacement [mm]
8mm/s

(b)

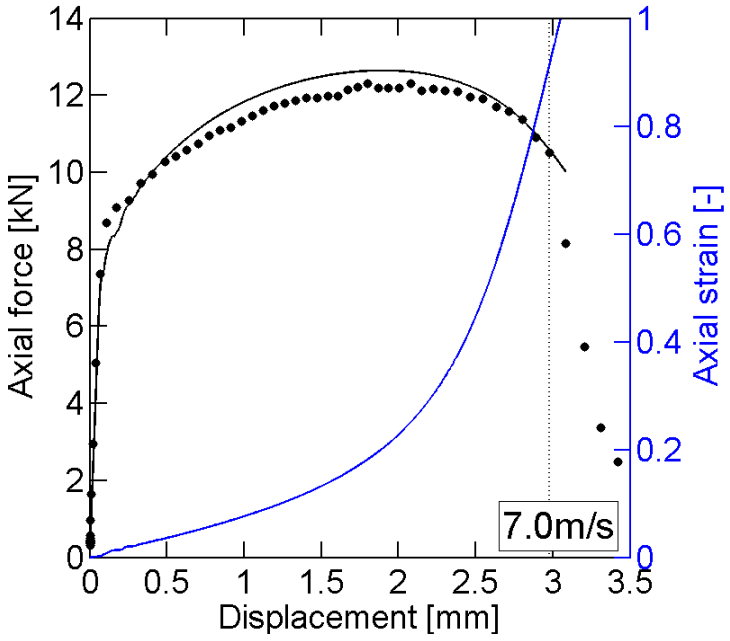

(c)

Figure 4-8: Experimental (points) and simulation (solid curves) results for the notched tensile specimen with a $R = 20mm$ radius, at (a) low, (b) intermediate and (c) high strain rate. Force displacement curves are in black and central logarithmic axial strain versus displacement curves in blue. The dashed lines depict the instant of fracture.

4.5.2 Comparison of numerical and experimental results

Figures 4-6 to 4-8 present a comparison between results from numerical simulations (solid lines) of all tensile experiments and experimental measurements (solid dots). The instant of the onset of fracture is depicted for all experiments through a vertical dashed line. Recall that only the force-displacement curves of the 6.65mm notched tensile experiments (in black in Fig. 4-6) are used to calibrate the proposed plasticity model. All other results may be seen as model validation.

Uniaxial engineering stress strain curves are shown in Fig. 4-7. The numerical engineering strain is computed according to Eq. 4-1 from the displacements of nodes positioned at the same location as DIC reference points, while the numerical engineering stress is obtained from the force applied at the specimen boundaries normalized by the gage section initial cross section area. Experimental results at both intermediate (in red in Fig. 4-7) and high strain rate (in blue in Fig. 4-7) are extremely

well predicted, as numerical results (solid lines) and experimental measurements (solid dots) lie almost exactly on top of each other up to fracture. Note that the loss of load carrying capacity preceding fracture is correctly predicted in both cases. Concerning the low strain rate experiment (in black in Fig. 4-7), the stress strain curve is well predicted in the range of uniform elongation (before maximum engineering stress is reached). However, the force level is underestimated after the onset of necking, resulting in a predicted force 7% lower than the experimental one at the onset of fracture.

In Fig. 4-8, we show the simulated force-displacement curves (solid black lines) of the 20mm notch geometry for low (Fig. 4-8a), intermediate (Fig. 4-8b) and high (Fig. 4-8c) strain rates. The agreement with experimental results is very good all the way to the onset of fracture. The relative difference between experimental and predicted forces does not exceed 3%.

The comparison of the evolution of the surface axial strain at the center of the gage section of notched specimens with respect to the displacement (depicted in blue in Figs. 4-6 and 4-8) also shows a good agreement. Irrespective of the notch radius and the strain rate, the simulations are able to describe the characteristic increases in strain rates that have been observed in the experiments. Relative differences between simulation and DIC strains in case of the 6.65mm notch geometry are about 5% at low strain rate (Fig. 4-6a) and 6% at intermediate strain rate (Fig. 4-6b) at the onset of fracture. For the 20mm notch geometry (Fig. 4-8), the computed strain almost exactly corresponds to the DIC strain, with less than 1% relative error for both strain rates.

4.6 Loading histories to fracture

Stress and strain fields are heterogeneous both in-plane and through the thickness in all experiments performed, because of specimen geometries and plastic flow localization through necking. It is therefore not possible to obtain an accurate estimate of the evolution of stress, strain and strain rate up to fracture from either global (force-displacement curve) or local (surface strains from DIC) experimental measurements (Dunand and Mohr, 2010, [48]). Instead the evolutions of stress state, strain and strain rate are obtained from the Finite Element simulations presented in Section 4.5. From

each simulation, the loading histories are extracted from the integration point where the equivalent plastic strain is highest at the onset of fracture, which is thereby assumed to be the location where fracture initiates. Recall that the onset of fracture is considered to be reached in the simulation when the imposed displacement corresponds to the experimentally measured displacement at which a first crack appears at the specimen surface.

Figures 4-9 to 4-11 summarize the loading histories to fracture in all experiments. The evolutions of strain rate and stress state are shown in Figs. 4-9 and 4-10, respectively. Figure 4-11 depicts the evolution of the equivalent plastic strain versus stress state for all geometries and loading conditions.

The plastic localization associated with necking has a profound influence on the local material state. Despite constant velocities applied to the specimen boundaries, the local strain rate dramatically increases after the onset of necking. In the 20mm notch specimens, the equivalent plastic strain rate is 20 times larger at the onset of fracture than before the onset of necking. In the low strain rate experiment, the strain rate increases from $5\text{x}10^{-4}\text{s}^{-1}$ to 10^{-2}s^{-1} (black line in Fig. 4-9b). The increase ranges from 0.53s^{-1} to 10.5s^{-1} in the intermediate strain rate experiment (in red in Fig. 4-9b) and from 500s^{-1} to $10.2\text{x}10^{3}\text{s}^{-1}$ in the high strain rate experiment (in blue in Fig. 4-9b). Similar increases of strain rates are observed in the 6.65 notch experiment (Fig. 4-9c). In uniaxial tension experiments (Fig. 4-9a), the increase of strain rate due to necking is even more pronounced. In the low strain rate loading (in black in Fig. 4-9a), the equivalent plastic strain rate is 40 times larger at the onset of fracture ($\dot{\bar{\varepsilon}}^{p}=3.2\text{x}10^{-2}\text{s}^{-1}$) than before necking ($\dot{\bar{\varepsilon}}^{p}=8\text{x}10^{-4}\text{s}^{-1}$).

Figure 4-10 depicts the stress state trajectory in the (η, ξ) space for the three low strain rate experiments, while the loading trajectories in the $(\eta, \bar{\varepsilon}^{p})$ space and the $(\xi, \bar{\varepsilon}^{p})$ space are shown for all experiments in Fig. 4-11a and 4-11b respectively. Solid points in Figs. 4-10 and 4-11 mark the onset of fracture. Even though experiments are performed on a sheet material, the stress states at fracture (solid dots in Fig. 4-10) significantly differ from the plane stress condition (represented by a dashed line in Fig. 4-10). After the onset of necking, the triaxiality increases (Fig. 4-11a) and the third invariant decreases (Fig. 4-11b) continuously in all experiments. In the specific case of

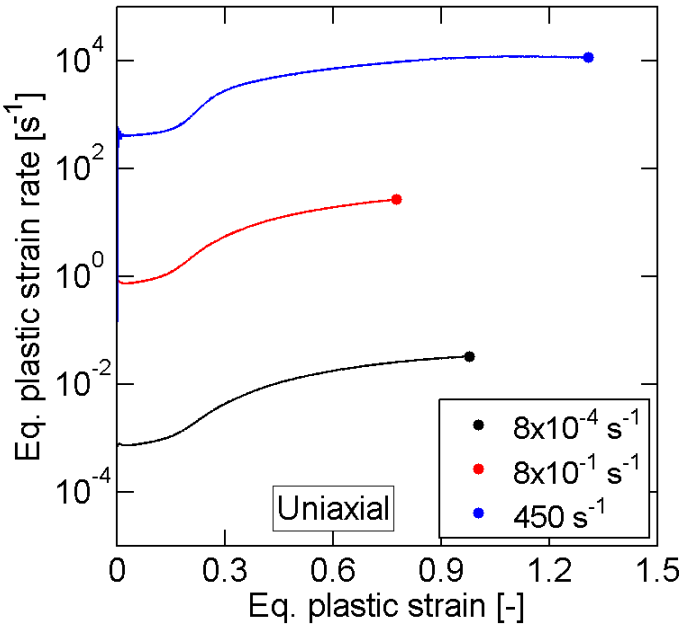
Eq. plastic strain rate [s-1]
10^4
10^2
10^0
10^-2
10^-4
0
0.3
0.6
0.9
1.2
1.5
Eq. plastic strain [-]
Uniaxial
8x10^-4 s^-1
8x10^-1 s^-1
450 s^-1

(a)

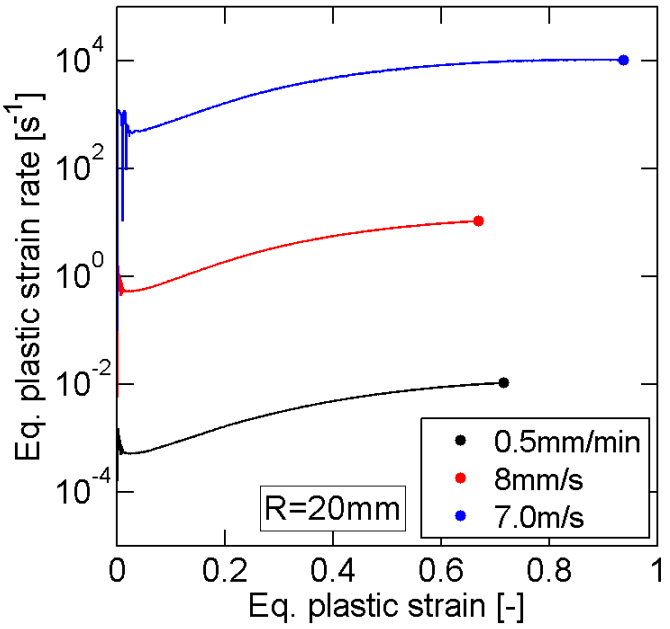
Eq. plastic strain rate [s-1]
10^4
10^2
10^0
10^-2
10^-4
0
0.2
0.4
0.6
0.8
1
Eq. plastic strain [-]
R=20mm
0.5mm/min
8mm/s
7.0m/s

(b)

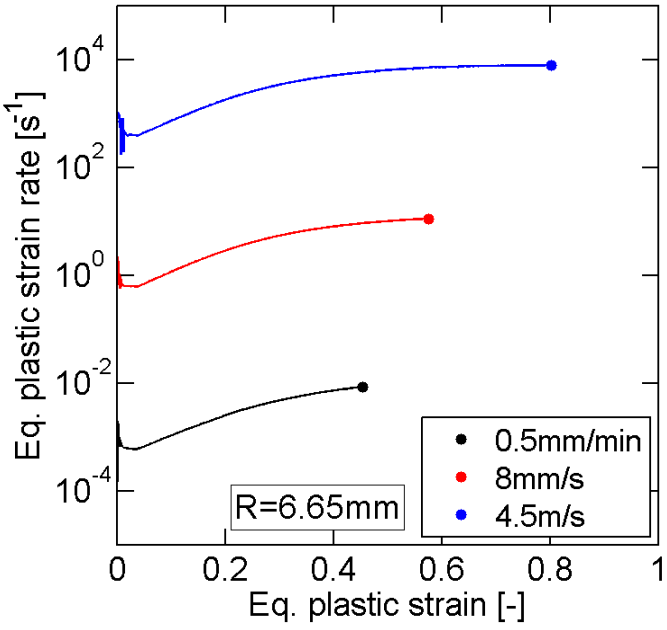

(c)

Figure 4-9: Numerical prediction of the evolution of equivalent plastic strain rate versus equivalent plastic strain at the location where fracture is assumed to initiate in (a) uniaxial tension, (b) 20mm notch tension and (c) 6.65mm notched tension experiments. Solid dots indicate the onset of fracture.

uniaxial tension at high strain rate, the triaxiality ramps up from $\eta = 0.33$ to $\eta = 0.85$ while the third invariant decreases from $\xi = 1$ down to $\xi = 0.26$.

The equivalent plastic strain reached at the onset of fracture, or fracture strain ε_f, strongly depends on both the stress state and the strain rate. In a given range of strain rate, the fracture strain monotonically decreases when moving from uniaxial tension to TPS tension. At low strain rate (black curves in Fig. 4-11), the fracture strain is 60% higher in the 20mm notch specimen ($\varepsilon_f = 0.72$) and 118% higher in the uniaxial specimen ($\varepsilon_f = 0.98$) than in the 6.65mm notch specimen ($\varepsilon_f = 0.45$). The dependence of the fracture strain to strain rate appears to be stress state dependent. In case of the 6.65mm notch specimen, it increases monotonically with strain rate, from $\varepsilon_f = 0.45$ to $\varepsilon_f = 0.58$ at intermediate strain rate and $\varepsilon_f = 0.80$ at high strain rate. In the case of 20mm notch tension specimens, however, the dependence is non-monotonic. The fracture strain at intermediate strain rate ($\varepsilon_f = 0.67$) is lower than at

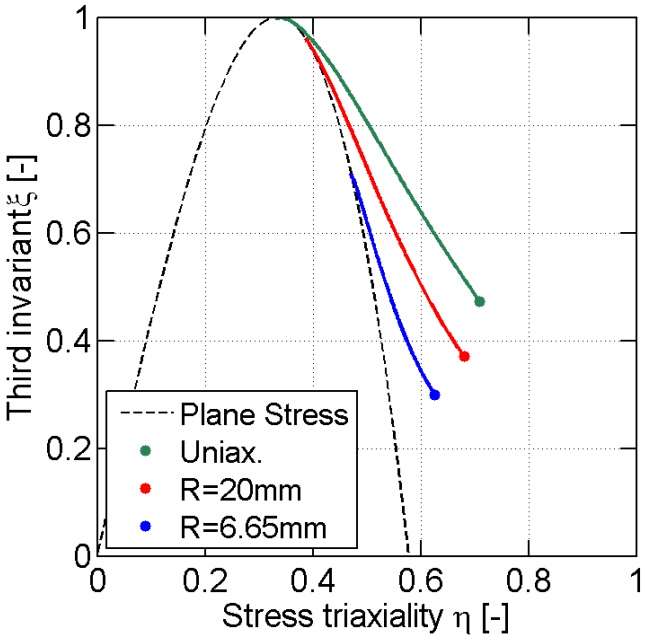

Figure 4-10: Loading path in the (η, ξ) plane for low strain rate experiments. Solid dots indicate the instant of fracture. The black dashed line shows the relation between stress triaxiality and third stress invariant in case of plane stress condition.

low strain rate ($\varepsilon_f = 0.72$) by 7%, but it is highest at high strain rate ($\varepsilon_f = 0.94$). The effect of strain rate is even more pronounced with the uniaxial tension specimen, in which the fracture strain at intermediate strain rate ($\varepsilon_f = 0.77$) is lower than at low strain rate ($\varepsilon_f = 0.98$) by 21%, while it is higher at high strain rate ($\varepsilon_f = 1.31$) by 34%.

Note that for a given geometry, the stress state evolution is more or less independent from the strain rate, as shown in Fig. 4-11. Differences in the fracture strain for different loading conditions on a given specimen are therefore attributed to the dependence of the material ductility to strain rate, and not to a variation in the stress state evolution.

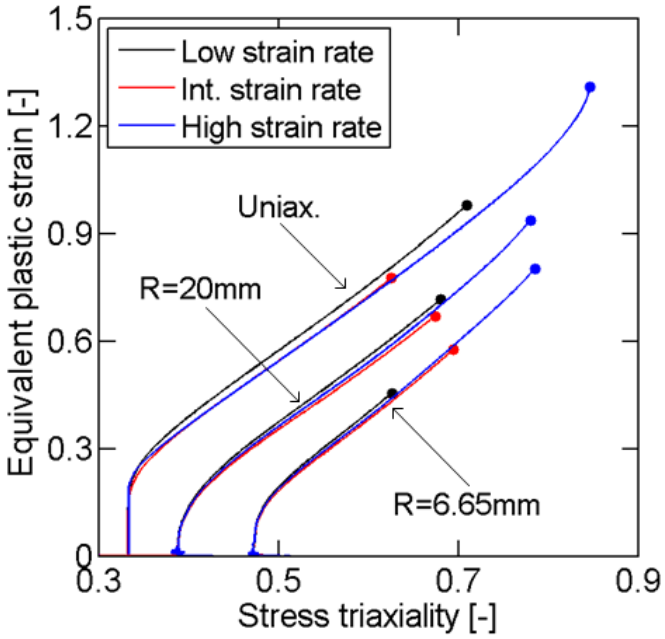

(a)

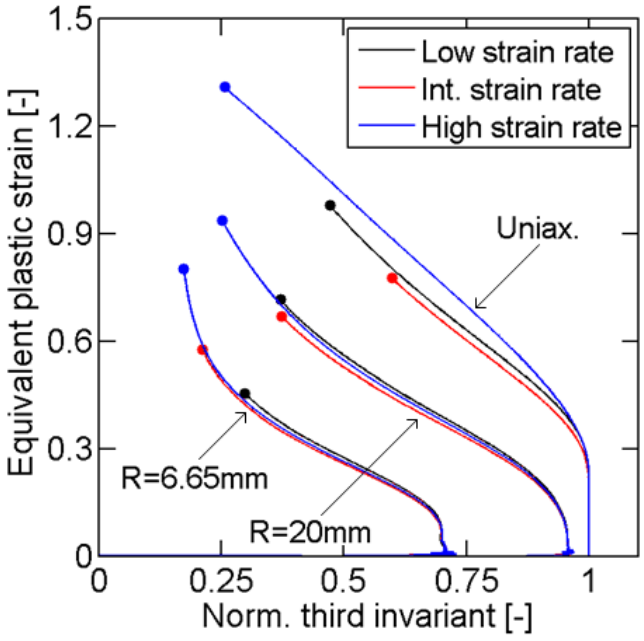

(b)

Figure 4-11: Loading paths to fracture at low (black lines), intermediate (red lines) and high strain rate (blue lines). (a) Evolution of equivalent plastic strain versus stress triaxiality and (b) evolution of equivalent plastic strain versus normalized third stress invariant in all experiments. Solid points depict the onset of fracture.

4.7 Conclusion

The deformation behavior of TRIP780 steel sheets is investigated for different stress states over a wide range of strain rates. Tensile experiments have been carried on notched specimens as well as on uniaxial specimens, using a hydraulic testing machine (for low and intermediate strain rates) and a Split Hopkinson Pressure Bar system (for high strain rate loadings). Positive, but rather weak, strain rate sensitivity is observed. Constitutive equations derived from the MTS theory are proposed to capture the dependence of the material behavior to strain rate as well as the plastic anisotropy observed at low strain rate. The model is calibrated with an inverse optimization method from the force-displacement response of notched tensile specimens deformed at different strain rates, up to fracture. A comparison between experimental results and detailed Finite Element simulations of all the experiments show that the constitutive model can predict accurately the material behavior over all the range of strain rates and stress states considered. In particular, the material behavior at large strains, after the onset of localized necking, is well captured.

A hybrid experimental-numerical approach is followed to evaluate the material loading histories up to the onset of ductile fracture in all experiments. It is shown that the equivalent strain at the onset of fracture is significantly higher at high strain rate than at low and intermediate strain rates. However, results reveal that the dependence of the fracture strain to strain rate is not similar in all types of experiments carried out. In particular the material ductility is lower at intermediate strain rate than at low strain rate for stress states close to uniaxial tension, while the opposite is observed for stress states close to transverse plane strain tension. As a result, the effects of strain rate and stress state should not be considered separately when developing and calibrating rate-dependent fracture models for AHSS sheets.

Chapter 5

Numerical methods for accurate and efficient ductile fracture predictions

Contents

Abstract

The influence of spacial discretization in FE simulations on predictions of mechanical response and ductile fracture in AHSS structures is analysed. The inability of shell elements to accurately predict the post-necking behavior of sheet materials is highligted. On the contrary predictions independent from the mesh characteristics are obtained with solid elements if sufficiently fine meshes are used. However, intensive computation efforts associated with the use of fine meshes of solid elements to model sheet structures such as automootive parts make it unsuitable to an industrial

[7] The work described in this chapter has been carried out at E.S.I. group in Rungis, France, as part of a six month part-time collaboration.

environment. A dynamic shell-to-solid re-meshing technique is considered to benefit from both the numerical efficiency of shells and the accuracy of fine solid meshes. Comparisons of numercial predictions using re-meshing to experimental results show a significant increase of the accuracy of fracture predictions compared to shell simulations, and substantial time savings compared to solid simulations.

5.1 Introduction

With the generalization of virtual engineering practices in the development and design of new vehicles, an accurate and predictive modeling of ductile fracture in sheet materials has become a significant issue. However, in an industrial context, an appropriate balance must be found between numerical efficiency and accuracy. Finite element simulations of the mechanical response of sheet structures are therefore commonly performed with shell elements, which allow for faster computations. However, fracture predictions using shell elements are often compromised by the dependence of shell models submitted to large deformation to the mesh size.

This chapter focuses on the influence of the finite element modeling on ductile fracture predictions in Advanced High Strength Steel sheets. For that purpose the influence of the type of elements used and their characteristic size is investigated. Finite element simulations of a flat notched specimen submitted to tension (which is typically used to characterize experimentally the onset of ductile fracture in sheet materials) are carried out with both shell and solid elements, with five different mesh densities. Simulation results are compared in terms of the predicted force displacement curves and the predicted displacement at which the onset of ductile failure occurs, and the local stress, strain and damage evolutions are also analyzed. Results show that in the early stages of the simulation, both shell and solid elements give comparable results, regardless of the mesh size. However fracture predictions are significantly different, depending on the mesh size and type. The critical instant after which shell elements give inaccurate results is the onset of through-the-thickness localization. After the onset of localized necking, shells are not able to predict the local stress state correctly, resulting in a spurious localization of the deformation and inaccurate and mesh-size-dependent fracture predictions. Solid elements, however, are able to predict the material

evolution after the onset of necking, and give results independent from the mesh size if it is small enough. This increased accuracy is obtained at the expense of computational efficiency.

Consequently, a shell-to-solid re-meshing technique permitting to refine locally the shell mesh into solid elements during the simulations, in areas where the sheet material experiences localized necking, is presented. Improved shell simulations using re-meshing are carried out and evaluated. The accuracy of the re-meshing technique is evaluated based on numerical simulations of tensile fracture experiments and on a comparison between numerical predictions and experimental results. It is shown that the accuracy of shell simulations is increased when using re-meshing. In particular, the post-necking behavior of the sheet material can be captured correctly. In addition, using shell-to-solid re-meshing offers about 75% savings on the computational cost compared to simulations with solid elements.

In this chapter we limit our attention to low strain rate experiments and rate-independent plasticity and fracture models.

5.2 An uncoupled fracture model for Advanced High Strength Steel sheets

We make use of a rate-independent simplification of the plasticity model proposed in Chapter 4. The onset of ductile farcture will be modeled independently using the so-called Modified Mohr-Coulomb (MMC) model (Bai and Wierzbicki, 2010, [7]). The predictive capabilities of the constitutive and fracture models described thereafter are not investigated here. The reader is referred to Mohr et al. (2010, [122]) and Dunand and Mohr (2011, [49]) for a critical evaluation.

5.2.1 Plasticity model

For the present sheet material, nearly the same stress-strain curve is measured for different specimen orientations even though the r-values are direction dependent. As

detailed in Mohr et al. (2010, [122]), we make use of a planar isotropic quadratic yield function,

$$f(\boldsymbol{\sigma}, k) = \bar{\sigma} - k = 0 \quad , \quad \bar{\sigma} = \sqrt{(\boldsymbol{P}\boldsymbol{\sigma}) \cdot \boldsymbol{\sigma}} \tag{5-1}$$

in conjunction with a non-associated flow rule

$$\boldsymbol{\varepsilon_p} = d\lambda \frac{\partial g}{\partial \boldsymbol{\sigma}} \tag{5-2}$$

$d\lambda \geq 0$ denotes the plastic multiplier. The anisotropic quadratic flow potential reads

$$g = \sqrt{(\boldsymbol{G}\boldsymbol{\sigma}) \cdot \boldsymbol{\sigma}} \tag{5-3}$$

P and **G** are symmetric positive-semidefinite matrices, with $\bar{\sigma} = 0$ and $g = 0$ if and only if $\boldsymbol{\sigma}$ is a hydrostatic stress state. The values for the non-zero components of **P** and **G** are given in Table 5-1. $\boldsymbol{\sigma}$ denotes the Cauchy stress vector in material coordinates,

$$\boldsymbol{\sigma} = [\sigma_0 \quad \sigma_{90} \quad \sigma_n \quad \tau \quad \tau_{0n} \quad \tau_{90n}]^T \tag{5-4}$$

The components σ_0, σ_{90} and σ_n represent the true normal stress in the rolling, transverse and out-of-plane directions; τ denotes the corresponding in-plane shear stress, while τ_{0n} and τ_{90n} represent the corresponding out-of-plane shear stresses. Isotropic strain hardening is described as

$$dk = h(\bar{\varepsilon}^p) d\bar{\varepsilon}^p \tag{5-5}$$

where $h = h(\bar{\varepsilon}^p)$ defines the strain hardening modulus. The strain hardening response of the material is modeled by a saturation law

$$h(\bar{\varepsilon}^p) = H_0 \left(1 - \frac{k(\bar{\varepsilon}^p)}{k_\infty}\right)^r \tag{5-6}$$

5.2.2 Fracture model

The original Mohr-Coulomb failure criterion (Mohr, 1900, [127]) is formulated in the stress space and assumes that failure occurs when the shear and normal stresses on any plane of normal vector $\boldsymbol{n}$ verify the condition

$$\max_{\mathbf{n}}(\tau + c_1\sigma_n) = c_\alpha \tag{5-7}$$

with the friction coefficient c_1 and the cohesion c_α. Bai and Wierzbicki (2010, [7]) transformed Eq. (5-7) into the space of stress triaxiality, Lode angle and equivalent plastic strain to fracture assuming proportional monotonic loading, a pressure and Lode angle dependent isotropic plasticity model, and isotropic strain hardening according to the power law. The resulting explicit expression for the fracture strain reads

$$\hat{\varepsilon}(\eta,\bar{\theta}) = \left\{c_2\left[c_3 + \frac{\sqrt{3}}{2-\sqrt{3}}(c^{ax}(\bar{\theta}) - c_3)\left(\sec\left(\frac{\bar{\theta}\pi}{6}\right) - 1\right)\right]\cdot \left[\sqrt{\frac{1+c_1^2}{3}}\cos\left(\frac{\bar{\theta}\pi}{6}\right) + c_1\left(\eta + \frac{1}{3}\sin\left(\frac{\bar{\theta}\pi}{6}\right)\right)\right]\right\}^{-\frac{1}{n}} \tag{5-8}$$

with

$$c^{ax}(\bar{\theta}) = \begin{cases} 1 & \text{for } \bar{\theta} \geq 0 \\ c_{ax} & \text{for } \bar{\theta} < 0 \end{cases} \tag{5-9}$$

The exponent n describes the strain hardening of the material. The coefficient c_2 is related to c_α in Eq. (5-7), while c_3 and c_{ax} characterize the dependence of the underlying plasticity model on the third stress invariant. c_3 controls the amount of Lode angle dependence of the fracture locus and $c^{ax}(\bar{\theta})$ controls the asymmetry of the fracture locus with respect to the plane $\bar{\theta} = 0$. Despite the discontinuity of $c^{ax}(\bar{\theta})$, the fracture strain $\hat{\varepsilon}(\eta,\bar{\theta})$ is a continuous function of the stress invariants η and $\bar{\theta}$. To apply the MMC fracture model for non-proportional loadings, Bai and Wierzbicki (2010, [7]) make use of Eq. (5-8) as reference strain in Eq. (2-19).

5.3 Influence of Finite Element modeling on ductile fracture predictions

The influence of the type of elements (brick vs shell) and their characteristic dimensions are investigated on numerical simulations of a tensile experiment on a flat specimen with circular notches of radius 6.67mm, as sketched in Fig. 4-1c. Parameters for the constitutive model described in Section 5.2 have been calibrated on an extensive

Table 5-1: Material parameters for the TRIP780 steel

Yield function	F_{11} [-]	F_{22} [-]	F_{33} [-]	F_{44} [-]	F_{12} [-]	F_{13} [-]	F_{23} [-]
	1.00	1.00	1.06	2.94	-0.47	-0.53	-0.53
Flow potential	G_{11} [-]	G_{22} [-]	G_{33} [-]	G_{44} [-]	G_{12}[-]	G_{13} [-]	G_{23} [-]
	1.00	0.94	1.00	2.64	-0.47	-0.53	-0.47
Hardening	k_0 [MPa]	k_∞ [MPa]	H_0 [MPa]	r [-]			
	459	1173	20425	1.867			
MMC	c_1 [-]	c_2 [-]	c_3 [-]	c_{ax} [-]	n [-]		
	0.3472	0.9098	1.7003	1.546	0.204		

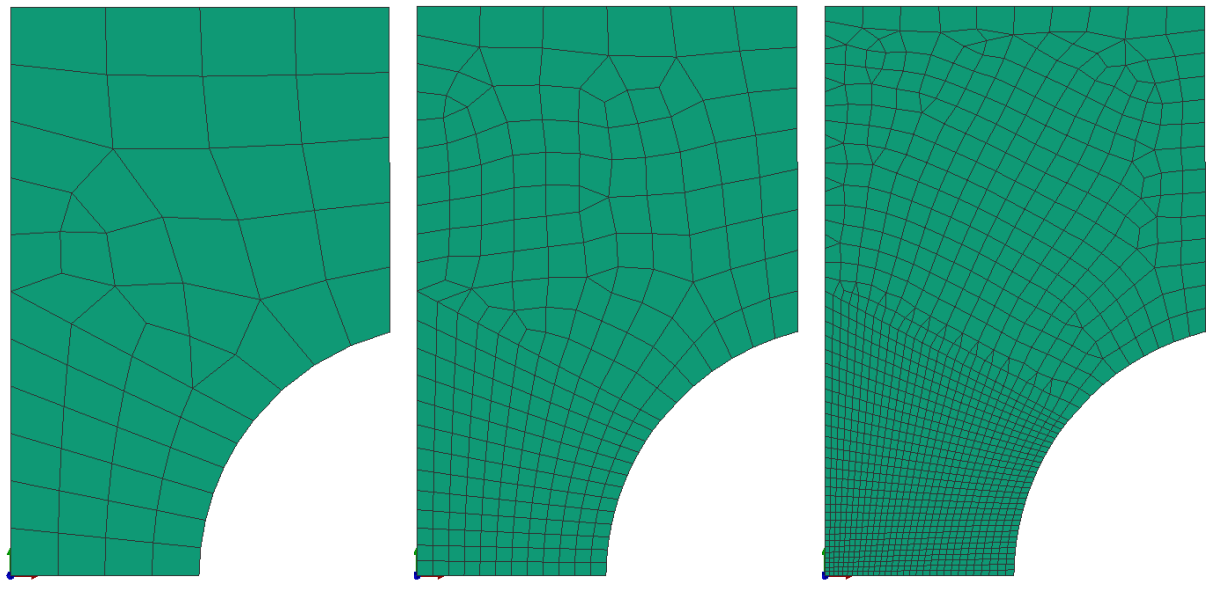

(a) (b) (c)

Figure 5-1: Meshes of the notched tensile specimen. (a) very coarse mesh; (b) medium mesh and (c) very fine mesh.

set of multi-axial fracture experiments carried out on TRIP780 steel (Mohr et al., 2010, [122]; Dunand and Mohr, 2011, [49]). Note that this material comes from a different production batch than the one used in Chapters 3, 4 and 6. Materials parameters are thus slightly different.

5.3.1 Methodology

Finite element simulations are run with five different mesh densities, shown in Fig. 5-1:

(i) very coarse mesh with an element edge length of $l_e = 1250\mu m$ at the specimen center and $n_t = 1$ elements in thickness direction (half thickness),

(ii) coarse mesh with $l_e = 830\mu m$ and $n_t = 2$;

(iii) medium mesh with $l_e = 415\mu m$ and $n_t = 4$;

(iv) fine mesh with $l_e = 200\mu m$ and $n_t = 8$;

(v) very fine mesh with $l_e = 100\mu m$ and $n_t = 12$.

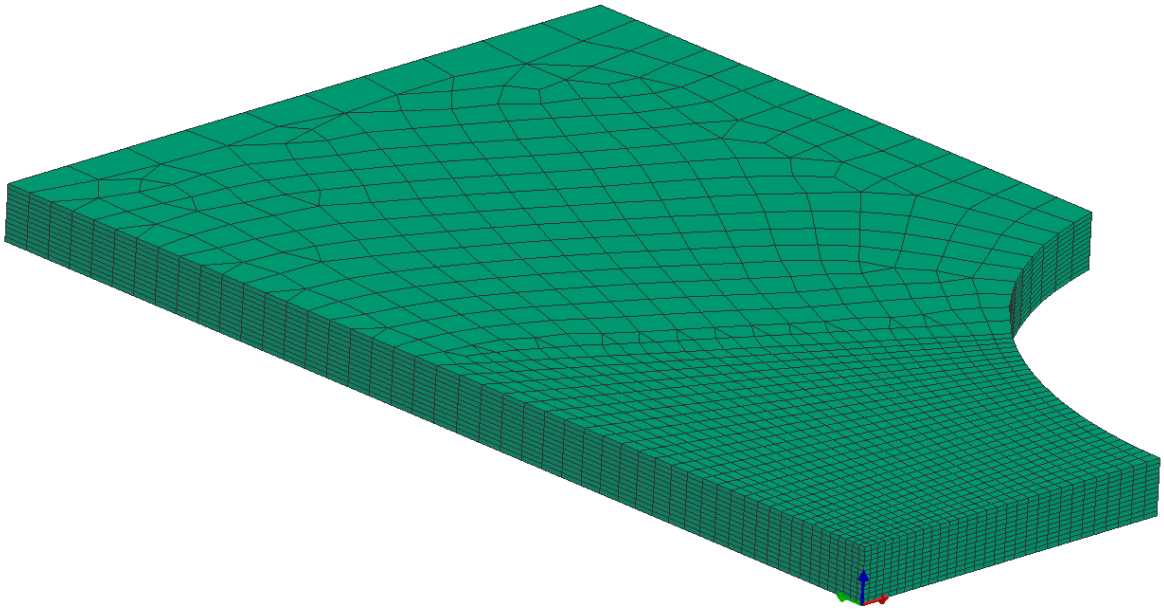

Figure 5-2: View of the very fine mesh with 12 solid elements through the half-thickness

Note that the medium shell mesh corresponds to current standard practices in industrial simulations of car crash tests. Meshes with both only shell and only solid elements are considered. For a given density, shell and solid meshes are identical in the sheet plane. Only the number of elements through the thickness varies (1 for shell, $2n_t$ for solids). Because of the symmetries of the notched specimen, only $1/4$ of the specimen is meshed, and half the thickness for solid meshes. A displacement boundary condition is imposed to the upper boundary of the specimen (constant velocity). All simulations are run up to an imposed displacement of 1.5mm. Fracture is assumed to occur when the critical damage $D = 1$ is reached at any integration point in the model. Note that element deletion is not used in the present simulations.

5.3.2 Results for shell elements

Force displacement curves predicted with the five meshes are depicted in Fig. 5-3. The instant at which fracture occurs is highlighted by a solid square on each curve. After the maximum of force is reached (which corresponds to the onset of localization of the plastic flow through the thickness of the specimen (localized necking)), simulation results show a very strong dependence to mesh size. More specifically, the finer the mesh, the more abrupt the force decreases after necking and the smaller the fracture displacement. It must be noted that simulation results do not converge as the mesh is refined. For most of the mesh densities, fracture occurs earlier than in the experiment. With the very fine mesh, fracture occurs in the simulation just after the maximum of force is reached.

Figure 5-4 compares the evolution of damage (solid line) and equivalent plastic strain (dashed line) at the center of the specimen for the very fine (in red) and very coarse mesh (in black). Both simulations give the same results before the maximum of force (displacement smaller than 0.8mm). But after the maximum of force, the evolution of damage and plastic strain strongly depends on the mesh size. For the very fine mesh, damage exhibits a sharp increase after necking, leading to an almost instantaneous fracture after the maximum of force.

Regardless of the element dimensions, all the deformation localizes in a band of 1 element width at the center of the gage section after the maximum of force is reached,

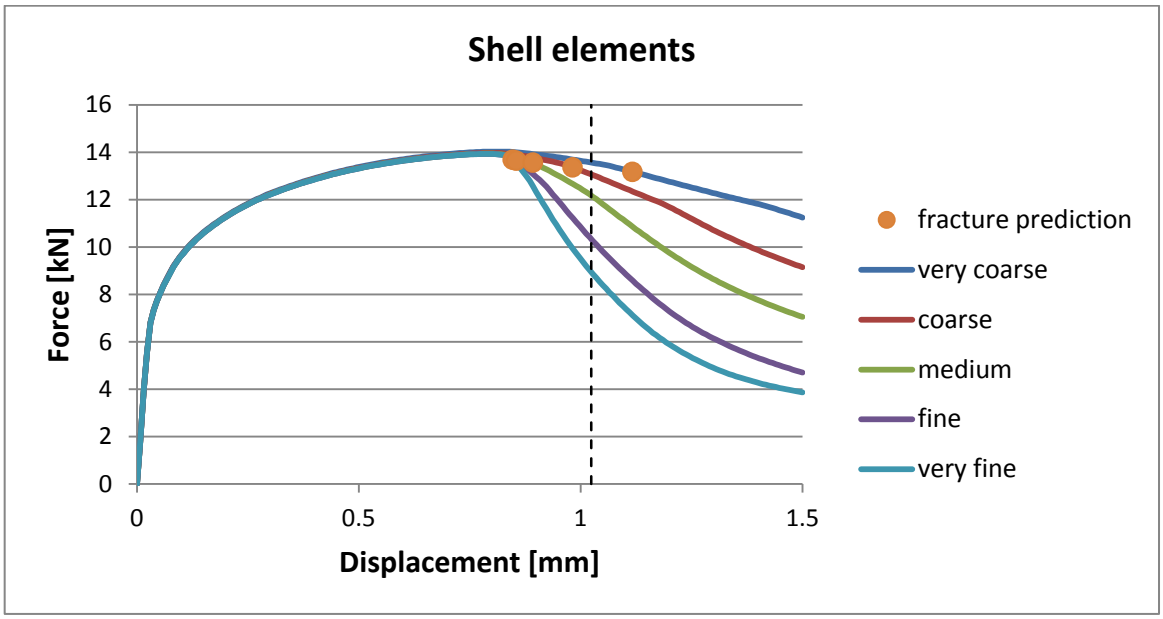

Figure 5-3: Predicted force displacement curves with shell elements. The predicted instant of fracture is shown by a solid circle for each simulation. The experimental instant of fracture is depicted by a dashed black line.

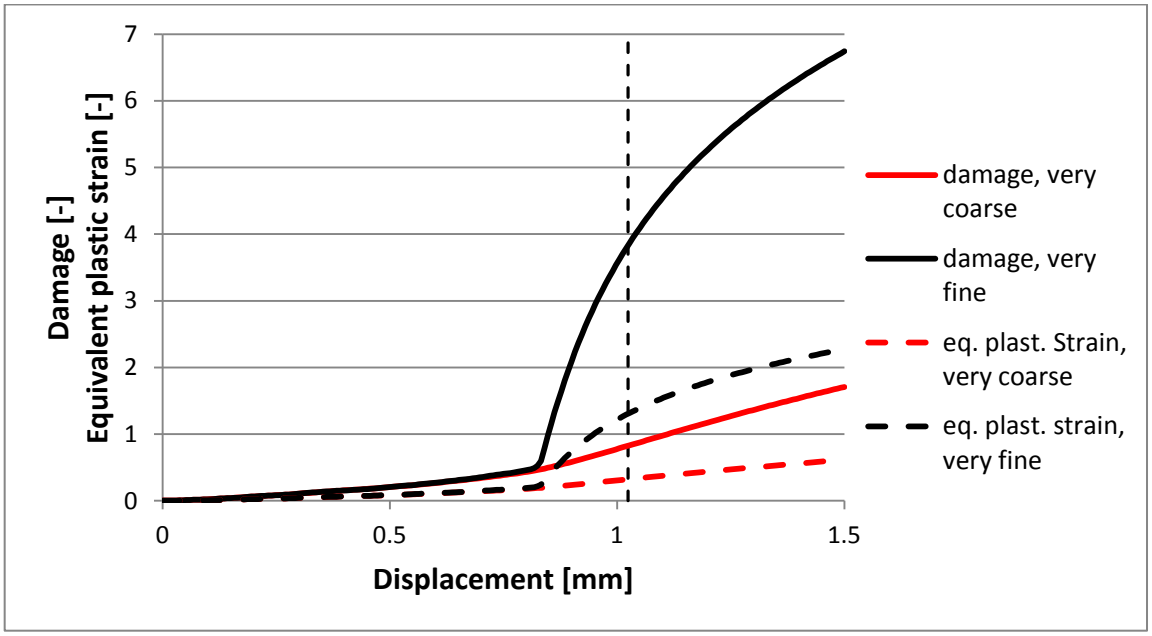

Figure 5-4: Evolution of damage and equivalent plastic strain at the center of the notched specimen, for the very fine (red) and very coarse (black) meshes with shell elements. The experimental instant of fracture is depicted by a dashed black line.

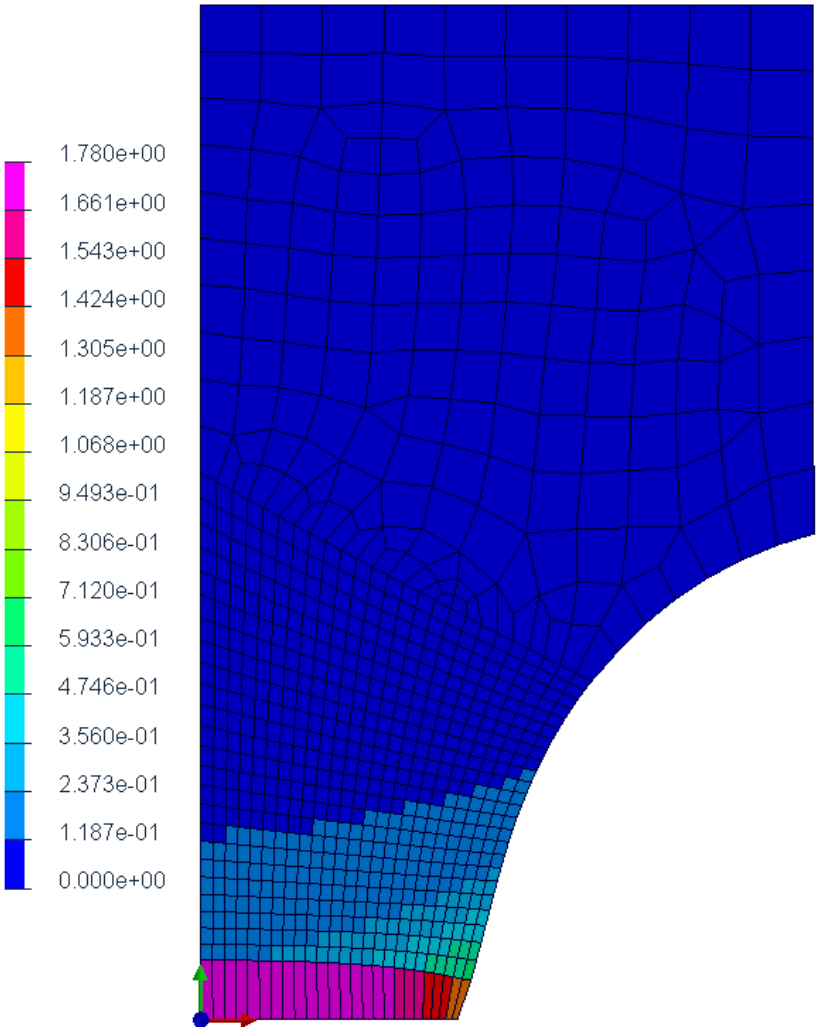

Figure 5-5: Contour plot of equivalent plastic strain after the maximum of force , using a fine mesh of shell elements

as illustrated in Fig. 5-5. This spurious localization leads to very high values of strain and damage inside that band, so that fracture occurs right after the maximum force when using fine meshes.

After necking, a three dimensional stress state develops in the material. In particular, through-the-thickness stresses appear and permit to bring additional strain hardening capabilities that is needed to compensate sheet thinning. However those mechanisms cannot be captured by shell elements, in which the state of stress is necessarily plane stress. As a result, shells cannot predict correctly the material evolution (stress and strain state) after necking, regardless of the element size. To

illustrate this point, Fig. 5-6 depicts the evolution of the stress triaxiality and equivalent plastic strain at the center of the specimen, when a medium mesh is used. After necking (at an equivalent plastic strain of about 0.2), the stress triaxiality increases but rapidly saturates at a value of $\eta = 0.57$, which corresponds to transverse plane strain tension: it is the maximum of triaxiality achievable under plane stress with traction applied in only one direction. However, in the actual specimen, higher triaxialities are reached, because of the three dimensional stress state that develops.

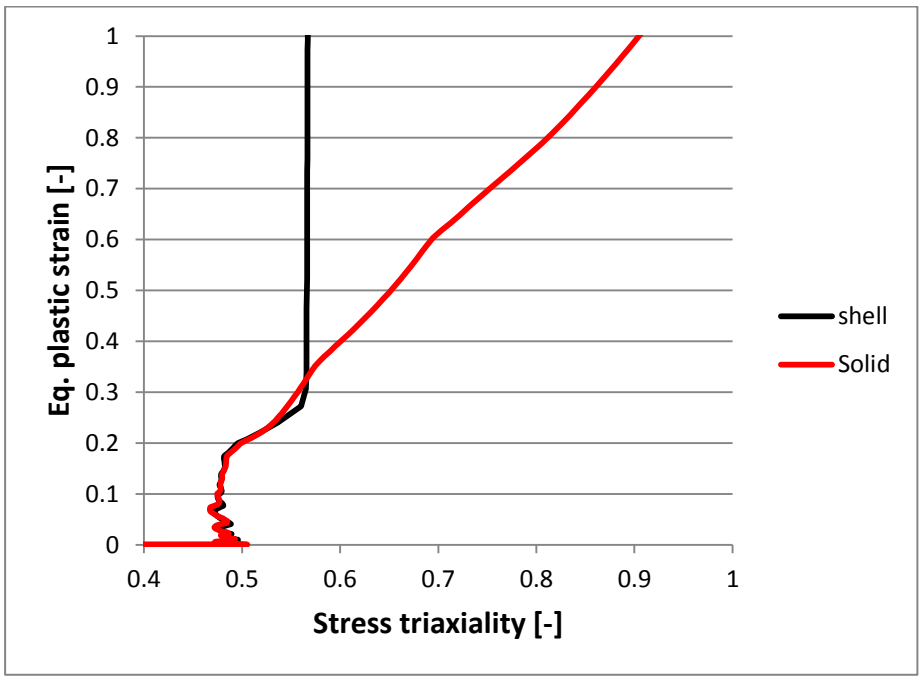

Figure 5-6: Evolution of the stress triaxiality and the equivalent plastic strain at the center of the specimen, as predicted by a fine mesh of shell elements (black line) and solid elements (red line).

5.3.3 Results for solid elements

Force displacement curves predicted with the five different solid meshes are depicted in Fig. 5-7. The instant at with fracture occurs is highlighted by a solid square on each curve. All simulations predict the same force displacement curve before the maximum of force, but some differences become noticeable thereafter. However, it should be noted that the medium, fine and very fine mesh predict the same force res-

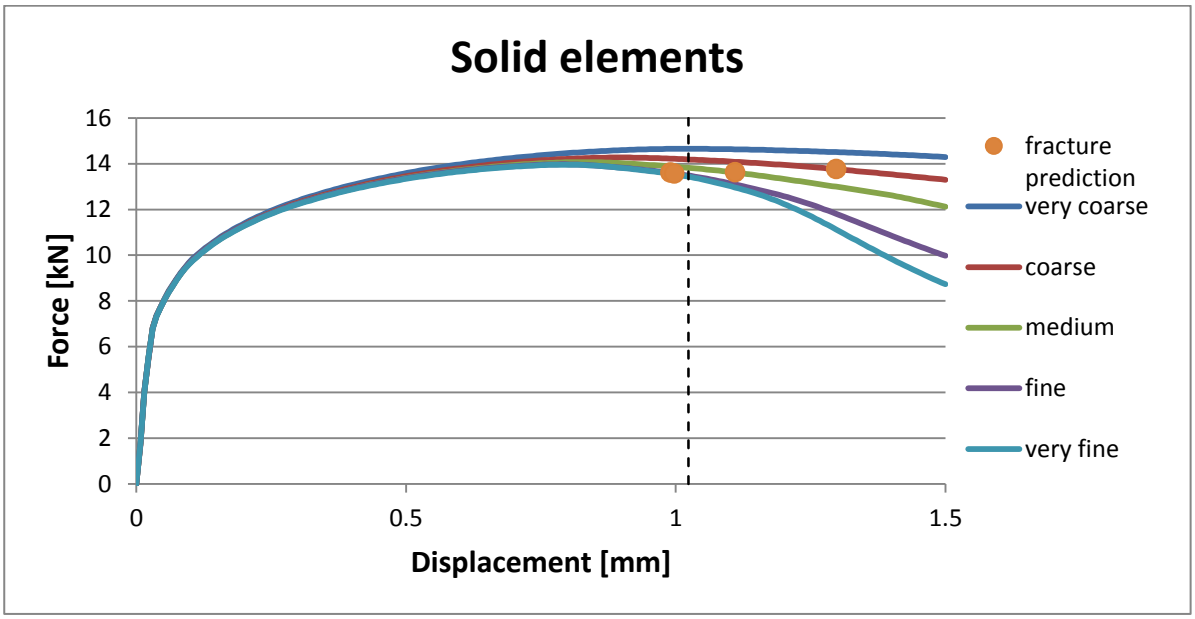

Figure 5-7: Predicted force displacement curves with solid elements. The predicted instant of fracture is shown by a solid circle for each simulation. The experimental instant of fracture is depicted by a dashed black line.

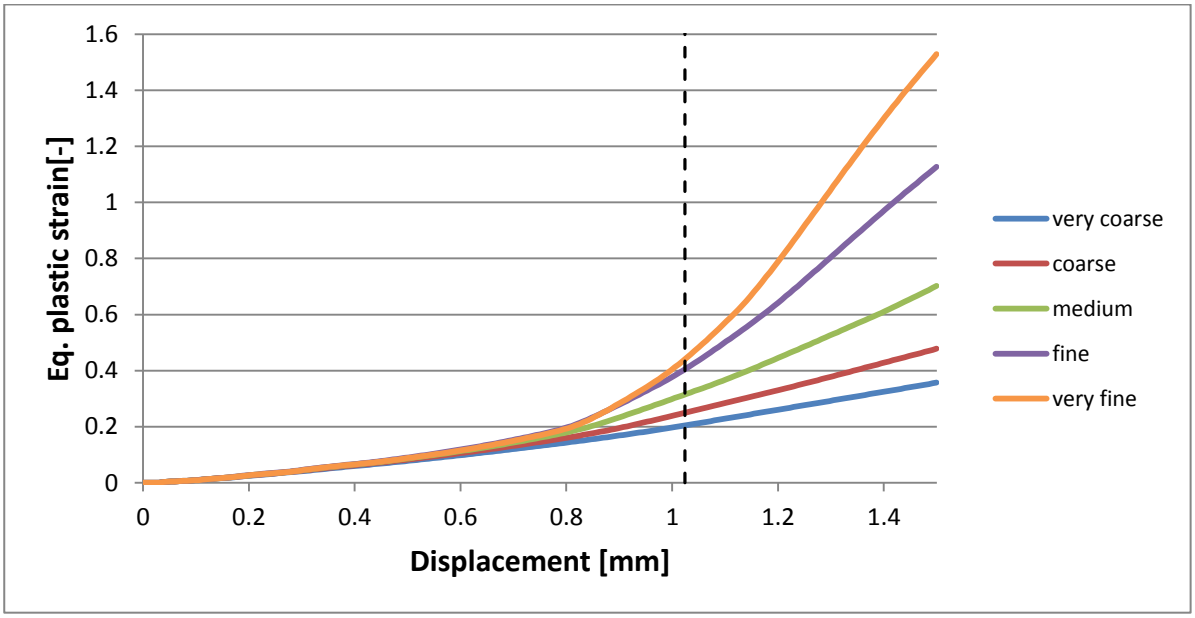

Figure 5-8: Evolution of the equivalent plastic strain at the center of the gage section for different mesh densities. The experimental instant of fracture is depicted by a dashed black line.

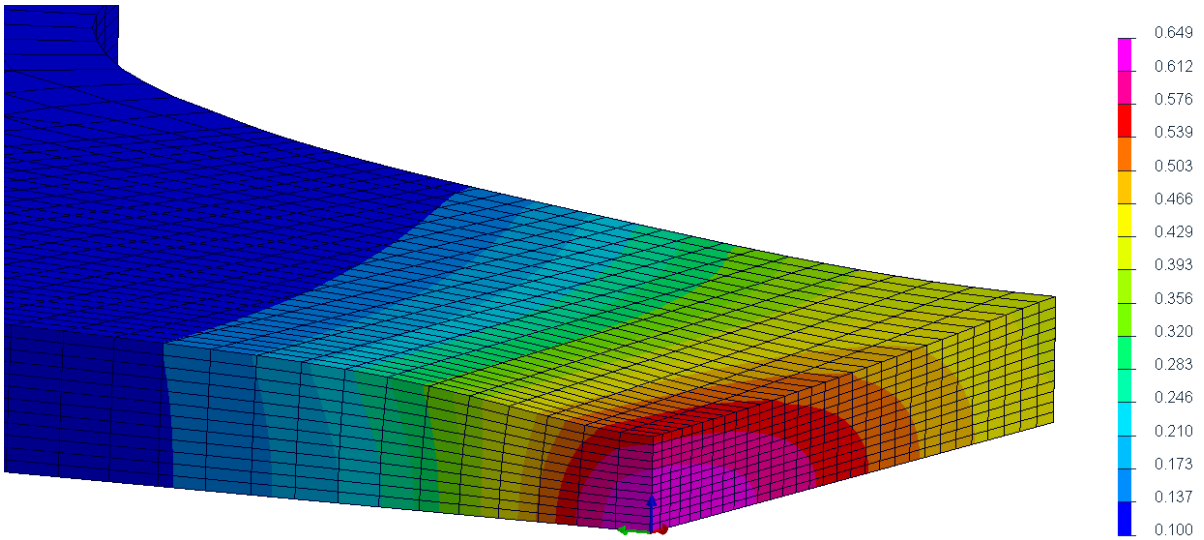

Figure 5-9: Contour plot of equivalent plastic strain after the onset of localized necking, with the very fine solid mesh.

ponse up to a displacement of 1mm, while the fracture displacement is 1.03mm: results converge as the mesh is refined. Similarly, the predicted fracture displacement decreases as the mesh is refined, but eventually converges: almost the same fracture displacement is predicted by the fine and very fine mesh.

The evolution of the equivalent plastic strain at the center of the gage section is depicted for all five mesh densities in Fig. 5-8. As for force-displacement curves, all curves are identical for displacements lower than 0.8mm, which corresponds to the maximum of force. After that instant, results become mesh size-dependent: the finer the higher, the steeper the increase of equivalent plastic strain. However, at least in the range of displacements lower than the experimental fracture displacement (black dashed line in Fig. 5-8), results converge as the mesh is refined: for displacements lower than $1mm$, the evolution of equivalent plastic strain is the same with the fine and very fine meshes.

The force displacement curves depicted in Fig. 5-7 exhibit a maximum of force (for a displacement of about 0.8mm). This maximum corresponds to the onset of localized necking at the center of the specimen gage section. As shown in Fig. 5-9, localized necking provokes a severe thickness reduction at the center of the specimen,

and through-the-thickness gradients in the stress and strain fields. In addition, a three dimensional stress state develops, with significant out-of plane stresses building up.

Solid meshes with more than 1 layer of elements in the thickness direction can predict the three dimensional stress states that develops in the material after the onset of localized necking. Figure 5-6 depicts the evolution of equivalent plastic strain and stress triaxiality at the center of the specimen with a fine solid mesh (in red). The simulation is able to capture the increase of stress triaxiality after necking due to the building-up of out-of-plane stresses.

5.3.4 Comparison shell-solid

Before the onset of necking, shell and solid elements give the same results, regardless of the mesh density. Differences between mesh types and mesh densities become noticeable – and significant – only after the onset of through-the-thickness necking.

Figure 5-10 shows the predicted fracture displacement as a function of the mesh characteristic length. With both shell elements and solid elements, the prediction of fracture displacement seems to converge with respect to mesh size: the fine and very fine meshes lead to same results. In case of solid elements, the converged result is very close to the experimental displacement to fracture. However, in case of shell elements, the prediction for the fracture displacement converges towards the value of displacement at which the maximum of force occurs, which means that the accuracy of fracture predictions using shell elements cannot be increased by "tuning" the material parameters of the fracture model.

Table 5-2: CPU time (in s) for different mesh types and densities

	Very coarse	Coarse	Medium	Fine	Very fine
Shell	5.4	16	39	241	616
Solid	5.9	31	215	2913	11346

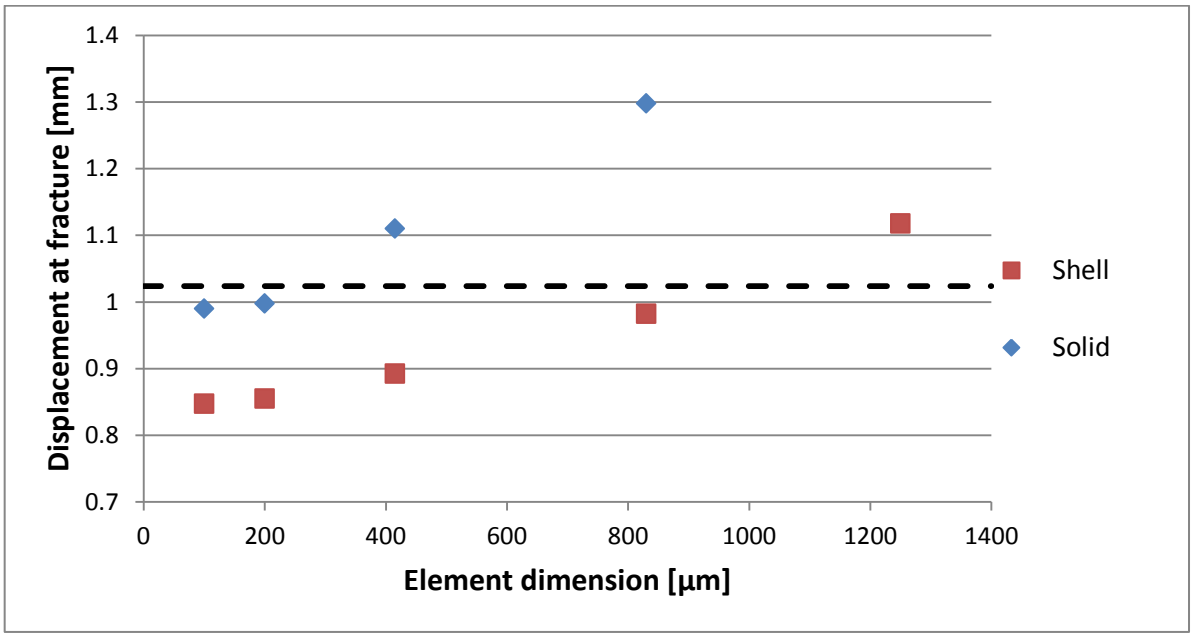

Figure 5-10: Predicted displacement at which fracture occurs with shell (red) and solid (blue) elements, for different mesh densities.

The additional accuracy of fine solid meshes comes at the expense of a prohibitive computational cost, as shown in Table 5-2. In order to get an accurate fracture prediction and converged results (fine mesh of solid elements), the computation time is 200 more important than with meshes currently used in crash simulations (medium mesh of shell elements).

To summarize:

- Shell and solid elements provide same results before through-the-thickness localization of the stress and strain fields,
- After the onset of localization,
    - Shell elements cannot predict correctly the local stress and strain state.
    - Shell elements give results (loads predictions, evolution of plastic strain and damage…) that are strongly dependent on the mesh size, and results do not converge as the mesh is refined.
    - Solid elements can predict correctly the local stress and strain state.

- Solid elements give results (fracture prediction, loads predictions…) that dependent on the mesh size if the meshes are too coarse, but results do converge when the mesh is refined.

It is clear that shell elements cannot be used to get accurate fracture predictions. In most fracture criteria, the increase of damage during straining depends on the local stress state and the evolution of plastic strain, which are not captured correctly by shells after the onset of localized necking. Moreover, it seems not possible to get predictive fracture results with shells because of the spurious localization and strong mesh density dependence of shell simulations. Results depend on mesh size, and mesh size that give most accurate results depends on the problem that is investigated: defining a "recommended shell size" could be done when investigating well known cases, but may not be applied to different geometries and/or loading conditions and/or materials.

Solid element meshes, with an element size of $200\mu m$ or less, give converged and accurate results. With such meshes, the accuracy and predictive capabilities of the simulations depend mostly on the fracture criterion itself, and no more on the finite element modeling. However such fine meshes lead to a significant increase in the computation time.

5.3.5 Mixed shell-solid model

Since the main issue with shell elements is their inability to predict the post-necking behavior of the sheet material, a possible improvement would be to use a mixed shell-solid model, where most of the specimen is meshed with shell elements (for computational efficiency) and only the area that might experience localize necking is meshed with solids. Such a mixed mesh is shown in Fig. 5-11. Here a fine mesh density, with $2n_t = 16$ elements through the total sheet thickness is used.

Special care is required to connect shell and solid elements in that model. The mesh is made such that at the interface, to all nodes from solid elements corresponds a node from a shell element. Therefore the in-plane displacements of all nodes from solids are constrained to be equal to the in-plane displacements of the corresponding node from a shell (here the specimen is not submitted to bending). No displacement constraint in the thickness direction is imposed, to allow for thickness reduction.

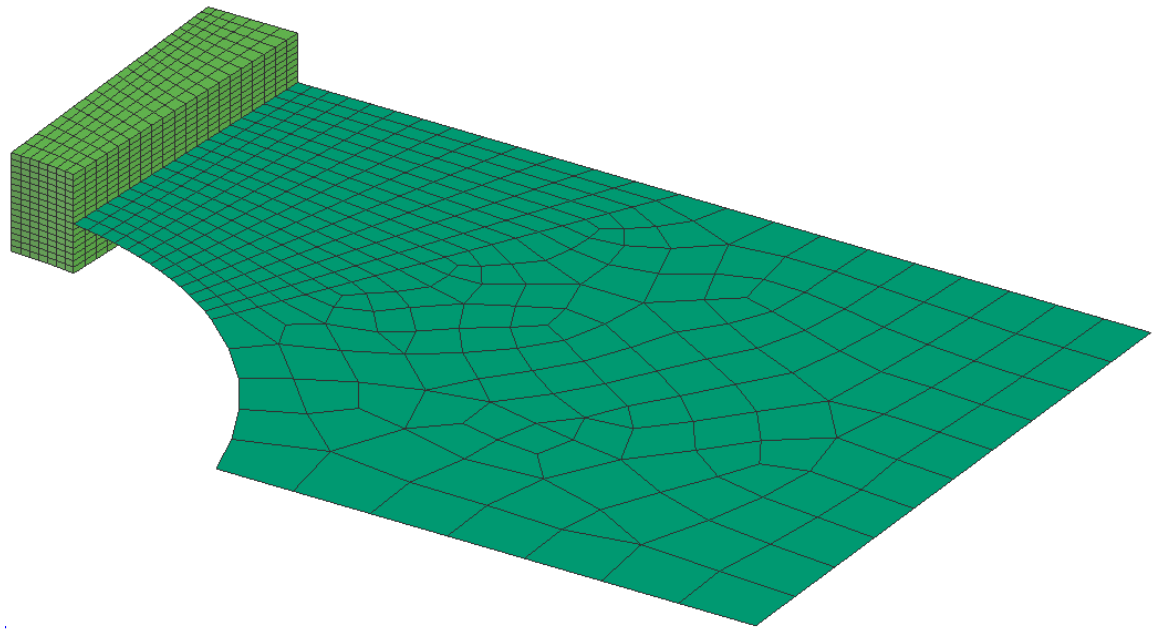

Figure 5-11: Mixed mesh with local refinement of solid elements.

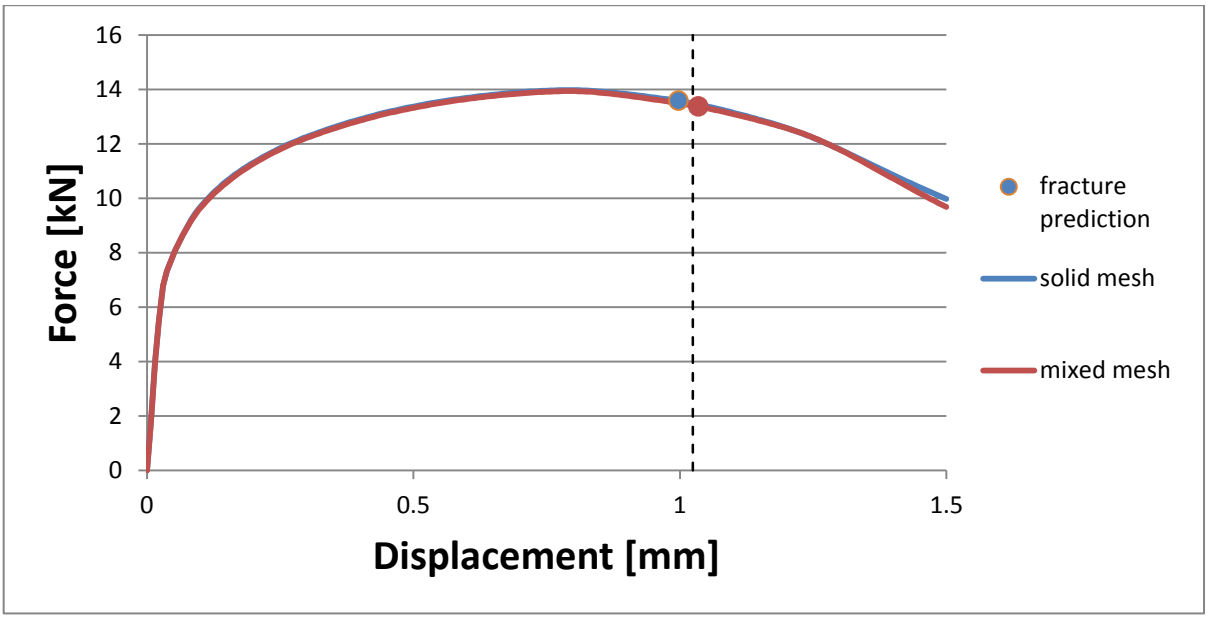

Figure 5-12: Force displacement curves and fracture predictions using a solid mesh and a mixed mesh. The experimental instant of fracture is depicted by a dashed black line.

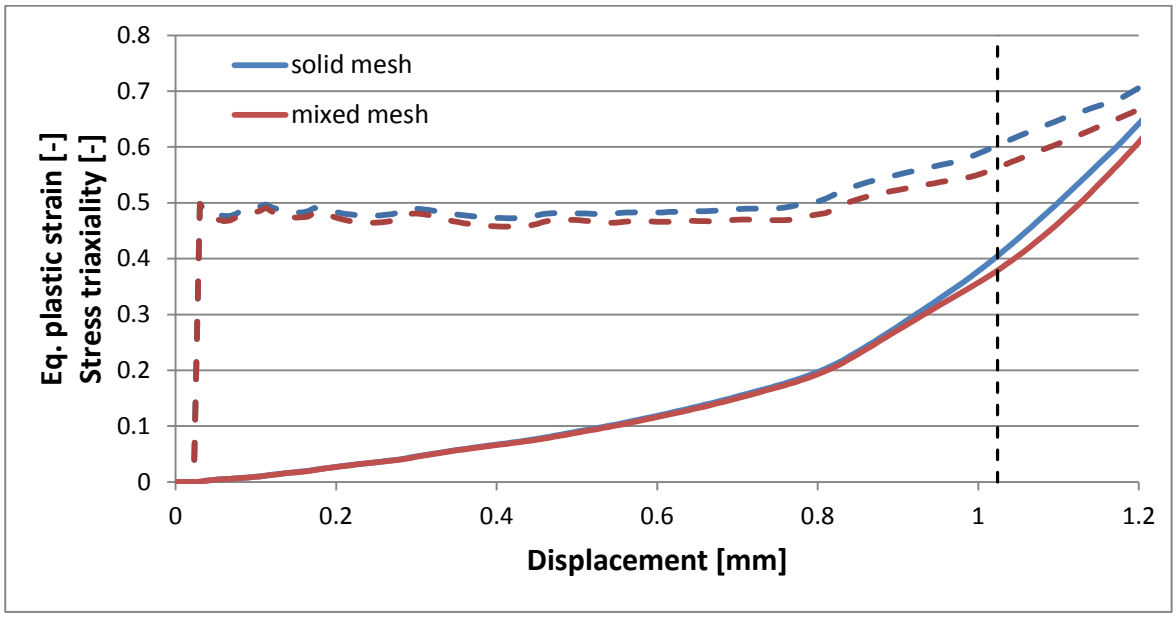

Figure 5-13: Evolution of equivalent plastic strain (solid lines) and stress triaxiality (dashed lines) at the center of the gage section, with a solid mesh (in blue) and a mixed mesh (in red). The experimental instant of fracture is depicted by a dashed black line.

Figure 5-12 depicts the force-displacement curves obtained with the fine solid mesh (in blue) and with the mixed mesh (in red). Both curves lie almost perfectly on top of each other, demonstrating that the mixed model is able to predict the load carrying capacity of the specimen, even after the onset of localized necking. Predictions of the fracture displacement are also very close in both models, only differing by about 3%. Local stress and strain states at the center of the specimen gage section are depicted in Fig. 5-13 for both models. Even though the evolution of equivalent plastic strain (solid red line in Fig. 5-13) is similar in both models up to the onset of fracture, the mixed model tends to underestimate the stress triaxiality (dashed red line in Fig. 5-13), leading to a different accumulation of damage and, *in fine*, a slightly different prediction for the fracture displacement.

The mixed model leads to results that are very close to a full solid model, at a better computational cost. The CPU time to compute the mixed model is only half that of the solid model, as shown in Table 5-3. Yet, an obvious limitation of this mixed

approach is that one needs to know where localization will occur a priori, in order to mesh correctly and efficiently the model.

Table 5-3: CPU time (in s) for the solid and mixed models

Solid model	Mixed model
2913	1581

5.4 Dynamic shell-to-solid re-meshing

It has been shown that solid elements are required in the post-necking range to get accurate simulation results and fracture predictions, while shell elements give satisfactory results before the onset of necking at a much lighter cost. A solution to reduce further the computation time without compromising the accuracy of the fracture predictions would thus be to start from a mesh of only shell elements and switch locally to solid elements where localization is likely to occur. This dynamic re-meshing from shell to solid elements has been implemented in the explicit Finite Element solver PamCrash (ESI Group, [144]). The goal of the present section is to perform an assessment of this re-meshing technique in terms of result accuracy and computational efficiency.

5.4.1 Principle

The principle of the shell-to-solid re-meshing technique is described in Fig. 5-14, which corresponds to the simulation of a tension test. Starting from a very coarse shell mesh (Fig. 5-14a), the shell elements in the specimen gage section are transformed into finer solid elements when a critical equivalent plastic strain is reached (Fig. 5-14b and 5-14c). All local state variables (stresses, strains…) are automatically mapped from the integration points of the shell element to the integration points of the new solid mesh. Note that all the solid elements replacing a single shell elements and located in the same layer in the sheet plane are initialized with the same value for all state variables

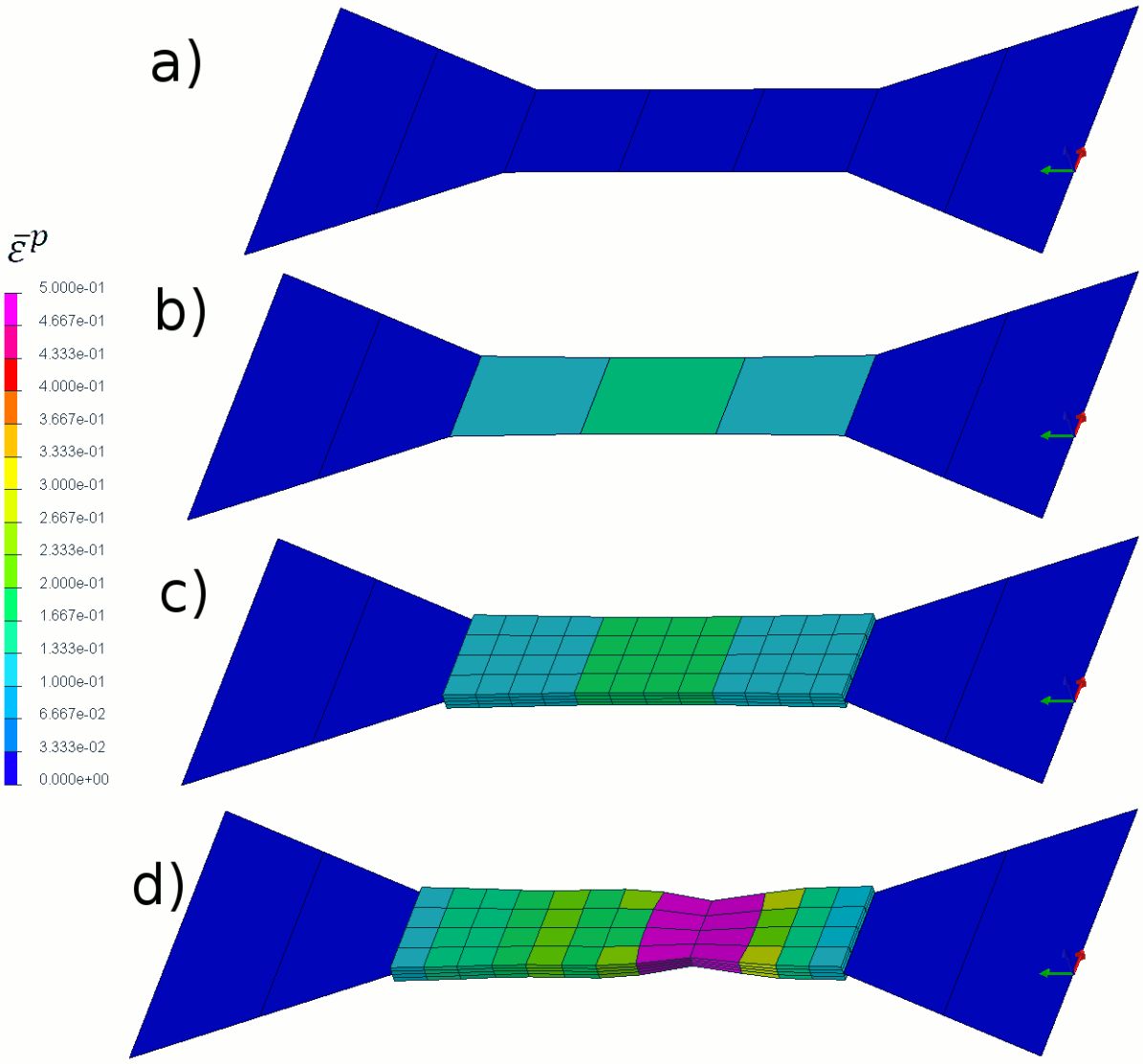

Figure 5-14: Simulation of a tension test using shell-to-solid re-meshing. (a) initial mesh; (b) Before the re-meshing step; (c) after the re-meshing step and (d) neck development.

(as can be seen in Fig. 5-14 for the equivalent plastic strain): there is no in-plane interpolation of the local fields between different integration points. However interpolation is performed in the through-the-thickness direction, as a shell typically features multiple integration points through the thickness, which do not necessarily match the number of generated solids in the thickness direction. This method permits to correctly account for bending deformations and bending moments during the re-

meshing process. A localized neck is then able to develop within the solid mesh (Fig. 5-14d).

Shell-to-solid re-meshing has two major effects on computational time:

- It increases significantly the total number of degrees of freedom and element integration points of the model,
- In an explicit time integration scheme, newly generated solid elements are associated to a stable time increment much smaller than that of the shell elements they are replacing, being of smaller dimensions.

In order not to penalize the complete model with a reduced time increment, and since re-meshing often only concerns a small region of the model geometry, solid elements are isolated in a separate sub-model. A multi-model coupling technique then permits to use different time increments for the shell and solid elements [144]. In this case, nodes located at the interface of shell and solid elements are linked with non-linear springs, in order to transmit loads and velocities while running on different time increments.

Plasticity and fracture models defined in Section 5.2, and the routines needed to map relevant variables (stresses, strains, damage indicator) from shell elements to solid elements during re-meshing have been implemented into the Finite Element software PamCrash to carry out the work described thereafter.

5.4.2 Simple example

Before analyzing complex fracture problems, we start by evaluating the shell-to-solid re-meshing technique on a simulation of a simple tension test on a sheet specimen, as shown in Fig. 5-14.

5.4.2.1 Numerical model and results

The initial shell model of the tension specimen is depicted in Fig. 5-14a. The gage section is 30mm long and 10mm wide and is meshed with only three shell elements. To load the specimen, displacements are imposed to one boundary, while the other is fixed. A non-associated quadratic plasticity model, as described in section 5.2,

is used along with the material parameters given in Table 5-1. No fracture criterion is used so far.

The shell-to-solid re-meshing option is activated. When an equivalent plastic strain of $\varepsilon^p = 0.18$ is reached at any integration point of a shell element, it is replaced by solids. Each re-meshed shell is decomposed into 4 solid elements in each in-plane direction, and 4 elements in the thickness direction, as shown in Fig. 5-14c.

The resulting load-displacement curve is depicted with a blue line in Fig. 5-15. The instant when re-meshing occurs is characterized by a significant spike in the applied load, followed by an almost complete drop of the load. The applied load comes back to the level before re-meshing only after an additional imposed displacement of about 0.2mm. In between, the model deforms purely elastically. After some plastic deformation of the generated solid elements, a diffuse and then localized neck forms in the solid mesh, as visible in Fig. 5-14d. This neck leads to a smooth decrease of the applied load, as described in the previous section.

During the re-meshing step, springs that link shell and solid models are created with zero internal load, while they replace material that was loaded up to its yielding point. Therefore this transient behavior corresponds to a transfer of load between the initially unloaded springs and the elastically loaded shell and solid elements. It ends when the model reaches equilibrium, i.e. when the level of load applied before re-meshing is attained.

The evolution of the kinetic energy in the model in shown in Fig. 5-16. Clearly, the total kinetic energy is higher after re-meshing. This additional energy comes from the additional mass introduced by the springs created to link the shell and solid elements models. In this specific simulation, the mass of the springs (which is chosen automatically by the solver based on stability criteria) is twice the mass of the generated solid elements. In addition a transient period exists right after re-meshing, where the kinetic energy in the solid model exhibits very large oscillations. This transient corresponds to the time the springs initialized with a zero velocity need to reach equilibrium (constant non-zero velocity). Note that a constant velocity is imposed to the boundaries of the model.

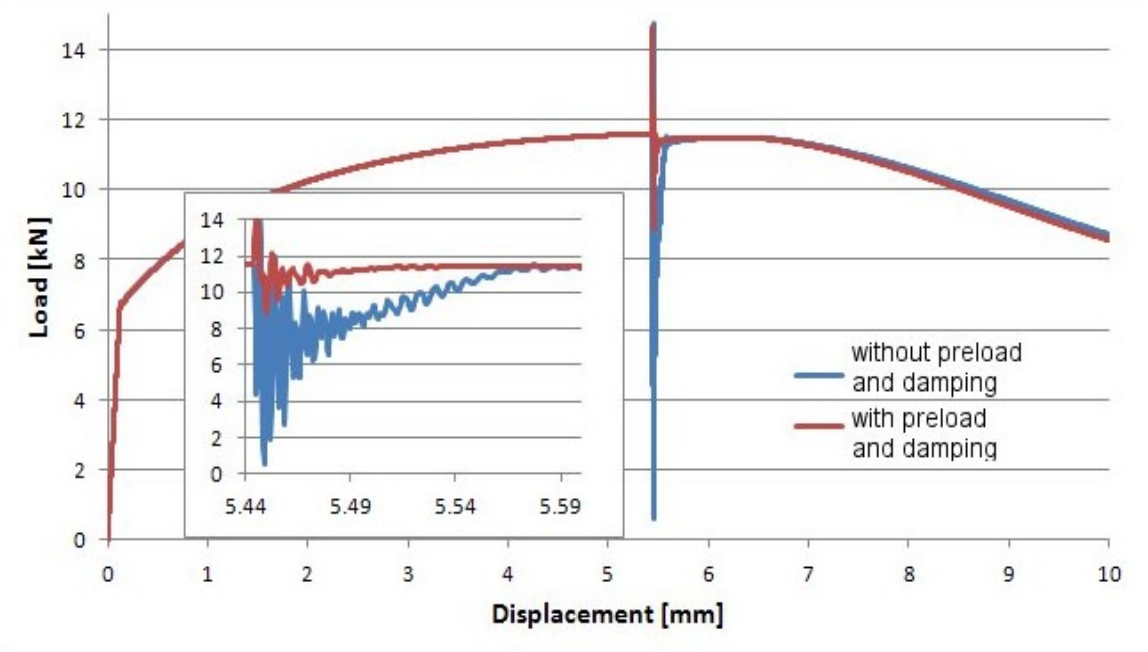

Figure 5-15: Force displacement curve of a tensile test with re-meshing, with (red) or without (blue) pre-load and damping.

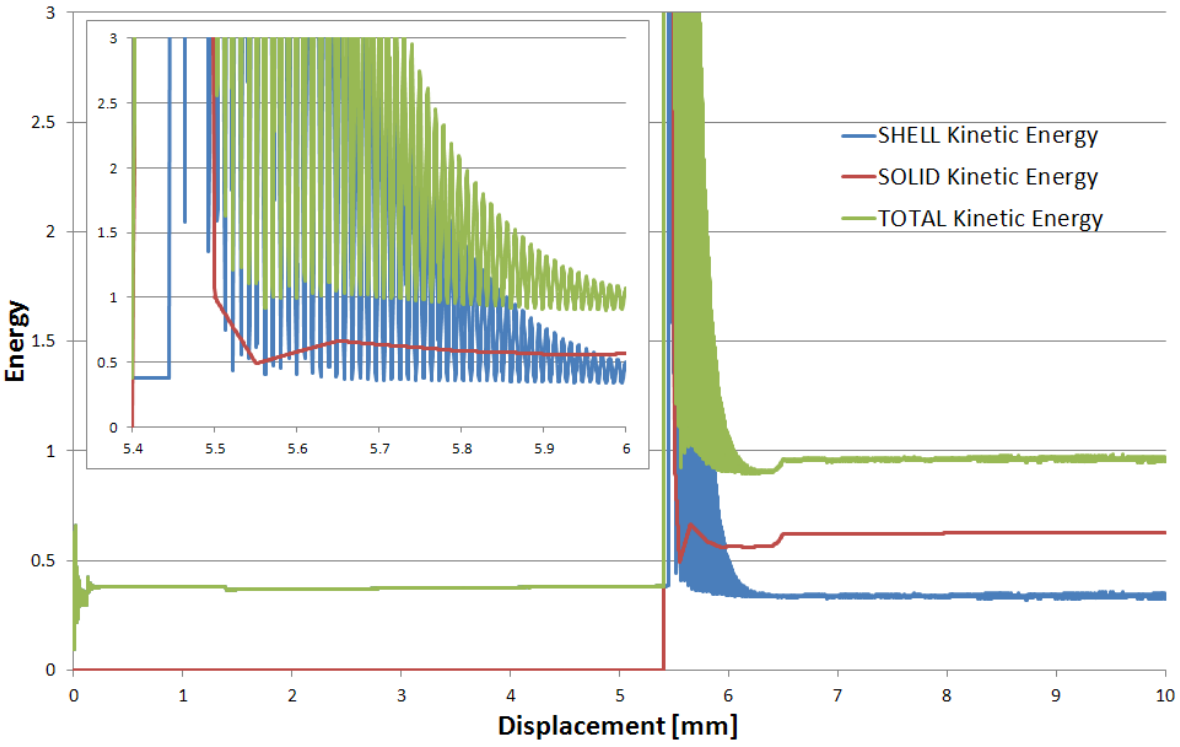

Figure 5-16: Evolution of the model kinetic energy.

5.4.2.2 Influence of modeling parameters

Different parameters are implemented to reduce the transient following the re-meshing step:

- Pre-load can be introduced in the springs,
- Proportional damping and non-linearity can also be introduced in the spring behavior.

An initial load is introduced in the springs linking nodes from the shell model and nodes from the solid model. The pre-load is chosen equal to the contribution to the nodal force coming from elements that are being re-meshed at the instant of re-meshing. In addition, proportional damping in the spring permits to reduce the oscillations of kinetic energy visible in Fig. 5-15. The force-displacement curve obtained using both pre-load and damping is shown in red in Fig. 5-15. The drop of force at the instant of re-meshing, as well as resulting oscillations, are significantly reduced.

Similarly, defining a non-linear behavior for the spring (so that the spring load is no more proportional to its elongation) can help reduce the transient to a small extent. This type of behavior penalizes an excessive extension or compression of the spring. However it has been found that using a non-linear behavior has much less influence on the transient than pre-loading the spring or using damping.

5.4.3 Application to basic fracture experiments

The next step in assessing the performances of the re-meshing technique consists of comparing its predictions against real fracture experiments.

5.4.3.1 Experiments

We use experimental results described in [48]. In this work, tensile experiments have been performed on three different specimen geometries sketched in Fig. 5-17: notched tensile specimens with a notch radius of $R = 6.65mm$ and $R = 20mm$, respectively, and a tensile specimen with a $8mm$ diameter central hole. The central

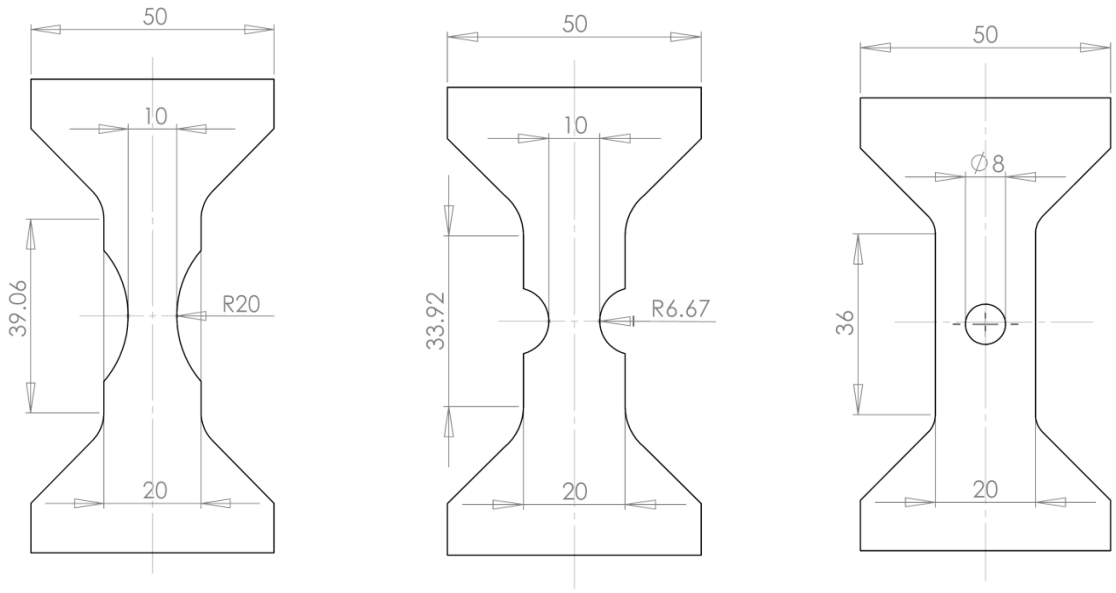

Figure 5-17: Flat tensile specimens with different notched radii and with a central hole.

hole specimen permits to characterize the onset of ductile fracture under a state of uniaxial tension, while notched tensile specimens allow for fracture characterization under higher triaxialities. All experiments are performed on a TRIP780 Advanced High Strength steel sheet, whose material characterization is given in Table 5-1.

5.4.3.2 Numerical models

For each specimen, we consider three different numerical simulations:

1. The geometry is meshed with a coarse mesh of shell elements (as described in Section 5.3: shells are $0.8mm$ long in each direction). The re-meshing capability is switched off.
2. The geometry is initially meshed the shell elements, with the same density as in case 1. The re-meshing capability is switched on: when an equivalent plastic strain of 0.18 is reached at any integration point of a shell, this element and its neighbors (in a region of 5mm radius) are replaced by solid elements. Each shell is replaced by 4x4 solid elements in both in-plane directions, and 16 elements in the thickness direction. The density of solid elements corresponds

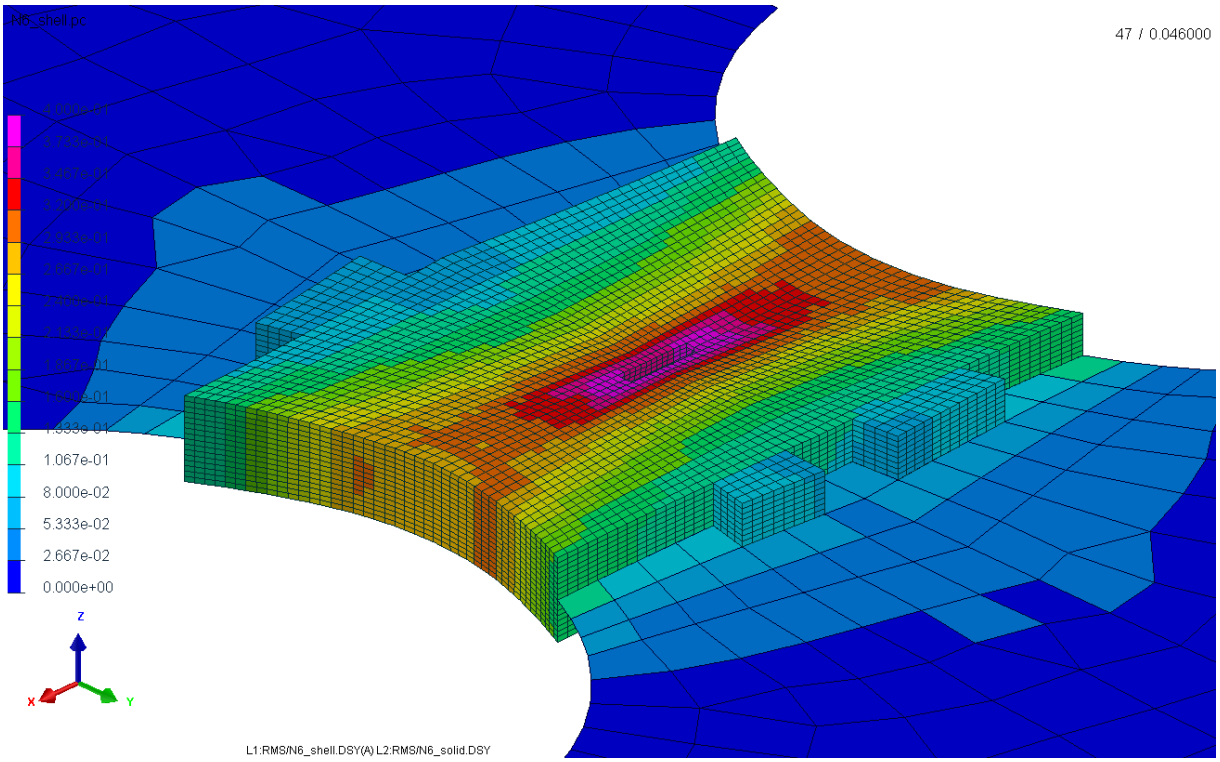

Figure 5-18: Contour plot of equivalent plastic strain in a $6.65mm$ notched tensile specimen after re-meshing of the gage section center. Central elements have already failed.

to that of the fine mesh described in Section 5.3, with an in-plane length of $200\mu m$ and thickness of $100\mu m$.

3. The geometry is meshed with solid elements only. The density corresponds to the one obtained after re-meshing in case 2.

We make use of the modeling parameters that have been recommended previously for the re-meshing operation. In all simulations, element deletion is performed when a damage value of 1.0 is reached at any integration point of an element.

5.4.3.3 Results and discussion

Figure 5-18 shows the result of the re-meshing procedure for the $6.65mm$ notched tensile specimen. All the shell elements located at the center of the gage

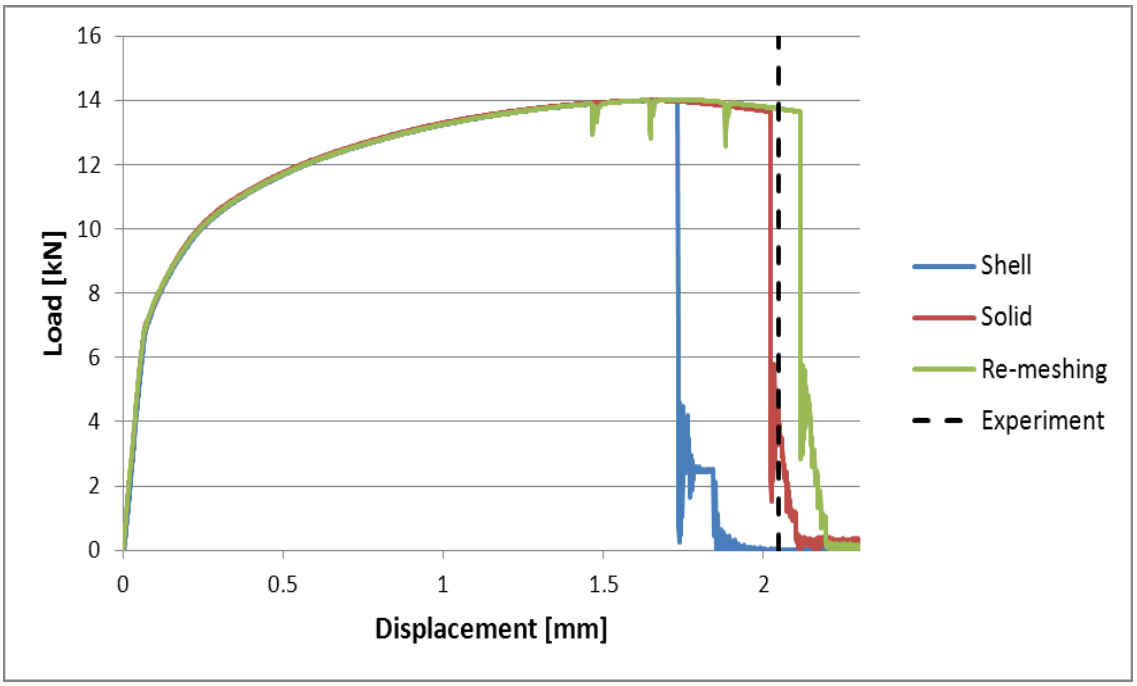

Figure 5-19: Predicted force displacement curve of the $6.5mm$ notched tensile test with re-meshing. The experimental instant of fracture is depicted by a dashed black line.

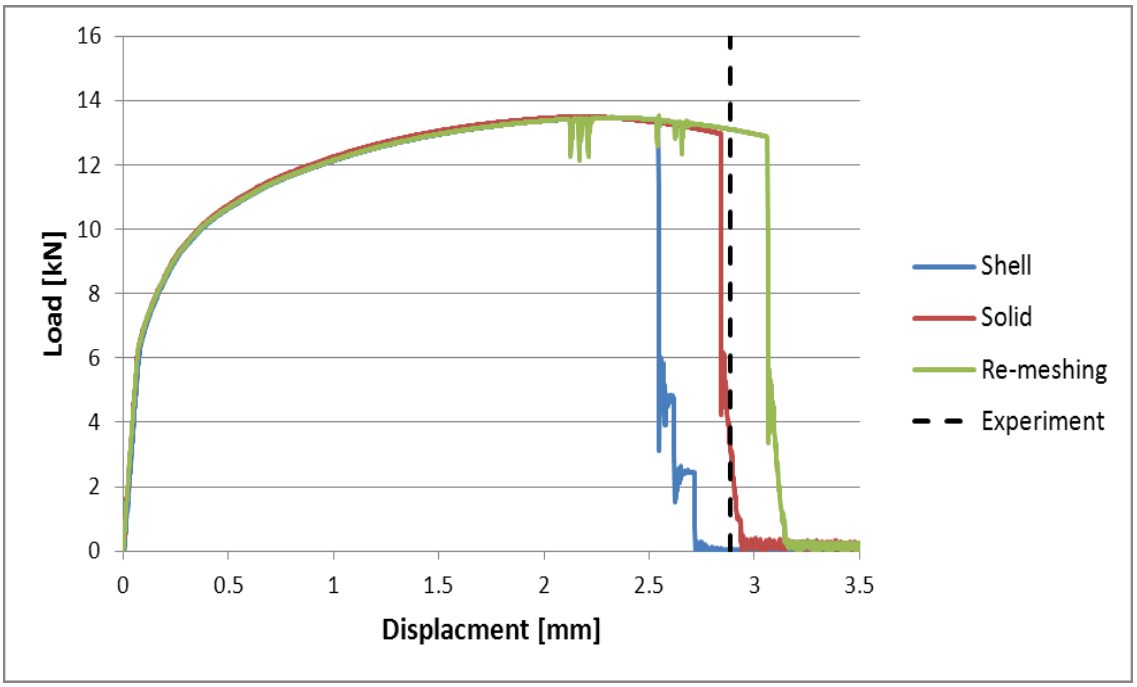

Figure 5-20: Predicted force displacement curve of the $20mm$ notched tensile test with re-meshing. The experimental instant of fracture is depicted by a dashed black line.

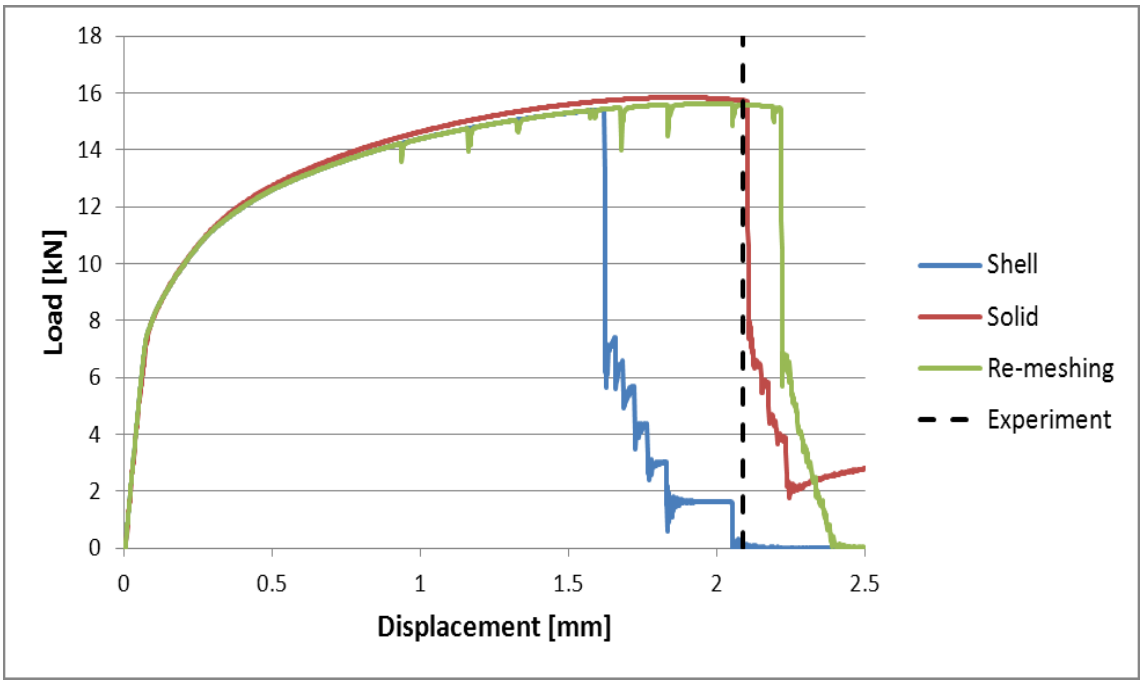

Figure 5-21: Predicted force displacement curve of the central hole tensile test with re-meshing. The experimental instant of fracture is depicted by a dashed black line.

section have been replaced by very fine solid elements. The picture is taken after the onset of fracture (crack initiation), and before the complete failure of the specimen: deleted elements (which correspond to a small crack) can be spotted at the center of the specimen, where the plastic strain is the highest.

Load-displacement curves predicted for the three geometries are depicted in Figs. 5-19 to 5-21. Results using shell elements only (case 1) are in blue, solid elements (case 3) in red and results using re-meshing (case 2) are in green. In all simulations, the abrupt drop of force corresponds to the onset of fracture, while small oscillations visible on the results of simulations using re-meshing (green lines in Figs. 5-19 to 5-21) correspond to re-meshing steps as explained in Section 5.4.2. In addition to the predicted load-displacement curves, the experimental instant of fracture is depicted with a black dashed line for the three geometries. For all geometries, the load-displacement curve features a maximum of force before fracture, which corresponds to the onset of through-the-thickness localization of the stress and strain fields within the specimen gage sections.

For the three fracture experiments considered, simulations using fine solid elements (case 3) predict the instant of fracture with a very good accuracy. As already detailed in section 5.4, simulations using shell elements always under-estimate the fracture displacement. In fact in shell simulations failure occurs just after the maximum of force is reached, as those elements cannot capture correctly the post-necking behavior of the sheet material. When using shell-to-solid re-meshing (green curves in Figs. 5-19 to 5-21), fracture occurs later than when only solid elements are used (red curves). The fracture displacement is over-estimated by 4% for the $6.65mm$ notched tensile specimen, by 7% for the $20mm$ notched tensile specimen and by 5% for the specimen with a central hole. Note that with re-meshing, simulations with initially only shell elements are able to predict correctly the applied load after its maximum.

The evolution of equivalent plastic strain, stress triaxiality and damage at the integration point which fails first are depicted in Figs. 5-22 to 5-24, for the $20mm$ notched tensile specimen. Results from the simulation with solid elements only are shown in red while results using re-meshing are in green. Note that two major re-meshing steps occur in that simulation, the first one at a displacement of about $2.1mm$

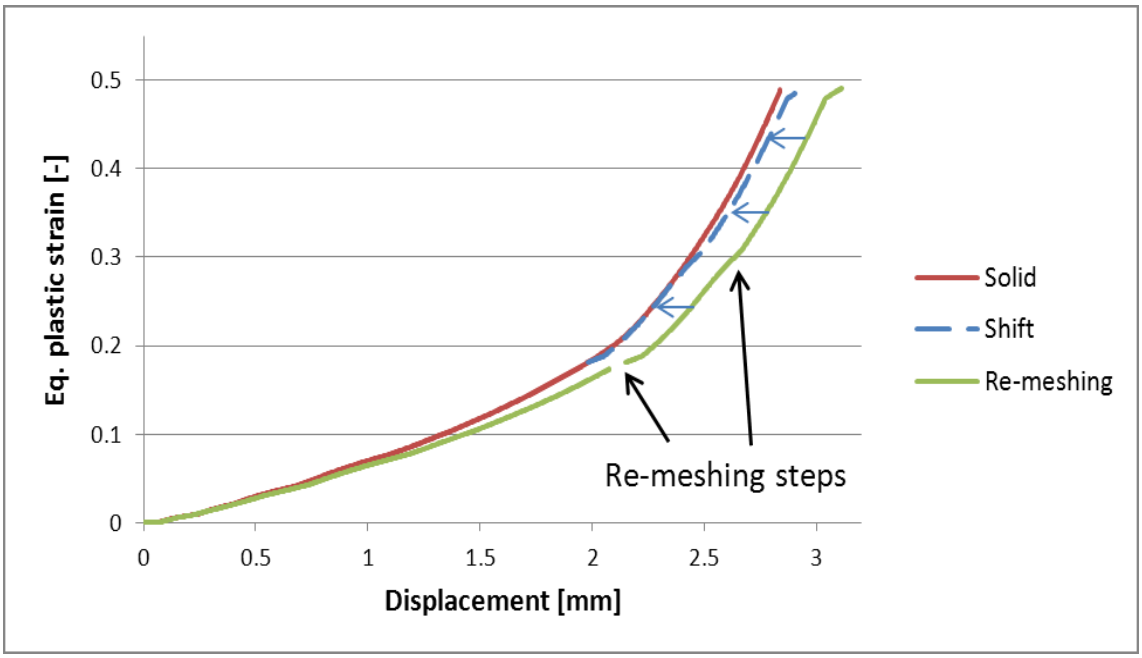

Figure 5-22: Evolution of equivalent plastic strain at the center of the $20mm$ notched tensile specimen, predicted using a solid mesh or re-meshing.

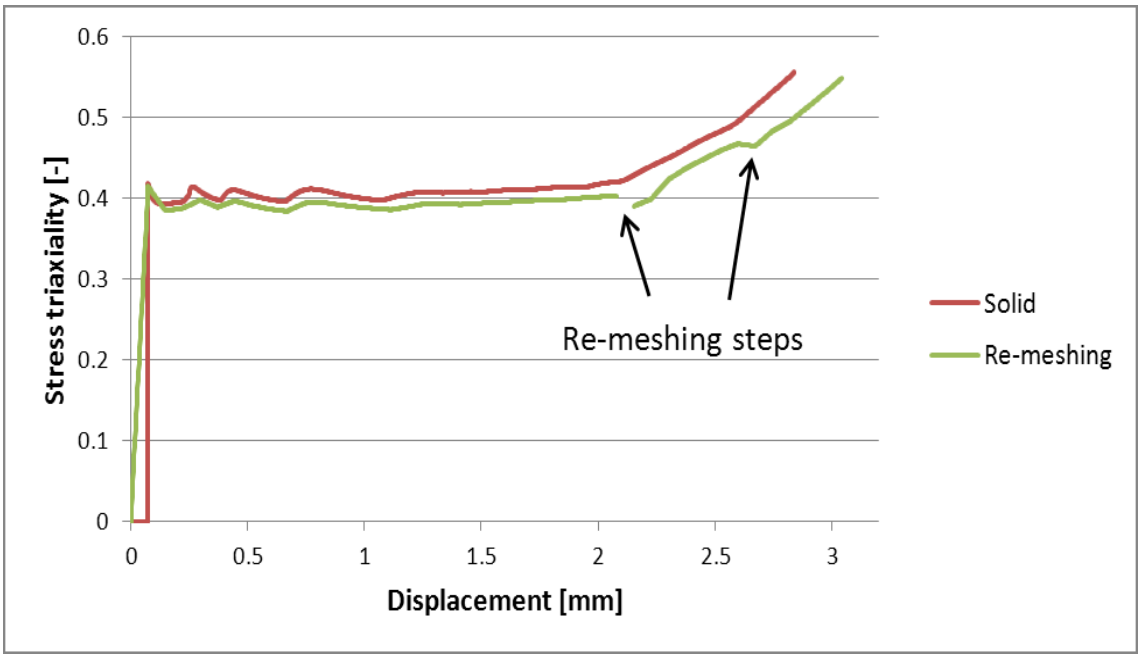

Figure 5-23: Evolution of stress triaxiality at the center of the $20mm$ notched tensile specimen, predicted using a solid mesh or re-meshing.

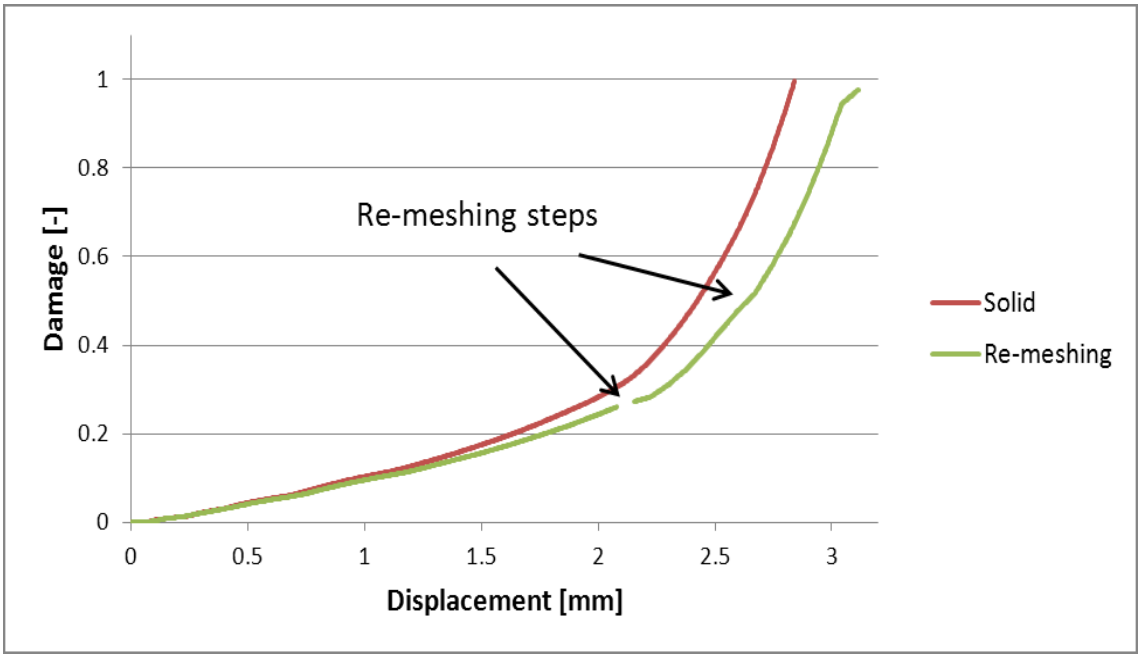

Figure 5-24: Evolution of damage at the center of the $20mm$ notched tensile specimen, predicted using a solid mesh or re-meshing.

where approximately 41,000 solid elements are generated at the center of the gage section, and a second step at a displacement of about $2.6mm$ where 10,000 new solid elements are added to extend the re-meshed area. Before the first re-meshing step, i.e. when only shell elements are present, both the equivalent plastic strain (in Fig. 5-22) and the stress triaxiality (in Fig. 5-23) are underestimated at the center of the gage section compared to results from solid elements (simulation #3, in red). As a result, at the instant of the first re-meshing step, the damage indicator is lower by 15% than in the simulation with only solids. After re-meshing, i.e. when the the center of the specimen gage section is meshed with solid elements, the evolution of equivalent plastic strain is comparable in both simulations: when shifted by the offset due to the inaccuracy of shells, the curve from the re-meshing simulation (in blue in Fig. 5-22) lies almost exactly on top of the curve from the solid simulation (in red in Fig. 5-22). Only a small discrepancy is noticeable at the instant of the second re-meshing step.

The evolution of stress triaxiality (Fig. 5-23) is also slightly underestimated by shell elements before the first re-meshing step. However, unlike for the equivalent plastic strain, differences between the solid simulation and the re-meshing simulation are significant after re-meshing occurred. In particular significant drops of the triaxiality occur at each re-meshing step. Those drops in the stress state correspond to the transient period following the re-meshing step described in Section 5.4.2. In spite of those local drops, it can be noted that the re-meshing simulation is able to capture the increase of triaxialty due to localized necking that occurs before fracture.

Therefore it can be concluded that the over-estimation of the predicted fracture displacement in the simulation with re-meshing is due to under-estimation by shell elements of the plastic strain, stress triaxiality and damage in the early stages of the simulation (before the first re-meshing step) and, to a small extent, to partial unloading that occurs during the subsequent re-meshing steps.

CPU times for the three geometries, using only solid elements and with re-meshing, are summarized in Table 5-4. Note that in all cases, the computation time is reduced by about 75% when re-meshing is used. However it is still much more than when using shell elements only. For all three geometries, the number of generated solid elements is very large compared to the initial number of shells elements. Therefore the computation is controlled by the sub-model containing the generated solids. In case of a

simulation of a larger part, where the ratio of generated solids to shell elements would be smaller, it is obvious that the time savings using re-meshing would be greater.

Table 5-4: CPU time (in s) when using re-meshing

Geometry	$6.5mm$ notch	$20mm$ notch	Central hole
Re-meshing	32,300	40,900	52,300
Only solid	126,800	129,800	204,900

5.5 Conclusion

In this chapter, the influence of spacial discretization of Finite Element models on ductile fracture predictions in sheet metals has been investigated. In addition, possible improvements coming from dynamic shell-to-solid re-meshing during the simulations have been assessed.

Based on numerical simulations of a tensile experiment on a flat specimen with circular notches using different element types (both shells and solids) as well as different mesh densities, it has been shown that shells cannot predict the post-necking behavior of sheet materials, regardless of mesh density. As a result spurious localization occurs at the onset of necking, leading to premature failure of the specimen. On the other hand, solids elements are able to predict the through-the-thickness localization that occurs before ductile fracture in AHSS, and thus allow for accurate predictions of the onset of ductile fracture when used in conjunction with suitable fracture initiation models. However very fine meshes (with an element length of about $100\mu m$) are required in order to get converged[8] numerical results: improved accuracy comes at the expense of computational efficiency.

Automatic re-meshing of shell into solid elements is considered to improve the accuracy of simulations with shell elements. The accuracy of the re-meshing technique is evaluated based on numerical simulations of tensile fracture experiments and

[8] In the sense that using a finer mesh would not change the numerical results.

comparison of numerical predictions to experimental results. Concerning the prediction of the onset of ductile fracture, it is shown that simulations with re-meshing are more accurate that those with shell elements only. However, simulations with re-meshing do not match the accuracy of simulations with solid elements only. It is worth mentioning that most of the inaccuracy originates in the first stages of the simulations, before re-meshing when the mesh is composed by shell elements only. In addition, re-meshing permits to predict correctly the post-necking behavior of sheet materials, which cannot be done with shell elements. A correct prediction of local material state of deformation and stress is necessary when trying to predict crack orientation and propagation.

Chapter 6

Analysis of the failure micro-mechanisms

Contents

Abstract

The evolution of damage and the mechanisms responsible for ductile failure are identified in the TRIP steel sheet submitted to different stress states, using optical and scanning electron microscopy. Experiments are performed on tensile specimens and on disk specimens submitted to out-of-plane hemispherical punching, thereby covering stress states from uniaxial to equi-biaxial tension. For each specimen geometry, experiments have been interrupted prior to fracture at different stages of deformation: onset of through the thickness necking and 95%, 99% of the displacement at which fracture initiates. Micrographs of samples extracted from the deformed specimens permit to evaluate the material damage for increasing amounts of accumulated plastic strain, and identify rupture mechanisms. It is shown that the critical mechanism

[9] This Chapter is reproduced from: Dunand M., Mohr D. and Ravi-Chandar K., "Shear fracture of Advanced High Strength Steels: Mechanism Analysis and Micromechanical modeling". *Submitted.*

responsible for material failure is the localization of the plastic deformation in a shear band initiating at a grown and isolated void. The orientation of the fracture surface is controlled by the shear band direction.

6.1 Introduction

Damage mechanisms leading to ductile failure are generally described in terms of void nucleation, void growth and finally void linkage that form cracks. An extensive review of ductile fracture mechanisms can be found in Garrison and Moody (1987, [63]). Observation and characterization of damage mechanisms is traditionally done by means of optical and Scanning Electron microscopy. This destructive approach only gives access to two-dimensional information. High resolution tomography and laminography are now increasingly used for non-destructive three-dimensional observation of damage in metallic materials (e.g. Morgeneyer et al, 2008, [128]; Maire et al., 2012, [117]).

In this Chapter, attention is limited to studying the mechanisms leading to ductile failure under biaxial tension, i.e. plane stress states between uniaxial tension and equi-biaxial tension. A series of interrupted tensile experiments is performed on specimens extracted from TRIP780 steel sheets. A specimen with a central hole is used to study uniaxial tension, while notched flat specimens cover intermediate stress states in the vicinity of plane strain tension. In addition, interrupted punch experiments are performed to investigate the failure mechanism under equi-biaxial tension. Micrographs of specimens corresponding to different stages of loading prior to failure are analyzed in view of void nucleation and growth as well as localization of plastic deformation at the grain level. The experimental observations suggest that shear band formation is the governing failure mechanism under biaxial tension.

6.2 Macroscopic analysis: experiments and simulations

Different experiments are performed to shed some light on the fracture mechanism at stress states in the vicinity of biaxial tension. A finite element simulation

is performed of each experiment to provide access to the local stress and strain fields inside the specimen. The reliability of the numerical simulation and the underlying plasticity model is not demonstrated here as it is covered by previous publications on this material (Dunand and Mohr (2010, 2011, [48-50]) and Mohr et al. (2010, [122])), as well as in Chapter 5. Instead, we focus on describing the experimental and numerical results at the macroscopic level in the present section, before moving to the microscopic level in the sequel.

6.2.1 Notched tension experiments

Tensile experiments are performed on flat notched specimens (Fig. 6-1a). Specimens are 20mm wide in the shoulder area and feature a minimum width of 10mm at the center. The notch radius is R=6.65mm. Experiments are carried out under displacement control at a constant crosshead velocity of 0.5mm/min. Planar Digital Image Correlation (2D-DIC) is used to measure the relative displacement of the specimen boundaries and the displacement field at the center of the gage section.

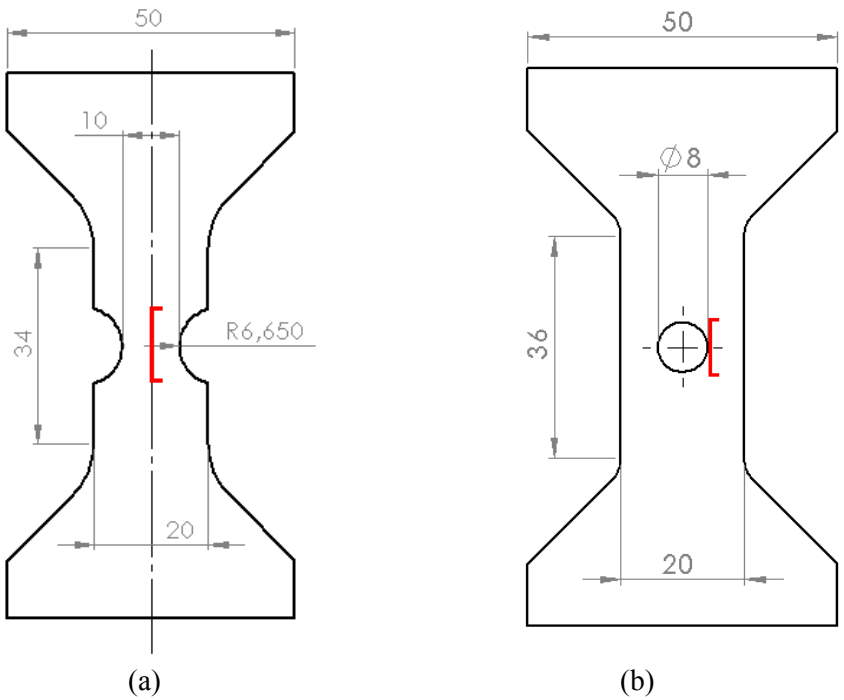

Figure 6-1: Tensile specimens with (a) a notch radius 6.65mm and (b) tensile specimen with central hole. Red marks depict the position from where micrography samples are extracted.

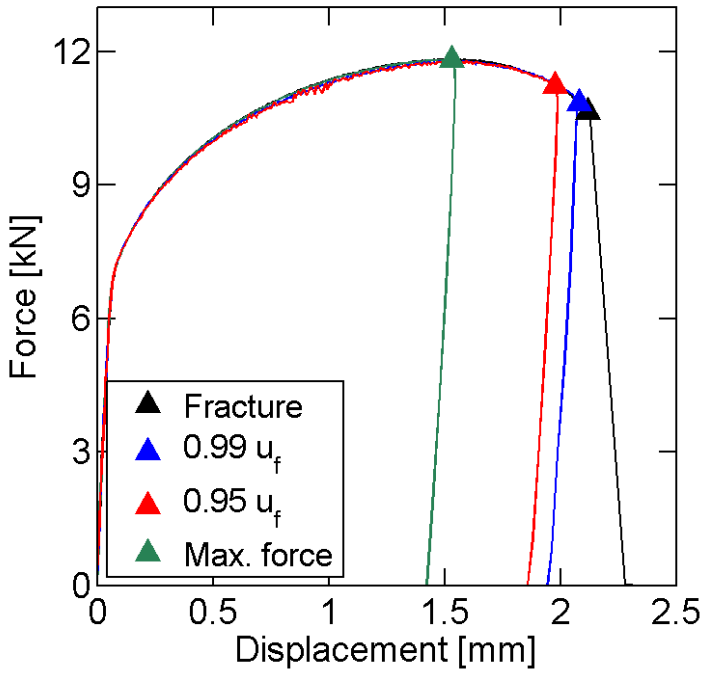
Force [kN]
Displacement [mm]
Fracture
0.99 u_f
0.95 u_f
Max. force
0
3
6
9
12
0
0.5
1
1.5
2
2.5

(a)

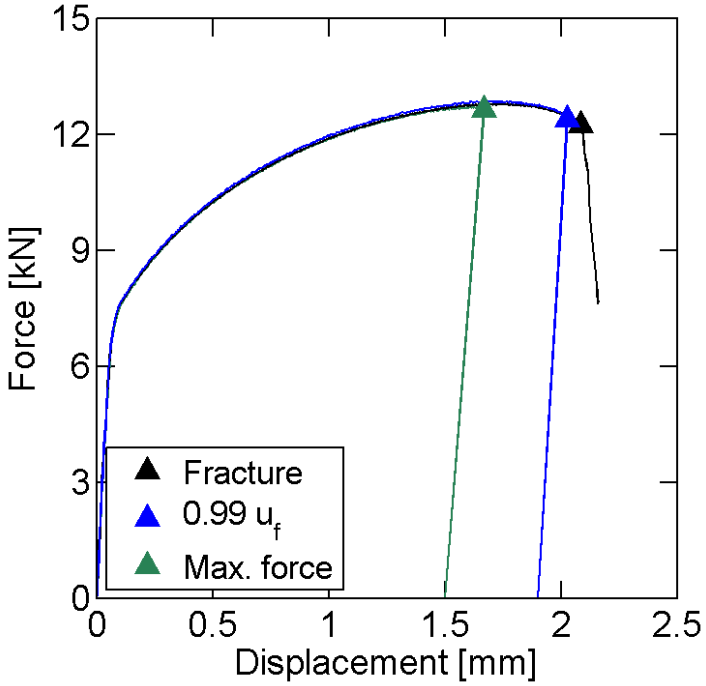
Force [kN]
Displacement [mm]
Fracture
0.99 u_f
Max. force
0
3
6
9
12
15
0
0.5
1
1.5
2
2.5

(b)

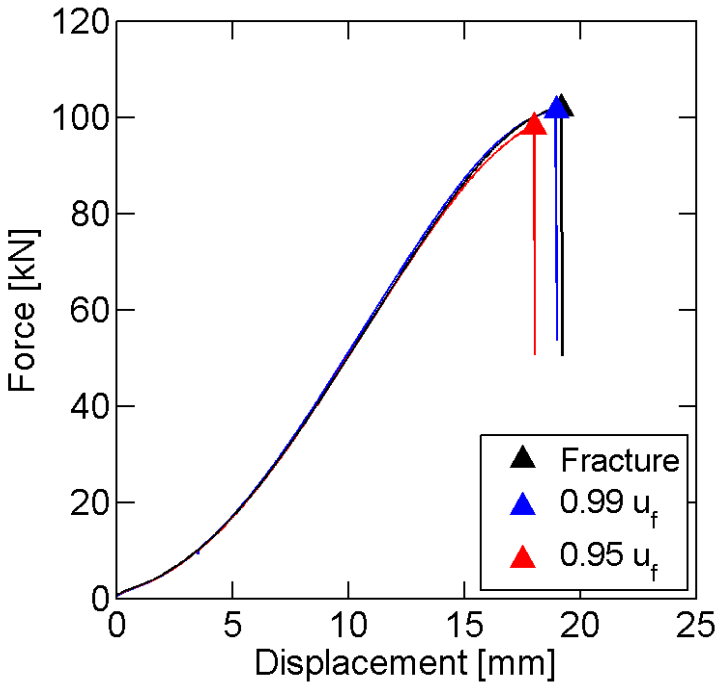

(c)

Figure 6-2: Force displacement curves of the (a) notched tensile experiment, (b) central hole tensile experiment and (c) punch experiment.

The measured force-displacement curve is depicted in black in Fig 6-2a. A force maximum is reached before fracture occurs, roughly corresponding to the instant of the onset of through-the-thickness necking. Beyond the onset of necking, steep gradients in the stress and strain fields develop both in-plane and through-the-thickness at the center of the specimen gage section (Fig. 6-3).

The plane stress condition prevail up to the onset of through-thickness necking. Thereafter, a stress in specimen thickness direction builds up. The corresponding plots of the estimated loading paths at the specimen center, i.e. the evolution of the equivalent plastic strain as a function of the stress triaxiality and the Lode angle parameter, therefore show a pronounced kink associated with necking followed by an increase in stress triaxiality and a decrease in the Lode angle parameter (Fig. 6-4). The reader is referred to Dunand and Mohr (2010, [48]) for more details on the numerical model.

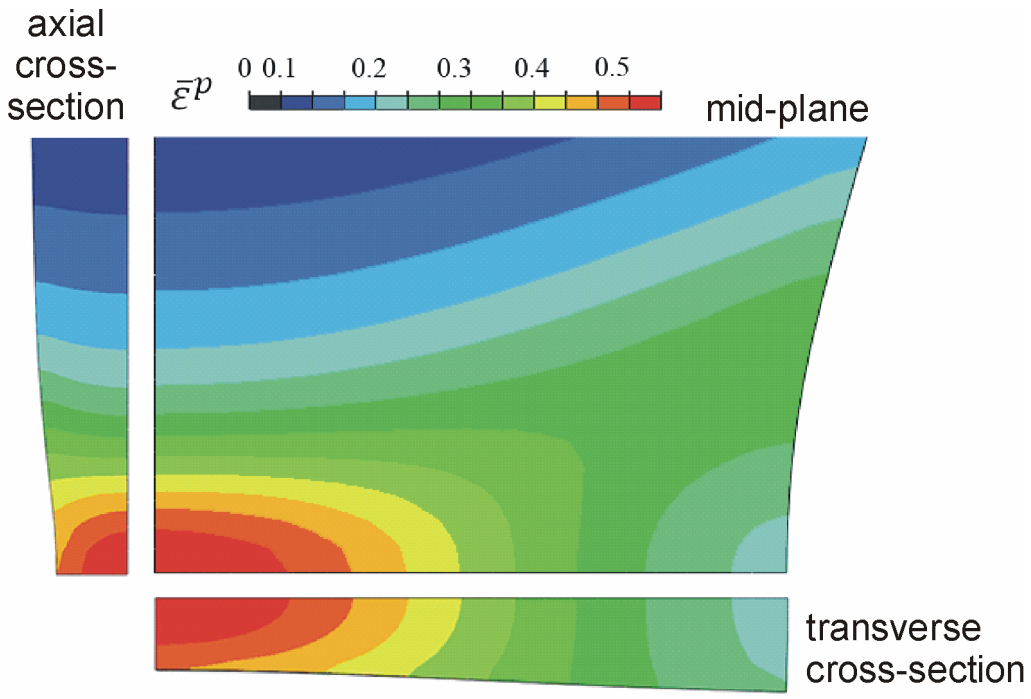

Figure 6-3: Contour plot of the equivalent plastic strain at the instant of the onset of fracture in a notched specimen.

In addition to the monotonic experiment all the way to fracture, the experiment is repeated for additional specimens, but interrupted prior to fracture at different stages of deformation: maximum of force; 95% and 99% of the displacement at which fracture initiates. Due to the excellent repeatability of the experiments for the material at hand, the corresponding force-displacement curves lie on top of each other (Fig. 6-2a). The end points of the interrupted experiments are therefore highlighted by a triangle symbol in Fig. 6-2a and 6-4.

6.2.2 Tension on a specimen with a central hole

In close analogy with the experimental program on the notched tension specimen, experiments are performed on a tensile specimen with a central hole (Fig. 6-1b). The hole has a diameter of 8mm while the ligaments to the left and right of the hole are each 6mm wide. Following exactly the same procedure as for the notched specimen, a monotonic experiment is performed all the way to fracture, followed by a series of

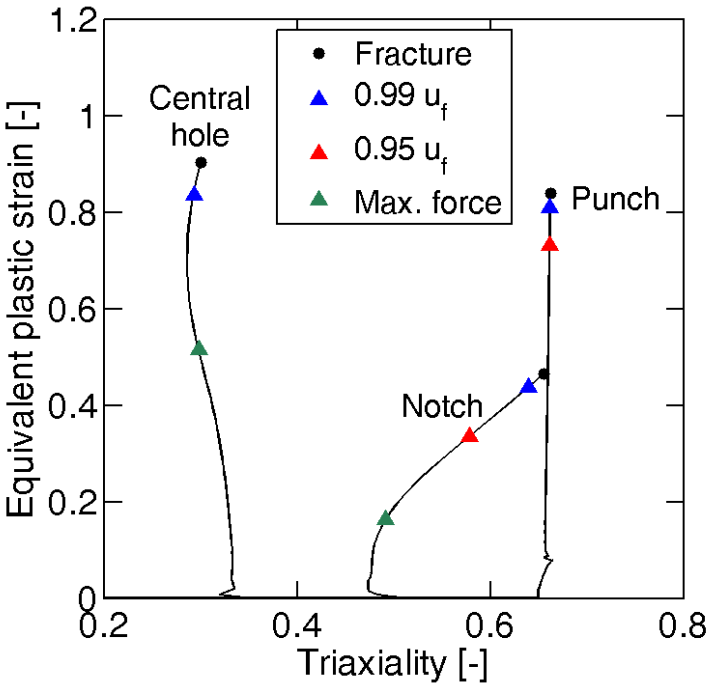

(a)

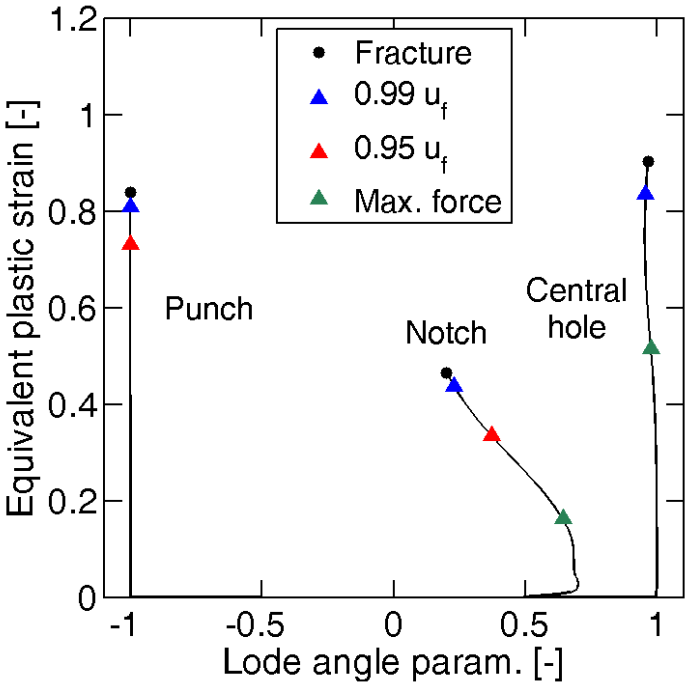

(b)

Figure 6-4: Loading paths to fracture. (a) Evolution of equivalent plastic strain versus stress triaxiality and (b) evolution of equivalent plastic strain versus Lode angle. Solid points depict the onset of fracture.

interrupted experiments ending at maximum of force and 99% of the displacement of total failure, respectively. Corresponding force-displacement curves are shown in Fig. 6-2b.

The cracks are assumed to initiate near the boundary of the central hole. The corresponding finite element simulation shows that through-thickness necking occurs in the hole ligaments, with the strongest thickness reduction of up to 38% at a distance of 0.9mm from the hole boundary. The evolution of the stress state at an integration point located at the specimen mid-plane near the hole boundary is shown in Fig. 6-4. Due to the proximity to the hole boundary, the stress state remains close to uniaxial tension all the way to fracture, i.e. the stress triaxiality and Lode angle parameter are close to 0.33 and 1.0, respectively. Selected views of the deformed FEA mesh at the instant of onset of fracture are shown in Fig. 6-5 with a contour plot of the axial plastic strain.

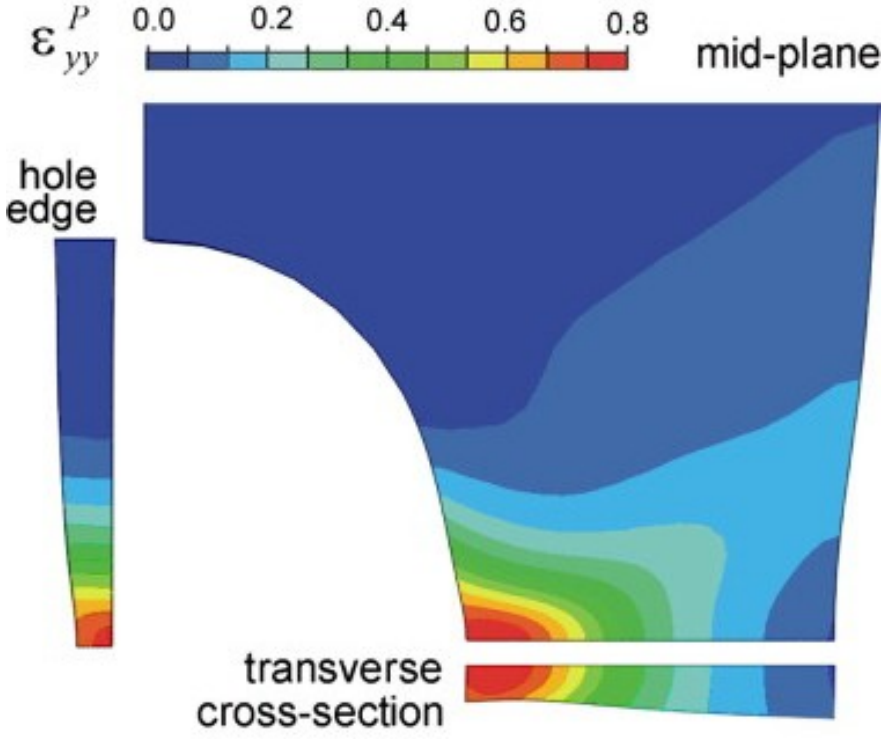

Figure 6-5: Specimen with a central hole: contour plot of plastic axial strain at the instant of the onset of fracture.

6.2.3 Punch Experiment

In order to characterize the material response for equi-biaxial tension, a sheet specimen is clamped on a circular die and subsequently loaded through a hemispherical punch. The punch and die have a diameter of 44.5mm and 100mm, respectively. The clamping pressure is applied through eight M10-12.9 screws. The experiment is carried out on a screw-driven universal testing machine (MTS, Model G45) at a constant punch velocity of 5mm/min. In order to limit the effects of friction, a stack of six oil-lubricated 90μm thick Teflon layers is put between the specimen and the punch during each test. Three-dimensional Digital Image Correlation is used to measure the out-of-plane deformation of the specimen. The applied force versus punch displacement curve is depicted in black in Fig. 6-2c; it increases monotonically until a sharp drop in the force level is observed at the instant of the onset of fracture. Fracture occurs at the top of the dome, where the stress state is close to equi-biaxial tension.

As for the tensile experiments, we also carry out interrupted punch experiments where loading was stopped at 95% and 99% of the punch displacement at which fracture initiates. Corresponding superposing force-displacement curves are shown in Fig. 6-2c with triangle-symbols indicating the points of interruption. The accompanying finite element simulations shows the absence of through-thickness necking. As a result, the loading path to fracture remains more or less proportional, i.e. both the stress triaxiality and the Lode angle parameter remained constant at 0.66 and -1.0, respectively.

6.2.4 Dependence of the strain to fracture on stress state

The results from the above experiments along with the computational analysis provide insight into the stress state dependency of the strain to fracture. Here, the "strain to fracture" is defined as the largest achievable macroscopic strain prior to the formation of cracks or narrow bands of localization of plastic deformation. This definition is very useful from an engineering point of view. From a physical point of view, it might be more meaningful to define the strain to fracture at smaller length scale. For instance, in polycrystalline materials, it could be associated with the plastic deformation at the grain level up to the point of micro-crack formation. Clearly, the use

of the latter definition would require more involved material models that can predict the strains at the grain level.

Taking a purely phenomenological macroscopic approach (see discussion in Section 2.2), stress triaxiality and Lode angle parameter dependent damage indicator models have been developed recently to describe the effect of stress state on the strain to fracture (e.g. Bai and Wierzbicki, 2010, [7]; Mohr and Marcadet, 2012, [125]). For biaxial tension, these models predict a minimum in the strain to fracture for transverse plane strain tension, while the strain to fracture is supposed to increase monotonically towards the respective limiting cases of uniaxial tension and equi-biaxial tension. It is the goal of the subsequent two sections, to provide a physics-based explanation of this characteristic drop in the strain to fracture for plane strain tension.

6.3 Fractographic analysis

6.3.1 Sample preparation

Cross-sectional cuts are prepared from the tested specimens for microscopic inspection. For the tensile experiments (notched and central hole specimens), the observation plane is the one containing the axial and thickness directions. A red solid line in Fig. 6-1 indicates the projection of the observed cross-sections on the specimen surface. For the punch experiment, the observation plane includes the thickness and transverse sheet direction, since the first cracks always formed parallel to the sheet rolling direction.

The sheet cutting is done using a wire saw. The samples preparation follows closely the procedure described in the Metals Handbook vol.8 (1990, [5]). The samples are first mounted in a conductive phenolic mounting compound filled with aluminum particles. They are then ground and polished. The final polishing step is performed with a $1\mu m$ diamond paste. Etching is finally performed using a 2% Nital solution.

6.3.2 Microscopic observations of polished cross-sections

A series of micrographs of the notched tensile specimens is shown in Fig. 6-6 as recorded with the Back-Scattered Electron (BSE) detector of a *FEI XL40* scanning electron microscope operating at $15kV$. According to our finite element analysis, the corresponding accumulated equivalent plastic strains at the specimen center are: $\bar{\varepsilon}^p = 0.17$ (maximum force, Fig. 6-6a), $\bar{\varepsilon}^p = 0.34$ (95% displ., Fig. 6-6b) and $\bar{\varepsilon}^p = 0.44$ (99% displ., Fig. 6-6c).

At maximum force (Fig. 6-6a), the specimen already exhibits noticeable damage in the form of voids. The area fraction of voids is about $4\text{x}10^{-3}$ in Fig. 6-6a, while virtually no voids are visible in the undeformed material (Fig. 1-1). The position of the voids suggests that they nucleated at the ferrite/martensite and/or ferrite/austenite grain boundaries. Strain incompatibilities between the different phases may induce more rapid debonding at the phase interfaces (Jacques et al., 2001, [87]). Moreover, most of the visible voids are aligned parallel to the loading direction (which also coincides with the sheet rolling direction). Lorthios et al. (2010, [114]) observed similar nucleation patterns in TWIP steels by means of x-ray tomography. Note that the undeformed material shows segregation bands of austenite (Fig. 1-1), which seem to be favored sites for void nucleation. Some voids have also nucleated away from the segregation bands at apparently random locations in the specimens.

Figure 6-6b ($0.95u_f$) shows a polished cross-section for significantly higher equivalent plastic with an estimated maximum of $\bar{\varepsilon}^p = 0.34$ at the specimen center. At this stage of deformation, the area fraction of voids has increased to about $7.4\text{x}10^{-3}$. However, it is important to note that the average size of the voids is very similar to that of the voids observed at maximum force. In other words, the measured increase in void volume fraction is not due to void growth. Instead, it is due to additional void nucleation. Based on x-ray tomography quantitative observations made on a DP600 steel sheet and its phase constituents, Maire et al. (2008, [116]) and Bareggi et al. (2012, [12]) also concluded that the average void diameter does not increase during straining, while additional damage is mainly due to the nucleation of new cavities. At $0.95u_f$, the observed void alignments are longer than those at maximum force. Voids

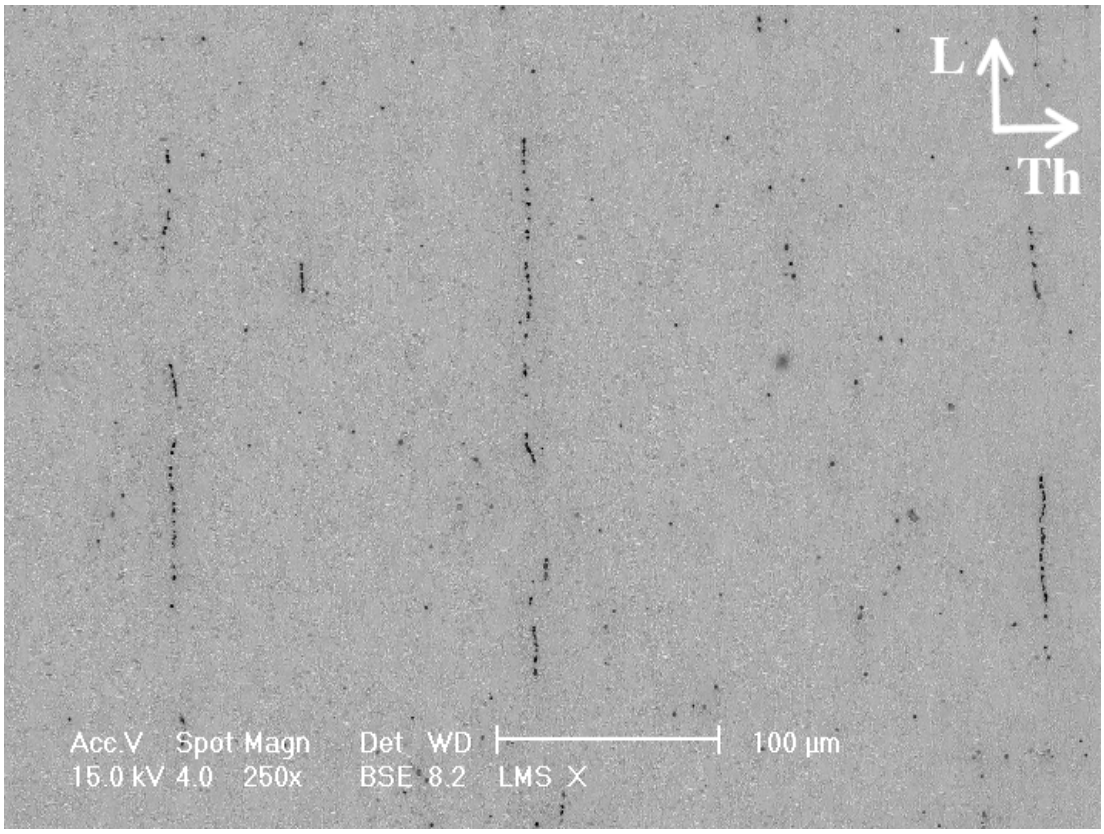
L
Th
Acc.V Spot Magn Det WD 100 µm
15.0 kV 4.0 250x BSE 8.2 LMS X

(a)

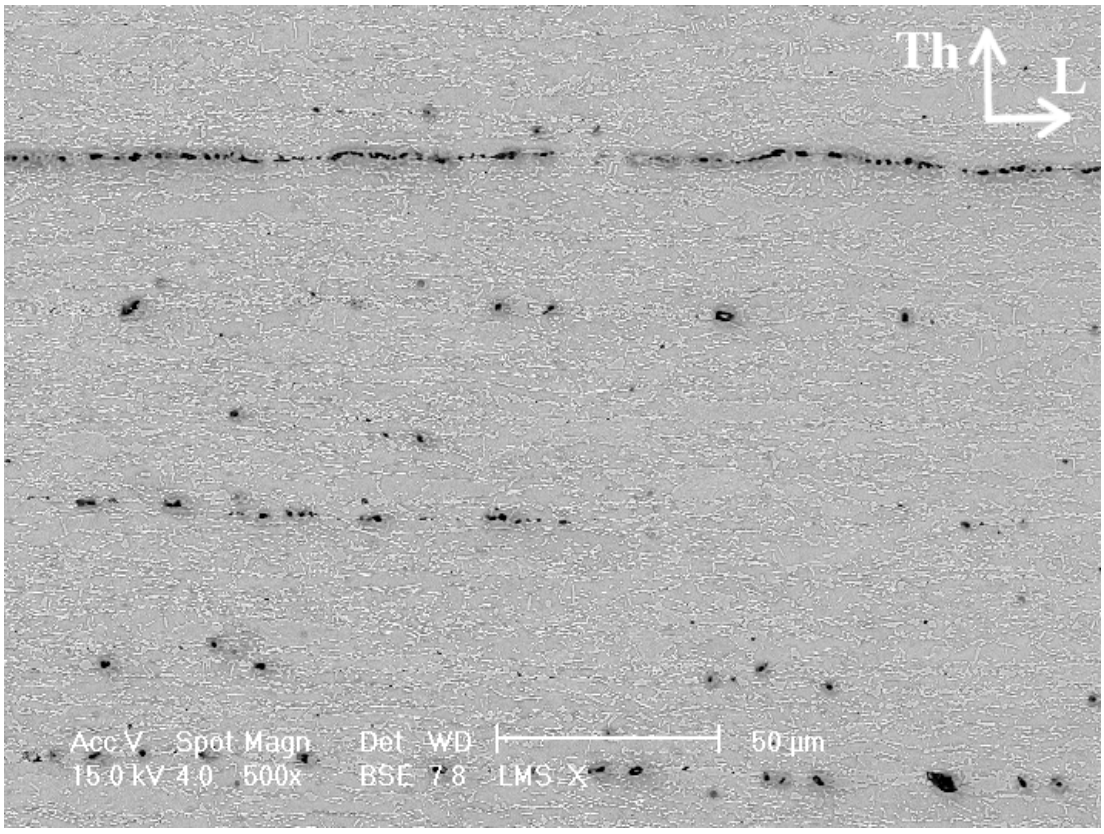
Th
L
Acc.V Spot Magn Det WD 50 µm
15.0 kV 4.0 500x BSE 7.8 LMS X

(b)

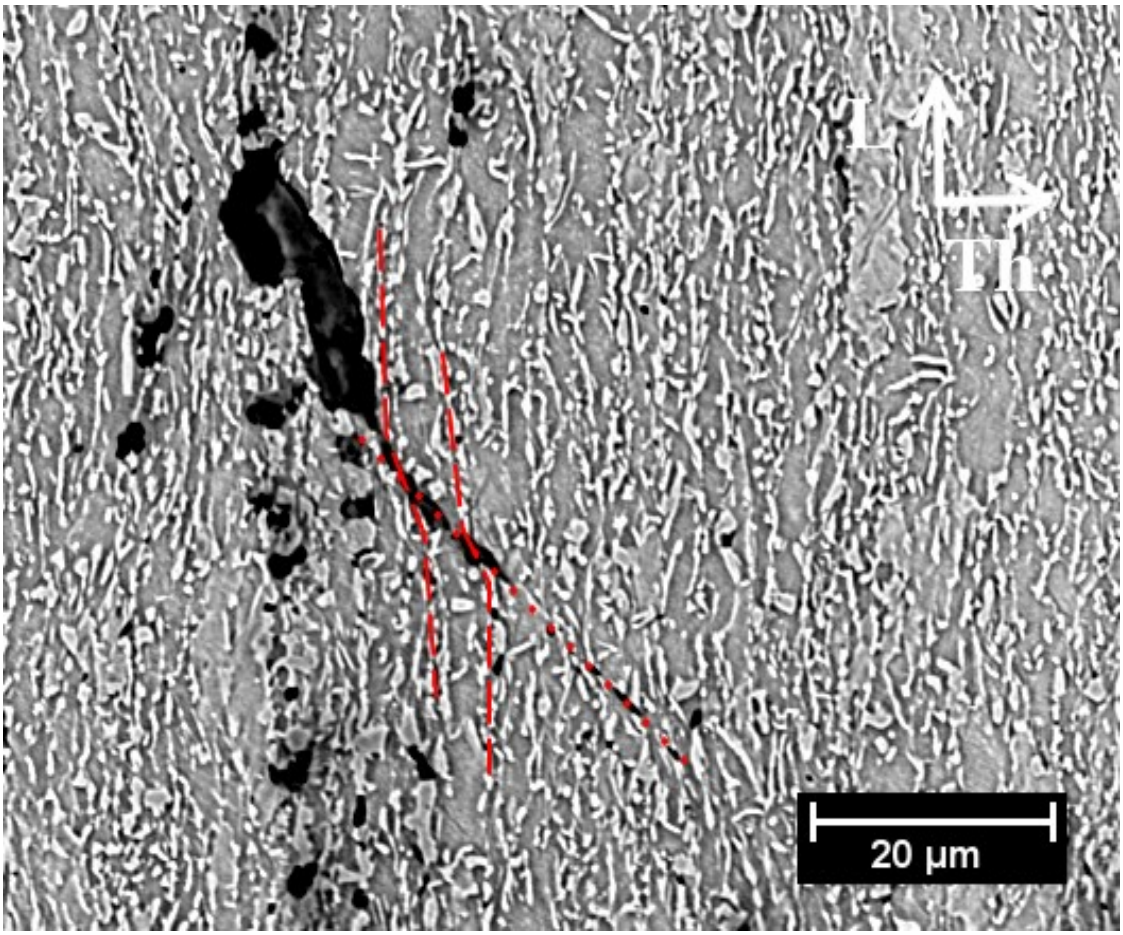

(c)

Figure 6-6: SEM micrographs from notched tensile experiments interrupted at (a) the maximum of force, (b) 95% of the displacement to fracture and (c) 99% of the displacement to fracture. The *L* and *Th* orientations correspond to the specimen loading direction and through-the-thickness direction, respectively.

seem to nucleate at both ends of the alignments. Void coalescence is also observed among voids within the same alignment, thereby forming microcracks parallel to the loading direction.

At 99% of the displacement to fracture, the observed mesostructure is similar to that at 95% of the displacement to fracture. However, at a higher magnification, the inspection of martensite grain bands (bright phase in Fig. 6-6c) shows signs of shear cracks. The martensite grains are organized in more or less straight bands along the

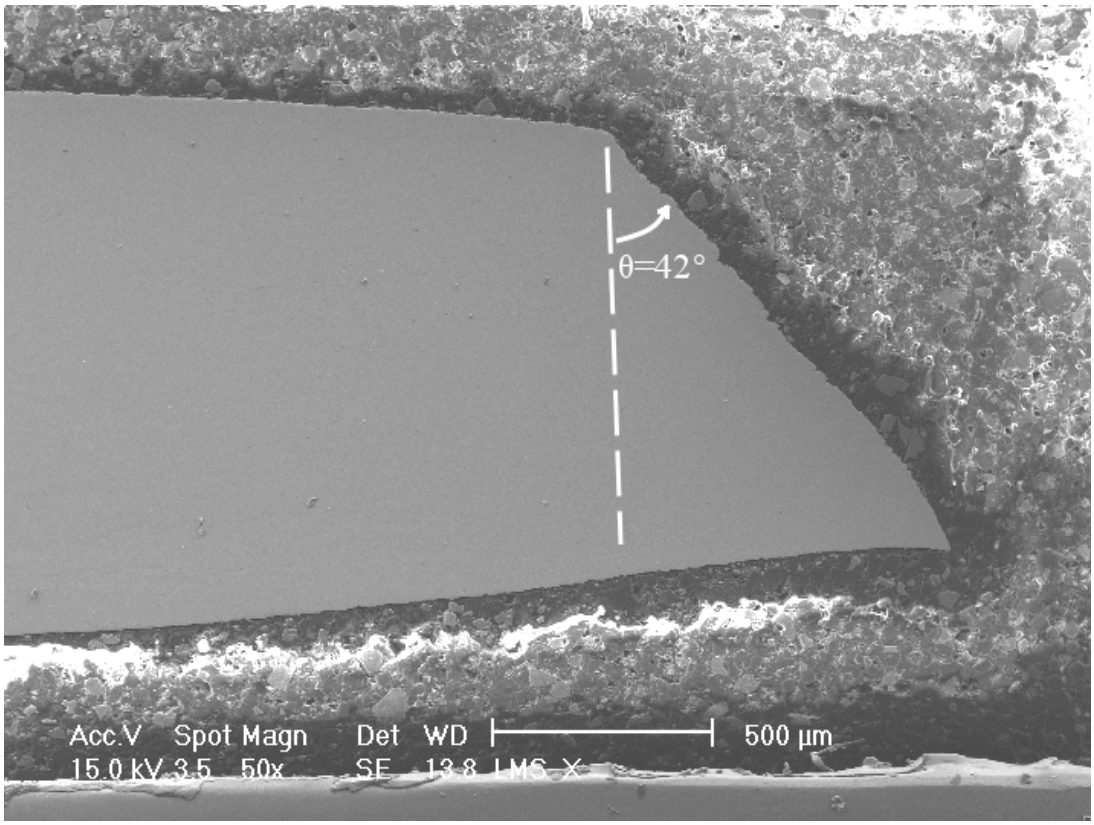
θ=42°
Acc.V Spot Magn Det WD 500 µm
15.0 kV 3.5 50x SE 13.8 LMS X

(a)

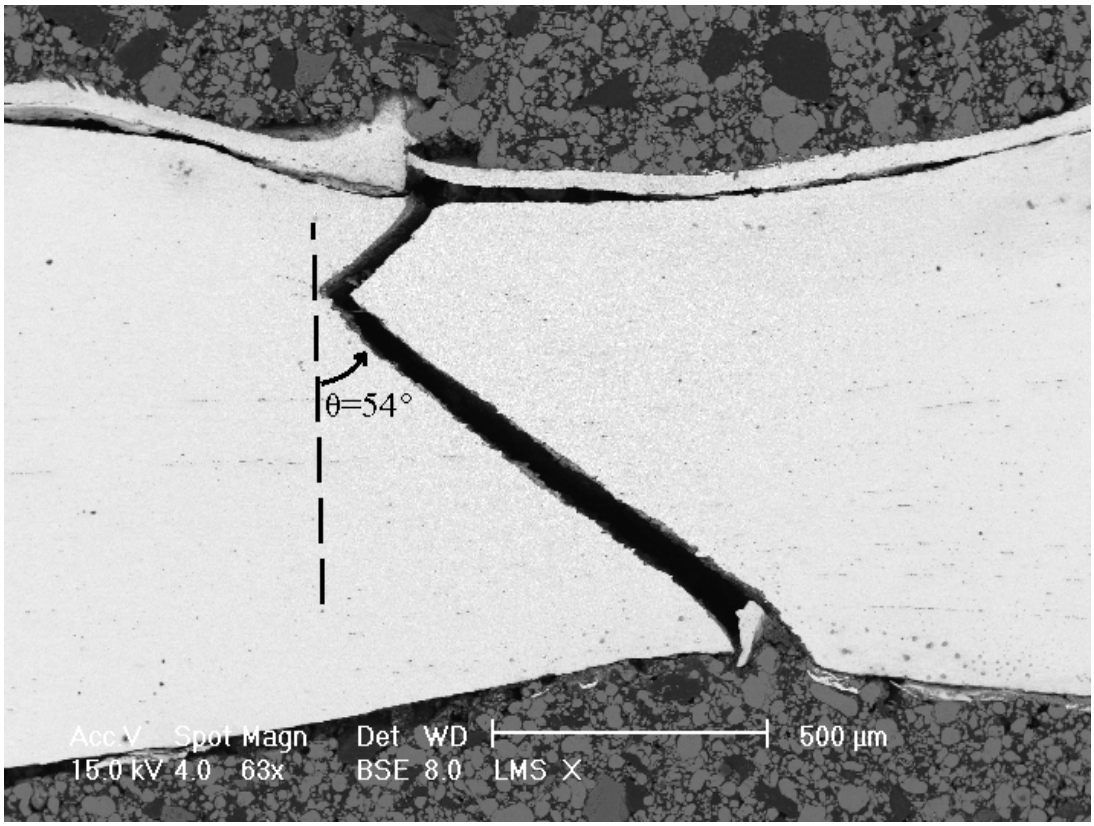
θ=54°
Acc.V Spot Magn Det WD 500 µm
15.0 kV 4.0 63x BSE 8.0 LMS X

(b)

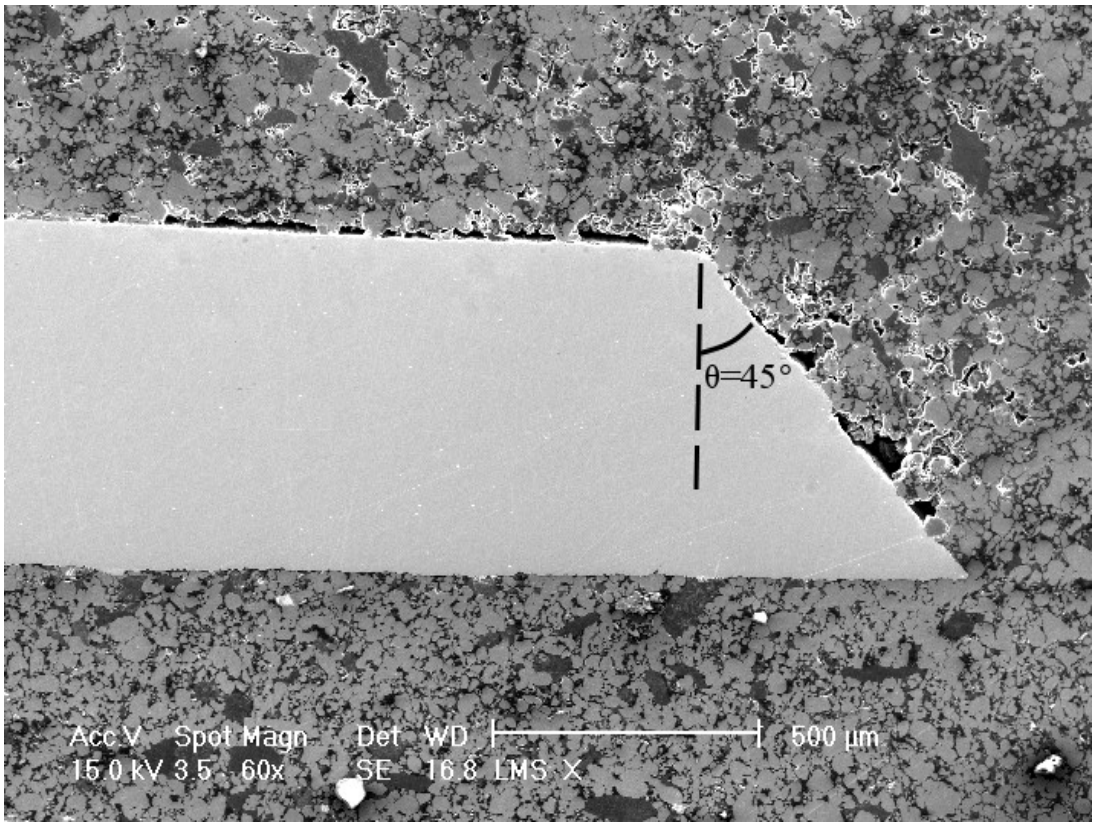

(c)

Figure 6-7: Cross sections of post-mortem specimens of (a) notched tensile experiment, (b) central hole experiment and (c) punch experiment.

rolling direction. Two such bands have been highlighted by red dashed lines in Fig. 6-6c. Prior to the fracture of the entire specimen (i.e. at 99% displ.), a tangential and normal discontinuity becomes apparent in the martensite bands. Figure 6-6c also shows a large hole at the top left which is disregarded because we think that it is just the trace of grains that have been torn out during polishing.

We note that remarkably similar observations are made when analyzing the corresponding cross-sectional cuts for tension with a central hole and even for the punch specimen. The corresponding micrographs of interrupted specimens are therefore not shown for conciseness. The longitudinal cross sections of the fractured notched and punch specimens all show straight slanted cracks (Fig. 6-7). In particular, the fracture surface is inclined at an angle of about 45° with respect to plane of the sheet. The only

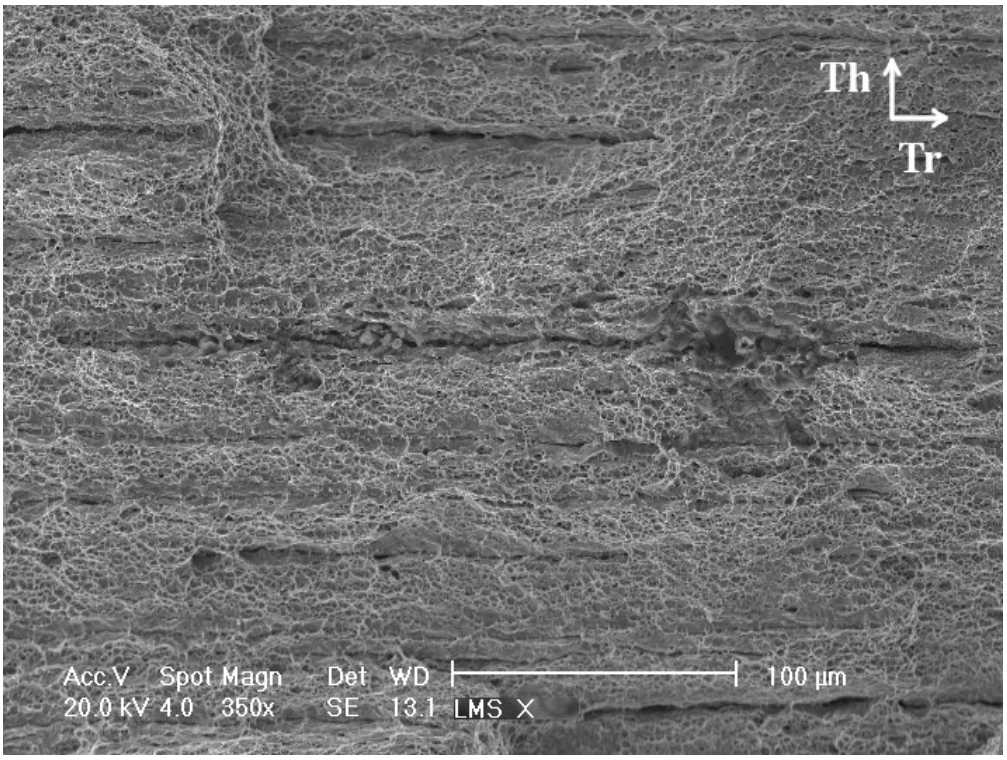

(a)

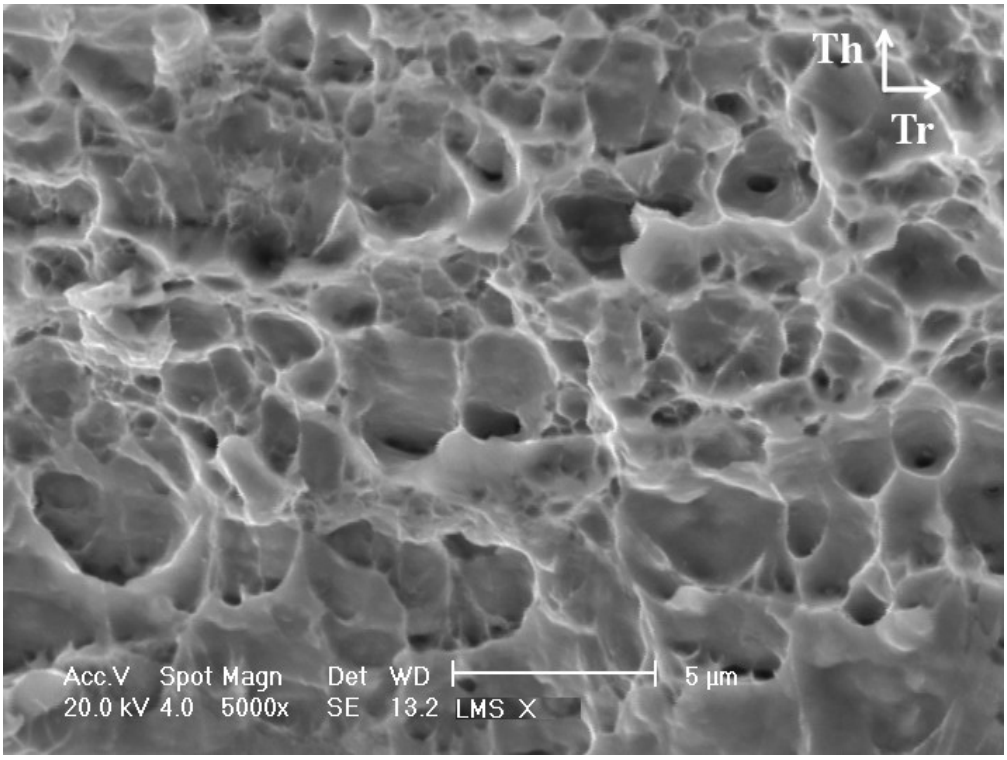

(b)

Figure 6-8: SEM fractographs from a broken notched tensile specimen. The *Th* and *Tr* orientations correspond to the through-the-thickness and specimen transverse directions, respectively.

exception is the central hole specimen, which features a V-shaped fracture surface (Fig. 6-7b).

6.3.3 Fracture surfaces

SEM fractographs from a notched tensile specimen are presented in Fig. 6-8. The fracture surface presents a dimple pattern with a dimple size of about $2\mu m$ (Fig. 6-8b). The eccentricity of the black apex of the dimples with respect to the bright circumference (Fig. 6-8b) suggests that the ellipsoidal dimples are inclined towards the thickness direction. At a smaller magnification (Fig. 6-8a), the fracture surface features continuous dark lines of narrow valleys that are parallel to the specimen surface. It resembles a laminate with multiple layers of $50\mu m$ to $100\mu m$ thickness. The layer thicknesses are similar to the distances between the void bands observed in the cross-sectional cuts. It is speculated that these valley lines corresponds to the intersection of the crack surface with the void necklaces.

6.3.4 Effect of strain rate on damage

Even though technological solution are available to perform interrupted experiments in Split Hopkinson Bar systems (e.g. Nemat-Nasser et al., [134]), it has not been implemented as part of this thesis. Damage mechanisms taking place at high strain rate are thus not formally identified. However, fracture surfaces and cross-sections of post-mortem specimens submitted to high strain rate loadings are similar to those describes hereinabove. It is therefore assumed that damage mechanisms are comparable at low and high strain rates.

6.4 Mechanical interpretation of the observations

Based on the above observations, the following comments with regards to the mechanism leading to ductile fracture under biaxial tension can be made:

1. Voids nucleate at ferrite/martensite and ferrite/austenite grain boundaries, preferably along alignments parallel to the specimen loading direction

Nucleation takes place before necking, i.e. at zero out-of-plane stress. At this stage, the plastic strains are small ($\bar{\varepsilon}^p < 0.2$) as compared to those reached at the onset of fracture ($\bar{\varepsilon}^p > 0.45$).

2. The void volume fraction increases mostly because of new nucleations (and not due to the growth of existing voids).
3. Through-thickness necking is just a structural deformation mode which localizes the deformation to a small zone within the specimen. At the length scale associated with necking (sheet thickness), the material can still be considered as a homogenous continuum.
4. The local increase in stress triaxiality due to necking has no noticeable effect on the size of the voids. Furthermore, a similar void size is observed for tension with central hole (triaxiality of 0.33), notched tension and in a punch experiment (triaxiality of 0.66).
5. Coalescence occurs within void alignments (necklace mechanism) thereby forming microcracks parallel to the specimen loading direction. However, it appears that those microcracks and voids do not compromise the material's load carrying capacity along the axial direction.
6. Voids acts as material imperfections that trigger the localization of the plastic flow into a narrow band of localized plastic deformation. At this stage, a homogeneous description of the material is expected to become invalid. Due to the 45° orientation of the final fracture surface with respect to the axial direction, shear localization is considered as the dominant mechanism of plastic localization.
7. Secondary voids nucleate within the band of localized plastic deformation. The secondary voids eventually coalesce and create a macroscopic crack, independent of the microcracks associated with the necklace mechanism.

Among all steps involved in the ductile fracture process, we consider the localization of deformation in a narrow band as the most important precursor at the macroscopic level before cracks are formed at the grain level. It is worth noting that already more than 30 years ago, researchers considered shear localization as the

dominant mechanism leading to fracture of metals (e.g. Rice, 1976, [151]). On the other hand, the role of void growth and void shape changes appears to be secondary. These effects are probably only important within the band of localized deformation where other material heterogeneities (grain anisotropy and grain boundaries) may also come into play.

6.5 Conclusion

Damage mechanisms responsible for ductile failure of the TRIP steel at low strain rate have been characterized. Selected experiments, covering all the range of biaxial stresses, are carried out and interrupted at different levels of deformation. Samples extracted from the deformed specimens are analyzed by means of Optical and Scanning Electron Microscopy in order to identify the evolution of damage mechanisms. Observations show that interfaces between ferrite and martensite grains constitute preferred sites for void nucleation, which occurs at relatively low strains. However, void growth is not significant for all stress states considered. Damage increases mostly through nucleation of new cavities during deformation. It is found that the critical mechanism leading to fracture is a localization of the plastic flow at the grain scale into a planar band of shear deformation.

Chapter 7

Modeling of the failure mechanisms

Contents

Abstract

A numerical model is developped to investigate the influence of the stress state and strain rate on the onset of localization of the plastic flow in a void-containing material. A three-dimensional unit cell containing an initially spherical void is submitted to proportional loadings in the macroscopic stress space. Fully periodic boundary conditions are applied. The range of stress states considered are limited to biaxial tension, i.e. from uniaxial to equi-biaxial tension under plane stress conditinos. The model is able to predict qualitatively the dependence of ductility to the stress state observed experimentaly, as well as the increase of ductility at high strain rate.

[10] This Chapter is reproduced from: Dunand M., Mohr D. and Ravi-Chandar K., "Shear fracture of Advanced High Strength Steels: Mechanism Analysis and Micromechanical modeling". *In preparation.*

7.1 Introduction

The localization of plastic deformation within a narrow band is often an important precursor to ductile fracture. Following the works of Marciniak and Kuczynski (1964, [118]) and Rice (1977, [151]), it is common practice to predict the onset of localization based on macroscopic constitutive theories through infinite band localization analysis (e.g. Mear and Hutchinson, 1985, [120], Duszek and Perzyna, 1991, [53]). As noted by Rice (1977, [151]), the identified onset of localization corresponds to the loss of ellipticity of the governing equilibrium equations. Consequently, onset of localization maps can also be directly computed by assessing the loss of ellipticity of incremental moduli (Michel et al., 2007, [121]; Danas and Ponte Castaneda, 2012, [42]).

For most metals, the strains at the onset of localization are very large. As a consequence, the effect of voids on the elasto-plastic moduli, even for very low porosities, needs to be taken into account when computing the instant of the onset of localization. This requires advanced constitutive theories such as the Gurson model (Gurson, 1977, [70]) and its extensions accounting for void nucleation (e.g. Chu and Needleman, 1980, [35]), for the loss of load-carrying capacity associated with void coalescence (e.g. Tvergaard and Needleman, 1984, [181]), for void shape effects (e.g., Gologanu et al., 1993, 1994, [67, 68]; Garajeu et al., 2000, [62]; Pardoen and Hutchinson, 2000, [146]) and for plastic anisotropy (e.g., Benzerga et al., 2004, [18]). As shown by Nahshon and Hutchinson (2008, [130]), additional modifications representing shear softening are necessary to obtain reasonable predictions of strain localization at low stress triaxialities.

Unit cell models provide a computationally-expensive alternative to macroscopic constitutive theories to describe the large deformation response of metals of low porosity. The early analysis with unit cell models was mostly limited to two-dimensional models, e.g. axisymmetric mechanical systems with spheroidal voids (e.g. Koplik and Needleman, 1988, [97]; Brocks et al, 1995, [21]; Pardoen and Hutchinson, 2000, [146]) or plane strain models with cylindrical voids (e.g. Tvergaard, 1981, [177]). Fully three-dimensional models have only been employed rather recently for plane strain conditions (e.g. Scheyvaerts et al., 2011, [158]; Nielsen et al., 2012, [136]; Rahman et al., 2012, [150]) and selected three-dimensional stress states (e.g. Barsoum

and Faleskog, 2007, 2011, [14, 16]; Tekoglu et al., 2012, [174]). Aside from the macroscopic response, unit cell models provide valuable insight in the local deformation fields and allow for the detailed analysis of the void growth and coalescence process (e.g. Scheyvaerts et al., 2011, [158]). As discussed by Pardoen and Hutchinson (2000, [146]), it is useful to define *void growth* as the phase prior to the localization of deformation inside the intervoid ligament, while *void coalescence* describes the deformation process thereafter. Normal localization may be seen as diffuse necking of the ligament, while shear localization is characterized by the development of a shear band at the microscale. Due to the inherent periodicity of microstructures defined through unit cell models, the *onset of coalescence* corresponds to the *onset of normal and/or shear localization* of plastic flow within a narrow band at the scale of the void.

Substantial efforts have been devoted to the development of micromechanics-based coalescence criteria. The first generation of coalescence criteria (Brown and Embury, 1973, [23]; Thomason, 1985, [175]; Benzerga 2002, [17]) is primarily concerned with the prediction of internal necking as a function of the void shape, relative spacing and the applied maximum normal stress. The effect of shear in addition to normal loads on the coalescence has been addressed recently by Tekoglu et al. (2012, [174]). They demonstrate that the introduction of non-linear parameter functions into the Benzerga model leads to an excellent agreement with their unit cell simulations for combined shear and tension. Furthermore, Tekoglu et al. (2012, [174]) present a micromechanical analysis to come up with an analytical coalescence model for general loading conditions.

Reliable experimental results on ductile fracture at low stress triaxialities are still difficult to obtain because of significant experimental challenges associated with the proper introduction of loading, the inherent localization deformation at the macroscopic level (necking), and the detection of the onset of fracture (e.g. Bao and Wierzbicki, 2004, [11]; Mohr and Henn, 2007, [124]; Brunig et al., 2008, [26]; Fagerholt et al., 2010, [55]; Gao et al., 2011, [61]; Dunand and Mohr, 2011, [50]; Haltom et al., 2013, [72]). Numerical results on localization are therefore of particular value for the development of ductile fracture modes at low stress triaxialities. Tvergaard (2008, 2009, [178, 179]) analyzed the behavior of a row of circular cylindrical holes under

shear loading. He reports the formation of rotating micro-cracks as the result of void closure at low stress triaxialities. Furthermore, he points out that a maximum in the macroscopic shear stress accompanies the onset of localization of plastic flow. Nielsen et al. (2012, [136]) confirmed these observations using a three-dimensional unit cell model. In his most recent work, Tvergaard (2012, [180]) considered a square unit cell with a cylindrical void and fully periodic boundary conditions. By varying the normal stress during shearing, he found that increasing the stress triaxiality facilitates failure through shear localization.

Barsoum and Faleskog (2007, [14]) performed a micromechanical analysis on three-dimensional unit cells with spherical voids for combined tension and shear loading. Their model represents a layer of preexisting voids in a Levy-von Mises material; it features a height to width ratio of 2:1 along with periodic boundary conditions on all three pairs of parallel boundaries. Using a kinematic condition comparing the deformation gradient rate inside and outside a band of localization (as proposed by Needleman and Tvergaard, 1992, [132]), they define the onset of shear localization and report the corresponding macroscopic von Mises equivalent strain as strain to failure (due to localization). Their simulation results for a constant stress triaxiality of 1.0 elucidate the effect of the Lode parameter on shear localization for stress states between generalized shear and axisymmetric tension. Their computational results also agree well with the observations from experiments where coalescence occurred by internal necking (triaxiality above 0.7). However, for low stress triaxialities and stress states closer to generalized shear, the macroscopic strains to failure predicted by the unit cell model are significantly higher than those found experimentally.

Gao et al. (2010, [60]) applied macroscopic normal stresses along the symmetry axes of a cubic unit cell with a spherical void and boundaries that remain flat and perpendicular throughout deformation. Assuming that void coalescence occurs when the macroscopic strain state shifts to a uniaxial strain state, they computed the corresponding macroscopic effective strain as a function of the stress triaxiality (ranging from 0.33 to 2) and of the Lode angle. Their results indicate that the macroscopic strain to coalescence increases monotonically as a function of the Lode angle from axisymmetric tension to axisymmetric compression. Furthermore, their simulations indicate that this Lode angle effect on coalescence becomes more

pronounced at low stress triaxialities. They also show that the effective strain to coalescence decreases when assuming a Gurson instead of a Levy-von Mises matrix.

More recently, Barsoum and Faleskog (2011, [16]) made use of their unit cell model to investigate the localization of deformation into a narrow planar band different from the plane of normal stress axisymmetry and for a wider range of stress states. Irrespective of the stress state, they observe the lowest macroscopic effective strain to localization for bands oriented at an angle of about 45° with respect to the direction of the minimum principal macroscopic stress. The computed localization loci for stress triaxialities ranging from 0.75 to 2 show the lowest strains to localization for generalized shear. The loci are approximately symmetric with respect to the Lode parameter, showing slightly higher localization strains for axisymmetric compression than axisymmetric tension.

Assuming the localization of plastic deformation into a narrow band as the governing precursor of ductile fracture, an attempt is made in this Chapter to predict the "strain to fracture" as a function of the stress state based on localization analysis. For this we consider a cube of material which contains a spherical void. The void is not introduced to investigate the effect of void growth on the elasto-plastic behavior at the macroscale. Instead the hollow sphere is introduced to act as an imperfection which triggers the localization of plastic deformation. The unit cell model includes specific kinematic constraints on the cell degrees of freedom that permit to control precisely the applied macroscopic stress state as well as the orientation of the macroscopic principal stresses. The onset of localization is characterized by a geometric criterion comparing deformation gradient rates inside and outside the band of localization. The cell model is used to predict a macroscopic strain at the onset of shear localization, as well as the orientation of the plane of localization with respect to the principal stress directions. Describing the cell matrix material as rate-independent, the full range of biaxial stresses is covered. Numerical predictions qualitatively agree with experimental results presented in Section 6. In addition, calculations are done with the rate-dependent plasticity model defined in Chapter 4 for isothermal low strain rate and adiabatic high strain rate loadings. The increase of the failure strain at high strain rate is well predicted by the cell model.

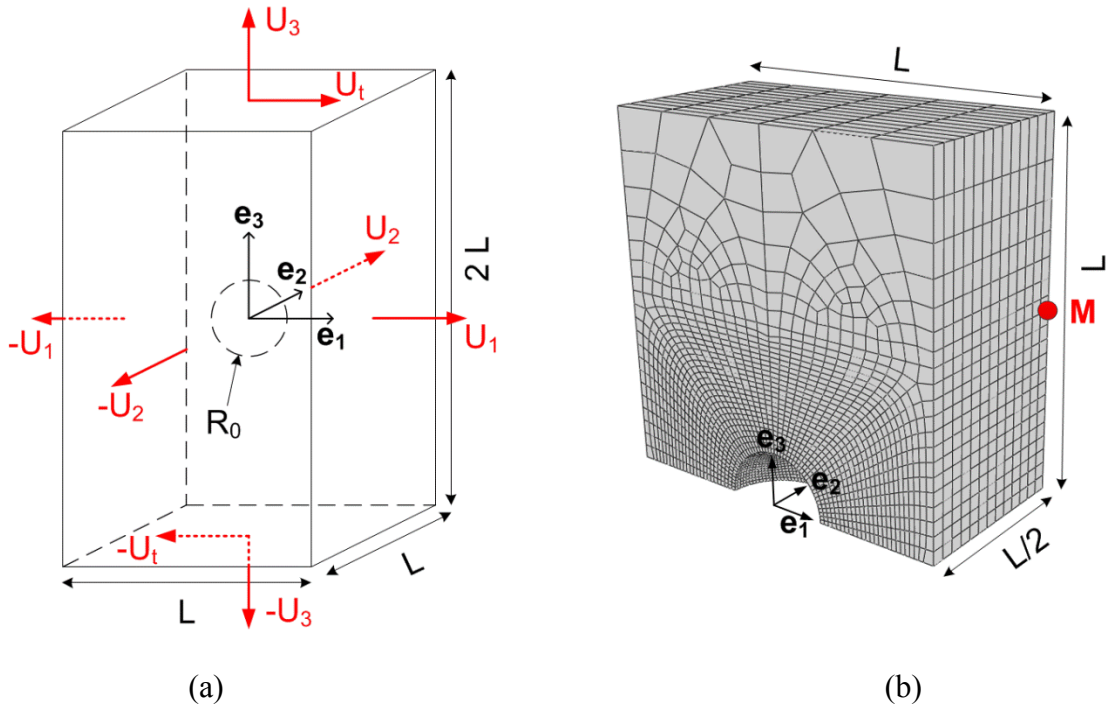

Figure 7-1: (a) unit cell initial geometry and (b) FEA mesh representing half of the cell.

7.2 Micromechanical modeling

An orthogonal parallelepipedic unit cell is chosen since periodic boundary conditions can be easily prescribed without any restriction on the stress state (Fig. 7-1a). In addition to periodic boundary conditions, the unit cell is subject to proportional loading in the macroscopic stress space. In other words, the ratios of the principal values of the macroscopic stress tensor are kept constant up to the onset of localization. For an isotropic unit cell, these ratios can be directly linked to the macroscopic stress triaxiality and the Lode angle parameter. Consequently, the plastic work up to shear localization can then be easily computed as a function of the stress state.

However, one immediate consequence of this choice of a parallelepipedic unit cell is the loss of isotropy. The results will be generated for an infinite medium with spherical defects that are located at the vertices of an orthorhombic lattice in the initial configuration, leading to a topological orthotropy of the model. Moreover, the shape of the spherical defects changes throughout loading, introducing another deviation from

the assumption of isotropy (morphological anisotropy). As will be explained in detail below, two measures are taken to minimize the effect of spurious anisotropy on our simulation results: firstly, a very low defect volume fraction corresponding to that observed experimentally is chosen; secondly, the orientation of the applied macroscopic principal stresses are constantly updated such that they coincide with the major axes of the ellipsoidal approximation of the shape of the deforming defect.

7.2.1 3D unit cell model geometry and boundary conditions

The undeformed unit cell consists of a rectangular cuboid of matrix material containing a spherical void at its center. We introduce the fixed Cartesian frame $[\boldsymbol{e_1}, \boldsymbol{e_2}, \boldsymbol{e_3}]$ corresponding to the normals to the cell's outer surfaces in the initial (undeformed) configuration. We limit our attention to a unit cell with the initial edge lengths $L_1 = L_2 = L$ and $L_3 = 2L$ (Fig. 7-1a); the height-to-width ratio of $L_3/L_1 = 2$ is chosen to facilitate the detection of localization using a purely kinematic criterion. The cell features a central spherical void of radius $R = 0.15L$ which corresponds to an initial porosity of $f_0 \cong 0.7\%$.

Defining the macroscopic deformation gradient $\boldsymbol{F}$ as the spatial average of the local deformation gradient over the unit cell volume, the boundary conditions are chosen such that a gradient of the form

$$\boldsymbol{F} = F_{11}\boldsymbol{e}_1 \otimes \boldsymbol{e}_1 + F_{22}\boldsymbol{e}_2 \otimes \boldsymbol{e}_2 + F_{33}\boldsymbol{e}_3 \otimes \boldsymbol{e}_3 + F_{13}\boldsymbol{e}_1 \otimes \boldsymbol{e}_3 \tag{7-1}$$

can be applied to the unit cell. In other words, the unit cell is subject to normal loading along all its boundaries and shear loading in the $\boldsymbol{e}_1$-$\boldsymbol{e}_3$-plane. Denoting the average normal displacement along a boundary of normal $\pm\boldsymbol{e}_i$ as $\pm U_i$, and the average tangential displacements along the direction $\pm\boldsymbol{e_1}$ on the boundaries of normal the surfaces of normal $\pm\boldsymbol{e_3}$ as $\pm U_T$, the macroscopic deformation gradient reads

$$\boldsymbol{F} = \begin{bmatrix} 1 + \dfrac{2U_1}{L} & 0 & \dfrac{U_T}{L} \\ 0 & 1 + \dfrac{2U_2}{L} & 0 \\ 0 & 0 & 1 + \dfrac{U_3}{L} \end{bmatrix} \tag{7-2}$$

For the isotopic matrix material, the associated mechanical problem is symmetric with respect to the $(\boldsymbol{e}_1, \boldsymbol{e}_3)$ plane, and antisymmetric with respect to the $(\boldsymbol{e}_1, \boldsymbol{e}_2)$ plane. Thus, only one quarter of the cell ($-L/2 \leq X_1 \leq L/2$, $0 \leq X_2 \leq L/2$ and $0 \leq X_3 \leq L$) is considered (Fig. 7-1b) for finite element analysis. The geometry is discretized with eight-node solid elements with an edge length increasing from $0.01L$ to $0.1L$.

Symmetry conditions are imposed to the boundaries of the quarter model with the normal vectors $\pm\boldsymbol{e_2}$,

$$\begin{cases} u_2(X_1, 0, \mathrm{X_3}) = 0 \\ u_2(X_1, \mathrm{L}/2, \mathrm{X_3}) = U_2 \end{cases} \tag{7-3}$$

while anti-symmetry conditions (with respect to the $(\boldsymbol{e}_1, \boldsymbol{e}_2)$-plane) plane are imposed to the boundary of normal vector $-\boldsymbol{e}_3$,

$$\begin{cases} u_1(X_1, X_2, 0) + u_1(-X_1, X_2, 0) = 0 \\ u_2(X_1, X_2, 0) - u_2(-X_1, X_2, 0) = 0 \\ u_3(X_1, X_2, 0) + u_3(-X_1, X_2, 0) = 0 \end{cases} \tag{7-4}$$

Both tangential and normal displacements are applied to the boundary of normal vector $+\boldsymbol{e}_3$, i.e.

$$\begin{cases} u_1(X_1, X_2, L) + u_1(-X_1, X_2, L) = 2U_T \\ u_2(X_1, X_2, L) - u_2(-X_1, X_2, L) = 0 \\ u_3(X_1, X_2, L) + u_3(-X_1, X_2, L) = 2U_3 \end{cases} \tag{7-5}$$

The periodicity conditions for the boundaries of normal vectors $\pm\boldsymbol{e}_1$ read

$$\begin{cases} u_1(L/2, X_2, X_3) - u_1(-L/2, X_2, X_3) = 2U_1 \\ u_2(L/2, X_2, X_3) - u_2(-L/2, X_2, X_3) = 0 \\ u_3(L/2, X_2, X_3) - u_3(-L/2, X_2, X_3) = 0 \end{cases} \tag{7-6}$$

Note that the periodicity boundary conditions impose a strong kinematic restriction on the possible formation of a planar band of localized plastic deformation. It can only take the vector $\boldsymbol{e}_3$ as normal vector in order to be kinematically admissible.

7.2.2 Macroscopic rate of deformation tensor

According to the above boundary conditions, the four displacement degrees of freedom,

$$\boldsymbol{u}[t] = \{U_1, U_2, U_3, U_T\}^T \tag{7-7}$$

control the average deformation gradient in the unit cell. Introducing the current velocity vector $\dot{\boldsymbol{u}}[t]$, the macroscopic rate of deformation tensor can be calculated,

$$\begin{aligned}\boldsymbol{D} = \mathrm{sym}\left(\dot{\boldsymbol{F}}\boldsymbol{F}^{-1}\right) &= \frac{2\dot{U}_1}{L+2U_1}\boldsymbol{e}_1\otimes\boldsymbol{e}_1 + \frac{2\dot{U}_2}{L+2U_2}\boldsymbol{e}_2\otimes\boldsymbol{e}_2 \\ &+ \frac{\dot{U}_3}{L+U_3}\boldsymbol{e}_3\otimes\boldsymbol{e}_3 \\ &+ \frac{1}{2(L+U_3)}\left(\dot{U}_t - 2\dot{U}_1\frac{U_t}{L+2U_1}\right)(\boldsymbol{e}_1\otimes\boldsymbol{e}_3 + \boldsymbol{e}_3\otimes\boldsymbol{e}_1)\end{aligned} \tag{7-8}$$

The corresponding velocity gradient features only four non-zero components which are summarized in a rate of deformation vector

$$\boldsymbol{d} = \{D_{11}, D_{22}, D_{33}, 2D_{13}\}^T \tag{7-9}$$

And expressed as a linear function of the current macroscopic velocities,

$$\boldsymbol{d} = \boldsymbol{Q}[t]\dot{\boldsymbol{u}} \tag{7-10}$$

with the time-dependent linear transformation

$$\boldsymbol{Q}[t] = \begin{bmatrix} \frac{2}{L+2U_1} & 0 & 0 & 0 \\ 0 & \frac{2}{L+2U_2} & 0 & 0 \\ 0 & 0 & \frac{1}{L+U_3} & 0 \\ \frac{-1}{L+U_3}\frac{2U_t}{L+2U_1} & 0 & 0 & \frac{1}{L+U_3} \end{bmatrix} \tag{7-11}$$

7.2.3 Control of the macroscopic stress state

The macroscopic stress tensor $\boldsymbol{\Sigma}[t]$ is defined as the spatial average of the current local Cauchy stress field $\boldsymbol{\sigma}[\boldsymbol{x}, t]$,

$$\boldsymbol{\Sigma} = \frac{1}{V}\int_V \boldsymbol{\sigma}[\boldsymbol{x}, t]dV \tag{7-12}$$

with $V[t]$ denoting the current macroscopic volume of the unit cell. $\boldsymbol{\Sigma}$ is fully characterized by its principal stresses $\Sigma_I \geq \Sigma_{II} \geq \Sigma_{III}$ and principal stress directions $\boldsymbol{p_I}$, $\boldsymbol{p_{II}}$ and $\boldsymbol{p_{III}}$. In this study we focus on biaxial tension under plane stress condition only

$$0 \leq \frac{\Sigma_{II}}{\Sigma_I} \leq 1 \quad \text{and} \quad \Sigma_{III} = 0 \tag{7-13}$$

However, without actually explicitly calculating the macroscopic stress tensor, the stress ratio $\psi = \Sigma_{II}/\Sigma_I$ will be kept constant and the plane stress condition maintained throughout the simulations through a time-dependent kinematic constraint on the applied macroscopic velocities $\dot{\boldsymbol{u}}$.

Consider first the rate of mechanical work for the unit cell at time t. It may be written as

$$\dot{W} = \boldsymbol{p} \cdot \dot{\boldsymbol{u}} = V\, \boldsymbol{\Sigma} : \boldsymbol{D} = V\, \boldsymbol{\sigma} \cdot \boldsymbol{d} \tag{7-14}$$

In (7-14), $\boldsymbol{p}$ denotes the vector of the work conjugate forces to the macroscopic translational degrees of freedom, while the vector $\boldsymbol{\sigma}$ is work conjugate to $\boldsymbol{d}$. It summarizes four of the six independent components of the symmetric macroscopic Cauchy stress tensor,

$$\boldsymbol{\sigma} = \{\Sigma_{11}, \Sigma_{22}, \Sigma_{33}, \Sigma_{13}\}^T \tag{7-15}$$

It is assumed that the shear components Σ_{12} and Σ_{23} (which may become non-zero due to the deformation induced anisotropy at the mesoscale) remain always small as compared to the other stress components and are thus neglected thereafter. In addition the normal $\boldsymbol{e_3}$ to the plane of possible localization is expected to be orthogonal to the second principal stress direction $\boldsymbol{p_{II}}$ (Rudnicki and Rice, 1975, [153]). Therefore we

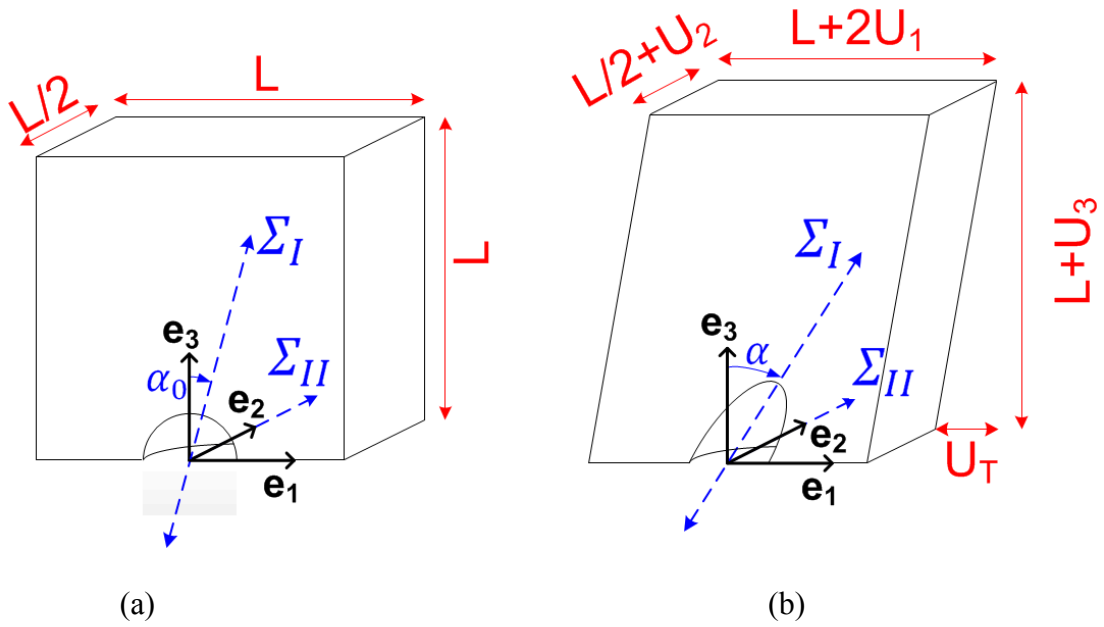

(a) (b)

Figure 7-2: Unit cell model in its (a) initial and (b) deformed configuration. Imposed displacements are shown in red while the applied macroscopic stress is represented in blue.

also assume that $\boldsymbol{p_{II}} = \boldsymbol{e_2}$ and $\Sigma_{22} = \Sigma_{II}$. Defining α the angle between the first principal stress direction $\boldsymbol{p_I}$ and the normal $\boldsymbol{e_3}$ to the plane of localization (Fig. 7-2), the stress vector may be written as

$$\boldsymbol{\sigma} = \Sigma_I \{\sin^2\alpha \quad \psi \quad \cos^2\alpha \quad \sin\alpha\cos\alpha\}^T \tag{7-16}$$

or, alternatively,

$$\boldsymbol{\sigma} = \sigma[t]\boldsymbol{a}[\psi,\alpha] \tag{7-17}$$

where $\sigma[t] \geq 0$ is a monotonically increasing amplitude function, and the unit vector $\boldsymbol{a} \in \mathbb{R}^4$ represents the direction of the stress tensor in the stress space

$$\boldsymbol{a} = \frac{1}{\sqrt{1 + \dfrac{\psi^2 + \cos^2\alpha}{\sin^4\alpha}}} \left\{1 \quad \frac{\psi}{\sin^2\alpha} \quad \operatorname{cotan}^2\alpha \quad \operatorname{cotan}\alpha\right\}^T \tag{7-18}$$

Note that $\boldsymbol{a}$ is not constant as α will evolve during cell loading.

Instead of specifying four non-homogeneous boundary conditions on the components of $\boldsymbol{p}$, a new set of translational degrees of freedom $\dot{\tilde{\boldsymbol{u}}}$ is created through the linear transformation of $\dot{\boldsymbol{u}}$,

$$\dot{\tilde{\boldsymbol{u}}} = \boldsymbol{A}[t]\dot{\boldsymbol{u}} \tag{7-19}$$

where the transformation $\boldsymbol{A}[t]$ is chosen such that Eq. (7-12) is satisfied by specifying homogeneous conditions on all but one component of the work-conjugate force vector

$$\tilde{\boldsymbol{p}} = \boldsymbol{A}^{-T}[t]\boldsymbol{p} = \tilde{p}(t)\boldsymbol{e_i} \tag{7-20}$$

with $\boldsymbol{e_i}$ denoting one of the four orthogonal basis vectors of $\mathbb{R}^4$. Rewriting the rate of work, we have

$$\dot{W} = \tilde{\boldsymbol{p}} \cdot \dot{\tilde{\boldsymbol{u}}} = V\,\boldsymbol{\sigma} \cdot \boldsymbol{Q}\dot{\boldsymbol{u}} = V(\boldsymbol{Q}\boldsymbol{A}^{-1})^T\boldsymbol{\sigma} \cdot \dot{\tilde{\boldsymbol{u}}} \tag{7-21}$$

In the weak formulation of the unit cell problem, Eq. (7-16) must be fulfilled for any $\dot{\tilde{\boldsymbol{u}}}$ and hence

$$\tilde{\boldsymbol{p}} = V(\boldsymbol{Q}\boldsymbol{A}^{-1})^T\boldsymbol{\sigma} \tag{7-22}$$

Satisfaction of the boundary condition $\tilde{\boldsymbol{p}} = \tilde{p}[t]\boldsymbol{e_i}$ implies $\boldsymbol{\sigma} = \sigma[t]\boldsymbol{a}$ if the transformation matrix $\boldsymbol{A}$ satisfies the identity

$$V\sigma[t](\boldsymbol{Q}\boldsymbol{A}^{-1})^T\boldsymbol{a} = \tilde{p}[t]\boldsymbol{e_i} \tag{7-23}$$

Among all invertible transformation matrices that satisfy (7-18), we chose $\boldsymbol{A}[t]$ such that $\boldsymbol{Q}\boldsymbol{A}^{-1}$ becomes a rotation matrix,

$$\boldsymbol{Q}\boldsymbol{A}^{-1} = \boldsymbol{a}\otimes\boldsymbol{e_1} + \boldsymbol{b}\otimes\boldsymbol{e_2} + \boldsymbol{c}\otimes\boldsymbol{e_3} + \boldsymbol{d}\otimes\boldsymbol{e_4} \tag{7-24}$$

with the unit vectors $\boldsymbol{b}$, $\boldsymbol{c}$ and $\boldsymbol{d}$ being orthogonal to $\boldsymbol{a}$. Note that we also randomly chose the first component of $\tilde{\boldsymbol{p}}$ as the only non-zero force component, while a zero force boundary condition is imposed on the remaining three degrees of freedom. It is emphasized that the matrix $\boldsymbol{A}$ is a function of time due to the time dependency of $\boldsymbol{Q}$ and $\boldsymbol{a}$.

By updating the coordinate transformation at each time step, we maintain the stress-state constant. Furthermore (and probably more importantly), the simulations can be performed under displacement control for the first degree of freedom. Instead of prescribing the time history of the first component of $\tilde{\boldsymbol{p}}$, the work-conjugate velocity (first component of $\dot{\tilde{\boldsymbol{u}}}$) is applied. This change to displacement control is necessary to compute the unit cell response beyond "peak load".

7.2.4 Stress orientation evolution

As already discussed, the unit cell model presents a topological anisotropy in its undeformed configuration. Moreover a morphological anisotropy is introduced during loading as the defect geometry evolves through both stretching and rotation (if $U_T \neq 0$). During deformation, the rotation $\boldsymbol{R}$ of the material is defined through the decomposition of the deformation gradient

$$\boldsymbol{F} = \boldsymbol{V}\boldsymbol{R} \tag{7-25}$$

with $\boldsymbol{V} = \boldsymbol{V}^T$ denoting the left stretch tensor. Due to the two sources of anisotropy, calculation results may depend on the material rotation.

In this work, it is chosen to focus on co-rotational loadings only: the evolution of the principal stress directions are coupled with the rotation of the material, as illustrated in Fig. 7-2. After expressing $\boldsymbol{R}$ as a rotation of angle $\alpha - \alpha_0$ about the $\boldsymbol{e_2}$ axis and decomposing the deformation gradient according to Eq. 7-25, the evolution of the principal stress directions reads

$$\tan(\alpha - \alpha_0) = \frac{F_{13}}{F_{11} + F_{33}} \tag{7-26}$$

The reader is referred to Dunand and Mohr (2013) for more details on implications of this choice of co-rotational loadings on the localization analysis results.

7.2.5 Computation of the onset of localization for a given stress state

Once the onset of localization is reached, all plastic deformation is expected to accumulate close to the plane of localization $(\boldsymbol{e_1}, \boldsymbol{e_2})$ while partial elastic unloading should take place away from it. Let $\boldsymbol{F_U}$ be the volume average of the deformation gradient of the upper quarter of the unit cell delimited by $L/2 \leq X_3 \leq L$, in which the deformation is close to homogeneous, and M the material point located at $\boldsymbol{X_M} = \{L/2\,, L/2\,, L/2\}^T$ (Fig. 7-1b). $\boldsymbol{F_U}$ can then be approximated as

$$\boldsymbol{F_U} \simeq \begin{bmatrix} F_{11} & 0 & \dfrac{U_t - (u_1^M - U_1)}{L/2} \\ 0 & F_{22} & 0 \\ 0 & 0 & 1 + \dfrac{U_3 - u_3^M}{L/2} \end{bmatrix} \tag{7-27}$$

where u_1^M and u_3^M are the displacements of M in the $\boldsymbol{e_1}$ and $\boldsymbol{e_3}$ directions, respectively. Following Needleman and Tvergaard (1992, [132]), the localization of deformation into a narrow planar band is considered to occur when

$$\xi \equiv \frac{\|\dot{\boldsymbol{F}}\|}{\|\dot{\boldsymbol{F}}_{\boldsymbol{U}}\|} \gg 1 \tag{7-28}$$

where the tensorial norm $\|\cdot\|$ is defined as $\|\boldsymbol{X}\| = \sqrt{\boldsymbol{X}:\boldsymbol{X}}$. We consider that the onset of localization is reached when $\xi > 5$. Note that the localization criterion defined by Eq. 7-28 is exclusively geometric. In practice the localization indicator ξ is evaluated at the end of each time increment and simulations are automatically stopped when the critical value $\xi = 5$ is attained.

The total energy φ dissipated in the cell is obtained from the calculation. Since plastic deformation is the only dissipative mechanism modeled in the simulation, we introduce a measure of the macroscopic equivalent plastic strain ε^p of the cell based on the hardening behavior of the matrix material (Eq. 5-6) and defined implicitly as

$$\varphi(\varepsilon^p) = V_0 \int_0^{\varepsilon^p} Y(\varepsilon)\, d\varepsilon \tag{7-29}$$

where V_0 is the initial volume of the cell. The total dissipation and strain at the onset of localization (i.e. when $\xi = 5$) are denoted φ_L and ε_L, respectively. Similarly, the stress orientation at the onset of localization is denoted α_L. Note that α_L represents the angle between the first principal stress direction and the normal to the band of localization of the plastic deformation.

It is emphasized that the unit cell model has only two parameters: the biaxial stress ratio ψ and the initial stress orientation α_0. Calculations are run with different stress ratios in the range $0 \leq \psi \leq 1$, $\psi = 0$ corresponding to uniaxial tension and $\psi = 1$ to equibiaxial tension. Note that the initial stress orientation α_0^* leading to the most favorable localization is not known a-priori. It is found by minimizing the dissipation at failure:

$$\alpha_0^* = \arg\min_{\alpha_0} D_L \tag{7-30}$$

7.3 Simulation results

All the calculations presented in Section 7.3 have been performed with a rate-independent Levy-von Mises matrix material. Strain hardening of the matrix is described by a saturation law (Eq. 5-6). Strain hardening parameters given in Table 5-1 are used. This choice of a simplified plasticity model is driven by a need to reduce the computation time associated with a unit cell calculation. The influence of strain rate is therefore not addressed here, but will be discussed in Section 7.4.

7.3.1 Onset of localization

Figure 7-3 illustrates the evolution of the unit cell geometry at different stages of deformation for a biaxial stress ratio of $= 0.5$: before the onset of localization ($\xi < 5$,

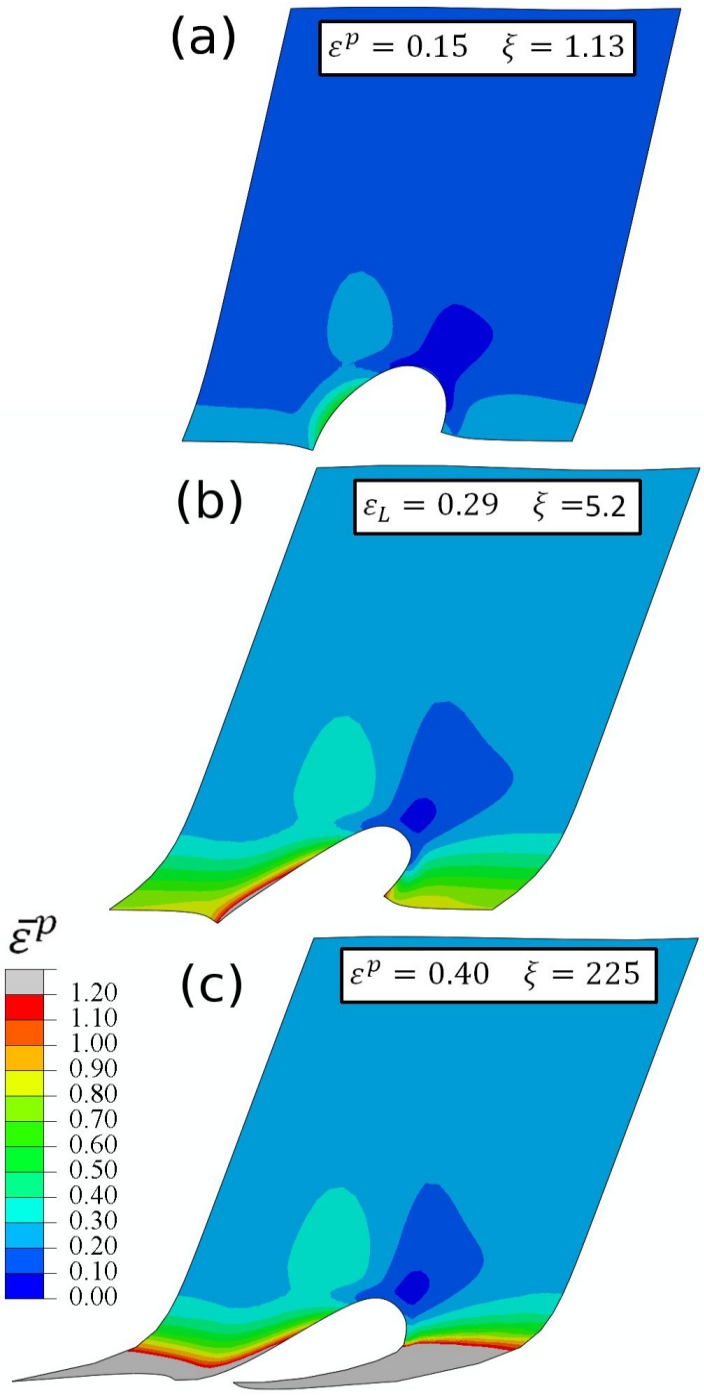

Figure 7-3: Contour plot of equivalent plastic strain in the $(\boldsymbol{e_1}, \boldsymbol{e_3})$ plane (a) before localization (macroscopic equivalent strain of $\varepsilon^p = 0.15$), (b) at the onset of localization ($\varepsilon^p = 0.29$) and (c) beyond localization ($\varepsilon^p = 0.4$) for a biaxial stress ratio of $\psi = 0.5$.

Fig. 7-3a), at the onset of localization ($\xi \simeq 5$, Fig. 7-3b) and after the onset of localization ($\xi \gg 5$, Fig. 7-3c). Contour plots of equivalent plastic strain are shown in the $(\boldsymbol{e_1}, \boldsymbol{e_3})$ plane. The corresponding macroscopic stress-strain curve and evolution of localization indicator ξ are depicted in red in Fig. 7-4a and Fig. 7-4b, respectively. Before localization, the deformation is approximately homogeneous in the cell, with small strain concentrations in the vicinity of the cavity. A localization of the plastic deformation is clearly visible in Fig. 7-3b, resulting in a pronounced shearing of the central section of the cell. However the deformation stays approximately homogenous in the upper and lower parts of the unit cell, thereby validating the hypothesis made in Section 7.2.5. In particular the cell edges remain straight outside the band of localization.

The localization indicator ξ (red line in Fig. 7-4b) increases slowly in the first stages of the deformation, followed by a sudden and dramatic increase occurring about a macroscopic strain of $\varepsilon^p = 0.29$. This divergence of ξ defines the onset of localization according to Eq. 7-28. Note that the onset of localization also corresponds to a maximum of the load carrying capacity of the unit cell (red solid dot in Fig. 7-4a). The subsequent loss of load carrying capacity is associated with partial elastic unloading of the unit cell matrix. As a result, no plastic deformation occurs in the upper part of the unit cell (i.e. outside the band of localization) beyond the onset of localization, as shown in Figs. 7-3b and 7-3c. Instead, the macroscopic deformation imposed to the cell results in increasing shearing of its central section, all the additional plastic strain accumulating in the ligaments surrounding the cavity.

In the first stages of deformation (Figs. 7-3a and 7-3b) the initially spherical cavity elongates and progressively rotates about the $\boldsymbol{e_2}$ direction. Beyond the onset of localization, however, the cavity collapses because of the intense shearing occurring in the $(\boldsymbol{e_1}, \boldsymbol{e_2})$ plane (Fig. 7-3c). As a result, the defect volume fraction (depicted with a black solid line in Fig. 7-7b) first increases until the onset of localization is reached (solid dot in Fig. 7-7b), and then decreases in the last stages of the cell deformation.

It is emphasized that the accuracy of the present numerical simulations in the post-localization range is questionable. Extremely high strains are reached beyond the

onset of localization, resulting in highly distorted elements in the ligaments around the cavity. To cope with this numerical issue, re-meshing of the unit cell during the

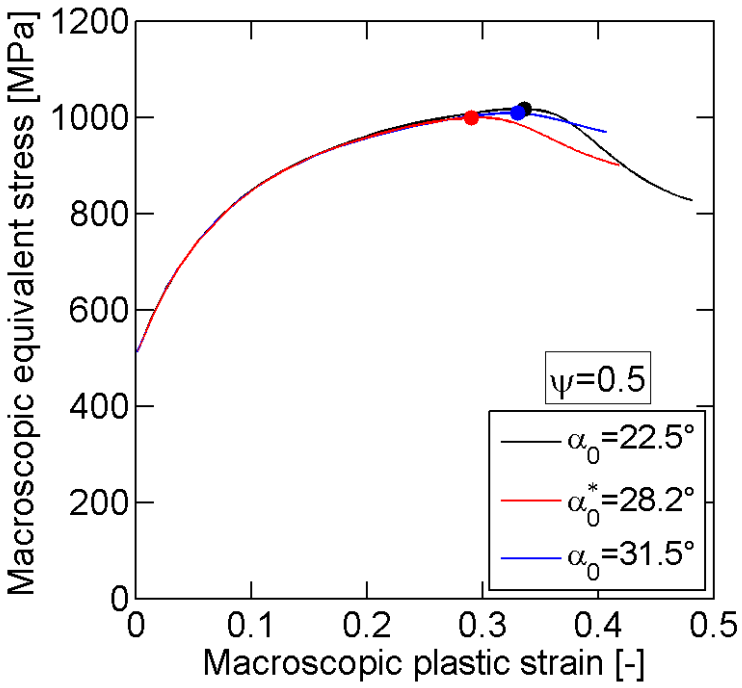

(a)

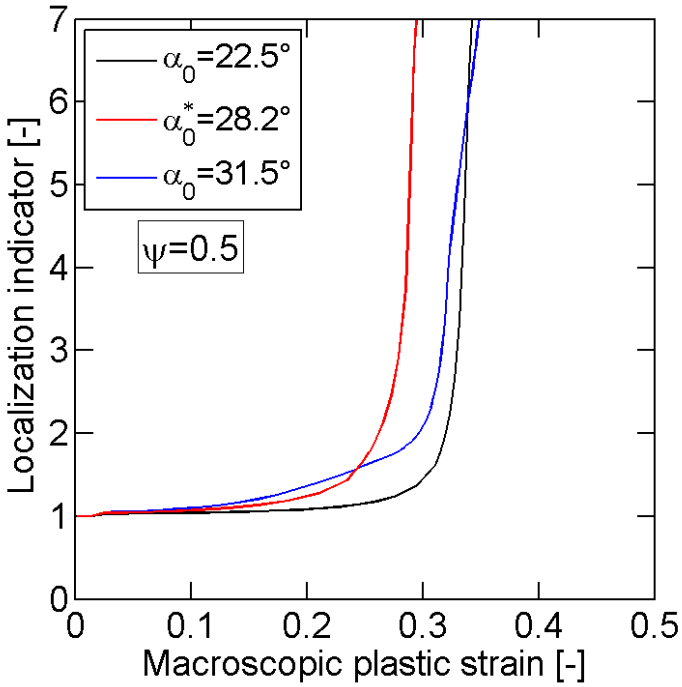

(b)

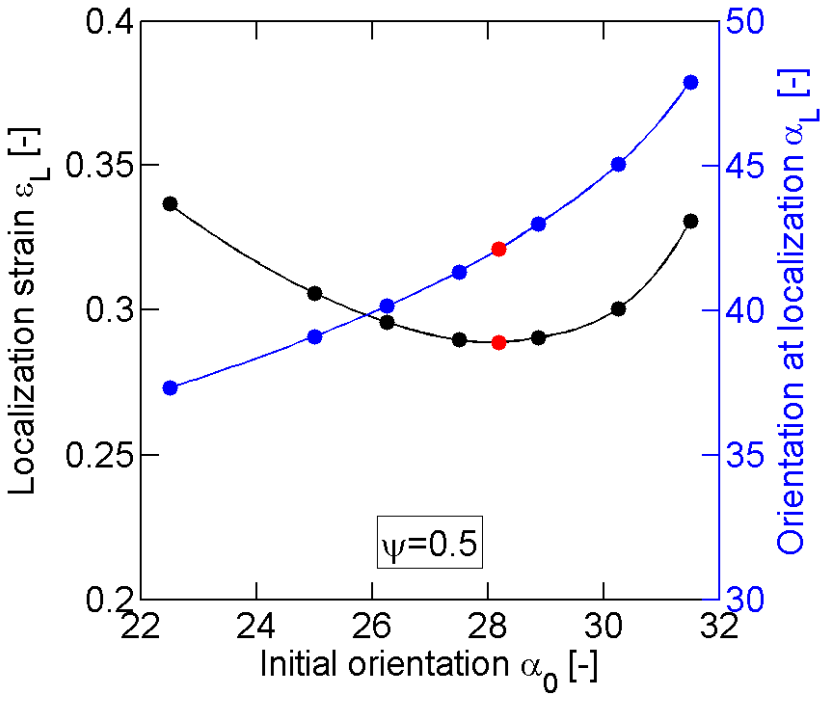

(c)

Figure 7-4: Influence of initial stress orientation on the onset of localization for $\psi = 0.5$. (a) Macroscopic stress-strain curves, (b) evolution of the localization indicator ξ and (c) predicted macroscopic strains ε_L and stress orientations α_L at the onset of localization for different initial stress orientations α_0. Solid dots in (a) mark the onset of localization, while each dot in (c) corresponds to a unit cell calculation.

calculation could be used to limit element distortion (e.g. Tvergaard, 2012, [180]). Moreover a proper constitutive modeling of the matrix material behavior at such high strains is still an open question. However the scope of the present work is limited to characterizing the onset of localization, in which case the aforementioned issues are not relevant.

7.3.2 Effect of anisotropy

The influence of the structural anisotropy of the unit cell model on the onset of localization is illustrated in Fig. 7-4. A series of calculations are run with the same loading state (biaxial stress ratio of $\psi = 0.5$) but with different orientations of the first

principal stress: $\alpha_0 = 22.5°$ (in black in Fig. 7-4), $\alpha_0 = 28.2°$ (in red in Fig. 7-4) and $\alpha_0 = 31.5°$ (in blue in Fig. 7-4). The macroscopic stress-strain curves (Fig. 7-4a) are identical prior to the onset of localization (marked with solid dots): the macroscopic behavior of the unit cell does not exhibit significant anisotropy. The evolution of the localization indicator ξ with respect to the macroscopic equivalent strain ε^p is shown in Fig. 7-4b for the three initial stress orientations. It shows a clear dependence to α_0. As a result, the instant of the onset of localization also depends on α_0. The model anisotropy therefore induces anisotropy in the onset of plastic flow localization.

The macroscopic strain ε_L at which localization occurs in the case $\alpha_0 = 28.2°$ is smaller by about 15% than when $\alpha_0 = 22.5°$ and $\alpha_0 = 31.5°$. Figure 7-4c depicts the dependence of ε_L to α_0 in the range $22.5° \leq \alpha_0 \leq 31.5°$. Each dot in Fig. 7-4c corresponds to a cell calculation. A minimum is reached for $\alpha_0^* = 28.2°$ (red dot in Fig. 7-4c), which therefore corresponds to the initial stress orientation most favorable to localization, as defined by Eq. 7-30. The localization strain ε_L will only refer to this minimum thereafter. In practice, Eq. 7-30 is minimized with an relative tolerance of 3% on α_0^*, resulting in an inaccuracy of less than 0.5% on ε_L.

At the same time, the stress orientation at the onset of localization α_L (in blue in Fig. 7-4c) also depends on ξ. Note that α_L represents the angle between the normal to the plane of plastic localization and the first principal direction of the macroscopic stress. α_L monotonically increases with respect to α_0. A direct consequence is that the inaccuracy affecting α_L for the optimal initial orientation α_0 is about 2°.

Recall that to account for this anisotropy, the orientation of the applied macroscopic principal stresses are constantly updated such that they coincide with the major axes of the ellipsoidal approximation of the shape of the deforming defect, as explained in Section 7.2.4. Figure 7-5 depicts the evolution of the cavity shape in the $(\boldsymbol{e_1}, \boldsymbol{e_3})$ plane (solid lines in Fig. 7-5) along with the orientation of the first principal macroscopic stress (dashed lines in Fig. 7-5). Results presented in Fig. 7-5 correspond to uniaxial tension ($\psi = 0$) with an initial stress orientation of $\alpha_0 = 3°$. The initially spherical cavity (in black in Fig. 7-5) deforms into ellipsoidal shape and increasingly elongates as the cell is deformed. In addition the cavity also rotates as an increasing transverse displacement U_T is imposed. At the same time, the stress orientation α

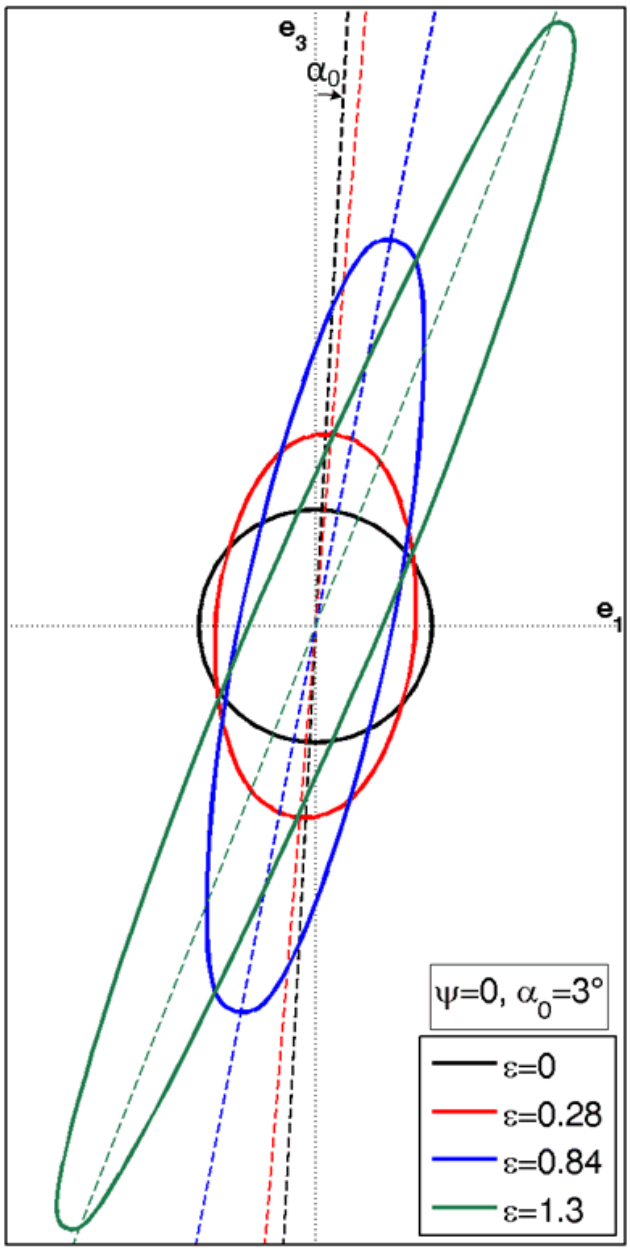

Figure 7-5: Cavity shape evolution during deformation under uniaxial tension $(\psi = 0)$. Solid lines represent the cavity contour in the $(\boldsymbol{e_1}, \boldsymbol{e_3})$ plane for increasing amounts of deformation. Dashed lines indicate the orientation of the first principal macroscopic stress applied to the unit cell.

evolves according to Eq. 7-26. Note that first principal stress directions (dashed lines in Fig. 7-5) remain almost parallel to the major axis of the cavity throughout loading, up to macroscopic strains of $\varepsilon^p = 1.3$ (in green in Fig. 7-5).

7.3.3 Influence of the biaxial stress ratio on localization

A series of calculations are performed for biaxial stress ratios in the range $0 \leq \psi \leq 1$. For each stress ratio, the optimal initial stress orientation α_O^* is found by minimizing Eq. 7-30, thereby defining a macroscopic localization strain ε_L and a stress orientation at localization α_L. Recall that calculations are performed under proportional stress state: the biaxial stress ratio ψ is kept constant during loading.

Results are presented in Fig. 7-6. Solid dots correspond to stress states for which ε_L and α_L were calculated according to the procedure described above, while solid lines in Fig. 7-6a correspond to a spline cubic interpolation of the data points. Figure 7-6a represents the dependence of the localization strain ε_L to the biaxial stress ratio ψ. Figure 7-6b depicts the dependence of the stress orientation at localization α_L to ψ. The uncertainty associated with the determination of α_L is shown with error bars.

The localization strain ε_L exhibits a strong and non-monotonic dependence to the biaxial stress ratio ψ. It features a minimum for stress states around $\psi = 0.5$ and increases when moving towards axisymmetric stress states ($\psi = 0$ and 1), thereby confirming the existence of a plane strain valley in the macroscopic strain at failure when a shear localization of the plastic deformation is taken as the dominant failure mechanism. The macroscopic strain at the onset of localization is about three times higher for equibiaxial tension ($\psi = 1$) than for transverse plane strain tension ($\psi = 0.5$). Note that the localization strain diverges close to uniaxial tension. In our calculation no localization occurred for biaxial stress ratios $\psi < 0.05$.

The stress orientation at localization α_L, i.e. the inclination of the normal to the band of plastic localization with respect to the first principal stress direction, also depends on the biaxial stress ratio. It exhibits a minimum close to transverse plane strain tension ($\alpha_L \approx 42°$ for $\psi = 0.5$) and increases when moving towards equibiaxial tension ($\alpha_L \approx 45°$ for $\psi = 1$) and uniaxial tension($\alpha_L \approx 50°$ for $\psi = 0.07$). In the case

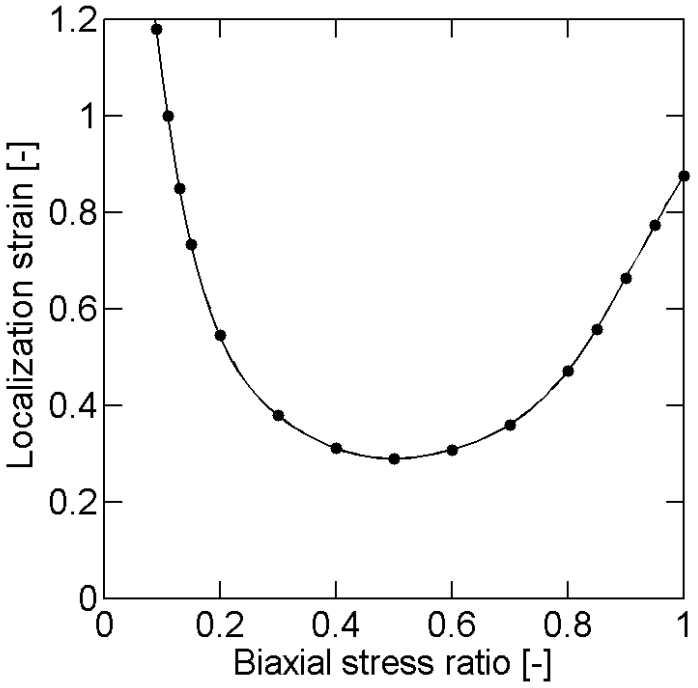

(a)

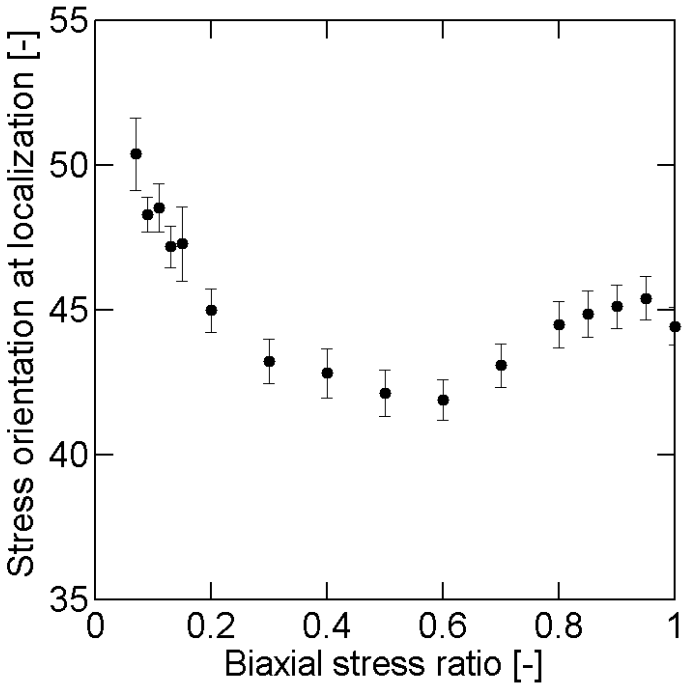

(b)

Figure 7-6: Dependence of (a) the macroscopic strain ε_L and (b) the stress orientation α_L at the onset of localization to the biaxial stress ratio ψ. Dots correspond to unit cell calculations.

of the experiments presented in Section 6.2, α_L would correspond to the angle between the fracture surface and the sheet thickness direction, as shown in Fig. 6-7. The predictions of the unit cell model correlate well to the surface orientations measured on post-mortem specimens for the three different specimen geometries.

7.3.4 Influence of the defect volume fraction

All calculation results discussed above were obtained with a unit cell featuring a cavity with an initial relative dimension of $R/L = 0.15$, resulting in an initial defect volume fraction of 0.72%. However the initial defect volume fraction is expected to influence significantly simulation results and more specifically the instant at which localization occurs.

The dependence of unit cell calculation results to the initial defect volume fraction is illustrated in Fig. 7-7. Simulations are performed under a biaxial stress ratio of $\psi = 0.5$ with three different cavity sizes: $R/L = 0.1$ (in red in Fig. 7-7), $R/L = 0.15$ (in black in Fig. 7-7) and $R/L = 0.2$ (in blue in Fig. 7-7). The corresponding initial defect volume fractions are 0.21%, 0.72% and 1.71%, respectively. Note that results depicted in Fig. 7-7 are obtained with the respective optimal initial stress orientation α_0^* in the three cases. Macroscopic stress strain curves are shown in Fig. 7-7a while Fig. 7-7b depicts the evolution of the defect volume fraction. The onsets of localization are marked with solid dots.

The initial defect volume fraction has a strong influence on the localization strain ε_L, which is 60% larger for a small cavity ($\varepsilon_L = 0.46$, in red in Fig. 7-7) than for a medium cavity ($\varepsilon_L = 0.29$, in black in Fig. 7-7) and 30% smaller for a large cavity ($\varepsilon_L = 0.20$, in red in Fig. 7-7). The macroscopic equivalent stress-strain curves are also affected by the initial defect volume fraction. A larger cavity tends to reduce the cell load carrying capacity, as shown in Fig. 7-7a. Note the dependence of the load carrying capacity to the cavity size is more pronounced at large macroscopic strains. At a macroscopic strain of 0.2, the macroscopic equivalent stress is 6% lower with a large cavity than with a small one, and 1.5% lower with a medium cavity than with a small one.

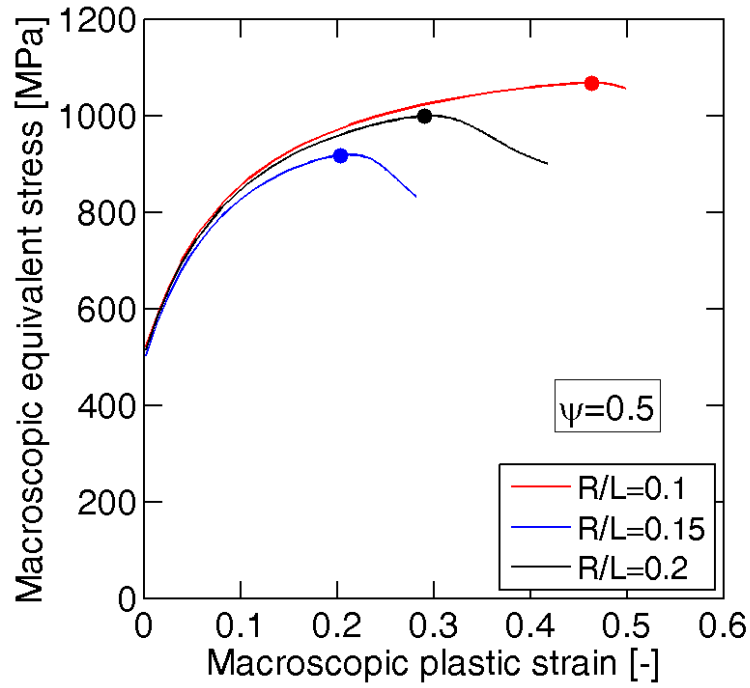

(a)

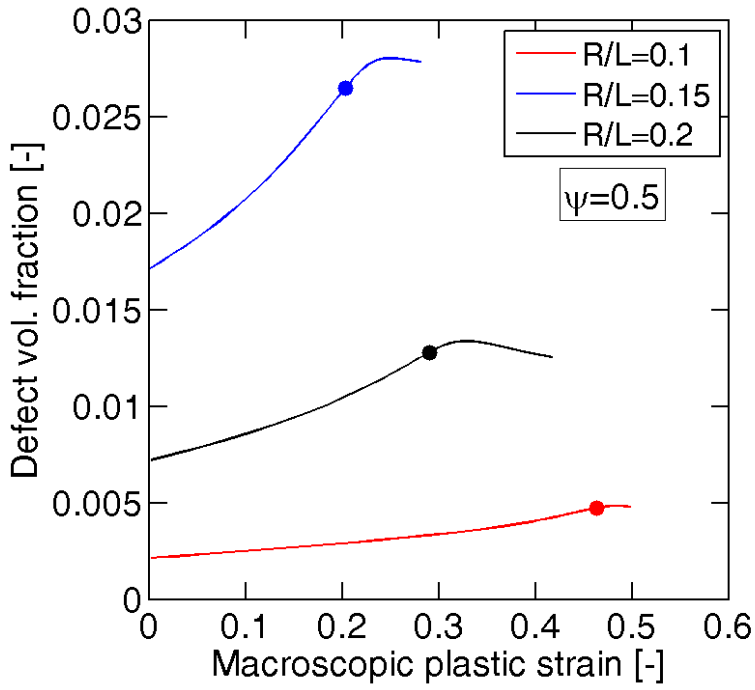

(b)

Figure 7-7: Influence of the initial defect volume fraction on (a) macroscopic stress-strain curves and (b) the evolution of the defect volume fraction for a biaxial stress ratio of $\psi = 0.5$. Red curves correspond to an initial defect volume fraction of 0.21%, black curves of 0.71% and blue curves to 1.68%. Solid dots indicate the onset of localization.

Table 7-1: Material parameters used for rate-dependent cell calculations

Strain hardening parameters				
s_0 [MPa]	s_∞ [MPa]	H_0 [MPa]	r [-]	
400	1,000	18,000	2.0	
Strain rate sensitivity parameters				
$\dot{\varepsilon}_0$ [s^{-1}]	ΔF [J]	p [-]	q [-]	χ [-]
1.7×10^{6}	3×10^{-19}	0.14	1.1	0.7

The volume of the small cavity (in red in Fig. 7-7b) is increased by 122% at the onset of localization, while for the large cavity (in blue in Fig. 7-7b) the increase is 54% only. It should be mentioned that the growth rate of the defect volume fraction normalized by the initial defect volume fraction is more or less identical in the three configurations considered here. A larger relative cavity growth is therefore mostly due to the higher failure strain of cells with small cavities. The defect volume fraction decreases after the onset of localization is reached in all three cases, as the cavity collapses due to the intense shearing affecting the central section of the unit cell.

7.4 Rate-dependent localization analysis

The localization analysis model developed in Section 7.2 is used to evaluate the effect of strain rate on the onset of localization. For that purpose the behavior of the unit cell matrix material is modeled with the rate- and temperature-dependent constitutive equations presented in Section 4.4. Material parameters are given in Table 7-1. Due to the very high computational efforts required to reach the onset of localization when the rate-dependent plasticity model is used, only one stress state is considered thereafter, characterized by a biaxial stress ratio $\psi = 0.5$.

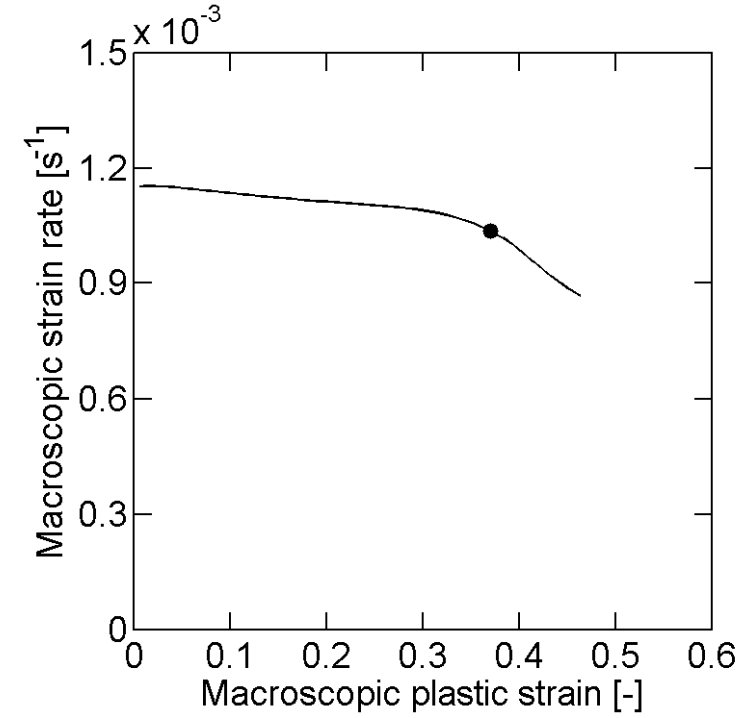

(a)

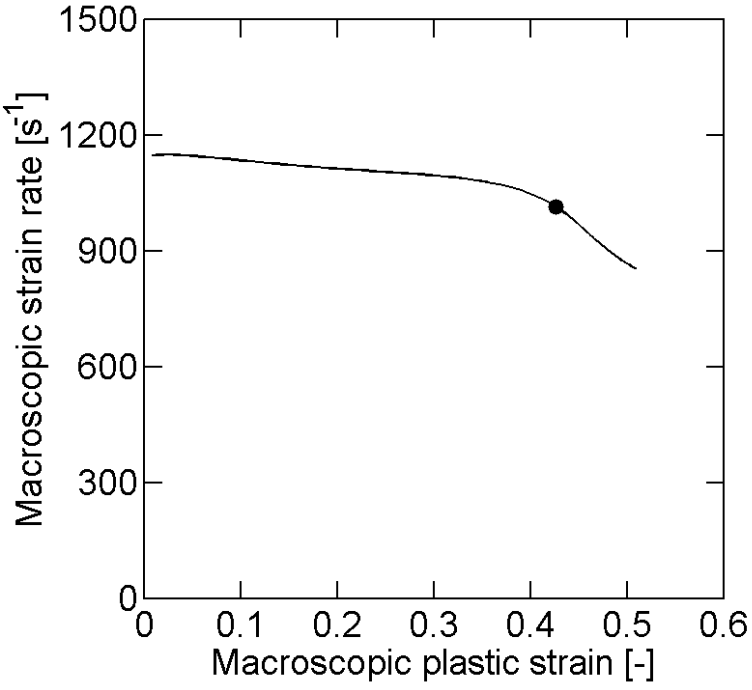

(b)

Figure 7-8: Evolution of the macroscopic equivalent strain rate in rate dependent cell calculations. (a) Isothermal loading at low strain rate and (b) adiabatic loading at high strain rate for a biaxial stress ratio of $\psi = 0.5$. Solid dots indicate the onset of localization.

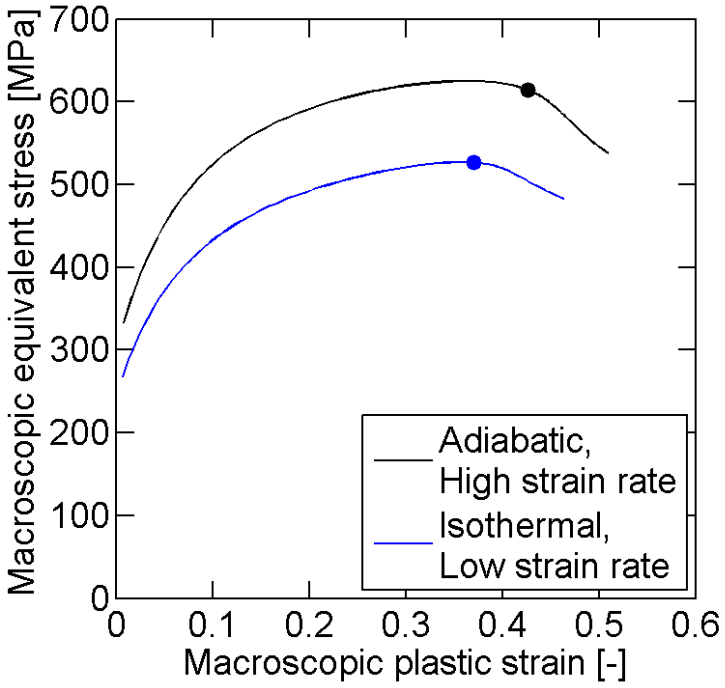

(a)

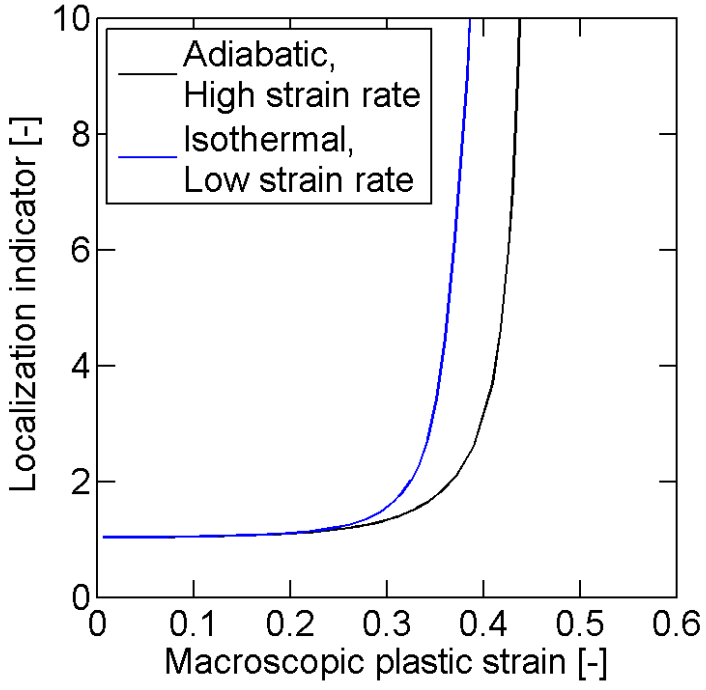

(b)

Figure 7-9: Influence of strain rate on localization for a biaxial stress ratio of $\psi = 0.5$. (a) Macroscopic stress-strain curves and (b) evolution of the localization indicator. Results from the low strain rate isothermal loading are in blue, and from the high strain rate adiabatic loading in black. Solid dots indicate the onset of localization.

Two loading conditions are considered: (1) isothermal loading at low strain rate and (2) adiabatic loading at high strain rate. The temperature increase under adiabatic loading is computed at each integration point according to Eq. 4-10. At very high strain rates, microscale inertia may influence void growth and ductile fracture (e.g. Jacques et al., 2012, [85]). However, a static approach is used here to solve the boundary value problem: inertia is not taken into account when solving the equilibrium equation in order to limit the computational cost.

The evolution of the macroscopic strain rate[11] is depicted in Fig. 7-8 for both loading conditions. The isothermal loading corresponds to a macroscopic strain rate of about $10^{-3}s^{-1}$ (Fig. 7-8a), while a strain rate of $10^{3}s^{-1}$ is reached in case of the adiabatic loading (Fig. 7-8b). Note that the macroscopic strain rate is approximately constant before the onset of localization (depicted with solid dots in Fig. 7-8). However it decreases significantly beyond the onset of localization, as most of the unit cell then experiences a partial elastic unloading.

Results for the two loading conditions are presented in Fig. 7-9. They correspond to the initial stress orientation α_0^* that minimizes the plastic dissipation at the onset of localization, as defined by Eq. 7-30. Figure 7-9a depicts the macroscopic stress-strain curves at low (blue curve in Fig. 7-9) and high strain rate (black curve in Fig. 7-9), while the evolution of the localization indicator is shown in Fig. 7-9b. The strain rate sensitivity of the matrix material has two major effects on the unit cell behavior. The load carrying capacity of the cell is higher by about 20% at high strain rate. In addition, the onset of localization is delayed at high strain rate. The localization strain is 17% higher at high strain rate ($\varepsilon_L = 0.42$) than at low strain rate ($\varepsilon_L = 0.36$). Note that at high strain rate, the onset of localization of the plastic flow does not correspond to the maximum of load carrying capacity of the unit cell. The maximum of macroscopic stress is reached at a macroscopic plastic strain of 0.37, while the onset of localization occurs at a strain of 0.42.

[11] Macroscopic strain, strain rate and stress are defined as the volume averages of the equivalent plastic strain, strain rate and stress, respectively (Eq. 7-7).

7.5 Conclusion

A numerical model based on a cubic unit cell containing a spherical cavity is developed to evaluate the effect of stress state and strain rate on the onset of localization of plastic deformation into a shear band. The investigation is limited to proportional biaxial macroscopic stress states. Fully periodic boundary conditions are applied to the cell, and a kinematic constraint is implemented to control the macroscopic stress state while deforming the cell under imposed displacements. In addition the macroscopic principal stress directions are constantly updated during loading in order to match the rotation of the cavity. The onset of localization is characterized by a geometric criterion that compares the deformation gradient rates inside and outside the band of localization. The most favorable orientation of the band of localization with respect to the principal stress directions is found by minimizing the total plastic dissipation at failure.

A first series of calculations is performed assuming a rate-independent Levy-von Mises matrix material in order to evaluate the effect of macroscopic stress state on localization. Plane stress conditions ranging from uniaxial to equi-biaxial tension are considered. The localization analysis confirms the existence of a plane strain valley of ductility: the strain to localization is lower for plane strain tension than for axisymmetric tension (uniaxial or equibiaxial). In addition, predictions of the inclination of the band of plastic localization with respect to the principal stress direction correspond to the orientation of the fracture surfaces on broken specimens. A second series of calculations is performed to evaluate the effect of strain rate on localization under plane strain tension. Both a low strain rate isothermal loading and a high strain rate adiabatic loading are considered. In close analogy to results from the hybrid experimental-numerical investigation presented in Chapter 4, the localization analysis predicts a higher failure strain at high strain rate.

The good agreement between experimental observations and model predictions confirms that localization of the plastic deformation into a shear band is the leading mechanism responsible for fracture of the TRIP material.

Chapter 8
Conclusion

Contents

8.1 Summary of the contributions

A new experimental setup is developed for the high strain rate testing of sheet materials under tensile loading, based on a Split Hokinson Pressure Bars system. Numerical and experimental validations show that the proposed design permits an almost oscillation-free measure of the force applied to the specimen for strain rates up to 1,000 s^{-1}. Used in conjunction with a High Speed Video Imaging system and Digital Image Correlation, it allows for an accurate characterization of the material behavior at high strain rate, as well as a precise detection of the onset of ductile fracture.

A hybrid experimental-numerical method is proposed to characterize the effect of strain rate and stress state on the ductile fracture properties of sheet materials. It is successfully applied to TRIP780 steel sheets. An extensive experimental program is carried out, covering a wide range of stress states and strain rates. It involves different types of specimens and the simultaneous measurement of global displacements, applied forces and local surface strains. The comparison of specimen responses at different strain rates reveals of positive rate-sensitivity of the material behavior. In all experiments, in-plane and through-the-thickness localization of the plastic deformation

occurs prior to fracture. Therefore the loading history and material state at the onset of fracture cannot be derived from global or surface measurements. Instead, detailed Finite Element simulations of each experiment are carried out. Assuming that fracture initiates at the location where the equivalent plastic strain is the highest when experimentally measured fracture displacement is reached, loading histories to fracture are extracted from the numerical results. At low strain rate, it is shown that in the vicinity of biaxial tension, the equivalent plastic strain at fracture is minimum close to plane strain tension, while it increases when approaching the limiting cases of uniaxial tension and equi-biaxial tension. Furthermore a complex (and stress dependent) dependence of the ductility to strain rate is highlighted. Close to plane strain, ductility monotonically increases with strain rate while the fracture strain is lowest at intermediate strain rate close to uniaxial tension.

Special attention is paid to two components controlling the accuracy of the hybrid experimental-numerical method: (a) the constitutive model and (b) the spacial discretization used in Finite Element simulations. A rate-dependent plasticity model inspired from the MTS theory is proposed to account for the rate- and temperature-sensitivity of the material behavior, as well as plastic anisotropy observed at low strain rate. A calibration procedure based on an inverse optimization method is described. The predictive capabilities of the plasticity model are evaluated by comparing local and global experimental measurements to numerical predictions over all the range of strains, strain rates and stress states considered. A very good correlation is observed. In particular, the post-necking behavior of the material is well predicted.

The influence of geometric discretization on Finite element predictions of the onset of fracture is analyzed. It is shown that shell elements cannot predict the post-necking behavior of sheet materials, and thus cannot be used in view of accurate predictions of the onset of ductile fracture in sheet structures. On the other hand, solid element simulations can provide accurate (and mesh-size independent) predictions if sufficiently fine meshes are used, at the expense of computational efficiency. Consequently, a shell-to-solid re-meshing technique is presented and evaluated for industrial applications. It yields a significant increase of accuracy compared to shell simulations at a computational cost much lower than with solid simulations.

The damage and ductile fracture mechanisms are identified for biaxial stress states. Microscopy observations are performed on samples extracted from specimens submitted to different amounts of deformation. Investigations reveal that the critical mechanism leading to material failure is a shear localization of the plastic deformation occurring at the grain scale in the neighborhood of a grown void. Consequently a numerical analysis of the plastic flow localization in a void-containing material is carried out. It is based on a cavity-containing three-dimensional unit cell submitted to periodic boundary conditions. A specific numerical procedure permitting to control the macroscopic stress state applied to the cell as well as its orientation through displacement loading is used. Anisotropy of the unit cell model is partially accounted for. A series of calculation performed for proportional biaxial stress states show that the assumption of failure by shear localization at the microscale permits to reproduce qualitatively the dependence of ductility to stress state evidenced in macroscopic experiments. It also predicts a higher ductility in a high strain rate adiabatic loading than in a low strain rate isothermal loading.

8.2 Future research

8.2.1 High strain rate experiments

The high strain rate tensile setup presented in Chapter 3 permits to cover biaxial stress states between uniaxial and transverse plane strain tension: it can achieve biaxial stress ratios in the range $0 \leq \psi \leq 0.5$. Within the scope of the present thesis, a high velocity punching experiment based on a direct impact setup was developed. It allows for fracture characterization at high strain rate, in the vicinity of equibiaxial tension ($\psi = 1$). The sheet specimen, punch and clamping system are identical to those used for the low strain rate punching experiments described in Section 6.2.3.

However, preliminary punching experiments reveal an important scatter in the experimental results. Figure 8-1 depicts force versus punching displacement curves for two specimens impacted with the same initial punch velocity of 5m/s. Both the force level and the punch displacement at fracture show non-negligible differences. Further

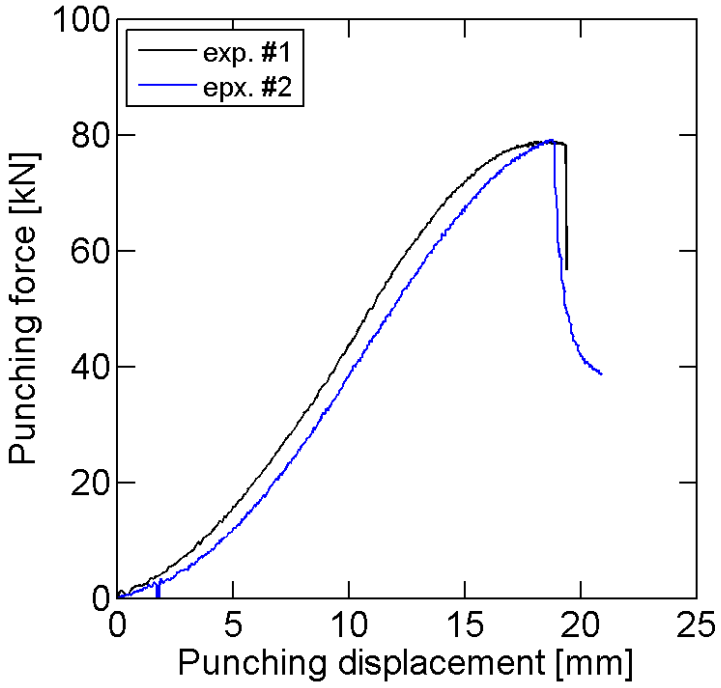

Figure 8-1: Scatter in high velocity equi-biaxial punch experiments. The initial punch velocity is 5m/s.

research is needed to get a better understanding of this experiment, in order to obtain reliable and repeatable results. In particular, the effect of friction between the sheet specimen and the punch (with high slipping velocities and temperatures at the interface) needs to be investigated.

In spite of those limitations, the high velocity punch experiment may be used to evaluate the fracture strain under equi-biaxial tension at high strain rate. Assuming an associated von Mises plasticity and a homogeneous plastic strain distribution through the sheet thickness, the equivalent plastic strain at fracture $\bar{\varepsilon}_f$ is related to the sheet thinning according to

$$\bar{\varepsilon}_f = \log\frac{t_i}{t_f} \tag{8-1}$$

where t_i (resp. t_f) is the initial sheet thickness (resp. at fracture). Note that thickness measurements on fractured specimens reveal that no localized necking occurs before fracture for the investigated TRIP material, at low or high strain rate in the equi-biaxial

punch test. In both experiments depicted in Fig. 8-1, the sheet thickness is reduced from $t_i = 1.42mm$ to $t_f = 0.55mm$ at fracture, indicating an approximate equivalent plastic strain at fracture of $\bar{\varepsilon}_f = 0.98$. In the low velocity punch experiment presented in Section 6.2, a fracture strain under equi-biaxial tension of $\bar{\varepsilon}_f = 0.83$ was obtained, thereby confirming that the material ductility is higher at high than at low strain rate.

8.2.2 Influence of temperature

All experiments presented in this manuscript have been carried out at room temperature. In intermediate and high strain rate experiments, the material temperature increases locally during deformation due to plastic dissipation. The constitutive model presented in Chapter 4 can predict correctly the material behavior under such loading conditions, as discussed in Section 4.5.2.

Figure 8-2 presents true stress-strain curves from isothermal uniaxial tension experiments carried out at low strain rate, at different temperatures. The end point of the curves corresponds to the onset of necking. Temperature has a clear influence on the material behavior. At a strain of 0.15, the stress level is higher by 15% at room temperature (in black in Fig. 8-2) than at 120°C (in green in Fig. 8-2). However, the initial yield stress is almost identical for all temperatures. The constitutive model proposed in Chapter 4 is not able to predict this type of behavior. Its use shall therefore be limited to loadings initially at room temperature.

Temperature influences mainly the strain hardening capabilities of the material at low strains. Recall that in the TRIP material considered here, part of the strain hardening originates from transformation of the retained austenite into martensite. Furthermore, the austenite-to-martensite transformation is hindered at high temperatures (e.g. Olsen and Cohen, 1975, [142]), leading to less hardening (and thus a lower stress) at 120°C than at 20°C. However it seems that most of the phase transformation occurs at low strains: hardening moduli are similar at all temperatures beyond strains of 0.1 (Fig. 8-2). Note that in intermediate and high strain rate experiments, plastic dissipation below strains of 0.1 does not lead to a significant temperature increase. Adiabatic loading conditions have therefore a limited impact on phase transformation in the present TRIP steel. As a result, the proposed plasticity

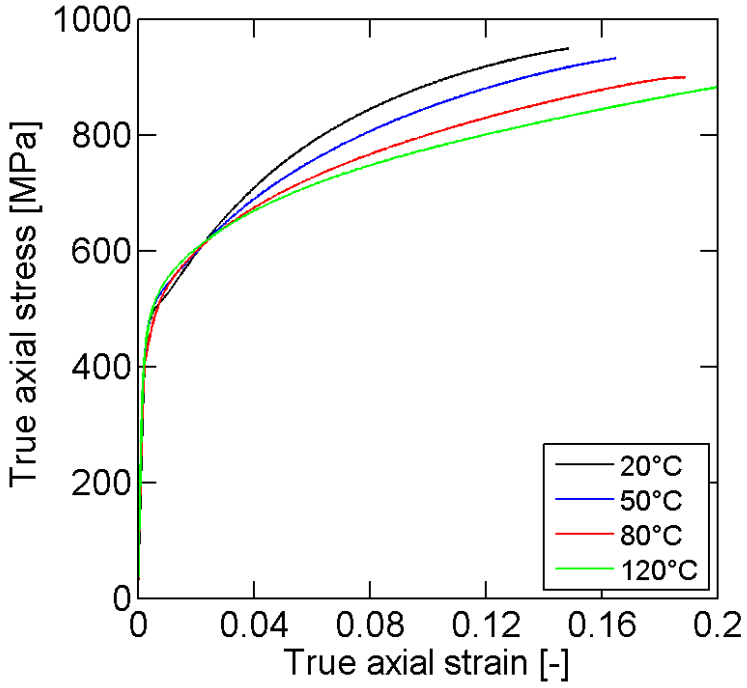

Figure 8-2: Isothermal uniaxial tension experiments at different temperatures. True stress-strain curves up to the onset of necking.

model can predict accurately the material behavior at high strain rate without explicitly accounting for phase transformation.

8.2.3 Rate-dependent fracture model

A complex dependence of the onset of fracture to both stress state and strain rate has been identified. The hybrid experimental-numerical analysis developed in Chapter 4 should be repeated on different grades of AHSS to assess whether this behavior is specific to the present TRIP material, or whether it corresponds to a more general trend among the AHSS family.

Most existing phenomenological rate-dependent fracture models assume a separation of the effects of stress state and strain rate on failure (e.g. Jonhson and Cook, 1985, [89]; Khan and Liu, 2012, [92]). Consequently, they cannot predict the fracture behavior identified in Chapter 4. A suitable macroscopic fracture model is still to be developed.

8.2.4 Rate-dependent localization analysis

The dependence to strain rate of the onset of plastic localization at the microscale has been characterized for one stress state only in Chapter 7. Furthermore only isothermal low strain rate and adiabatic high strain rate loading conditions were considered. Extending the analysis to the all range of biaxial stress states and intermediate strain rates would permit to evaluate whether the model can predict the coupled dependence of the onset of fracture to stress state and strain rate

Performing the analysis for all biaxial stress states can be readily performed at low and high strain rates with the micromechanical model described in Section 7.2 and the isothermal and adiabatic implementations of the constitutive equations detailed in Appendix A.

Appendix A

Numerical implementation of the rate-dependent plasticity model

A.1 Time integration scheme

The constitutive model defined in Section 4.4 has been implement in the Finite Element Analysis package Abaqus [1] as a user material through the *UMAT* subroutine interface in the implicit solver Abaqus/Standard, and the *VUMAT* subroutine in the explicit solver Abaqus/explicit. The user material subroutine is called by the solver at each time increment during an analysis to compute the Cauchy stress and internal variables at the end of the increment for all integration points, knowing the material state at the beginning of the increment and the total deformation evolution over the time increment. Formally, the subroutine must perform the following operation:

- Knowing $\boldsymbol{\sigma_n}$ and s_n,
- Given $\boldsymbol{\Delta\varepsilon}$,
- Compute $\boldsymbol{\sigma_{n+1}}$ and s_{n+1} satisfying the constitutive model.

where the subscript $\cdot_n$ denotes the quantity $\cdot$ at the end of increment n at time t, and the subscript $\cdot_{n+1}$ denotes the quantity $\cdot$ at the end of increment $n+1$ at time $t+\Delta t$. $\boldsymbol{\sigma}$ is the Cauchy stress, s the hardening internal variable and $\boldsymbol{\Delta\varepsilon}$ the increment of total strain over the time increment.

Note that both the strain rate function f (Eq. 4-18) and the strain hardening function g (Eq. 4-15) introduce strong non-linearity in the constitutive equations. Special care is thus required to develop a robust algorithm solving the aforementioned problem, as the strain increment $\boldsymbol{\Delta\varepsilon}$ can be arbitrarily large in implicit analyses. In particular, a backward Euler time integration scheme is chosen to integrate the constitutive equations as it is unconditionally stable.

A.1.1 Isothermal loading

The constitutive equations, discretized between the beginning and the end of the time increment Δt, can be rewritten as

$$\mathcal{F}(\boldsymbol{\sigma_{n+1}}) - \bar{\sigma}_{n+1} = 0 \tag{A-2}$$

$$\Delta\bar{\varepsilon}^p - \Delta t\, f(\bar{\sigma}_{n+1}, s_{n+1}) = 0 \tag{A-3}$$

$$\Delta s - \Delta t\, g(\bar{\sigma}_{n+1}, s_{n+1}) = 0 \tag{A-4}$$

$$\mathcal{F}(\boldsymbol{\sigma_{n+1}})\Delta\bar{\varepsilon}^p - \mathcal{G}(\boldsymbol{\sigma_{n+1}})\Delta\lambda = 0 \tag{A-5}$$

$$\boldsymbol{\sigma_{n+1}} - \boldsymbol{\mathcal{C}}\left(\boldsymbol{\varepsilon_{n+1}} - \boldsymbol{\varepsilon_n^p} - \Delta\boldsymbol{\varepsilon^p}\right) = \mathbf{0} \tag{A-6}$$

$$\Delta\boldsymbol{\varepsilon^p} - \Delta\lambda \left.\frac{\partial \mathcal{G}}{\partial \boldsymbol{\sigma}}\right|_{n+1} = \mathbf{0} \tag{A-7}$$

We introduce the trial stress, corresponding to a fully elastic loading

$$\boldsymbol{\sigma^{Trial}} = \boldsymbol{\mathcal{C}}\left(\boldsymbol{\varepsilon_{n+1}} - \boldsymbol{\varepsilon_n^p}\right) \tag{A-8}$$

Since $\partial\mathcal{G}/\partial\boldsymbol{\sigma}$ is a purely deviatoric tensor, Eqs A-5 and A-6 can be rewritten as

$$\frac{1}{2\mu}\left(\boldsymbol{\sigma_{n+1}} - \boldsymbol{\sigma^{Trial}}\right) + \Delta\lambda \left.\frac{\partial \mathcal{G}}{\partial \boldsymbol{\sigma}}\right|_{n+1} = \mathbf{0} \tag{A-9}$$

where μ is the elastic shear modulus. Therefore the material state at the end of the increment is obtained by solving for $\boldsymbol{\sigma_{n+1}}$, $\bar{\sigma}_{n+1}$, $\Delta\bar{\varepsilon}^p$, Δs and $\Delta\lambda$ the system

$$\begin{cases} \Phi_1 \equiv \mathcal{F}(\boldsymbol{\sigma_{n+1}}) - \bar{\sigma}_{n+1} = 0 \\ \Phi_2 \equiv \Delta\bar{\varepsilon}^p - \Delta t\, f(\bar{\sigma}_{n+1}, s_{n+1}) = 0 \\ \Phi_3 \equiv \Delta s - \Delta t\, g(\bar{\sigma}_{n+1}, s_{n+1}) = 0 \\ \Phi_4 \equiv \mathcal{F}(\boldsymbol{\sigma_{n+1}})\Delta\bar{\varepsilon}^p - \mathcal{G}(\boldsymbol{\sigma_{n+1}})\Delta\lambda = 0 \\ \boldsymbol{\Phi_5} \equiv \dfrac{1}{2\mu}\left(\boldsymbol{\sigma_{n+1}} - \boldsymbol{\sigma^{Trial}}\right) + \Delta\lambda \left.\dfrac{\partial \mathcal{G}}{\partial \boldsymbol{\sigma}}\right|_{n+1} = \mathbf{0} \end{cases} \tag{A-10}$$

Note that if $\mathcal{F}\left(\boldsymbol{\sigma^{Trial}}\right) \leq s_a$, the loading is purely elastic and the solution is $\Delta\bar{\varepsilon}^p = \Delta s = \Delta\lambda = 0$, $\boldsymbol{\sigma_{n+1}} = \boldsymbol{\sigma^{Trial}}$. It should also be mentioned that in case of a standard von Mises yield surface with an associated flow rule, Eq. A-9e can be reduced to a scalar equation (Sumo & Hughes, 1998, [159]). With a non-associated flow rule this

simplification is not possible as the three tensiorial components in Eq. A-9e have different directions in the deviatoric space.

A Newton-Raphson iterative method is used to solve Eq. A-9 for $\boldsymbol{x} = \{\boldsymbol{\sigma_{n+1}}, \bar{\sigma}_{n+1}, \Delta\bar{\varepsilon}^p, \Delta s, \Delta\lambda\}^T$

1. A first guess $\boldsymbol{x_0}$ is assumed,
2. The residue $\boldsymbol{\Phi} = \{\Phi_1, \Phi_2, \Phi_3, \Phi_4, \boldsymbol{\Phi_5}\}^T$ is evaluated,
3. Convergence check: if $|\boldsymbol{\Phi}| < \text{tolerance}$, then the system is solved. Else:
4. Linearize Eq. A-9 about $\boldsymbol{x_k}$:

$$\begin{cases} \Phi_1 + \dfrac{\partial \mathcal{F}}{\partial \boldsymbol{\sigma}} \cdot \delta\boldsymbol{\sigma} - \delta\bar{\sigma} = 0 \\ \Phi_2 + \delta(\Delta\bar{\varepsilon}^p) - \Delta t \left(\dfrac{\partial f}{\partial \bar{\sigma}} \delta\bar{\sigma} + \dfrac{\partial f}{\partial s} \delta(\Delta s) \right) = 0 \\ \Phi_3 + \delta(\Delta s) - \Delta t \left(\dfrac{\partial g}{\partial \bar{\sigma}} \delta\bar{\sigma} + \dfrac{\partial g}{\partial s} \delta(\Delta s) \right) = 0 \\ \Phi_4 + \left(\Delta\bar{\varepsilon}^p \dfrac{\partial \mathcal{F}}{\partial \boldsymbol{\sigma}} - \Delta\lambda \dfrac{\partial \mathcal{G}}{\partial \boldsymbol{\sigma}} \right) \cdot \delta\boldsymbol{\sigma} + \mathcal{F}\, \delta(\Delta\bar{\varepsilon}^p) - \mathcal{G}\, \delta(\Delta\lambda) = 0 \\ \boldsymbol{\Phi_5} + \left(\dfrac{1}{2\mu}\mathbf{1} + \Delta\lambda \dfrac{\partial^2 \mathcal{G}}{\partial \boldsymbol{\sigma}^2} \right) \cdot \delta\boldsymbol{\sigma} + \dfrac{\partial \mathcal{G}}{\partial \boldsymbol{\sigma}} \delta(\Delta\lambda) = \mathbf{0} \end{cases} \tag{A-11}$$

where $\delta(\cdot) = \cdot_{k+1} - \cdot_k$. Equivalently, Eq. A-10 can be written

$$\boldsymbol{J_k} \cdot (\boldsymbol{x_{k+1}} - \boldsymbol{x_k}) = -\boldsymbol{\Phi_k} \tag{A-12}$$

5. Solve Eq. A-11 for $\boldsymbol{x_{k+1}}$ and iterate from 2.

A.1.2 Adiabatic loading

Because of the coupling between mechanical behavior and temperature defined by Eq. 4-8 and 4-10, the temperature θ_{n+1} at the end of the increment must be considered as an unknown of the constitutive model when considering adiabatic loadings. In that case the material state at the end of the increment is obtained by solving for $\boldsymbol{\sigma_{n+1}}$, $\bar{\sigma}_{n+1}$, $\Delta\bar{\varepsilon}^p$, Δs, $\Delta\lambda$ and $\Delta\theta$ the system

$$\begin{cases} \Phi_1 \equiv \mathcal{F}(\boldsymbol{\sigma_{n+1}}) - \bar{\sigma}_{n+1} = 0 \\ \Phi_2 \equiv \Delta\bar{\varepsilon}^p - \Delta t\, f(\bar{\sigma}_{n+1}, s_{n+1}, \theta_{n+1}) = 0 \\ \Phi_3 \equiv \Delta s - \Delta t\, g(\bar{\sigma}_{n+1}, s_{n+1}, \theta_{n+1}) = 0 \\ \Phi_4 \equiv \mathcal{F}(\boldsymbol{\sigma_{n+1}})\Delta\bar{\varepsilon}^p - \mathcal{G}(\boldsymbol{\sigma_{n+1}})\Delta\lambda = 0 \\ \Phi_5 \equiv \Delta\theta - \dfrac{\zeta}{\rho c}\bar{\sigma}_{n+1}\Delta\bar{\varepsilon}^p = 0 \\ \boldsymbol{\Phi_6} \equiv \dfrac{1}{2\mu}\left(\boldsymbol{\sigma_{n+1}} - \boldsymbol{\sigma^{Trial}}\right) + \Delta\lambda\dfrac{\partial\mathcal{G}}{\partial\boldsymbol{\sigma}} = \mathbf{0} \end{cases} \tag{A-13}$$

The same Newtown-Raphson method is used to solve Eq. A-12 than in case of isothermal loading.

A.1.3 First guess for the Newtown algorithm

The Newtown-Raphson scheme used to solve Eqs. A-9 and A-12 might not converge if the initial guess $\boldsymbol{x_0}$ is not close enough from the equation solution. Special care is thus required when choosing $\boldsymbol{x_0}$ to guarantee the robustness of the algorithm for arbitrary large strain increments $\boldsymbol{\Delta\varepsilon}$. Two different cases arise: (a) $\boldsymbol{\Delta\varepsilon}$ is smaller than the current elastic strain tensor $\boldsymbol{\varepsilon_n^e}$: $\mathcal{F}(\boldsymbol{\mathcal{C}}\cdot\boldsymbol{\Delta\varepsilon}) \leq \bar{\sigma}_n$; or (b) $\boldsymbol{\Delta\varepsilon}$ is larger than the current elastic strain tensor.

If $\boldsymbol{\Delta\varepsilon}$ is small (case a), then the initial guess $\boldsymbol{x_0}$ corresponds to a purely elastic step, as in standard return-mapping algorithms (Simo & Hughes, 1998, [159]):

$$\boldsymbol{\sigma_{n+1}^0} = \boldsymbol{\sigma^{Trial}} \quad \text{and} \quad \Delta\bar{\varepsilon}_0^p = \Delta s_0 = \Delta\lambda_0 = 0 \tag{A-14}$$

If $\boldsymbol{\Delta\varepsilon}$ is large, then a "small" sub-increment of strain $\boldsymbol{\Delta\varepsilon_s}$ is introduced, such that

$$\boldsymbol{\Delta\varepsilon} = N\boldsymbol{\Delta\varepsilon_s} \quad \text{with} \quad \begin{cases} \mathcal{F}(\boldsymbol{\mathcal{C}}\cdot\boldsymbol{\Delta\varepsilon_s}) \leq \bar{\sigma}_n \\ N \in \mathbb{N} \end{cases} \tag{A-15}$$

The initial guess $\boldsymbol{x_0^{(N)}}$ corresponding to the total strain increment $\boldsymbol{\Delta\varepsilon} = N\boldsymbol{\Delta\varepsilon_s}$ is then obtained by recurrence as being the final material state $\boldsymbol{x^{(N-1)}}$ corresponding to a partial strain increment of $\boldsymbol{\Delta\varepsilon} = (N-1)\boldsymbol{\Delta\varepsilon_s}$.

A.1.4 Explicit FEA solver

Explicit Finite Element solvers such as Abaqus/Explicit are only conditionally stable. Stability of their time integration scheme requires that the time increment Δt be smaller than the duration of propagation of an elastic wave in the smallest element in the model. As a result of this stability criterion (which is automatically enforced by the FEA solver by adjusting Δt as the mesh is deformed), the strain increment $\boldsymbol{\Delta\varepsilon}$ can always be considered as small, at least for the applications considered in this thesis. The initial guess $\boldsymbol{x_0}$ thus always corresponds to Eq. A-13.

Another consequence of having small strain increments is that the effect of the variation of temperature during the increment can be neglected. Only the isothermal case is implemented in Abaqus/Explicit. However, it is emphasized that if temperature variation is not considered to evaluate the material state evolution during the increment, the temperature is still updated at the end of the increment by the solver to account for dissipation effects and diffusion.

A.2 Material Jacobian

Implicit Finite Element solvers such as Abaqus/Standard [1] use a Newtown type iterative method for revising the nodal displacements in non-linear analyses. This requires the evaluation of the Jacobian matrix of the constitutive equation defined as

$$\boldsymbol{C} = \frac{\delta(\boldsymbol{\Delta\sigma})}{\delta(\boldsymbol{\Delta\varepsilon})} \tag{A-16}$$

$\boldsymbol{C}$ represents the variation of the increment of the Cauchy stress at the end of the time increment due to a perturbation of the increment of total strain.

A.2.1 Isothermal loading

In case of an isothermal loading, the constitutives equation can be expressed as

$$\begin{cases} \boldsymbol{\Delta\sigma} = \boldsymbol{C^{el}}\left[\boldsymbol{\Delta\varepsilon} - \Delta\lambda\dfrac{\partial \mathcal{G}}{\partial \boldsymbol{\sigma}}\right] \\ \Delta\varepsilon\ \mathcal{F} = \Delta\lambda\ \mathcal{G} \\ \Delta\varepsilon = \Delta t\ f(\mathcal{F}, s) \\ \Delta s = \Delta t\ g(\mathcal{F}, s) \end{cases} \tag{A-17}$$

Differentiation of Eq. A-16 gives

$$\left[\left(\boldsymbol{C^{el}}\right)^{-1} + \Delta\lambda\frac{\partial^2 \mathcal{G}}{\partial \boldsymbol{\sigma}^2}\right] \cdot \delta(\boldsymbol{\Delta\sigma}) = \delta(\boldsymbol{\Delta\varepsilon}) - \delta(\Delta\lambda)\frac{\partial \mathcal{G}}{\partial \boldsymbol{\sigma}} \tag{A-18}$$

$$\delta(\Delta\varepsilon)\mathcal{F} + \Delta\varepsilon\frac{\partial \mathcal{F}}{\partial \boldsymbol{\sigma}} \cdot \delta(\boldsymbol{\Delta\sigma}) = \ \delta(\Delta\lambda)\mathcal{G} + \Delta\lambda\frac{\partial \mathcal{G}}{\partial \boldsymbol{\sigma}} \cdot \delta(\boldsymbol{\Delta\sigma}) \tag{A-19}$$

$$\delta(\Delta\varepsilon) = \Delta t\left\{\frac{\partial f}{\partial \mathcal{F}}\frac{\partial \mathcal{F}}{\partial \boldsymbol{\sigma}} \cdot \delta(\boldsymbol{\Delta\sigma}) + \frac{\partial f}{\partial s}\delta(\Delta s)\right\} \tag{A-20}$$

$$\delta(\Delta s) = \Delta t\left\{\frac{\partial g}{\partial \mathcal{F}}\frac{\partial \mathcal{F}}{\partial \boldsymbol{\sigma}} \cdot \delta(\boldsymbol{\Delta\sigma}) + \frac{\partial g}{\partial s}\delta(\Delta s)\right\} \tag{A-21}$$

By successive substitutions, we get

$$\delta(\Delta s) = \frac{\Delta t}{1 - \Delta t\dfrac{\partial g}{\partial s}}\frac{\partial g}{\partial \mathcal{F}}\frac{\partial \mathcal{F}}{\partial \boldsymbol{\sigma}} \cdot \delta(\boldsymbol{\Delta\sigma}) \tag{A-22}$$

$$\delta(\Delta\varepsilon) = \Delta t\left[\frac{\partial f}{\partial \mathcal{F}} + \frac{\Delta t}{1 - \Delta t\dfrac{\partial g}{\partial s}}\frac{\partial f}{\partial s}\frac{\partial g}{\partial \mathcal{F}}\right]\frac{\partial \mathcal{F}}{\partial \boldsymbol{\sigma}} \cdot \delta(\boldsymbol{\Delta\sigma}) \tag{A-23}$$

$$\delta(\Delta\lambda) = \frac{1}{\mathcal{G}}\left\{\mathcal{F}\Delta t\left(\frac{\partial f}{\partial \mathcal{F}} + \frac{\Delta t}{1 - \Delta t\dfrac{\partial g}{\partial s}}\frac{\partial f}{\partial s}\frac{\partial g}{\partial \mathcal{F}}\right)\frac{\partial \mathcal{F}}{\partial \boldsymbol{\sigma}} + \left(\Delta\varepsilon\frac{\partial \mathcal{F}}{\partial \boldsymbol{\sigma}} - \Delta\lambda\frac{\partial \mathcal{G}}{\partial \boldsymbol{\sigma}}\right)\right\} \cdot \delta(\boldsymbol{\Delta\sigma}) \tag{A-24}$$

And finally, from Eqs. A-17 and A-23

$$\boldsymbol{C_{iso}} = \left[\left(\boldsymbol{C^{el}}\right)^{-1} + \Delta\lambda \frac{\partial^2 \mathcal{G}}{\partial \boldsymbol{\sigma}^2} + \frac{1}{\mathcal{G}} \frac{\partial \mathcal{G}}{\partial \boldsymbol{\sigma}} \otimes \left\{ \left(\Delta\varepsilon \frac{\partial \mathcal{F}}{\partial \boldsymbol{\sigma}} - \Delta\lambda \frac{\partial \mathcal{G}}{\partial \boldsymbol{\sigma}} \right) + \mathcal{F}\Delta t \left(\frac{\partial f}{\partial \mathcal{F}} + \frac{\Delta t}{1 - \Delta t \frac{\partial g}{\partial s}} \frac{\partial f}{\partial s} \frac{\partial g}{\partial \mathcal{F}} \right) \frac{\partial \mathcal{F}}{\partial \boldsymbol{\sigma}} \right\} \right]^{-1} \tag{A-25}$$

A.2.2 Adiabatic loading

Recall that in case of an adiabatic loading, the state equations can be written as

$$\begin{cases} \boldsymbol{\Delta\sigma} = \boldsymbol{C^{el}} \left[\boldsymbol{\Delta\varepsilon} - \Delta\lambda \frac{\partial \mathcal{G}}{\partial \boldsymbol{\sigma}} \right] \\ \Delta\varepsilon\, \mathcal{F} = \Delta\lambda\, \mathcal{G} \\ \Delta\varepsilon = \Delta t\, f(\mathcal{F}, s, \theta) \\ \Delta s = \Delta t\, g(\mathcal{F}, s, \theta) \\ \Delta\theta = K\, \mathcal{F}\, \Delta\varepsilon \end{cases} \tag{A-26}$$

where $K = \zeta/(\rho c)$. Differentiation of Eq. A-25 leads to

$$\left[\left(\boldsymbol{C^{el}}\right)^{-1} + \Delta\lambda \frac{\partial^2 \mathcal{G}}{\partial \boldsymbol{\sigma}^2} \right] \cdot \delta(\boldsymbol{\Delta\sigma}) = \delta(\boldsymbol{\Delta\varepsilon}) - \delta(\Delta\lambda) \frac{\partial \mathcal{G}}{\partial \boldsymbol{\sigma}} \tag{A-27}$$

$$\delta(\Delta\varepsilon)\mathcal{F} + \Delta\varepsilon \frac{\partial \mathcal{F}}{\partial \boldsymbol{\sigma}} \cdot \delta(\boldsymbol{\Delta\sigma}) = \delta(\Delta\lambda)\mathcal{G} + \Delta\lambda \frac{\partial \mathcal{G}}{\partial \boldsymbol{\sigma}} \cdot \delta(\boldsymbol{\Delta\sigma}) \tag{A-28}$$

$$\delta(\Delta\varepsilon) = \Delta t \left\{ \frac{\partial f}{\partial \mathcal{F}} \frac{\partial \mathcal{F}}{\partial \boldsymbol{\sigma}} \cdot \delta(\boldsymbol{\Delta\sigma}) + \frac{\partial f}{\partial s} \delta(\Delta s) + \frac{\partial f}{\partial \theta} \delta(\Delta\theta) \right\} \tag{A-29}$$

$$\delta(\Delta s) = \Delta t \left\{ \frac{\partial g}{\partial \mathcal{F}} \frac{\partial \mathcal{F}}{\partial \boldsymbol{\sigma}} \cdot \delta(\boldsymbol{\Delta\sigma}) + \frac{\partial g}{\partial s} \delta(\Delta s) + \frac{\partial g}{\partial \theta} \delta(\Delta\theta) \right\} \tag{A-30}$$

$$\delta(\Delta\theta) = K \left\{ \Delta\varepsilon \frac{\partial \mathcal{F}}{\partial \boldsymbol{\sigma}} \cdot \delta(\boldsymbol{\Delta\sigma}) + \mathcal{F}\delta(\Delta\varepsilon) \right\} \tag{A-31}$$

Substituting Eqs. A-29 and A-30 in Eq. A-28, we have

$$\left[1-\Delta t\,K\,\mathcal{F}\frac{\partial f}{\partial\theta}-\frac{\Delta t^2}{1-\Delta t\frac{\partial g}{\partial s}}\frac{\partial f}{\partial s}\,K\,\mathcal{F}\frac{\partial g}{\partial\theta}\right]\delta(\Delta\varepsilon)$$
$$=\Delta T\left\{\frac{\partial f}{\partial\mathcal{F}}+K\Delta\varepsilon\frac{\partial f}{\partial\theta}\right.$$
$$\left.+\frac{\Delta t}{1-\Delta t\frac{\partial g}{\partial s}}\frac{\partial f}{\partial s}\left(\frac{\partial g}{\partial\mathcal{F}}+K\Delta\varepsilon\frac{\partial g}{\partial\theta}\right)\right\}\frac{\partial\mathcal{F}}{\partial\boldsymbol{\sigma}}\cdot\delta(\boldsymbol{\Delta\sigma}) \tag{A-32}$$

Let define

$$\alpha=\frac{\frac{\partial f}{\partial\mathcal{F}}+K\Delta\varepsilon\frac{\partial f}{\partial\theta}+\frac{\Delta t}{1-\Delta t\frac{\partial g}{\partial s}}\frac{\partial f}{\partial s}\left(\frac{\partial g}{\partial\mathcal{F}}+K\Delta\varepsilon\frac{\partial g}{\partial\theta}\right)}{1-\Delta t\,K\,\mathcal{F}\frac{\partial f}{\partial\theta}-\frac{\Delta t^2}{1-\Delta t\frac{\partial g}{\partial s}}\frac{\partial f}{\partial s}\,K\,\mathcal{F}\frac{\partial g}{\partial\theta}} \tag{A-33}$$

Then

$$\delta(\Delta\varepsilon)=\Delta t\;\alpha\frac{\partial\mathcal{F}}{\partial\boldsymbol{\sigma}}\cdot\delta(\boldsymbol{\Delta\sigma}) \tag{A-34}$$

Substituting Eq. A-33 in Eq. A-27 we get

$$\delta(\Delta\lambda)=\frac{1}{\mathcal{G}}\left\{\left(\Delta\varepsilon\frac{\partial\mathcal{F}}{\partial\boldsymbol{\sigma}}-\Delta\lambda\frac{\partial\mathcal{G}}{\partial\boldsymbol{\sigma}}\right)+\mathcal{F}\Delta t\;\alpha\;\frac{\partial\mathcal{F}}{\partial\boldsymbol{\sigma}}\right\}\cdot\delta(\boldsymbol{\Delta\sigma}) \tag{A-35}$$

And finally, from Eq. A-26 and A-34

$$\boldsymbol{C_{adiab}}=\left[\left(\boldsymbol{C^{el}}\right)^{-1}+\Delta\lambda\frac{\partial^2\mathcal{G}}{\partial\boldsymbol{\sigma}^2}\right.$$
$$\left.+\frac{1}{\mathcal{G}}\frac{\partial\mathcal{G}}{\partial\boldsymbol{\sigma}}\otimes\left\{\left(\Delta\varepsilon\frac{\partial\mathcal{F}}{\partial\boldsymbol{\sigma}}-\Delta\lambda\frac{\partial\mathcal{G}}{\partial\boldsymbol{\sigma}}\right)+\mathcal{F}\Delta t\;\alpha\;\frac{\partial\mathcal{F}}{\partial\boldsymbol{\sigma}}\right\}\right]^{-1} \tag{A-36}$$

A.3 Material derivatives

A.3.1 Yield and flow potentials $\mathcal{F}$ and $\mathcal{G}$

The quadratic yield potential is defined as

$$\mathcal{F}(\boldsymbol{\sigma}) = \sqrt{(\boldsymbol{F}\boldsymbol{\sigma}) \cdot \boldsymbol{\sigma}} \tag{A-37}$$

Its gradient is therefore readily given by

$$\frac{\partial \mathcal{F}}{\partial \boldsymbol{\sigma}} = \frac{1}{\mathcal{F}} \boldsymbol{F}\boldsymbol{\sigma} \tag{A-38}$$

Similarly,

$$\frac{\partial \mathcal{G}}{\partial \boldsymbol{\sigma}} = \frac{1}{\mathcal{G}} \boldsymbol{G}\boldsymbol{\sigma} \tag{A-39}$$

A.3.2 Strain rate function f

The strain rate function defined in Eq. 4-8 reads

$$f(\mathcal{F}, s, \theta) = \dot{\varepsilon}_0 \exp\left\{-\frac{\Delta F}{k_B \theta}\left[1 - \left(\frac{\mathcal{F} - s_a}{s_{th}}\right)^p\right]^q\right\} \tag{A-40}$$

where

$$s_a = \frac{1}{1+\chi} s \quad \text{and} \quad s_{th} = \frac{\chi}{1+\chi} s \tag{A-41}$$

Therefore Eq. A-39 can be rewritten

$$f(\mathcal{F}, s, \theta) = \dot{\varepsilon}_0 \exp\left\{-\frac{\Delta F}{k_B \theta}\left[1 - \left(\frac{(1+\chi)\,\mathcal{F}/s - 1}{\chi}\right)^p\right]^q\right\} \tag{A-42}$$

Introducing

$$u \equiv \frac{(1+\chi)\,\mathcal{F}/s - 1}{\chi} \tag{A-43}$$

we get

$$f(u(\mathcal{F},s),\theta) = \dot{\varepsilon}_0 \exp\left\{-\frac{\Delta F}{k_B\theta}[1-u^p]^q\right\} \tag{A-44}$$

and

$$\frac{\partial f}{\partial u} = \frac{\Delta F}{k_B\theta} pq u^{p-1}(1-u^p)^{q-1} f \tag{A-45}$$

Then

$$\begin{cases} \dfrac{\partial f}{\partial \mathcal{F}} = \dfrac{\partial f}{\partial u}\dfrac{1}{\dfrac{\chi}{1+\chi}s} \\ \dfrac{\partial f}{\partial s} = -\dfrac{\mathcal{F}}{s}\dfrac{\partial f}{\partial \mathcal{F}} \end{cases} \tag{A-46}$$

The temperature partial derivative is given by

$$\frac{\partial f}{\partial \theta} = \frac{\Delta F}{k_B\theta^2}[1-u^p]^q f \tag{A-47}$$

A.3.3 Strain hardening function g

The strain hardening function g can be written as (Eq. 4-14)

$$g(\mathcal{F},s,\theta) = h(s)\, f(\mathcal{F},s,\theta) \tag{A-48}$$

with h corresponding to a saturation law

$$h(s) = H_0\left(1-\frac{s}{s^*}\right)^r \tag{A-49}$$

From Eq. A-48 we have

$$\frac{dh}{ds} = -\frac{r}{s^*}\frac{h}{1-\frac{s}{s^*}} \tag{A-50}$$

The partial derivatives of g are then given by

$$\begin{cases} \dfrac{\partial g}{\partial \mathcal{F}} = h\dfrac{\partial f}{\partial \mathcal{F}} \\ \dfrac{\partial g}{\partial s} = f\dfrac{dh}{ds} + h\dfrac{\partial f}{\partial s} \\ \dfrac{\partial g}{\partial \theta} = h\dfrac{\partial f}{\partial \theta} \end{cases} \tag{A-51}$$

Appendix B

Publications & Presentations

B.1 Refereed journal publications

[1] M. Dunand & D. Mohr (2010). "Hybrid Experimental-numerical Analysis of Basic Ductile Fracture Experiments for sheet metals", International Journal of Solids and Structures **47** (9), 1130-1143.

[2] D. Mohr, M. Dunand and H.W. Kim (2010). "Evaluation of Associated and Non-Associated Quadratic Plasticity Models for Advanced High Strength Steel Sheets under Multi-axial Loading", International Journal of Plasticity **26** (7), 939-956.

[3] M. Dunand & D. Mohr (2011). "On the Predictive Capabilities of the Shear Modified Gurson and the Modified Mohr-Coulomb Fracture Models over a Wide Range of Stress Triaxialities and Lode Angles", Journal of the Mechanics and Physics of Solids **59** (7), 1374-1394.

[4] M. Dunand & D. Mohr (2011). "Optimized Specimen for the Fracture Testing of Advanced High Strength Steels under Combined Normal and Shear Loading", Engineering Fracture Mechanics **78** (17), 2919-2934.

[5] M. Dunand, A. Maertens, M. Luo & D. Mohr (2012). "Experiments and Modeling of Anisotropic Aluminum Extrusions under Multi-axial Loading – Part I: Plasticity", International Journal of Plasticity **36**, 35-49.

[6] M. Luo, M. Dunand & D. Mohr (2012). "Experiments and Modeling of Anisotropic Aluminum Extrusions under Multi-axial Loading – Part II: Ductile Fracture", International Journal of Plasticity **32-33**, 36-58.

[7] M. Dunand, G. Gary & D. Mohr (2013). "Load-inversion Device for the High Strain Rate Tensile Testing of Sheet Materials with Hopkinson Pressure Bars", Experimental Mechanics *(In Press)*.

[8] M. Dunand, D. Mohr & K. Ravi-Chandar, "Shear Fracture of Advanced High Strength Steel: Fractography and Micromechanical modeling", *Submitted for publication*.

[9] M. Dunand & D. Mohr, "Rate-dependent behavior of Advanced High Strength steels under multi-axial loading: characterization and modeling at large strains", *Submitted for publication*.

[10] M. Dunand & D. Mohr, "Effect of Lode parameter on plastic flow localization at low stress triaxialities", *Submitted for publication*.

B.2 Conference proceedings

[1] M. Dunand & D. Mohr, "Plasticity of Aluminum Extrusions under Combined Normal and Shear Loading", Proc. 15th International Symposium on Plasticity in St Thomas, USVI, edited by A.S. Khan, 2009.

[2] D. Mohr, F. Ebnoether and M. Dunand, "Plasticity and Fracture of Advanced High Strength Steel Sheets under Combined Tensile and Shear Loading", in Dynamic Behavior of Materials, edited by A. Rusinek and P. Chevrier, pp. 147-154.

[3] M. Dunand & D. Mohr, "Ductile fracture of TRIP780 sheets under multi-axial loading", AIP Conference Proceedings Vol. 1252, 1295-1302, 2010 (Proceedings of the 10th Int. Conf. on Numerical Methods in Industrial Forming Processes Dedicated to Pr. O.C. Zienkiewicz in Pohang, Republic of Korea, edited by F. Barlat, Y.H. Moon and M.G. Lee).

[4] M. Dunand & D. Mohr, "On the limitations of Shear-modified Gurson models: Comparison of numerical predictions with experimental results for ductile fracture under combined tension and shear loading", Proc. 17th International

Symposium on Plasticity in Puerto Vallarta, Mexico, edited by A.S. Khan, 2011.

[5] M. Dunand & D. Mohr, "Ductile fracture of AHSS sheets under multi-axial loading: experiments and modeling", AIP Conference Proceedings Vol. 1383, 484-491, 2011 (Proceedings of the 8th Int. Conf. on Numerical Simulation of 3D sheet metal forming processes in Seoul, Republic of Korea, edited by K. Chung).

[6] M. Dunand & D. Mohr, "On the modeling of damage and ductile fracture in advanced high strength steel sheets using void cell calculations", Proceedings of the 23rd International Congress of Theoretical and Applied Mechanics in Beijing, China, August 19-24, 2012.

[7] M. Dunand & D. Mohr, "High strain rate tensile testing of sheet materials using three Hopkinson pressure bars", Proceedings of the 10th International DYMAT Conference in Freiburg, Germany, September 2nd-7th, 2012.

[8] M. Dunand & D. Mohr, "Effect of Strain Rate and Stress State on the Ductile Fracture of AHSS Sheets: a Micromechanical Analysis", Proceedings of the International Deep Drawing Research Group 12' Conference in Mumbai, India, November 25-29, 2012.

[9] M. Dunand & A. Kamoulakos, "Application of shell-to-solid re-meshing to accurate ductile fracture predictions in Advanced High Strength steel sheets", Proceedings of the 3rd International Conference on Engineering against Failure in Kos, Greece, June, 2013

B.3 Presentations

[1] M. Dunand & D. Mohr, "Plasticity of Aluminum extrusions under combined and shear loading", 15th International Symposium on Plasticity in St Thomas, USVI, January 3rd-6th, 2009.

[2] M. Dunand & D. Mohr, “Determination of ductile fracture properties of TRIP steel using notched tensile specimens”, 5th MIT Workshop on Experimental and Computational Fracture Mechanics in Cambridge, USA, April 2009.

[3] D. Mohr & M. Dunand, “Onset of Fracture in Advanced High Strength Steels Under Multi-axial Loading”, ASME Exposition and Congress, Lake Buena Vista, USA, November 17th, 2009.

[4] M. Dunand & D. Mohr, “Assessment of the accuracy of selected fracture experiments”, 6th MIT Workshop on Experimental and Computational Fracture Mechanics in Cambridge, USA, November 19th, 2009.

[5] M. Dunand & D. Mohr, “Standardized fracture model identification procedure based on butterfly experiments”, 6th MIT Workshop on Experimental and Computational Fracture Mechanics in Cambridge, USA, November 19th, 2009.

[6] M. Dunand & D. Mohr, “Ductile fracture of TRIP780 steel under multi-axial loading”, 10th Int. Conf. on Numerical Methods in Industrial Forming Processes in Pohang, South Korea, June 7th, 2010.

[7] M. Dunand & D. Mohr, “Comparison of the performances of the MMC fracture model with shear modified Gurson models”, 7th MIT Workshop on Experimental and Computational Fracture Mechanics in Cambridge, USA, October 7th, 2010.

[8] M. Dunand & D. Mohr, “Ductile fracture under multi-axial loadings: Comparison of numerical predictions with experimental results”, 17th International Symposium on Plasticity in Puerto Vallarta, Mexico, January 5th, 2011.

[9] M. Dunand & D. Mohr, “Ductile fracture of AHSS sheets under multi-axial loadings: Experiments and modeling”, 8th International Conference on Numerical Simulation of 3D sheet metal forming processes in Seoul, South Korea, August 24th, 2011.

[10] M. Dunand, G. Gary & D. Mohr, “A Hybrid Experimental-numerical Method to Characterize the Effect of Strain Rate on Sheet Metal Fracture”, 8th

International Conference on Numerical Simulation of 3D sheet metal forming processes in Seoul, South Korea, August 24th, 2011.

[11] M. Dunand, G. Gary & D. Mohr, “A new SHPB technique to study strain rate dependent fracture”, 8th MIT Workshop on Experimental and Computational Fracture Mechanics in Cambridge, USA, October 6th, 2011.

[12] M. Dunand & D. Mohr, “Microscopic Analysis of the fracture mechanisms of AHSS”, Interim meeting of the MIT/Industry Fracture Consortium in Paris, France, March 23rd, 2012.

[13] M. Dunand & D. Mohr, “Reliable procedure for high strain rate tensile testing of sheet materials”, Interim meeting of the MIT/Industry Fracture Consortium in Paris, France, March 23rd, 2012.

[14] M. Dunand & D. Mohr, “Ductile fracture mechanisms: micro-analysis and modeling”, 5th Forming Technology Forum in ETH Zurich, Swiss, June 4th, 2012.

[15] M. Dunand & D. Mohr, “Microscopic analysis of the fracture mechanisms of Advanced High Strength Steel sheets”, Jean Mandel Symposium on Damage and Rupture in Palaiseau, France, June 7th, 2012.

[16] M. Dunand & D. Mohr, “Experimental and numerical investigations of the damage and ductile fracture mechanisms in TRIP steel sheets”, 8th European Solid Mechanics Conference in Graz, Austria, July 12th, 2012.

[17] M. Dunand & D. Mohr, “On the modeling of damage and ductile fracture in Advanced High Strength Steel sheets using void cell caclulations”, 23rd International Congress of Theoretical and Applied Mechanics in Beijing, China, August 23rd, 2012.

[18] M. Dunand, G. Gary and D. Mohr, “High strain rate tensile testing of sheet materials using split Hopkinson Pressure bars”, 10th International DYMAT Conference in Freiburg, Germany, September 6th, 2012.

[19] M. Dunand & A. Kamoulakos, "Application of shell-to-solid re-meshing to accurate ductile fracture predictions in AHSS sheets", 9th MIT Workshop on Experimental and Computational Fracture Mechanics in Cambridge, USA, October 8th, 2012.

[20] M. Dunand & D. Mohr, "Rate-dependent plasticity of AHSS: model formulation and experimental validation", 9th MIT Workshop on Experimental and Computational Fracture Mechanics in Cambridge, USA, October 8th, 2012.

[21] C. Roth & M. Dunand, "Effect of strain rate on the fracture of DP590", 9th MIT Workshop on Experimental and Computational Fracture Mechanics in Cambridge, USA, October 8th, 2012.

[22] M. Dunand, G. Gary & D. Mohr, "Hybrid experimental-numerical characterization of the effect of strain rate on the ductile fracture properties of AHSS sheets", Journée des Doctorants – LMS, Palaiseau, France, October 16th, 2012.

[23] M. Dunand & D. Mohr, "Effect of stress state and strain rate on the ductile fracture of AHSS sheets", International Deep Drawing Research Group 12' Conference in Mumbai, India, November 26th, 2012.

[24] M. Dunand & D. Mohr, "Prediction of shear localization in AHSS", Interim meeting of the MIT/Industry Fracture Consortium in Paris, France, April 5th, 2013.

[25] M. Dunand & D. Mohr, "Coupled rate and temperature dependent plasticity model for AHSS", Interim meeting of the MIT/Industry Fracture Consortium in Paris, France, April 5th, 2013.

Bibliography

1. Abaqus (2011). "Reference manual v6.11". Abaqus Inc.

2. Abed, F. and F. Makarem (2012). "Comparisons of Constitutive Models for Steel Over a Wide Range of Temperatures and Strain Rates". *Journal of Engineering Materials and Technology-Transactions of the Asme* **134**(2).

3. Albertini, C. and M. Montagnani (1974). "Testing technique based on the split hopkinson pressure bar", in *Mechanical Properties at high rates of strain*, The Institute of Physics: London.

4. Angel, T. (1954). "Formation of martensite in austenitic stainless steels, effect of deformation, temperature and composition". *Journal of the Iron and Steel Institute*: p. 165.

5. ASM (1990). "Metallography, Structures and Phase Diagrams". Metals Handbook. Vol. 8. American Society for Metals.

6. Bai, Y. and T. Wierzbicki (2008). "A new model of metal plasticity and fracture with pressure and Lode dependence". *International Journal of Plasticity* **24**(6): p. 1071-1096.

7. Bai, Y.L. and T. Wierzbicki (2010). "Application of extended Mohr-Coulomb criterion to ductile fracture". *International Journal of Fracture* **161**(1): p. 1-20.

8. Balasubramanian, S. and L. Anand (2002). "Elasto-viscoplastic constitutive equations for polycrystalline fcc materials at low homologous temperatures". *Journal of the Mechanics and Physics of Solids* **50**(1): p. 101-126.

9. Banabic, D., H.J. Bunge, K. Pöhlandt, and A. Tekkaya (2000). "Formability of Metallic Materials". Berlin: Springer.

10. Banu, M., M. Takamura, T. Hama, O. Naidim, C. Teodosiu, and A. Makinouchi (2006). "Simulation of springback and wrinkling in stamping of a dual phase steel rail-shaped part". *Journal of Materials Processing Technology* **173**(2): p. 178-184.

11. Bao, Y. and T. Wierzbicki (2004). "A Comparative Study on Various Ductile Crack Formation Criteria". *Journal of Engineering Materials and Technology* **126**(3): p. 314-324.

12. Bareggi, A., E. Maire, O. Bouaziz, and M. Di Michiel (2012). "Damage in dual phase steels and its constituents studied by X-ray tomography". *International Journal of Fracture* **174**(2): p. 217-227.

13. Barlat, F., J.C. Brem, J.W. Yoon, K. Chung, R.E. Dick, D.J. Lege, F. Pourgoghrat, S.H. Choi, and E. Chu (2003). "Plane stress yield function for aluminum alloy sheets - part 1: theory". *International Journal of Plasticity* **19**(9): p. 1297-1319.

14. Barsoum, I. and J. Faleskog (2007). "Rupture mechanisms in combined tension and shear—Micromechanics". *International Journal of Solids and Structures* **44**(17): p. 5481-5498.

15. Barsoum, I. and J. Faleskog (2007). "Rupture mechanisms in combined tension and shear - Experiments". *International Journal of Solids and Structures* **44**(6): p. 1768-1786.

16. Barsoum, I. and J. Faleskog (2011). "Micromechanical analysis on the influence of the Lode parameter on void growth and coalescence". *International Journal of Solids and Structures* **48**(6): p. 925-938.

17. Benzerga, A.A. (2002). "Micromechanics of coalescence in ductile fracture". *Journal of the Mechanics and Physics of Solids* **50**(6): p. 1331-1362.

18. Benzerga, A.A., J. Besson, and A. Pineau (2004). "Anisotropic ductile fracture Part II: theory". *Acta Materialia* **52**(15): p. 4639-4650.

19. Benzerga, A.A. and J.B. Leblond (2010). "Ductile Fracture by Void Growth to Coalescence". *Advances in Applied Mechanics, Vol 44* **44**: p. 169-305.

20. Bodner, S.R. and Y. Partom (1975). "Constitutive equations for elastic-viscoplastic strain-hardening materials". *Journal of Applied Mechanics* **42**(2): p. 385-389.

21. Brocks, W., D.Z. Sun, and A. Honig (1995). "Verification of the transferability of micromechanical parameters by cell model calculations with visco-plastic materials". *International Journal of Plasticity* **11**(8): p. 971-989.

22. Broggiato, G.B., F. Campana, and L. Cortese (2008). "The Chaboche nonlinear kinematic hardening model: calibration methodology and validation". *Meccanica* **43**(2): p. 115-124.

23. Brown, L.M. and J.D. Embury (1973). "The initiation and growth of voids at second phase particles". In: *Proceedings of the Third International Conference on Strength of Metals and Alloys. ICSMA 3*, p. 164–169.

24. Brozzo, P., B. Deluca, and R. Rendina (1972). "A New Method for Prediction of Formability in Metal Sheets". In: *7th biennial Conference of the IDDRG*,

25. Brunig, M. (1999). "Numerical simulation of the large elastic-plastic deformation behavior of hydrostatic stress-sensitive solids". *International Journal of Plasticity* **15**(11): p. 1237-1264.

26. Brunig, M., O. Chyra, D. Albrecht, L. Driemeier, and M. Alves (2008). "A ductile damage criterion at various stress triaxialities". *International Journal of Plasticity* **24**(10): p. 1731-1755.

27. Brunig, M. and H. Obrecht (1998). "Finite elastic-plastic deformation behaviour of crystalline solids based on a non-associated macroscopic flow rule". *International Journal of Plasticity* **14**(12): p. 1189-1208.

28. Bussac, M.-N., P. Collet, G. Gary, and R. Othman (2002). "An optimisation method for separating and rebuilding one-dimensional dispersive waves from

multi-point measurements. Application to elastic or viscoelastic bars". *Journal of the Mechanics and Physics of Solids* **50**(2): p. 321-349.

29. Cao, J., W. Lee, H.S. Cheng, M. Seniw, H.P. Wang, and K. Chung (2009). "Experimental and numerical investigation of combined isotropic-kinematic hardening behavior of sheet metals". *International Journal of Plasticity* **25**(5): p. 942-972.

30. Casey, J. and T.D. Sullivan (1985). "Pressure dependency, strength-differential effect, and plastic volume expansion in metals". *International Journal of Plasticity* **1**: p. 39-61.

31. Chaboche, J.L. (1988). "Continuum damage mechanics. 1. General concepts". *Journal of Applied Mechanics-Transactions of the Asme* **55**(1): p. 59-64.

32. Chaboche, J.L. (1988). "Continuum damage mechanics: part ii—damage growth, crack initiation and crack growth". *Journal of Applied Mechanics-Transactions of the Asme* **55**(1): p. 65-72.

33. Chaboche, J.L. (2008). "A review of some plasticity and viscoplasticity constitutive theories". *International Journal of Plasticity* **24**(10): p. 1642-1693.

34. Chen, P. and M. Koc (2007). "Simulation of springback variation in forming of advanced high strength steels". *Journal of Materials Processing Technology* **190**(1-3): p. 189-198.

35. Chu, C.C. and A. Needleman (1980). "Void nucleation effects in biaxially stretched sheets". *J. Eng. Mater. Technol.* **102**(3): p. 240-256.

36. Clift, S.E., P. Hartley, C.E.N. Sturgess, and G.W. Rowe (1990). "Fracture prediction in plastic deformation processes". *International Journal of Mechanical Sciences* **32**(1): p. 1-17.

37. Cockcrof, M.G. and D.J. Latham (1968). "Ductility and the workability of metals". *Journal of the Institute of Metals* **96**: p. 33-39.

38. Conrad, H. (1964). "Thermally activated deformation of metals". *J. Metals* **16**: p. 582.

39. Cowper, G.R. and P.S. Symonds (1952). "Strain hardening and strain rate effects in the impact loading of cantilever beams", Brown University, Div. of Appl. Mech., Report no. 28.

40. Curtze, S., V.T. Kuokkala, M. Hokka, and P. Peura (2009). "Deformation behavior of TRIP and DP steels in tension at different temperatures over a wide range of strain rates". *Materials Science and Engineering: A* **507**(1–2): p. 124-131.

41. Cvitanic, V., F. Vlak, and Z. Lozina (2008). "A finite element formulation based on non-associated plasticity for sheet metal forming". *International Journal of Plasticity* **24**(4): p. 646-687.

42. Danas, K. and P.P. Castaneda (2012). "Influence of the Lode parameter and the stress triaxiality on the failure of elasto-plastic porous materials". *International Journal of Solids and Structures* **49**(11-12): p. 1325-1342.

43. Davies, R.M. (1948). "A Critical Study of the Hopkinson Pressure Bar". *Philosophical Transactions of the Royal Society of London. Series A, Mathematical and Physical Sciences* **240**(821): p. 375-457.

44. Delannay, L., I. Doghri, and O. Pierard (2007). "Prediction of tension-compression cycles in multiphase steel using a modified incremental mean-field model". *International Journal of Solids and Structures* **44**(22-23): p. 7291-7306.

45. Delannay, L., P. Jacques, and T. Pardoen (2008). "Modelling of the plastic flow of trip-aided multiphase steel based on an incremental mean-field approach". *International Journal of Solids and Structures* **45**(6): p. 1825-1843.

46. Duffy, J., J.D. Campbell, and R.H. Hawley (1971). "On the Use of a Torsional Split Hopkinson Bar to Study Rate Effects in 1100-0 Aluminium". *Journal of Applied Mechanics* **38**: p. 83-91.

47. Dunand, M., G. Gary, and D. Mohr (2013). "Load-Inversion Device for the High Strain Rate Tensile Testing of Sheet Materials with Hopkinson Pressure Bars". *Experimental Mechanics* **In Press**.

48. Dunand, M. and D. Mohr (2010). "Hybrid experimental-numerical analysis of basic ductile fracture experiments for sheet metals". *International Journal of Solids and Structures* **47**(9): p. 1130-1143.

49. Dunand, M. and D. Mohr (2011). "On the predictive capabilities of the shear modified Gurson and the modified Mohr–Coulomb fracture models over a wide range of stress triaxialities and Lode angles". *Journal of the Mechanics and Physics of Solids* **59**(7): p. 1374-1394.

50. Dunand, M. and D. Mohr (2011). "Optimized butterfly specimen for the fracture testing of sheet materials under combined normal and shear loading". *Engineering Fracture Mechanics* **78**(17): p. 2919-2934.

51. Durrenberger, L., J.R. Klepaczko, and A. Rusinek (2007). "Constitutive modeling of metals based on the evolution of the strain-hardening rate". *Journal of Engineering Materials and Technology-Transactions of the Asme* **129**(4): p. 550-558.

52. Durrenberger, L., A. Molinari, and A. Rusinek (2008). "Internal variable modeling of the high strain-rate behavior of metals with applications to multiphase steels". *Materials Science and Engineering a-Structural Materials Properties Microstructure and Processing* **478**(1-2): p. 297-304.

53. Duszek, M.K. and P. Perzyna (1991). "The localization of plastic deformation in thermoplastic solids". *International Journal of Solids and Structures* **27**(11): p. 1419-1443.

54. Ellwood, S., L.J. Griffiths, and D.J. Parry (1982). "A tensile technique for materials testing at high strain rates". *Journal of Physics E: Scientific Instruments* **15**(11): p. 1169.

55. Fagerholt, E., C. Dorum, T. Borvik, H.I. Laukli, and O.S. Hopperstad (2010). "Experimental and numerical investigation of fracture in a cast aluminium alloy". *International Journal of Solids and Structures* **47**(24): p. 3352-3365.

56. Field, J.E., S.M. Walley, W.G. Proud, H.T. Goldrein, and C.R. Siviour (2004). "Review of experimental techniques for high rate deformation and shock studies". *International Journal of Impact Engineering* **30**(7): p. 725-775.

57. Fischer, F.D., O. Kolednik, G.X. Shan, and F.G. Rammerstorfer (1995). "A note on calibration of ductile failure damage indicators". *International Journal of Fracture* **73**(4): p. 345-357.

58. Follansbee, P.S. and U.F. Kocks (1988). "A constitutive description of the deformation of copper based on the use of the mechanical threshold stress as an internal state variable". *Acta Metallurgica* **36**(1): p. 81-93.

59. Gao, X. and J. Kim (2006). "Modeling of ductile fracture: Significance of void coalescence". *International Journal of Solids and Structures* **43**(20): p. 6277-6293.

60. Gao, X.S., G.H. Zhang, and C. Roe (2010). "A Study on the Effect of the Stress State on Ductile Fracture". *International Journal of Damage Mechanics* **19**(1): p. 75-94.

61. Gao, X.S., T.T. Zhang, J. Zhou, S.M. Graham, M. Hayden, and C. Roe (2011). "On stress-state dependent plasticity modeling: Significance of the hydrostatic stress, the third invariant of stress deviator and the non-associated flow rule". *International Journal of Plasticity* **27**(2): p. 217-231.

62. Garajeu, M., J.C. Michel, and P. Suquet (2000). "A micromechanical approach of damage in viscoplastic materials by evolution in size, shape and distribution of voids". *Computer Methods in Applied Mechanics and Engineering* **183**(3-4): p. 223-246.

63. Garrison Jr, W.M. and N.R. Moody (1987). "Ductile fracture". *Journal of Physics and Chemistry of Solids* **48**(11): p. 1035-1074.

64. Gary, G. (2005). "DAVID Instruction Manual". Palaiseau, France.

65. Gerlach, R., S.K. Sathianathan, C. Siviour, and N. Petrinic (2011). "A novel method for pulse shaping of Split Hopkinson tensile bar signals". *International Journal of Impact Engineering* **38**(12): p. 976-980.

66. Gilat, A., T. Schmidt, and A. Walker (2009). "Full Field Strain Measurement in Compression and Tensile Split Hopkinson Bar Experiments". *Experimental Mechanics* **49**(2): p. 291-302.

67. Gologanu, M., J.B. Leblond, and J. Devaux (1993). "Approximate models for ductile metals containing nonspherical voids—case of axisymmetrical prolate ellipsoidal cavities". *Journal of the Mechanics and Physics of Solids* **41**(11): p. 1723-1754.

68. Gologanu, M., J.B. Leblond, and J. Devaux (1994). "Approximate models for ductile metals containing nonspherical voids—case of axisymmetrical oblate ellipsoidal cavities". *Journal of Engineering Materials and Technology-Transactions of the Asme* **116**(3): p. 290-297.

69. Greenwood, G.W. and R.H. Johnson (1965). "The deformation of metals under small stresses during phase transformation". *Proceedings of the Royal Society of London Series a-Mathematical and Physical Sciences* **283**(1394): p. 403.

70. Gurson, A.L. (1977). "Continuum theory of ductile rupture by void nucleation and growth: part i yield criteria and flow rules for porous ductile media". *Journal of Engineering Materials and Technology-Transactions of the Asme* **99**(1): p. 2-15.

71. Guzman, O., D.J. Frew, and W. Chen (2011). "A Kolsky tension bar technique using a hollow incident tube". *Measurement Science & Technology* **22**(4).

72. Haltom, S.S., S. Kyriakides, and K. Ravi-Chandar (2013). "Ductile Failure Under Combined Shear and Tension". *International Journal of Solids and Structures*(To appear).

73. Harding, J., E.O. Wood, and J.D. Campbell (1960). "Tensile testing of materials at impact rates of strain". *ARCHIVE: Journal of Mechanical Engineering Science 1959-1982 (vols 1-23)* **2**(2): p. 88-96.

74. Haugou, G., E. Markiewicz, and J. Fabis (2006). "On the use of the non direct tensile loading on a classical split Hopkinson bar apparatus dedicated to sheet metal specimen characterisation". *International Journal of Impact Engineering* **32**(5): p. 778-798.

75. Haugou, G., E. Markiewicz, J. Fabis, and G. Gary (2004). "Contribution to the definition of a partial overlapping plastic strain rates domain for moderate loadings – application to tensile testing on metallic materials". *International Journal of Crashworthiness* **9**(2): p. 187-194.

76. He, Z., Y. He, Y. Ling, Q. Wu, Y. Gao, and L. Li (2012). "Effect of strain rate on deformation behavior of TRIP steels". *Journal of Materials Processing Technology* **212**(10): p. 2141-2147.

77. Hershey, A.V. (1954). "Plasticity of isotropic aggregate of anisotropic facecentered cubic crystals". *Journal of Applied Mechanics-Transactions of the Asme* **21**(3): p. 241-249.

78. Hill, R. (1948). "A theory of the yielding and plastic flow of anisotropic metals". *Proceedings of the Royal Society of London Series a-Mathematical and Physical Sciences* **193**(1033): p. 281-297.

79. Hollomon, J.H. (1945). "Tensile deformation". *Transaction of AIME* **162**: p. 268-290.

80. Hopkinson, B. (1914). "A Method of measuring the pressure in the deformation of high explosives by impact of bullets". *Philosophical Transactions of the Royal Society A* **213**: p. 437-452.

81. Huh, H., W. Kang, and S. Han (2002). "A tension split Hopkinson bar for investigating the dynamic behavior of sheet metals". *Experimental Mechanics* **42**(1): p. 8-17.

82. Huh, H., S.B. Kim, J.H. Song, and J.H. Lim (2008). "Dynamic tensile characteristics of TRIP-type and DP-type steel sheets for an auto-body". *International Journal of Mechanical Sciences* **50**(5): p. 918-931.

83. Huh, J., H. Huh, and C.S. Lee "Effect of strain rate on plastic anisotropy of advanced high strength steel sheets". *International Journal of Plasticity*(0).

84. Ilyushin, A.A. (1963). "Plasticity. Foundations of the general mathematical theory". Moskva: Izd. AN SSSR (In Russian).

85. Jacques, N., S. Mercier, and A. Molinari (2012). "Effects of microscale inertia on dynamic ductile crack growth". *Journal of the Mechanics and Physics of Solids* **60**(4): p. 665-690.

86. Jacques, P., Q. Furnemont, A. Mertens, and F. Delannay (2001). "On the sources of work hardening in multiphase steels assisted by transformation-induced plasticity". *Philosophical Magazine a-Physics of Condensed Matter Structure Defects and Mechanical Properties* **81**(7): p. 1789-1812.

87. Jacques, P., Q. Furnémont, T. Pardoen, and F. Delannay (2001). "On the role of martensitic transformation on damage and cracking resistance in TRIP-assisted multiphase steels". *Acta Materialia* **49**(1): p. 139-152.

88. Johnson, G.R. and W.H. Cook (1983). "A constitutive model and data for metals subjected to large strains, high strain rates and high temperatures". In: *Proceedings of the 7th International Symposium on Ballistics*, p. 541-547.

89. Johnson, G.R. and W.H. Cook (1985). "Fracture characteristics of three metals subjected to various strains, strain rate, temperatures and pressures". *Engineering Fracture Mechanics* **21**(1): p. 31-48.

90. Kajberg, J. and K.G. Sundin (2013). "Material characterisation using high-temperature Split Hopkinson pressure bar". *Journal of Materials Processing Technology* **213**(4): p. 522-531.

91. Khan, A.S., M. Baig, S.-H. Choi, H.-S. Yang, and X. Sun (2012). "Quasi-static and dynamic responses of advanced high strength steels: Experiments and modeling". *International Journal of Plasticity* **30–31**(0): p. 1-17.

92. Khan, A.S. and H. Liu (2012). "Strain rate and temperature dependent fracture criteria for isotropic and anisotropic metals". *International Journal of Plasticity* **37**(0): p. 1-15.

93. Khan, A.S., Y. Sung Suh, and R. Kazmi (2004). "Quasi-static and dynamic loading responses and constitutive modeling of titanium alloys". *International Journal of Plasticity* **20**(12): p. 2233-2248.

94. Kim, J.-H., D. Kim, H.N. Han, F. Barlat, and M.-G. Lee (2013). "Strain rate dependent tensile behavior of advanced high strength steels: Experiment and constitutive modeling". *Materials Science and Engineering: A* **559**: p. 222-231.

95. Kocks, U.F., A.S. Argon, and M.F. Ashby (1975). "Thermodynamics and kinetics of slip", in *Progress in Material Science*, Pergamon: New York. p. 68-170.

96. Kolsky, H. (1949). "An Investigation of the Mechanical Properties of Materials at very High Rates of Loading". *Proceedings of the Physical Society. Section B* **62**(11): p. 676.

97. Koplik, J. and A. Needleman (1988). "Void growth and coalescence in porous plastic solids". *International Journal of Solids and Structures* **24**(8): p. 835-853.

98. Kothari, M. and L. Anand (1998). "Elasto-viscoplastic constitutive equations for polycrystalline metals: Application to tantalum". *Journal of the Mechanics and Physics of Solids* **46**(1): p. 51-67.

99. Lademo, O.G., O.S. Hopperstad, and M. Langseth (1999). "An evaluation of yield criteria and flow rules for aluminium alloys". *International Journal of Plasticity* **15**(2): p. 191-208.

100. Lassance, D., D. Fabregue, F. Delannay, and T. Pardoen (2007). "Micromechanics of room and high temperature fracture in 6xxx Al alloys". *Progress in Materials Science* **52**(1): p. 62-129.

101. Leblond, J.B. and M. Gologanu (2008). "External estimate of the yield surface of an arbitrary ellipsoid containing a confocal void". *Comptes Rendus Mécaniques* **336**(11-12): p. 813-819.

102. Leblond, J.B., G. Perrin, and J. Devaux (1995). "An improved Gurson-type model for hardenable ductile metals". *European Journal of Mechanics a-Solids* **14**(4): p. 499-527.

103. Lecroise, F. and A. Pineau (1972). "Martensitic transformations induced by plastic deformation in the Fe–Ni–Cr–C system". *Metallurgical Transactions* **3**(2): p. 387-&.

104. Lee, M.G., D. Kim, C. Kim, M.L. Wenner, R.H. Wagoner, and K.S. Chung (2007). "A practical two-surface plasticity model and its application to spring-back prediction". *International Journal of Plasticity* **23**(7): p. 1189-1212.

105. Lee, M.G., D. Kim, C.M. Kim, M.L. Wenner, R.H. Wagoner, and K. Chung (2005). "Spring-back evaluation of automotive sheets based on isotropic-kinematic hardening laws and non-quadratic anisotropic yield functions - Part II: characterization of material properties". *International Journal of Plasticity* **21**(5): p. 883-914.

106. Lee, W., K.H. Chung, D. Kim, J. Kim, C. Kim, K. Okamoto, R.H. Wagoner, and K. Chung (2009). "Experimental and numerical study on formability of friction stir welded TWB sheets based on hemispherical dome stretch tests". *International Journal of Plasticity* **25**(9): p. 1626-1654.

107. Lemaitre, J. (1985). "A continuum damage mechanics model for ductile fracture". *Journal of Engineering Materials and Technology-Transactions of the Asme* **107**(1): p. 83-89.

108. Leroy, G., J.D. Embury, G. Edward, and M.F. Ashby (1981). "A model of ductile fracture based on the nucleation and growth of voids". *Acta Metallurgica* **29**(8): p. 1509-1522.

109. Li, M., R. Wang, and M.B. Han (1993). "A Kolsky bar: Tension, tension-tension". *Experimental Mechanics* **33**(1): p. 7-14.

110. Li, Y. and K.T. Ramesh (2007). "An optical technique for measurement of material properties in the tension Kolsky bar". *International Journal of Impact Engineering* **34**(4): p. 784-798.

111. Liang, R. and A.S. Khan (1999). "A critical review of experimental results and constitutive models for BCC and FCC metals over a wide range of strain rates and temperatures". *International Journal of Plasticity* **15**(9): p. 963-980.

112. Lindholm, U. and L. Yeakley (1968). "High strain-rate testing: Tension and compression". *Experimental Mechanics* **8**(1): p. 1-9.

113. Lode, W. (1925). "Versuche über den einflub der mittleren hauptspannug auf die fliebgrenze". *Zeitschrift für angewandte mathematik und mechanik* **5**(2): p. 142-144.

114. Lorthios, J., F. Nguyen, A.F. Gourgues, T.F. Morgeneyer, and P. Cugy (2010). "Damage observation in a high-manganese austenitic TWIP steel by synchrotron radiation computed tomography". *Scripta Materialia* **63**(12): p. 1220-1223.

115. Lundberg, B. and A. Henchoz (1977). "Analysis of elastic waves from two-point strain measurement". *Experimental Mechanics* **17**(6): p. 213-218.

116. Maire, E., O. Bouaziz, M. Di Michiel, and C. Verdu (2008). "Initiation and growth of damage in a dual-phase steel observed by X-ray microtomography". *Acta Materialia* **56**(18): p. 4954-4964.

117. Maire, E., T. Morgeneyer, C. Landron, J. Adrien, and L. Helfen (2012). "Bulk evaluation of ductile damage development using high resolution tomography and laminography". *Comptes Rendus Physique* **13**(3): p. 328-336.

118. Marciniak, Z. and K. Kuczinski (1967). "Limit strains in the processes of stretch-forming sheet metal". *International Journal of Mechanical Sciences* **9**: p. 609-620.

119. McClintock, F. (1968). "A criterion of ductile fracture by growth of holes". *Journal of Applied Mechanics* **35**(2): p. 363-&.

120. Mear, M.E. and J.W. Hutchinson (1985). "Influence of yield surface curvature on flow localization in dilatant plasticity". *Mechanics of Materials* **4**(3-4): p. 395-407.

121. Michel, J.C., O. Lopez-Pamies, P.P. Castaneda, and N. Triantafyllidis (2007). "Microscopic and macroscopic instabilities in finitely strained porous elastomers". *Journal of the Mechanics and Physics of Solids* **55**(5): p. 900-938.

122. Mohr, D., M. Dunand, and K.H. Kim (2010). "Evaluation of associated and non-associated quadratic plasticity models for advanced high strength steel sheets under multi-axial loading". *International Journal of Plasticity* **26**(7): p. 939-956.

123. Mohr, D. and G. Gary (2007). "M-shaped Specimen for the High-strain Rate Tensile Testing Using a Split Hopkinson Pressure Bar Apparatus". *Experimental Mechanics* **47**(5): p. 681-692.

124. Mohr, D. and S. Henn (2007). "Calibration of stress-triaxiality dependent crack formation criteria: A new hybrid experimental-numerical method". *Experimental Mechanics* **47**(6): p. 805-820.

125. Mohr, D. and S. Marcadet (2012). "Extended Mohr-Coulomb (EMC) model: theory and application to DP590, DP780 and TRIP780 steel", Massachusetts Institute of Technology, Impact and Crashworthiness Laboratory, Technical report 242.

126. Mohr, D. and M. Oswald (2008). "A new experimental technique for the multi-axial testing of advanced high strength steel sheets". *Experimental Mechanics* **48**(1): p. 65-77.

127. Mohr, O. (1900). "Welche Umstande bedingen die Elastizitatsgrenze und den Bruch eines Materials". *Zeitschrift des Vereins Deutscher Ingenieure Band* **44**: p. 1524–1530.

128. Morgeneyer, T.F., M.J. Starink, and I. Sinclair (2008). "Evolution of voids during ductile crack propagation in an aluminium alloy sheet toughness test studied by synchrotron radiation computed tomography". *Acta Materialia* **56**(8): p. 1671-1679.

129. Mouro, P., G. Gary, and H. Zhao (2000). "Dynamic tensile testing of sheet metal". *J. Phys. IV France* **10**(PR9): p. 149-154.

130. Nahshon, K. and J.W. Hutchinson (2008). "Modification of the Gurson Model for shear failure". *European Journal of Mechanics a-Solids* **27**(1): p. 1-17.

131. Nahshon, K. and Z.Y. Xue (2009). "A modified Gurson model and its application to punch-out experiments". *Engineering Fracture Mechanics* **76**(8): p. 997-1009.

132. Needleman, A. and V. Tvergaard (1992). "Analyses of Plastic Flow Localization in Metals". *Applied Mechanics Reviews* **45**(3S): p. S3-S18.

133. Nelder, A. and R. Mead (1965). "A Simplex Method for Function Minimization". *Computer Journal* **7**: p. 308-313.

134. Nemat-Nasser, S., J.B. Issacs, and J.E. Starrett (1991). "Hopkinson Techniques for Dynamic Recovery Experiments". *Proceedings: Mathematical and Physical Sciences* **435**(1894): p. 371-391.

135. Nicholas, T. (1981). "Tensile testing of materials at high rates of strain". *Experimental Mechanics* **21**(5): p. 177-185.

136. Nielsen, K., J. Dahl, and V. Tvergaard (2012). "Collapse and coalescence of spherical voids subject to intense shearing: studied in full 3D". *International Journal of Fracture* **177**(2): p. 97-108.

137. Nielsen, K.L. and V. Tvergaard (2009). "Effect of a shear modified Gurson model on damage development in a FSW tensile specimen". *International Journal of Solids and Structures* **46**(3-4): p. 587-601.

138. Nielsen, K.L. and V. Tvergaard (2010). "Ductile shear failure or plug failure of spot welds modelled by modified Gurson model". *Engineering Fracture Mechanics* **77**(7): p. 1031-1047.

139. Ogawa, K. (1984). "Impact-tension compression test by using a split-Hopkinson bar". *Experimental Mechanics* **24**(2): p. 81-86.

140. Oh, S.I., C.C. Chen, and S. Kobayashi (1979). "Ductile failure in axisymmetric extrusion and drawing, part 2, workability in extrusion and drawing". *Journal of Engineering for Industry-Transactions of the Asme* **101**(1): p. 36-44.

141. Oliver, S., T.B. Jones, and G. Fourlaris (2007). "Dual phase versus TRIP strip steels: comparison of dynamic properties for automotive crash performance". *Materials Science and Technology* **23**(4): p. 423-431.

142. Olson, G. and M. Cohen (1975). "Kinetics of strain-induced martensitic nucleation". *Metallurgical and Materials Transactions A* **6**(4): p. 791-795.

143. Padmanabhan, R., A.J. Baptista, M.C. Oliveira, and L.F. Menezes (2007). "Effect of anisotropy on the deep-drawing of mild steel and dual-phase steel tailor-welded blanks". *Journal of Materials Processing Technology* **184**(1-3): p. 288-293.

144. Pam-Crash (2011). "Solver Reference Manual": ESI Group.

145. Papatriantafillou, I., M. Agoras, N. Aravas, and G. Haidemenopoulos (2006). "Constitutive modeling and finite element methods for TRIP steels". *Computer Methods in Applied Mechanics and Engineering* **195**(37-40): p. 5094-5114.

146. Pardoen, T. and J.W. Hutchinson (2000). "An extended model for void growth and coalescence". *Journal of the Mechanics and Physics of Solids* **48**(12): p. 2467-2512.

147. Peirs, J., P. Verleysen, W. Van Paepegem, and J. Degrieck (2011). "Determining the stress-strain behaviour at large strains from high strain rate tensile and shear experiments". *International Journal of Impact Engineering* **38**(5): p. 406-415.

148. Ponte Castaneda, P. (1992). "New variational principles in plasticity and their application to composite materials". *Journal of the Mechanics and Physics of Solids* **49**(1757-1788).

149. Quik, M., K. Labibes, C. Albertini, T. Valentin, and P. Magain (1997). "Dynamic Mechanical Properties of Automotive Thin Sheet Steel in Tension, Compression and Shear". *J. Phys. IV France* **07**(C3): p. 379-384.

150. Rahman, M.A., C. Butcher, and Z.T. Chen (2012). "Void evolution and coalescence in porous ductile materials in simple shear". *International Journal of Fracture* **177**(2): p. 129-139.

151. Rice, J.R. (1976). "The localization of plastic deformation". In: *Theoretical and Applied Mechanics (Proceedings of the 14th International Congress on Theoretical and Applied Mechanics, Delft, ed. W.T. Koiter)*, p. 207-220.

152. Rice, J.R. and D.M. Tracey (1969). "On the ductile enlargement of voids in triaxial stress fields". *Journal of the Mechanics and Physics of Solids* **17**(3): p. 201-&.

153. Rudnicki, J.W. and J.R. Rice (1975). "Conditions for the localization of deformation in pressure-sensitive dilatant materials". *Journal of the Mechanics and Physics of Solids* **23**(6): p. 371-394.

154. Rusinek, A., R. Cheriguene, A. Bäumer, and P. Larour (2008). "Dynamic behaviour of high-strength sheet steel in dynamic tension: experimental and

numerical analyses". *The Journal of Strain Analysis for Engineering Design* **43**(1): p. 37-53.

155. Rusinek, A. and J.R. Klepaczko (2001). "Shear testing of a sheet steel at wide range of strain rates and a constitutive relation with strain-rate and temperature dependence of the flow stress". *International Journal of Plasticity* **17**(1): p. 87-115.

156. Rusinek, A. and J.R. Klepaczko (2009). "Experiments on heat generated during plastic deformation and stored energy for TRIP steels". *Materials & Design* **30**(1): p. 35-48.

157. Rusinek, A., R. Zaera, and J.R. Klepaczko (2007). "Constitutive relations in 3-D for a wide range of strain rates and temperatures - Application to mild steels". *International Journal of Solids and Structures* **44**(17): p. 5611-5634.

158. Scheyvaerts, F., P.R. Onck, C. Tekoglu, and T. Pardoen (2011). "The growth and coalescence of ellipsoidal voids in plane strain under combined shear and tension". *Journal of the Mechanics and Physics of Solids* **59**(2): p. 373-397.

159. Simo, J.C. and T.J.R. Hughes (1998). "Computational Inelasticity". Berlin: Springer.

160. Smerd, R., S. Winkler, C. Salisbury, M. Worswick, D. Lloyd, and M. Finn (2005). "High strain rate tensile testing of automotive aluminum alloy sheet". *International Journal of Impact Engineering* **32**(1-4): p. 541-560.

161. Song, B., B.R. Antoun, K. Connelly, J. Korellis, and W.-Y. Lu (2011). "Improved Kolsky tension bar for high-rate tensile characterization of materials". *Measurement Science and Technology* **22**(4): p. 045704.

162. Spitzig, W.A. and O. Richmond (1984). "The effect of pressure on the flow stress of metals". *Acta Metallurgica* **32**(3): p. 457-463.

163. Staab, G. and A. Gilat (1991). "A direct-tension split Hopkinson bar for high strain-rate testing". *Experimental Mechanics* **31**(3): p. 232-235.

164. Stoughton, T.B. (2002). "A non-associated flow rule for sheet metal forming". *International Journal of Plasticity* **18**(5-6): p. 687-714.

165. Stoughton, T.B. and J.W. Yoon (2004). "A pressure-sensitive yield criterion under a non-associated flow rule for sheet metal forming". *International Journal of Plasticity* **20**(4-5): p. 705-731.

166. Stoughton, T.B. and J.W. Yoon (2008). "On the existence of indeterminate solutions to the equations of motion under non-associated flow". *International Journal of Plasticity* **24**(4): p. 583-613.

167. Stringfellow, R.G., D.M. Parks, and G.B. Olson (1992). "A constitutive model for transformation plasticity accompanying strain-induced martensitic transformations in metastable austenitic steels". *Acta Metallurgica Et Materialia* **40**(7): p. 1703-1716.

168. Sun, X., A. Soulami, K.S. Choi, O. Guzman, and W. Chen (2012). "Effects of sample geometry and loading rate on tensile ductility of TRIP800 steel". *Materials Science and Engineering: A* **541**(0): p. 1-7.

169. Sung, J.H., J.H. Kim, and R.H. Wagoner (2010). "A plastic constitutive equation incorporating strain, strain-rate, and temperature". *International Journal of Plasticity* **26**(12): p. 1746-1771.

170. Swift, H.W. (1952). "Plastic instability under plane stress". *Journal of the Mechanics and Physics of Solids* **1**(1): p. 1-18.

171. Tanimura, S., K. Mimura, and T. Umeda (2003). "New testing techniques to obtain tensile stress-strain curves for a wide range of strain rates". *J. Phys. IV France* **110**: p. 385-390.

172. Tarigopula, V., O.S. Hopperstad, M. Langseth, and A.H. Clausen (2008). "Elastic-plastic behaviour of dual-phase, high-strength steel under strain-path changes". *European Journal of Mechanics a-Solids* **27**(5): p. 764-782.

173. Tarigopula, V., O.S. Hopperstad, M. Langseth, A.H. Clausen, and F. Hild (2008). "A study of localisation in dual-phase high-strength steels under dynamic loading using digital image correlation and FE analysis". *International Journal of Solids and Structures* **45**(2): p. 601-619.

174. Tekoglu, C., J.B. Leblond, and T. Pardoen (2012). "A criterion for the onset of void coalescence under combined tension and shear". *Journal of the Mechanics and Physics of Solids* **60**(7): p. 1363-1381.

175. Thomason, P.F. (1985). "A 3-dimensional model for ductile fracture by the growth and coalescence of microvoids". *Acta Metallurgica* **33**(6): p. 1087-1095.

176. Turteltaub, S. and A.S.J. Suiker (2005). "Transformation-induced plasticity in ferrous alloys". *Journal of the Mechanics and Physics of Solids* **53**(8): p. 1747-1788.

177. Tvergaard, V. (1981). "Influence of voids on shear band instabilities under plane strain conditions". *International Journal of Fracture* **17**(4): p. 389-407.

178. Tvergaard, V. (2008). "Shear deformation of voids with contact modelled by internal pressure". *International Journal of Mechanical Sciences* **50**(10–11): p. 1459-1465.

179. Tvergaard, V. (2009). "Behaviour of voids in a shear field". *International Journal of Fracture* **158**(1): p. 41-49.

180. Tvergaard, V. (2012). "Effect of stress-state and spacing on voids in a shear-field". *International Journal of Solids and Structures* **49**(22): p. 3047-3054.

181. Tvergaard, V. and A. Needleman (1984). "Analysis of the cup-cone fracture in a round tensile bar". *Acta Metallurgica* **32**(1): p. 157-169.

182. Van Slycken, J., P. Verleysen, J. Degrieck, J. Bouquerel, and B.C. De Cooman (2007). "Dynamic response of aluminium containing TRIP steel and its constituent phases". *Materials Science and Engineering: A* **460-461**: p. 516-524.

183. Verleysen, P. and J. Degrieck (2004). "Optical measurement of the specimen deformation at high strain rate". *Experimental Mechanics* **44**(3): p. 247-252.

184. Verleysen, P., J. Degrieck, T. Verstraete, and J. Van Slycken (2008). "Influence of Specimen Geometry on Split Hopkinson Tensile Bar Tests on Sheet Materials". *Experimental Mechanics* **48**(5): p. 587-598.

185. Verleysen, P., J. Peirs, J. Van Slycken, K. Faes, and L. Duchene (2011). "Effect of strain rate on the forming behaviour of sheet metals". *Journal of Materials Processing Technology* **211**(8): p. 1457-1464.

186. Voce, E. (1948). "The relationship between stress and strain for homogeneous deformation". *Journal of the Institute of Metals* **74**: p. 537-562.

187. Voyiadjis, G.Z. and F.H. Abed (2005). "Microstructural based models for bcc and fcc metals with temperature and strain rate dependency". *Mechanics of Materials* **37**(2–3): p. 355-378.

188. Wang, C.Y. and Y.M. Xia (2000). "Validity of one-dimensional experimental principle for flat specimen in bar-bar tensile impact apparatus". *International Journal of Solids and Structures* **37**(24): p. 3305-3322.

189. Wei, X., R. Fu, and L. Li (2007). "Tensile deformation behavior of cold-rolled TRIP-aided steels over large range of strain rates". *Materials Science and Engineering: A* **465**(1-2): p. 260-266.

190. Wierzbicki, T., D. Mohr, and ICL team (2010). "Deliverables of the joint MIT/Industry AHSS fracture consortium", Massachusetts Institute of Technology, Impact and Crashworthiness Laboratory, Technical report 205.

191. Wierzbicki, T. and L. Xue (2005). "On the Effect of the Third Invariant of the Stress Deviator on Ductile Fracture", Massachusetts Institute of Technology, Impact and Crashwortiness Laboratory, Technical report 136.

192. Wilkins, M.L., R.D. Streit, and J.E. Reaugh (1980). "Cumulative Strain-Damage Model of Ductile Fracture: Simulation and Prediction of Engineering Fracture Tests", Lawrence Livermore National Laboratory,

193. Xue, L. (2008). "Constitutive modeling of void shearing effect in ductile fracture of porous materials". *Engineering Fracture Mechanics* **75**(11): p. 3343-3366.

194. Yoshida, F., T. Uemori, and K. Fujiwara (2002). "Elastic-plastic behavior of steel sheets under in-plane cyclic tension-compression at large strain". *International Journal of Plasticity* **18**(5-6): p. 633-659.

195. Zerilli, F.J. and R.W. Armstrong (1987). "Dislocation-mechanics-based constitutive relations for material dynamics calculations". *Journal of Applied Physics* **61**(5): p. 1816-1825.

196. Zhang, K.S., J.B. Bai, and D. Francois (2001). "Numerical analysis of the influence of the Lode parameter on void growth". *International Journal of Solids and Structures* **38**(32-33): p. 5847-5856.

197. Zhao, H. and G. Gary (1995). "A three dimensional analytical solution of the longitudinal wave propagation in an infinite linear viscoelastic cylindrical bar. Application to experimental techniques". *Journal of the Mechanics and Physics of Solids* **43**(8): p. 1335-1348.

198. Zhao, H. and G. Gary (1996). "The testing and behaviour modelling of sheet metals at strain rates from 10-4 to 104 s-1". *Materials Science and Engineering A* **207**(1): p. 46-50.

199. Zhao, H. and G. Gary (1997). "A new method for the separation of waves. Application to the SHPB technique for an unlimited duration of measurement". *Journal of the Mechanics and Physics of Solids* **45**(7): p. 1185-1202.

200. Zhao, H., G. Gary, and J.R. Klepaczko (1997). "On the use of a viscoelastic split hopkinson pressure bar". *International Journal of Impact Engineering* **19**(4): p. 319-330.